ABSTRACT

Title of dissertation: CONTRIBUTIONS TOWARDS THE DETAILED UNDERSTANDING OF ROTOR FLOW FIELDS IN GROUND EFFECT OPERATIONS

Joseph Ignazio Milluzzo III, Doctor of Philosophy, 2014

Dissertation directed by: Professor J. Gordon Leishman
Department of Aerospace Engineering

High-speed flow visualization and high-resolution particle image velocimetry experiments were conducted on a two-bladed rotor that was operated in a hovering state, both out of ground effect (well away from the ground) and in ground effect at several rotor heights. Recent advances in flow diagnostic instrumentation allowed measurements of the rotor wake to be performed with unprecedented levels of resolution. In particular, the goal of the present work was to gain a better understanding of the fluid dynamics of the wake sheets (and the blade tip vortices) that were trailed from the blades. The present work examined the effects produced by two blade sets: 1. A baseline untwisted blade, 2. A twisted blade with -17° of linear twist, and has revealed fluid dynamic details of the wake sheet that were hitherto unknown. For the measurements made with the rotor operating out of ground effect, the blade sets were tested at two blade loading coefficients of 0.053 and 0.08, although only the higher loading condition was tested with the rotors operating in ground effect. For the rotor operating out of ground effect, a helicoidal tip vortex was shown to form at the blade tip and the associated wake sheets were initially

laid down as small-scale counterrotating vortical pairs. However, this initial vorticity quickly diffused and the sheet was then convected as a concentrated bands of turbulence, including several dominant eddies. Several types of sheet dynamics were documented in the rotor wake, including sheet interactions with the tip vortices, the detailed behavior of this interaction depending on both the blade twist and the rotor thrust. At earlier wake ages, a sinusoidal wave-like perturbation was seen to be formed on the wake sheets, although the growth in wave amplitude was limited as the sheets were convected and stretched in the velocity gradients in the downstream wake. When the rotor was operated in ground effect, the vorticity in the wake sheets persisted to much older wake ages. Wave-like perturbations did not form on the wake sheets when the rotors were operating in ground effect because the outward radial stretching of the rotor wake in the presence of the ground suppressed their development. The wake sheets were found to convect to the ground and introduce significant vorticity into the near-wall flow field closer to the rotor, contributing to fluctuations in the local flow velocities. The flow field near the ground was also observed to be significantly affected by the use of twist on the blade, with the wake impinging on the ground further inboard and closer to the rotor, which also resulted in higher flow velocities being produced further downstream.

Contributions Towards the Detailed Understanding of Rotor Flow Fields in Ground Effect Operations

by

Joseph Ignazio Milluzzo III

Dissertation submitted to the Faculty of the Graduate School of the
University of Maryland, College Park in partial fulfillment
of the requirements for the degree of
Doctor of Philosophy
2014

Advisory Committee:

Minta Martin Professor J. Gordon Leishman, Chair/Advisor
Associate Professor James Baeder
Associate Professor Christopher Cadou
Assistant Professor Anya R. Jones
Professor Kenneth Kiger, Dean's Representative

Dedication

To my family and wife for their continued support, encouragement, love.

Acknowledgments

First and foremost I'd like to thank my advisor and committee chair Dr. J. Gordon Leishman for giving me the opportunity to work under his guidance on this project, and for encouraging and motivating me. I have learned a lot from Dr. Leishman over the last six years first as a Teaching Assistant moonlighting as a Research Assistant and then as a full-blown Graduate Research Assistant. I will always appreciate the opportunity he provided me to pursue my graduate degrees.

I would like to thank Associate Professor James Baeder, Associate Professor Christopher Cadou, Professor Kiger, and Assistant Professor Anya R. Jones for their contributions as members of my dissertation committee.

I would like to give special thanks to the Originals (Anish Sydney, David Mayo, and Joseph Ramsey), Ben Hance, Bharath Govindarajan, and Jamie Reel for their continued support, guidance, and encouragement. You guys helped keep me level headed when nothing seemed to be going right, relax when there was time, assisted with both the lab setup and data analysis, and could always be counted on when needed.

I want to thank all of the guys who I worked with in the lab over the past six years, Bradley Johnson, Ajay Baharani, Mark Glucksman-Glaser, Andrew Lind, Monica Syal, John Tritschler,and Juergen Rauleder for making it fun to come to work everyday.

I would additionally like to thank the U.S. Air Force Office of Scientific Research, who supported this work under a Multi-Disciplinary University Research Initiative, Grant No. FA9550-08-1-0406, and Douglas Smith the grant monitor.

My deepest appreciation to: my parents, Joseph and Karen, my sister, Kalena and

my beautiful new wife Brianna for their unrelenting love, support, and understanding. For being there for the good times and the bad, and helping me to always stay focused on the light at the end of the tunnel. Their unconditional love enabled me to accomplish all that I have.

Table of Contents

List of Tables viii

List of Figures ix

1 Introduction 1

1.1 Background to the Problem of Brownout 2

1.2 Fluid Mechanics of Brownout 7

1.3 Rotor Wake Dynamics in Ground Effect 10

1.4 Sediment Particle Entrainment Mechanisms 13

1.5 Survey of Prior Work Related to Rotor Wakes 17

1.5.1 Single- and Dual-Phase Experiments 18

1.5.2 Tip Vortex Measurements 20

1.5.3 Wake Sheet Measurements 26

1.5.4 Brownout Simulations 29

1.6 Objectives of the Current Work 32

1.7 Organization of the Dissertation 32

2 Description of the Experiments 35

2.1 Introduction 35

2.2 Rotor System 35

2.3 Performance Measurements 42

2.4 Ground Plane 43

2.5 Particle Image Velocimetry (PIV) System 43

2.5.1 Seeding of the Flows 47
2.5.2 Time-Resolved Flow Measurements 48
2.5.3 Phase-Resolved flow Measurements 50
2.5.4 Regions of Interest 52
2.5.5 Flow Measurement Challenges 53
2.6 Uncertainties in the Measurements 59
2.7 Summary 62

3 Results and Discussion 64
3.1 Introduction 64
3.2 Performance Measurements 65
3.3 Out of Ground Effect Flow Field Measurements 74
3.3.1 Flow Visualization 74
3.3.2 Particle Image Velocimetry (PIV) 83
3.3.2.1 Wake Displacements 83
3.3.2.2 Averaged Velocity Field Measurements 86
3.3.2.3 Vorticity in the Wake 95
3.3.2.4 Blade Tip Region 106
3.4 In Ground Effect Flow Field Measurements 153
3.4.1 Particle Image Velocimetry 153
3.4.1.1 Wake Displacements 153
3.4.1.2 Averaged Velocity Field Measurements 162
3.4.1.3 Instantaneous Flow Field Measurements 166

4 Conclusions 182

4.1 Conclusions 182

4.2 Suggestions for Future Work 185

Appendix 189

A Algorithm used to Calculate the Circulation 189

B Q-criterion Algorithm 192

Bibliography 195

List of Tables

2.1 Errors associated with the PIV measurements and the uncertainty in the measured velocity field. 61

3.1 Induced power factor and mean profile drag coefficient for the rotor with untwisted blades when operated at various heights above the ground. . . . 68

3.2 Induced power factor and mean profile drag coefficient for the rotor with twisted blades when operated at various heights above the ground. 68

List of Figures

1.1 Flow visualization in the form of natural condensation in the tip vortices trailed from: (a) Fixed-wing aircraft (Photo by Ryan Waters); (b) Rotary-wing aircraft (Photo by tiltrotortees.com). 3

1.2 A Helicopter landing and encountering brownout conditions (Courtesy USMC). 4

1.3 Erosion damage on a rotor blade caused by frequent operations in brownout conditions (Ref. 1). 5

1.4 A helicopter generating an intense brownout dust cloud in which it becomes immersed. (Courtesy USMC.) 8

1.5 A helicopter producing a more toroidal shaped brownout dust cloud. (Photo from Agusta Westland Inc.) 8

1.6 Schematic showing the different modes of sediment particle motion and the resulting dust generated by the rotor wake from a helicopter operating over a surface covered with loose sediment. 10

1.7 Representative flow visualization of a 2-bladed rotor wake for a rotor operating (taken from Ref. 2): (a) Out of ground effect; (b) In ground effect. 14

1.8 Schematic of the forces acting on a stationary particle on a sediment bed. 15

1.9 Schematic illustrating the various sediment transport mechanisms that may occur below a helicopter rotor when operating over a mobile sediment bed [3]. 17

2.1 Rectangular rotor blade that was tested, showing the dimensions and twist rate. 37
2.2 Schematic showing the experimental setup used to obtain flow field measurements in the wake of the rotor when operating out of ground effect. . 38
2.3 Schematic showing the experimental setup used to obtain flow field measurements in the wake of the rotor when operating in ground effect. 39
2.4 Drawing showing all the individual parts that comprised the rotor hub. . . 40
2.5 Schematic showing a side-view of the rotor and ground plane when the rotor was operated in ground effect. 41
2.6 Photograph of the rotor and ground plane used in performing the flow measurements. 44
2.7 Schematic of the basic algorithm used in the PIV analysis. 47
2.8 Definition of wake age of a vortex filament trailed from a rotor blade and blade azimuth position. 52
2.9 Regions in the wake generated by the rotor hovering out of ground effect where velocity field measurements were obtained using PIV. 54
2.10 Regions in the wake generated by the rotor hovering in ground effect where velocity field measurements were obtained using PIV. 54
2.11 Comparison of data storage requirements associated with an increase in camera resolution from 4 Mp to 11 Mp. 56
2.12 Reflections off the ground plane (a) before and (b) after the implementation of reduction techniques. 58

2.13 Relocation of correlated vector when the interrogation windows overlap the interface. 59

3.1 Plot of the measured power coefficient versus ideal power coefficient for each rotor operated operated: (a) Out of ground effect ($z/R = \infty$); (b) z/R = 1.5; (c) z/R = 1.0; and (d) z/R = 0.5. 69

3.1 (Cont'd) Plot of the measured power coefficient versus ideal power coefficient for each rotor operated : (a) Out of ground effect ($z/R = \infty$); (b) z/R = 1.5; (c) z/R = 1.0; and (d) z/R = 0.5. 70

3.2 Plot showing the measured values of the lift and drag coefficients versus angle of attack in the low angle of attack regime. Data from Ref. 4. 71

3.3 Plot of the figure of merit versus blade loading coefficient for different rotor heights above the ground for a rotor with: (a) Untwisted blades and (b) Twisted blades. 72

3.4 Plot of the power loading coefficient versus blade loading coefficient for different rotor heights above the ground for a rotor with: (a) Untwisted blades and (b) Twisted blades. 73

3.5 Representative flow visualization images at two rotor thrusts taken in the rotor wake near the tip of the untwisted blades at a blade reference angle of $\psi_b \approx 30^\circ$: (a) $C_T/\sigma = 0.053$; (b) $C_T/\sigma = 0.080$. 75

3.6 Representative flow visualization images at two rotor thrusts taken in the rotor wake near the tip of the twisted blades at a blade reference angle of $\psi_b \approx 30^\circ$: (a) $C_T/\sigma = 0.053$; (b) $C_T/\sigma = 0.080$. 76

3.7 Schematic showing the nature of the bound circulation distribution along the rotor blade and the corresponding flow features trailed into the wake by a rotor. 78

3.8 Flow visualization time-history of a tip vortex trailed from the rotor with the twisted blades operating at $C_T/\sigma = 0.053$ showing the consequences of the direct interaction of the trailed tip vortex with the following blade. . 81

3.8 (Cont'd) Flow visualization time-history of a tip vortex trailed from the rotor with the twisted blades operating at $C_T/\sigma = 0.053$ showing the consequences of the direct interaction of the trailed tip vortex with the following blade. 82

3.9 Plot of the axial and radial locations of the wake sheets and tip vortices for the rotor with the untwisted blades: (a) $C_T/\sigma = 0.053$; (b) $C_T/\sigma = 0.080$. 84

3.10 Plot of the axial and radial locations of the wake sheets and tip vortices for the rotor with the twisted blades: (a) $C_T/\sigma = 0.053$; (b) $C_T/\sigma = 0.080$. 85

3.11 Summary of the radial and axial tip vortex locations in the rotor wake as a function of wake age, ζ, for the rotors with the untwisted and twisted blades: (a) Normalized radial distance; (b) Normalized axial distance. . . 87

3.12 Measured time-averaged spanwise velocity distribution at varying axial locations in the wake trailed below the rotor with the untwisted blades: (a) $C_T/\sigma = 0.053$; (b) $C_T/\sigma = 0.080$. 89

3.12 (Cont'd) Measured time-averaged spanwise velocity distribution at varying axial locations in the wake trailed below the rotor with the untwisted blades: (a) $C_T/\sigma = 0.053$; (b) $C_T/\sigma = 0.080$. 90

3.13 Measured time-averaged spanwise velocity distribution at varying axial locations in the wake trailed below the rotor with the twisted blades: (a) $C_T/\sigma = 0.053$; (b) $C_T/\sigma = 0.080$. 91

3.13 (Cont'd) Measured time-averaged spanwise velocity distribution at varying axial locations in the wake trailed below the rotor with the twisted blades: (a) $C_T/\sigma = 0.053$; (b) $C_T/\sigma = 0.080$. 92

3.14 Predictions of the spanwise distributions of bound circulation for the untwisted and twisted blades at each rotor thrust condition using a free-vortex method. 94

3.15 Contours of the normalized total flow velocity for the rotor with the untwisted blades at a blade azimuth angle of $\psi_b = 10^\circ$: (a) $C_T/\sigma = 0.053$; (b) $C_T/\sigma = 0.080$ 96

3.15 (Cont'd) Contours of the normalized total flow velocity for the rotor with the untwisted blades at a blade azimuth angle of $\psi_b = 10^\circ$: (a) $C_T/\sigma = 0.053$; (b) $C_T/\sigma = 0.080$. 97

3.16 Contours of the normalized total flow velocity for the rotor with the twisted blades at a blade azimuth angle of $\psi_b = 10^\circ$: (a) $C_T/\sigma = 0.053$; (b) $C_T/\sigma = 0.080$. 98

3.16 (Cont'd) Contours of the normalized total flow velocity for the rotor with the twisted blades at a blade azimuth angle of $\psi_b = 10^\circ$: (a) $C_T/\sigma = 0.053$; (b) $C_T/\sigma = 0.080$. 99

3.17 Contours of instantaneous vorticity in the wake below the rotor with the untwisted blades at $\psi_b = 10^\circ$: (a) $C_T/\sigma = 0.053$; (b) $C_T/\sigma = 0.080$. 101

3.18 Contours of instantaneous vorticity in the wake below the rotor with the twisted blades at $\psi_b = 10^\circ$: (a) $C_T/\sigma = 0.053$; (b) $C_T/\sigma = 0.080$. 102

3.19 Contours of mean vorticity for the rotor with the untwisted blades at $\psi_b = 30^\circ$ for: (a) $C_T/\sigma = 0.053$; (b) $C_T/\sigma = 0.080$. 104

3.20 Contours of the mean vorticity for the rotor with the twisted blades at $\psi_b = 30^\circ$ for: (a) $C_T/\sigma = 0.053$; (b) $C_T/\sigma = 0.080$. 105

3.21 Representative contours of instantaneous vorticity showing the development of the wake sheet behind the rotor: (a) $\psi_b = 10^\circ$; (b) $\psi_b = 15^\circ$; (c) $\psi_b = 30^\circ$. 107

3.22 Contours of instantaneous vorticity and corresponding flow velocity vectors near the tip of the rotor with the twisted blades at a blade azimuth angle of $\zeta = 3^\circ$. 109

3.23 Measured swirl velocity profile for a single vortical element contained in the wake sheet as produced by the twisted blades at $\zeta = 3^\circ$ and the corresponding Vatistas et al. vortex model (Ref 5). 111

3.24 Variations in the local Richardson's number with distance from the vortex core for vortices in the wake sheet produced by the rotor with twisted blades for $\zeta = 3^\circ$ and $\zeta = 9^\circ$. 112

3.25 Phase-resolved instantaneous vorticity realizations at $\zeta = 6^\circ$ for the rotor with the untwisted blades showing the aperiodic nature of the wake sheet: (a) First realization; (b) Second realization; (c) Third realization; (d) Fourth realization. 114

3.25 (Cont'd) Phase-resolved instantaneous vorticity realizations at $\zeta = 6^\circ$ for the rotor with the untwisted blades showing the aperiodic nature of the wake sheet: (a) First realization; (b) Second realization; (c) Third realization; (d) Fourth realization. 115

3.25 (Cont'd) Phase-resolved instantaneous vorticity realizations at $\zeta = 6^\circ$ for the rotor with the untwisted blades showing the aperiodic nature of the wake sheet: (a) First realization; (b) Second realization; (c) Third realization; (d) Fourth realization. 116

3.25 (Cont'd) Phase-resolved instantaneous vorticity realizations at $\zeta = 6^\circ$ for the rotor with the untwisted blades showing the aperiodic nature of the wake sheet: (a) First realization; (b) Second realization; (c) Third realization; (d) Fourth realization. 117

3.26 Phase-resolved instantaneous vorticity realizations at $\zeta = 6^\circ$ for the rotor with the twisted blades showing the aperiodic nature of the wake sheet: (a) First realization; (b) Second realization; (c) Third realization; (d) Fourth realization. 118

3.26 (Cont'd) Phase-resolved instantaneous vorticity realizations at $\zeta = 6^\circ$ for the rotor with the twisted blades showing the aperiodic nature of the wake sheet: (a) First realization; (b) Second realization; (c) Third realization; (d) Fourth realization. 119

3.26 (Cont'd) Phase-resolved instantaneous vorticity realizations at $\zeta = 6^\circ$ for the rotor with the twisted blades showing the aperiodic nature of the wake sheet: (a) First realization; (b) Second realization; (c) Third realization; (d) Fourth realization. 120

3.26 (Cont'd) Phase-resolved instantaneous vorticity realizations at $\zeta = 6^\circ$ for the rotor with the twisted blades showing the aperiodic nature of the wake sheet: (a) First realization; (b) Second realization; (c) Third realization; (d) Fourth realization. 121

3.27 Contours of instantaneous vorticity in the wake generated by the rotor with untwisted blades operating at $C_T/\sigma = 0.08$ for: (a) $\zeta = 6^\circ$; (b) $\zeta = 30^\circ$. 122

3.27 (Cont'd) Contours of instantaneous vorticity in the wake generated by the rotor with untwisted blades operating at $C_T/\sigma = 0.08$ for: (a) $\zeta = 6^\circ$; (b) $\zeta = 30^\circ$. 123

3.28 Contours of instantaneous vorticity in the wake generated by the rotor with twisted blades operating at $C_T/\sigma = 0.08$ for: (a) $\zeta = 6^\circ$; (b) $\zeta = 30^\circ$. . 124

3.28 (Cont'd) Contours of instantaneous vorticity in the wake generated by the rotor with twisted blades operating at $C_T/\sigma = 0.08$ for: (a) $\zeta = 6^\circ$; (b) $\zeta = 30^\circ$. 125

3.29 Contours of instantaneous vorticity near the tip of the untwisted blade at the low thrust condition (i.e., $C_T/\sigma = 0.053$): (a) $\psi_b = 0^\circ$; (b) $\psi_b = 3^\circ$; (c) $\psi_b = 6^\circ$; (d) $\psi_b = 9^\circ$. 126

3.29 (Cont'd) Contours of instantaneous vorticity near the tip of the untwisted blade when at C_T/σ = 0.053: (a) $\psi_b = 0°$; (b) $\psi_b = 3°$; (c) $\psi_b = 6°$; (d) $\psi_b = 9°$. 127

3.29 (Cont'd) Contours of instantaneous vorticity near the tip of the untwisted blade at C_T/σ = 0.053: (a) $\psi_b = 0°$; (b) $\psi_b = 3°$; (c) $\psi_b = 6°$; (d) $\psi_b = 9°$. 128

3.29 (Cont'd) Contours of instantaneous vorticity near the tip of the untwisted blade at C_T/σ = 0.053: (a) $\psi_b = 0°$; (b) $\psi_b = 3°$; (c) $\psi_b = 6°$; (d) $\psi_b = 9°$. 129

3.30 Contours of instantaneous vorticity near the tip of the untwisted blade at C_T/σ = 0.080: (a) $\psi_b = 0°$; (b) $\psi_b = 3°$; (c) $\psi_b = 6°$; (d) $\psi_b = 9°$. 130

3.30 (Cont'd) Contours of instantaneous vorticity near the tip of the untwisted blade at C_T/σ = 0.080: (a) $\psi_b = 0°$; (b) $\psi_b = 3°$; (c) $\psi_b = 6°$; (d) $\psi_b = 9°$. 131

3.30 (Cont'd) Contours of instantaneous vorticity near the tip of the untwisted blade at C_T/σ = 0.080: (a) $\psi_b = 0°$; (b) $\psi_b = 3°$; (c) $\psi_b = 6°$; (d) $\psi_b = 9°$. 132

3.30 (Cont'd) Contours of instantaneous vorticity near the tip of the untwisted blade at C_T/σ = 0.080: (a) $\psi_b = 0°$; (b) $\psi_b = 3°$; (c) $\psi_b = 6°$; (d) $\psi_b = 9°$. 133

3.31 Contours of instantaneous vorticity near the tip of the twisted blade at C_T/σ = 0.053: (a) $\psi_b = 0°$; (b) $\psi_b = 3°$; (c) $\psi_b = 6°$; (d) $\psi_b = 9°$. 134

3.31 (Cont'd) Contours of instantaneous vorticity near the tip of the twisted blade at C_T/σ = 0.053: (a) $\psi_b = 0°$; (b) $\psi_b = 3°$; (c) $\psi_b = 6°$; (d) $\psi_b = 9°$. 135

3.31 (Cont'd) Contours of instantaneous vorticity near the tip of the twisted bladeat C_T/σ = 0.053: (a) $\psi_b = 0°$; (b) $\psi_b = 3°$; (c) $\psi_b = 6°$; (d) $\psi_b = 9°$. 136

3.31 (Cont'd) Contours of instantaneous vorticity near the tip of the twisted blade at C_T/σ = 0.053: (a) $\psi_b = 0°$; (b) $\psi_b = 3°$; (c) $\psi_b = 6°$; (d) $\psi_b = 9°$. 137

3.32 Contours of instantaneous vorticity near the tip of the twisted blade at $C_T/\sigma = 0.080$: (a) $\psi_b = 0°$; (b) $\psi_b = 3°$; (c) $\psi_b = 6°$; (d) $\psi_b = 9°$. 139

3.32 (Cont'd) Contours of instantaneous vorticity near the tip of the twisted blade at $C_T/\sigma = 0.080$: (a) $\psi_b = 0°$; (b) $\psi_b = 3°$; (c) $\psi_b = 6°$; (d) $\psi_b = 9°$. 140

3.32 (Cont'd) Contours of instantaneous vorticity near the tip of the twisted blade at $C_T/\sigma = 0.080$: (a) $\psi_b = 0°$; (b) $\psi_b = 3°$; (c) $\psi_b = 6°$; (d) $\psi_b = 9°$. 141

3.32 (Cont'd) Contours of instantaneous vorticity near the tip of the twisted blade at $C_T/\sigma = 0.080$: (a) $\psi_b = 0°$; (b) $\psi_b = 3°$; (c) $\psi_b = 6°$; (d) $\psi_b = 9°$. 142

3.33 Representative tip vortex characteristics a function of wake age for a rotor operating in ground effect: (a) Peak swirl velocity; (b) Vortex core size. . 145

3.34 Plot of the measured peak circulation in the tip vortex versus wake age normalized by the total circulation in the outboard portion of the wake sheet. 146

3.35 Plot showing the total positive, negative, and predicted circulation trailed from the tip region of the: (a) Untwisted blade; (b) Twisted blade. 147

3.36 Example of the affect of camera resolution on the ability to resolve the axial velocity induced by the wake sheet: (a) 11 Mp camera; (b) 4 Mp camera; (c) 2 Mp camera. 150

3.37 Example of the affect of camera resolution on the ability to resolve the vorticity contained in the wake sheet: (a) 11 Mp camera; (b) 4 Mp camera; (c) 2 Mp camera. 151

3.38 Plot of the axial and radial locations of the wake sheets and tip vortices when operating in ground effect with: (a) Untwisted blades; (b) Twisted blades. 155

3.39 Schematic showing the reference frames used for the rotor when operating: (a) Out of ground effect; (b) In ground effect. 156

3.40 Plot of the axial and radial locations (using a rotor based reference frame) of the wake sheets and tip vortices in ROIs 1 and 2 using a rotor based reference frame for the rotor with untwisted blades operated: (a) Out of ground effect ($z/R = \infty$); (b) In ground effect ($z/R = 1.0$). 160

3.41 Plot of the axial and radial locations (for a rotor based reference frame) of the wake sheets and tip vortices in ROIs 1 and 2 for the rotor with the twisted blades operated: (a) Out of ground effect ($z/R = \infty$); (b) In ground effect ($z/R = 1.0$). 161

3.42 Summary of the tip vortex locations (using a ground based reference frame) in the rotor wake as a function of wake age, ζ, for the rotors with the untwisted and twisted blades: (a) Normalized radial distance; (b) Normalized axial distance. 163

3.43 Schematic showing the wake generated by a rotor operating in ground effect. 166

3.44 Measured time-averaged spanwise velocity distribution at varying axial locations in ROIs 1–4 for the rotor with untwisted blades when operated at $z/R = 1.0$ off the ground plane. 167

3.45 Measured time-averaged spanwise velocity distribution at varying axial locations in ROIs 1–4 for the rotor with twisted blades when operated at $z/R = 1.0$ off the ground plane. 168

3.46 Measured time-averaged velocity distribution at varying radial locations in ROIs 5 and 6 for the rotor with the untwisted blades. 169

3.47 Measured time-averaged velocity distribution at varying radial locations in ROIs 5 and 6 for the rotor with the twisted blades. 170

3.48 PIV measurements of the instantaneous realization of the flow field in ROIs 1 and 2 for the rotor with the untwisted blades at a blade azimuth angle $\psi_b = 30^\circ$. Background contours are of velocity magnitude. 171

3.49 PIV measurements of the instantaneous realization of the flow field in ROIs 1 and 2 for the rotor with the twisted blades at a blade azimuth angle $\psi_b = 30^\circ$. Background contours are of velocity magnitude. 172

3.50 Instantaneous realization of the flow field in ROIs 1 and 2 for the rotor with the untwisted blades at a blade azimuth angle $\psi_b = 30^\circ$. Background contours are of vorticity. 176

3.51 Instantaneous realization of the flow field in ROIs 1 and 2 for the rotor with the twisted blades at a blade azimuth angle $\psi_b = 30^\circ$. Background contours are of vorticity. 177

3.52 Instantaneous realization of the flow field in ROIs 5 and 6 for the rotor with the untwisted blades at a blade azimuth angle $\psi_b = 30^\circ$. Background contours are of vorticity. 178

3.53 Instantaneous realization of the flow field in ROIs 5 and 6 for the rotor with the twisted blades at a blade azimuth angle $\psi_b = 30°$. Background contours are of vorticity. 179

3.54 Instantaneous realization of the flow field in ROIs 5 and 6 for the rotor with the untwisted blades at a blade azimuth angle $\psi_b = 30°$. Background contours are of the wall-normal velocity. 180

3.55 Instantaneous realization of the flow field in ROIs 5 and 6 for the rotor with the twisted blades at a blade azimuth angle ψ_b 30°. Background contours are of the wall-normal velocity. 181

A.1 Path enclosing a tip vortex utilized for evaluating the line integral. 191

A.2 Contours of instantaneous vorticity near the tip of the twisted blades when operating at $C_T/\sigma = 0.080$. 191

Nomenclature

A	Rotor disk area, πR^2 , ft^2
d_1, d_2	Empirical constants for the sectional drag coefficient
d_{diff}	Diffraction limited minimum image diameter, μm
d_τ	Particle image diameter, μm
C_{d_0}	Zero-lift drag coefficient
C_{l_α}	Lift curve slope, rad^{-1}
C_P	Rotor power coefficient, $P/\rho A\Omega^3 R^3$
$C_{P_{\text{ideal}}}$	Ideal rotor power coefficient, $C_T^{3/2}/\sqrt{2}$
C_Q	Rotor power coefficient, $Q/\rho A\Omega^2 R^3$
C_T	Rotor thrust coefficient, $T/\rho A\Omega^2 R^2$
c	Rotor blade chord, ft
M	image magnification
N_b	Number of blades
P	Measured rotor power, hp
Q	Measured rotor torque, ft-lb
r_G, z_G	Ground based coordinate system, m, m
r_R, z_R	Rotor based coordinate system, m, m
r_c	Vortex core radius, m or ft
r_0	Initial core radius, m or ft
$\bar{r}$	Non-dimensional radial distance, r/r_c
R	Radius of blade, m or ft

Re_{tip}	Tip Reynolds number, $\omega Rc/\nu$
Re_v	Vortex Reynolds number, Γ_v/ν
Ri	Richardson number
T	Rotor thrust, lb
u, v	Velocities in r and z directions, respectively, ms^{-1}
V_{tip}	Rotor tip speed, ms^{-1}
V_θ	Swirl velocity, ms^{-1}
v_h	Hover induced velocity, $\sqrt{T/2\rho A}$, ms^{-1}
Γ_v	Circulation or vortex strength, m^2s^{-1}
Γ_N	Total negative circulation, m^2s^{-1}
Γ_P	Total positive circulation, m^2s^{-1}
$\Gamma_{\text{Predicted}}$	Predicted positive circulation, m^2s^{-1}
Δt	pulse separation time, s
Δx, Δy	grid spacing, m
ε_a	Acceleration uncertainty
ε_c	Curvature uncertainty
ε_M	Magnification uncertainty
$\varepsilon_{\Delta t}$	Pulse separation time uncertainty
μ	Dynamic viscosity, kg m^{-1} s^{-1}
ν	Kinematic viscosity, m^2s^{-1}

κ	Induced power factor
ρ	Flow density, kg m^{-3}
σ	Rotor solidity, $N_b c/\pi R$
σ_{rand}	Random error, μm
ψ_b	Blade azimuth angle, deg
Ω	Rotational speed of the rotor, rad s^{-1}
ω	Vorticity, $m^2 s^{-1}$
ζ	Wake age, deg

Abbreviations

CCD	Charge Coupled Device
CFD	Computational Fluid Dynamics
CMOS	Complementary Metal Oxide Semiconductor
DARPA	Defense Advanced Research Projects Agency
DAQ	Data Acquisition
FFT	Fast Fourier Transform
fps	Frames-Per-Second
FV	Flow Visualization
PIV	Particle Image Velocimetry
PR-PIV	Phase-Resolved Particle Image Velocimetry
TR-FV	Time-Resolved Flow Visualization
TR-PIV	Time-Resolved Particle Image Velocimetry

Chapter 1

Introduction

The ability of a helicopter to move forward, backward, side-to-side as well as to hover and take-off and land vertically make it uniquely suited for many different missions. For example, a helicopter is well-suited for missions performed in confined landing zones, over unprepared surfaces, and where a loiter and/or continuous hovering flight is required, i.e., for search and rescue, resupply, and insertion. For these reasons the modern helicopter has become an indispensable part of all military forces throughout the world. In particular, the U.S. Navy projects that by 2015 more than 50% of their pilots will be helicopter pilots, which is a significant increase over previous years. While the vertical take-off and landing capability of helicopters is indispensable for military applications, such a capability is also needed for many civilian applications, including search and rescue and medical evacuation (i.e., MEDEVAC) missions.

Unlike fixed-wing aircraft whose wakes are convected quickly away from the lifting surfaces from which they were generated (see Fig. 1.1a), the wake generated by a hovering rotor stays in relatively close proximity to the rotor blades; see Fig. 1.1b. Therefore, many aspects of rotor behavior (e.g. performance, unsteady airloads, vibrations, noise, etc.) are all affected by the induced flow effects produced by of the three-dimensional vortical wakes generated by the rotor blades. Furthermore, when operating in close proximity to an unprepared surface, the interactions of the rotor wake with the ground can rapidly

generate “brownout” conditions, which is a problem that has partly motivated the present research work. However, the problem of understanding the effect that the wake sheet has on the development of the rotor wake and in particular, the blade tip vortices is a long standing issue.

1.1 Background to the Problem of Brownout

The problem of brownout occurs when a rotorcraft takes off or lands over surfaces covered with loose, dry sediment, such as sand or dust. The complex fluid dynamic interactions of the rotor wake with the sediment bed can quickly generate an intense dust cloud that engulfs the entire vehicle. Figure 1.2 shows an example of a helicopter encountering brownout conditions during a landing in the desert. A similar phenomenon, known as whiteout, can occur under snowy conditions.

During near-ground operations, pilots determine the aircraft’s motion and spatial orientation using visual cues such as the horizon, features on the ground such as vegetation (e.g., grass, bushes, trees, etc.), and various other man-made structures that are nearby (e.g., buildings, lights, cars or trucks). The developing dust cloud can rapidly reduce the pilot’s ability to distinguish these necessary visual cues. Furthermore, the relative motion of the dust cloud in the pilots field of view can be perceived as apparent motion effects or vection illusions, which can cause the pilot to experience spatial disorientation [6, 7]. Because pilots rely almost exclusively on visual cues when flying near the ground, the sudden loss of these cues combined with other illusions makes the onset of brownout a serious safety of flight issue. In fact, brownout is the leading cause of human-factor



(a) Fixed-wing aircraft



(b) Rotary-wing aircraft

Figure 1.1: Flow visualization in the form of natural condensation in the tip vortices trailed from: (a) Fixed-wing aircraft (Photo by Ryan Waters); (b) Rotary-wing aircraft (Photo by tiltrotortees.com).



Figure 1.2: A Helicopter landing and encountering brownout conditions (Courtesy USMC).

related mishaps during military operations [8], and civil rotorcraft operations are not immune either [9], specifically those operations performed from unprepared surfaces such as fields.

In addition to being a safety of flight concern, the uplifted sediment particles in a brownout cloud can also create a harsh working environment for ground personnel. Another important issue is the that brownout can rapidly increase wear on critical mechanical components such as rotor blades, engines, and other mechanical components. For example, the leading edge of rotor blades are covered with metallic strips to prevent abrasion.

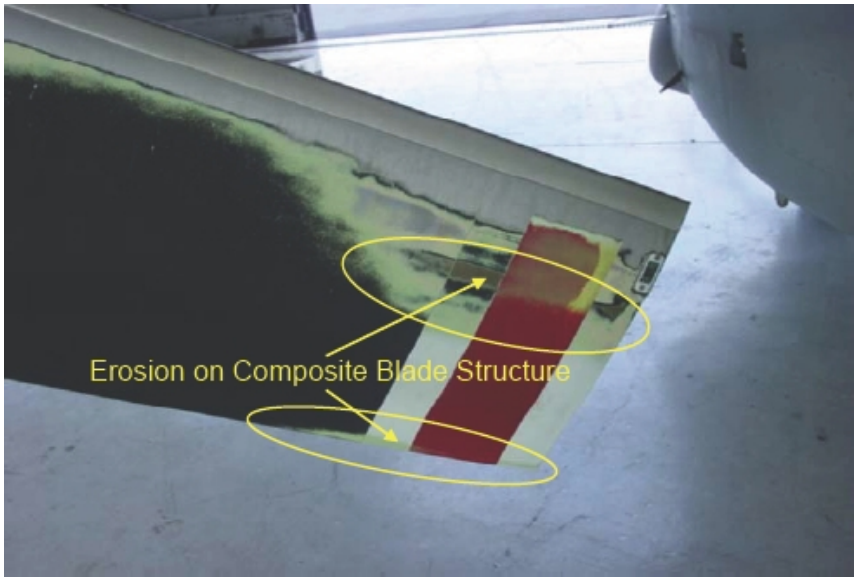

Figure 1.3: Erosion damage on a rotor blade caused by frequent operations in brownout conditions (Ref. 1).

However, Fig. 1.3 shows that the continued impact of dust particles can quickly erode these metallic strips to the underlying composite core [1]. Blade erosion can eventually affect the structural integrity of the rotor blades, to the point that they need to be replaced within tens of flight hours instead of the tens of thousands of hours for which they were otherwise designed. Engines can also suffer from serious wear after ingesting dust, opening up compressor clearances and reducing power output. The increased maintenance required to replace/repair worn components dramatically decreases the operational readiness of the aircraft.

Lately, technical efforts have been made to reduce the risk associated with flying rotorcraft under brownout conditions. The majority of this work has focused on developing advanced sensor technology and displays, such as Head-Up displays (HUD), Head-Down displays (HDD) or Helmet-Mounted displays (HMD), to allow the pilot to "see-

through" the brownout cloud and thereby increase their situational awareness, DARPA's Sandblaster, Lockheed Martin's Pathfinder, and PhLASH by the U.S. Air Force Research Laboratory (i.e., Ref. 10–12) being a few examples. While advanced avionics can significantly increase flight safety under brownout conditions, these systems do not solve the fundamental problem of sediment mobilization and uplift. To mitigate the problem of brownout at its source, therefore, a better understanding of the fluid dynamics of rotor wakes interacting with the ground is needed.

Pilots have also developed landing and takeoff strategies (e.g., using flight path management) to minimize operational time under brownout conditions [13]. A few such techniques include: 1. Flying close to the ground at high enough speeds to outpace the developing dust cloud before landing, and 2. Using increased rates of descent near the landing zone, thereby landing before the dust cloud has a chance to fully develop. However, these techniques can be dangerous and require the pilot to land the vehicle quickly and firmly before visibility is lost in the dust cloud. Furthermore, being able to land before visibility is lost depends on many factors, such as vehicle weight, density altitude, etc., and often requires the pilot to perform a "hard" landing, which can be detrimental to the aircraft as well as the crew.

A permanent solution to the problem of brownout may ultimately come through means that lead to a reduction of the overall severity of the brownout cloud. Vehicle design could emerge as one such solution, however, to do this a better understanding of the interaction of the rotor wake with the ground is required, i.e., to understand the underlying fluid dynamic mechanisms that are responsible for the generation of the brownout dust clouds. With this in mind, an examination of photographs and videography of he-

licopters encountering brownout conditions seems to indicate that some helicopters are more susceptible to generating intense brownout conditions than others [14].

One such helicopter (shown in Fig. 1.4) produces a severe brownout signature with the helicopter being almost completely engulfed by the large, dome-shaped cloud. However, the other helicopter shown in Fig. 1.5 clearly produces a region near the helicopter with better visibility for the pilot. In this case, the cloud has formed into a toroidal shape with the majority of the uplifted sediment being blown further away from the landing zone, leaving regions of fairly good visibility for the pilot. The significance of the rotor wake in this problem cannot be underestimated, and the effects of the rotor and airframe design characteristics may be very important too. To this end, the goal of the present work was to better quantify the fluid dynamics of the rotor wake as it interacted with a ground plane, this being done in the laboratory using a sub-scale rotor system.

1.2 Fluid Mechanics of Brownout

A understanding of the fluid dynamic mechanisms involved in the formation of a brownout cloud is a prerequisite for brownout mitigation. The problem of brownout is a two-phase fluid dynamics problem: 1. The carrier phase describes the three dimensional, unsteady flow from the wake produced by the rotor operating in ground effect, and 2. The dispersed phase consists of a nonuniform concentration of sediment particles that have been mobilized and uplifted by the interaction of the rotor wake with the sediment bed lying over the ground. The overall fluid dynamic complexity of brownout stems from the dual-phase nature of the flow, which significantly increases the complexity that is



Figure 1.4: A helicopter generating an intense brownout dust cloud in which it becomes immersed. (Courtesy USMC.)



Figure 1.5: A helicopter producing a more toroidal shaped brownout dust cloud. (Photo from Agusta Westland Inc.)

associated with measuring, understanding, and modeling the problem of brownout. The complexity of the problem is increased further because of the coupled nature of the carrier and dispersed phases of the flow, which can transfer momentum and energy between the flow phases.

A schematic of the fluid dynamic mechanisms and the aeolian (or sedimentology) processes involved in the problem of brownout is shown in Fig. 1.6. The mobilization of sediment particles will be influenced by the specific characteristics of the flow fields induced by the rotor wake on the ground. In particular, the rotor downwash and the vortical flow will induce an unsteady velocity field above the sediment bed. If the flow velocity and boundary layer shear stress exceeds some critical threshold, then the loose particles can become mobilized and uplifted into the flow. Some of the mobilized particles will fall back to the bed under the action of gravity, while others will encounter upward flow velocities, especially those induced by the tip vortices and turbulent eddies as they convect above the sediment bed. If the particles are then subsequently uplifted and convected into the flow, they can remain suspended or be reingested by the rotor. The more severe brownout problems seem to occur when the rotor reingests much of the suspended dust particles, bombarding them back onto the sediment bed at higher velocity, thereby dislodging many more particles and ejecting them into the flow [15]. Therefore, the fundamental nature of brownout usually manifests as a cascading process that leads to rapid increases in the total quantity and volume of airborne dust particles [3].

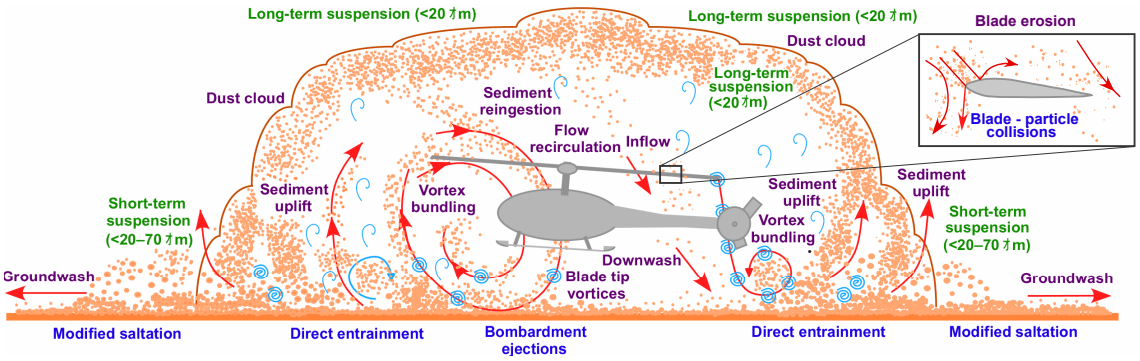

Figure 1.6: Schematic showing the different modes of sediment particle motion and the resulting dust generated by the rotor wake from a helicopter operating over a surface covered with loose sediment.

1.3 Rotor Wake Dynamics in Ground Effect

The presence of the ground below the rotor greatly influences the development of the rotor wake. It has been well documented in the literature that rotors operating in ground effect experience a significant increase in performance compared to operations away from the ground [16–21]. Research has shown that the thrust of a rotor hovering in ground effect increases for a given power supplied, or that a lower power is required for a rotor to hover in ground effect at the same thrust (or vehicle weight). This behavior arises because in ground effect the induced velocity at the rotor disk decreases as compared to rotor operation out of ground effect, thereby slightly increasing the angles of attack along the blades. Furthermore, for the rotor to produce the same thrust in ground effect, the rotor blades can operate at reduced pitch angles, which slightly decreases both the induced and profile power consumption of the rotor.

The action of the rotor wake is fundamental in the mobilization and uplift of loose

sediment. Therefore, a prerequisite to understanding the problem of brownout is to obtain a better understanding of the evolution of the rotor wake as it interacts with the ground. In this regard, the flow field generated by a rotor hovering in ground effect is very different to what would be obtained for the same rotor when its operating out of ground effect; see Fig. 1.7. These flow visualization images, which are taken in a radial plane through the rotor wake when the flow was seeded with smoke and illuminated by a laser light sheet, show slices of the helicoidal vortex filaments trailed from the rotor blade tips. These vortices become visible as the blade passes through the imaging plane and the smoke particles scatter the laser light. The vortex filaments can be identified in the flow visualization images by the presence of the darker, almost circular regions, which mark the inner regions of the vortex cores.

Notice from Fig. 1.7 that at early wake ages when the rotor is hovering out of ground effect the vortex cores appear relatively laminar, i.e., devoid of the turbulence that is present in the surrounding flow field; see Fig. 1.7a. However, after only 2–3 rotor revolutions, the action of turbulence and viscosity cause the tip vortices to diffuse their concentrated vorticity. Furthermore, the onset of instabilities in the downstream wake can cause adjacent turns of the helical vortex filaments to begin to interact with each other and even pair, further complicating the overall development of the downstream wake flow.

In addition to trailed tip vortex filaments, turbulent wake sheets are trailed from the inboard parts of the rotor blade, as shown in Fig. 1.7a. These sheets, which are often referred to as "wake sheets" [3,22,23], are of primary interest in the present work and can be identified by the shear layers that form in the smoke streaklines. From the flow measurements, Fig. 1.7a shows that these wake sheets contain a significant amount of turbulence

and vorticity. Furthermore, the wake sheets can be seen to convect axially quicker than the corresponding blade tip vortex and, therefore, interact with several sequential turns of the tip vortex, i.e., the sheet also interacts with older vortices.

In the corresponding in ground effect case shown in Fig. 1.7b, the wake initially contracts below the rotor. However, because the ground plane must be a streamline of the flow, the direction of the wake flow turns rapidly near the ground, changing from a primarily axial (downward) flow to a primarily radial (outward) flow and creating a wall-jet like flow along the ground plane. This wall-jet initially thins as the flow convects radially outward but then begins to thicken further downstream [2].

The radial expansion of the rotor wake along the ground also causes the vortex filaments to stretch along their lengths. This process results in a reintensification of their vorticity and so increasing the swirl velocities induced by the vortices [24, 25]. The mechanism of reintensification slows and can even counter the normal process of vorticity diffusion, thereby allowing the vortices to persist in a more concentrated form to significantly later wake ages (i.e., for 4 to 5 rotor revolutions or more); see Fig. 1.7b. The stretching of the vortex filaments can also significantly affect the process of sediment mobilization and uplift because of the larger induced velocities that are now generated over the sediment bed [3, 26]. Good explanations of the flow physics associated with rotors hovering in ground effect is given in Refs. 2, 3, 23, 26.

When flying near the ground, rotorcraft rarely operate in a steady hover instead pilots perform appropriate landing and takeoff maneuvers. In this case, the constant changes in rotor height near the ground increase the complexity of the flow fields considerably compared to that in a steady hover. Two characteristic flow regimes are often seen during

these flight maneuvers [27, 28]: 1. At low forward advance ratios, a recirculation region, and 2. At higher advance ratios a ground vortex region. Because sediment mobilization and uplift is directly related to the flow fields produced near the ground, these flow regimes will significantly affect the motion of the individual sediment particles [27–29].

1.4 Sediment Particle Entrainment Mechanisms

As previously explained, formation of a brownout cloud is caused by the flow field induced by the rotor and its wake. The interaction of the flow with the sediment bed results in the mobilization and uplift of sediment particles. Therefore, to understand the problem of brownout it is necessary to understand both the characteristics of the rotor wake as well as the physics involved in the transport of sediment. Sediment transport can be decomposed into two main fields of study: 1. Wind-driven particle transport where the sediment motion is caused by the wind, i.e. an aeolian flow, and 2. Hydrodynamic particle transport where sediment motion is caused by oceanic or riverine flows. The primary interest of the problem of brownout is sediment dynamics under the action of air, which has been studied extensively in the field of sedimentology, for example see the works of Bagnold [30] and Greeley and Iversen [31].

Wind-driven particle motion can be decomposed into three main processes: 1. Mobilization, which is marked by the initial motion of the particles because of the action of the external flow, 2. Entrainment, the process by which the sediment particles are uplifted from the bed by the fluid flow, and 3. Transport, which governs the path the sediment particles follow after being entrained into the flow field. The initial mobilization and en-

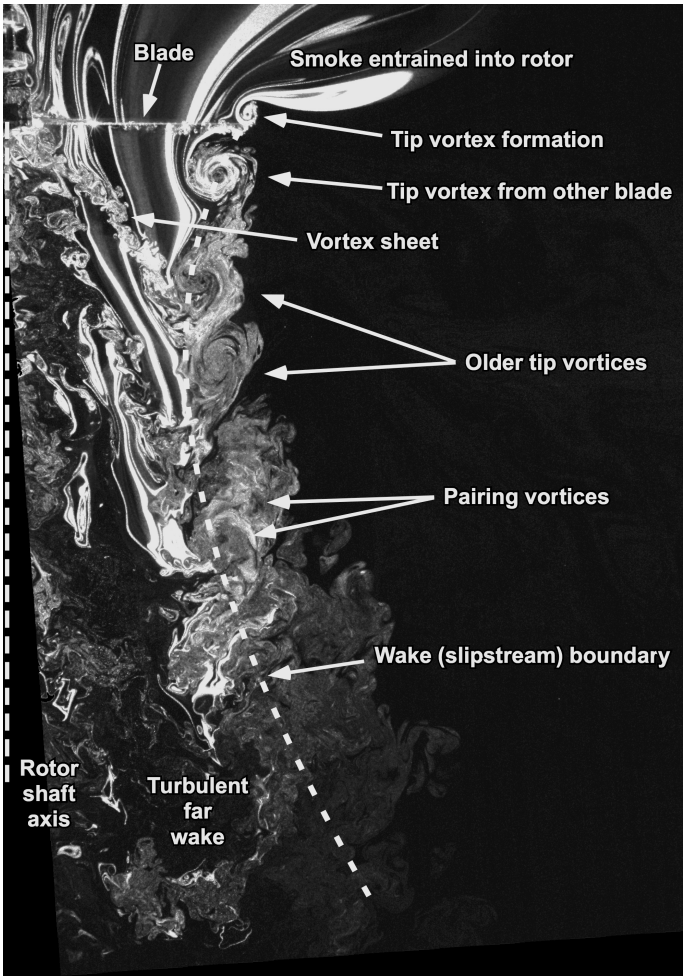

(a) Out of ground effect

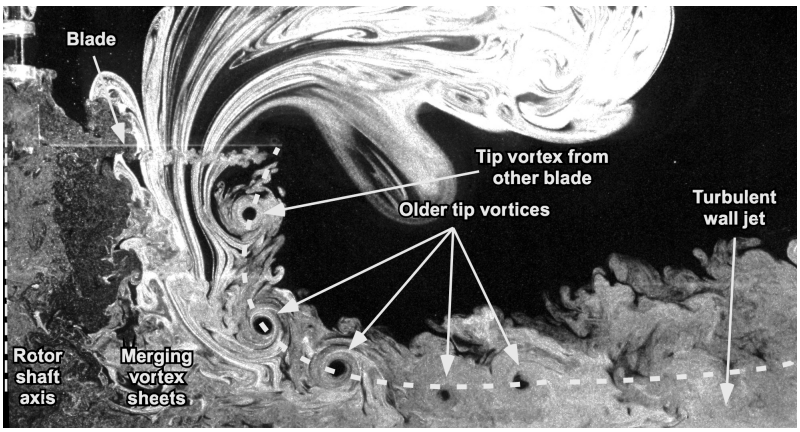

(b) In ground effect

Figure 1.7: Representative flow visualization of a 2-bladed rotor wake for a rotor operating (taken from Ref. 2): (a) Out of ground effect; (b) In ground effect.

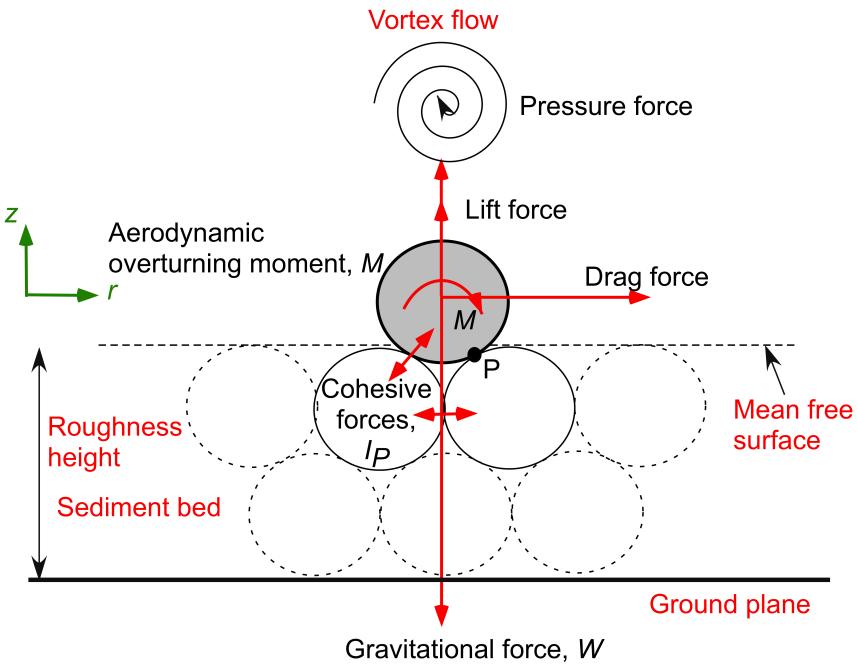

Figure 1.8: Schematic of the forces acting on a stationary particle on a sediment bed.

trainment of a sediment particle is governed by the relationship of the forces acting to keep it stationary (i.e., gravitational and inter-particle forces) to those acting to mobilize it (i.e., aerodynamic forces), as shown in Fig. 1.8. The aerodynamic forces arise from the shearing action of the boundary layer, and when these forces exceed the gravitational and inter-particle forces the sediment particles become mobilized (i.e., by direct aerodynamic entrainment). The vortical flow structures found in rotor induced flow fields also significantly affect the velocity field and the resulting shear stress distribution along the ground [32].

Rauleder and Leishman [33] related particle mobilization and uplift to the Reynolds stresses and discrete turbulence events near the ground. They documented the significance of turbulent events near the ground (i.e., which was expected to have their origin in the

trailed wake sheet) and their overall importance to the problem of brownout. Johnson et al. [26] and Sydney et al. [3] have performed experimental studies to examine the wake of a small-scale rotor interacting with a sediment bed, and have identified several sediment entrainment mechanisms that can occur simultaneously. Figure 1.9 shows a schematic of the different categorizes of initial particle motion that occur below a hovering rotor. The process of creep is characterized by the rolling motion of particles along the sediment bed, and occurs when the forces acting in the wall-normal direction are too small to uplift the particles, i.e., a large particle size or low wall-normal velocity. Some of these particles also encounter large upward fluctuations in the flow velocity and enter saltation, a mechanism that causes the particles to follow short ballistic-like trajectories before reimpacting the sediment bed. Saltation is one of the primary mechanisms involved in the transport of sediment particles in unidirectional flows.

Sydney et al. [3] showed that mobilized particles can be entrained by regions of vortex induced upwash and can be uplifted or suspended for long or short time periods. Once suspended, the particles can be reuplifted by other vortices or by regions of reasonably concentrated vorticity such as eddies. The uplifted particles are also capable of bombarding the sediment bed with relatively higher amounts of energy, thereby ejecting more particles into the near-wall flow by means of bombardment mechanisms. These ejected particles are then easily entrained into the near-wall flow where they are capable of being uplifted. This cascading process of bombardment and ejections an quickly lead to large amounts of sediment being uplifted and entrained into the near-wall flow.

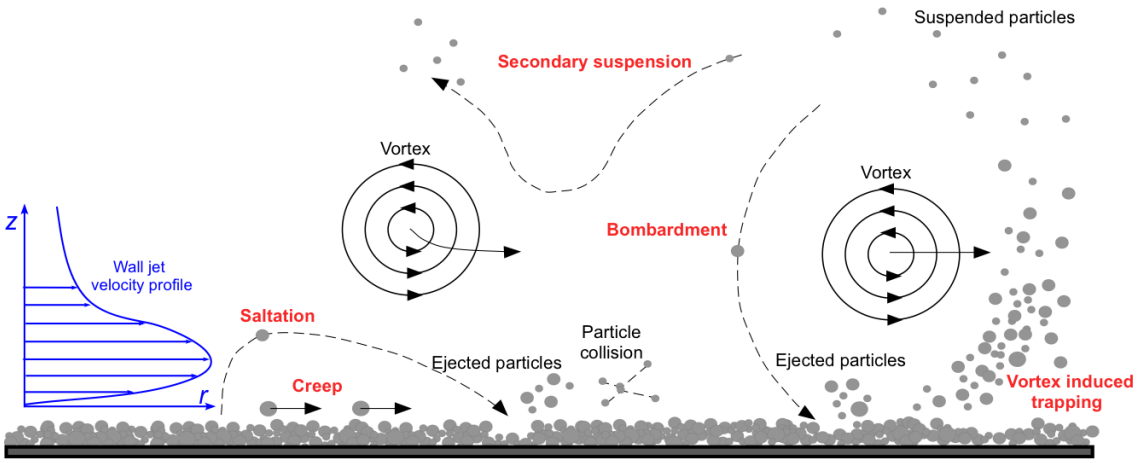

Figure 1.9: Schematic illustrating the various sediment transport mechanisms that may occur below a helicopter rotor when operating over a mobile sediment bed [3].

1.5 Survey of Prior Work Related to Rotor Wakes

Brownout is a multidisciplinary problem that involves, but is not limited to, fluid dynamics (i.e., the formation and interaction of the rotor wake), and sediment particle dynamics (i.e., particle mobilization and transport from the bed). From a rotor performance standpoint, a few experiments have been performed on rotors operating in ground effect [16–21]. These studies generally explored the vehicle performance benefits associated with rotors operating in ground effect. A considerable amount of prior laboratory work has also been performed to measure the evolution of the vortical wake produced by helicopter rotors, e.g., Refs. 34–44. However, fewer studies have focused on the behavior of the rotor wake in ground effect [14, 27, 28, 45–48], and there have been very few measurements of the flow field in the near-wall region on the ground below the rotor. Even fewer measurements have examined the dual-phase aspect of the brownout problem [3, 26, 32, 49].

1.5.1 Single- and Dual-Phase Experiments

Lee et al. [2] conducted experiments to examine the fluid dynamics the wake generated by a rotor as the wake interacted with a ground plane. Two-component particle image velocimetry (PIV) and flow visualization (FV) were used to evaluate the flow field for different rotor heights off the ground. In particular, they showed that as the rotor wake impinges on the ground it generates complex vortical structures and turbulence, which can result in transient flow excursions near the ground plane. They also noted the presence of the turbulent wake sheet that was seen to be entrained into the developing flow at the ground, which introduced a significant amount of vorticity and turbulent eddies. However, the measurement resolution was too low to document the detailed fluid dynamics of the wake sheet and how it contributed to the flow at the ground.

Milluzzo et al. [14] used PIV to examine the flow field generated by a one-bladed rotor operating in ground effect, with the goal of quantifying the effect of blade tip shape on the resulting flow at the ground. The blade tip shapes tested were a baseline rectangular blade, a simple swept tip, a BERP-like tip, and a slotted-tip. It was found that the flow field near the rotor was affected by changes in tip shape. Specifically, the BERP-like tip was found to trail a somewhat more diffused tip vortex compared to the rectangular and swept blade tips. The slotted-tip blade was found to significantly diffuse the developing tip vortex, which resulted in a more rapid growth of the vortex core. With the exception of the slotted-tip blade design, the interaction of the wake with the ground plane ultimately resulted in relatively similar flow fields being produced there. Furthermore, the unsteady turbulent flow along the ground plane contained significant amounts of turbulence, much

of which appeared to have originated from the wake sheet.

Recently, studies have expanded on this initial work by examining the wakes generated by small-scale rotors as they interacted with a ground plane covered with sediment particles [3, 26]. Johnson et al. [26] was one of the first to to perform PIV experiments to examine the dual-phase nature of the problem. Time-resolved, dual-phase flow visualization, PIV, and particle tracking velocimetry (PTV) were used to identify the mechanisms responsible for the entrainment, transport, and suspension of sediment particles in the wake of a hovering rotor. The interaction of the tip vortices with the bed was shown to be a primary cause of particle uplift and entrainment into the flow. This study was the first to document the effects of particle trapping by vortices, i.e., the suspension of sediment resulting from the strong localized upwash regions that were induced by the tip vortices.

Sydney et al. [3] built on the work of Johnson et al. [26] by using time-resolved flow visualization, as well as PIV and PTV measurements on the wake of a rotor system that was hovering at various heights above a mobile sediment bed. The rotor was tested in both single-bladed and two-bladed configurations. The particles used consisted of well-characterized glass microspheres in three diameter ranges: 1–38μm, 45–63μm, and 90–120μm. In addition to vortex-induced sediment uplift, they also documented other mechanisms of sediment transport and suspension, such as secondary particle suspension and the local bombardment of particles back onto the bed. Furthermore, the wake sheets were observed to be entrained into the developing flow near the ground, thereby affecting the near-wall flow field [3]. However, the resolution of the measurements was insufficient to understand the evolution and development of the wake sheets, as well as their contribution to the near-wall flow field.

Rauleder and Leishman [32] further analyzed time-resolved, dual-phase PIV and PTV measurements in the wake of a rotor hovering in ground effect in an effort to provide a better understanding of the near-wall flow field. Specifically, the affect of the turbulent nature of the rotor flow and embedded vorticity on sediment mobilization and transport was examined. They found that particle mobilization and uplift was strongly related to the Reynolds stresses and discrete turbulence events that occurred at the ground. They also showed the significance of the interaction of the wake sheet with the ground and the need for a better understanding of its characteristics to better understand the problem of brownout, which has partly motivated the present work.

All of the previous work performed in both single-phase (air only) [2, 14] and dual-phase (air and sediment particles) environments [3, 26, 32] have clearly shown the importance of the tip vortices in the development of the flow at the ground, and ultimately in problem of brownout. While these works [2, 3, 14, 26, 32] have documented the presence of trailed wake sheets in the wake of a rotor operating in ground effect, they lacked the necessary spatial resolution to quantify the effects of the wake sheets on the developing rotor wake. Therefore, one of the goals of the current work was to better characterize the development and evolution of the wake sheets trailed from the rotor blades and their effects on the downstream wake.

1.5.2 Tip Vortex Measurements

Caradonna and Tung [40] and Tung et al. [50] performed flow measurements on a two-bladed rotor operating in hover. The loading distribution along the span of the rotor

blade was examined using pressure measurements while simultaneously measuring the blade tip vortex structure and strength. Their goal was to aid in the development and validation of hover based performance methods. The tip vortex was observed to be comprised of four distinct regions: (1) A viscous core region where viscous diffusion dominates, (2) A turbulent mixing region where turbulent diffusion dominates and the tangential velocity reaches a maximum, (3) A transition region where the flow transitions from the turbulent region to the outer inviscid region, and (4) A irrotational region where circulation is constant. A vortex model was proposed that modeled these regions in a way analogous with boundary layer theory, which was similar to the fixed-wing tip vortex model proposed by Hoffman and Joubert [51]. Furthermore, Tung et al. [50] also documented that the initial tip vortex core radius was 4% of the rotor blade chord and the peak swirl velocity ranged from 40% to 60% of the blade tip speed. The peak swirl velocity was noted to decrease with increasing wake age. While the presence of a wake sheet was noted, no measurements were made to characterize its structure.

Martin and Leishman [52] used three-component LDV to examine the effect various tip shapes had on the wake of a single-bladed rotor in hover. They determined that changes in the geometry of the rotor wake was the main consequence of changes in tip shape. Sweeping the blade tip decreased both the radial and axial convection of the vortex, whereas blade taper increased the radial convection and decreased the axial convection. Using the measured swirl velocity profiles they found that tip shape had little effect on the vortex core growth rate, however differences were observed in the peak swirl velocities. After normalizing the peak swirl velocities by the blade loading coefficient, it was determined that the tapered blade reduced the initial peak swirl velocity by almost a factor of

two. A Ludwig stability analysis was used to identify the unstable regions of the vortex. It was determined that outside the core (between $r/r_c = 1.5$ and $r/r_c = 2.75$) there is a turbulence producing region that is unstable.

The idea of a multi-region vortex core was also investigated by Bradshaw [53], who developed an analogy between meteorological flows (stratified flows) and streamline curvature (rotating flows), which is based on the assertion that the flow rotation causes the higher speed fluid to prefer the outside of the vortex while conserving angular momentum, even if the density is assumed constant throughout the vortex. An equivalent Richardson number was developed using energy principles and is an expression for the local strength of the stratification. This parameter can be interpreted as a ratio of the turbulence produced or consumed inside the vortex as a result of centrifugal effects to the turbulence produced by shearing in the flow, and is derived directly from the turbulent kinetic energy budget [53, 54]. However, in the derivation of the Richardson number, Bradshaw derived the numerator and denominator in two different reference frames, which resulted in a maximum stability at the core radius of the vortex [55]. Holzapfel [54] corrected the definition by deriving the numerator and denominator in the same inertial reference frame.

Cotel [56], and Cotel and Breidenthal [55] analyzed the turbulence in a vortex using Bradshaw's "Richardson number" [53] and determined a stratification threshold that is a function of vortex Reynolds number. Their analysis is based on four non-dimensional parameters, the Richardson number, Reynolds number, Prandtl number, and persistence parameter. The persistence parameter is defined as the ratio of rotational to translational speed of the vortex. If the Richardson number is above a threshold based on the vortex

Reynolds number, the flow will remain laminar and any turbulence will be relaminarized. The ability of the vortex core to remain laminar means that the mechanism of vorticity diffusion occurs mainly from shear stresses at the molecular level, rather than by the more rapid diffusion that is associated with turbulence.

Leishman et al. [57] used three-dimensional LDV measurements to examine the formation, roll-up, and evolution of the tip vortex and corresponding wake sheet. They found that the vortex core and corresponding wake sheet appeared to interact substantially during the tip vortex roll-up process. Flow visualization showed that the tip vortex core was relatively laminar and was surrounded by a band of eddy-like structures. However, as these eddy-like structures were entrained into the vortex core they became re-laminarized. The Richardson number concept was used to explain this re-laminarization process, and the measurements suggested that the high streamline curvature around the vortex core prevented the formation of turbulence, as previously postulated by Bradshaw [53] and others [40, 50, 51, 55, 56].

Ramasamy and Leishman [58] developed a generalized tip vortex model that included the effects flow rotation on the turbulence inside a vortex. The model was developed using a model of the eddy viscosity distribution across the vortex core, while accounting for the suppressing effects flow rotation on the persistence and/or development of turbulence. Flow rotation effects were accounted for using the modified Richardson number [53, 55, 56], and it was shown that if the local Richardson number was above the threshold value the vortex could not sustain turbulence. The model was found to correlate well with measurements made at both laboratory-scale and full-scale, with increases in vortex Reynolds number corresponding to increases in turbulence levels within the vortex.

Ramasamy and Leishman [58] also compared the assumed eddy viscosity variation with the average eddy viscosity model suggested by Squire [59]. This model focused mainly on the effect of Reynolds number on the distribution of eddy viscosity in the vortex core as it related to the persistence of the vortex in the flow.

Bhagwat and Leishman [60] used three-component laser Doppler velocimetry (LDV) measurements around the blade and in the wake of a small-scale hovering rotor to determine the relationship between the tip vortex strength and spanwise circulation distribution. They estimated the spanwise circulation by using velocity field measurements around each blade section. They found many challenges that were associated with measuring the bound circulation, and that such measurements were possible only under certain conditions. The initial circulation strength of the tip vortices was found to be approximately 70% of the estimated peak bound circulation on the blades. However, the details of the wake sheet were not measured.

McAlister et al. [61] examined the wake trailed by a hovering two-bladed rotor using stereoscopic particle image velocimetry (PIV). In particular, the development of the tip vortex at early wake ages (i.e., less than one rotor revolution old) was characterized. The swirl velocity profile of the tip vortex was found to be asymmetric because of the influence of the rotor downwash. During the first rotor revolution, the vortex core was found to contain approximately 53% of the peak bound circulation along the span of rotor blade. The spanwise distribution of bound circulation was estimated using blade element momentum theory. While the presence of the wake sheet in the flow was documented, no detailed measurements were preformed.

Gupta and Loewy [62] used a small perturbation stability analysis of two infinite

helical interdigitated vortex filaments to examine the stability of a helicopter rotor wake in hover or axial climb. Instability modes were found to occur at all values of the wave number. The most unstable modes corresponded to the largest divergence in the axial locations of the vortex segments, which was found to increase as the helical pitch of the wake was decreased, by increasing number of vortex filaments, and for decreasing wave number. Furthermore, the stability of the wake was found to be significantly affected by the size of the vortex core, the maximum divergence rate decreasing as the vortex core size was increased.

Bhagwat and Leishman [44] also analyzed the stability characteristics of rotor wakes in hovering and axial climb and descent by using an eigenvalue analysis. It was determined that the stability of the rotor wake increased with increasing rotor thrust. The increased stability was a result of vortex separation distance (i.e., helical pitch of the wake), which had a stronger influence on the wake stability than vortex strength. Consequently, the divergence rates were seen to decrease with increasing rates of climb and increase with increasing rates of descent. The eigenvalue analysis also showed that a rotor wake is naturally unstable for wave numbers equal to half-integer multiples of the number of blades were found to produce the largest values of divergence rate, while the smallest values of divergence rate occurred at integer multiples of the blade number [44]. Additionally, vortex pairing, a phenomenon often seen in rotor wakes [63], was determined to be associated with a long-wave instability mode.

1.5.3 Wake Sheet Measurements

A review of previous work on the wake sheets trailed from hovering rotors showed that very few experiments have been able to measure the structure and evolution of the wake sheet. A seminal study on rotor wakes was performed by Landgrebe [36–38] where the effect rotor design (i.e., number of blades, blade twist, blade aspect ratio, etc.) had on the performance and wake geometry characteristics of hovering rotors were exposed. Landgrebe found that the axial convection rate of the tip vortices increased proportionally with increasing blade loading and disk loading, but decreased slightly with increasing blade twist. Furthermore, the axial convection of the tip vortex was found to be relatively constant until the following blade passage occurred, which increased the axial rate of convection.

Landgrebe [36–38] also documented the presence of a wake sheet that was trailed from the inboard part of the rotor blade. The wake sheet was found to convect axially at a rate that was approximately twice that of the corresponding tip vortex. It was also found that the axial convection of the sheet increased with disk loading and blade twist. The sheet was modeled by assuming a linear convection rate below the rotor, i.e., it convected quickest below the rotor blade tip and slowest near the root. Kocurek and Tangler [39] performed similar measurements to develop a generalized model of the rotor wake, but did not consider the contributions from the wake sheets in this model.

McAlister [64] performed flow visualization and three-component LDV measurements in the wake of a two-bladed hovering rotor. The velocity profile in the wake was found to be directly related to the position, size and convection rate of the wake sheet

and the tip vortices. McAlister also noted that even at early wake ages the position of the trailed tip vortex was found to "meander" (e.g., its spatial position was aperiodic) and the aperiodicity increased with increasing wake age. The tip vortex core size and peak swirl velocity were found to be 10% of the rotor blade chord and 30% of the rotor tip speed, respectively. McAlister also noted the presence of a wake sheet that was trailed from the inboard part of the blade section, which initially had a thickness close to that of the blade section. The wake sheet was also observed to convect axially faster than the convection of the corresponding tip vortex. The distribution of vorticity in the wake sheet was measured, but not with the resolution needed to expose its detailed structure.

More recently, Ramasamy et al. [22] performed dual-plane stereoscopic particle image velocimetry (PIV) measurements in the flow field below a hovering rotor, where they measured the three components of velocity and all nine components of the velocity gradient tensor. Additional high-resolution, two-component PIV measurements were also performed. They found that the sheet was composed of small counterrotating vortical flow structures (sometimes called Taylor–Görtler vortices), which form in this case as a result of the streamline curvature of the flow as well as the merging of the boundary layers over the upper and lower surfaces of the blade. These small vortices were found to contribute significant amounts of turbulence to the overall flow field as well as affecting the roll-up process of the tip vortices. The relatively high velocity gradients and velocity fluctuations generated by the Taylor–Görtler vortices were found to have a a significant affect on the transfer of momentum in the flow. While the work by Ramasamy et al. [22] provided key insight into the initial structure of the wake sheet, only the region of the sheet near the rotor blade tip was examined and then only at very early wake ages (i.e., for $\zeta < 6^{\circ}$).

Later, Ramasamy et al. [65] compared the rotor performance as well as flow fields generated by a three-bladed rotor with untwisted and highly twisted blades (i.e., tiltrotor-like blades). They used blade element momentum theory to further understand the likely effects of blade twist on rotor performance and the wake structure. The performance of the rotor with untwisted blades was determined to be comparable to that of the highly twisted blades, if not better, at the lower thrust conditions. However, at the higher rotor thrusts the highly twisted blade yielded improved levels of rotor performance over that of the untwisted blade. The untwisted blade was found to produce very similar flow fields at each of the thrust conditions tested, with a strong blade tip vortex and a weaker wake sheet being formed inboard. However, the convection rate of the tip vortices and wake sheets trailed from the highly twisted blades showed significant variations with rotor thrust. At the lower thrust conditions, the inflow was non-uniform with the highest downwash velocities being near the root of the blade and significant upwash velocities being formed near the blade tip, which resulted in the wake sheet taking on a very steep positive slope relative to the rotor plane. However, as the thrust was increased on the rotor with the highly twisted blades, the upwash region near the blade tip decreased until no discernible upwash region remained. At the higher thrust conditions, the wake sheet was observed to contain a significant amount of vorticity that was convected uniformly in the wake below the rotor.

While the work by Ramasamy et al. [65] has characterized the structure of the rotor wake for a rotor with both untwisted and highly twisted blades, to obtain measurements along the entire span of the blade a larger field of view had to be utilized, yielding only about 500 measurement points (flow vectors) per unit radius. Therefore, these investiga-

tors were unable to quantify the detailed structure of the entire wake sheet as it developed and evolved in the rotor wake. Furthermore, the measurements were performed by using two different airfoil sections, i.e., an airfoil used on the XV-15 rotor for the highly twisted blade and a NACA 0012 for the untwisted blade. These measurements were also preformed for out of ground effect conditions.

While a majority of previous work has documented the presence of a wake sheet in the wake of a hovering rotor, very few measurements have been performed to examine its detailed structure and development [22,36–38,64,65]. Of these measurements only those performed by Ramasamy et al. [22] had the necessary measurement resolution to resolve the vortical structure of the wake sheet, which has shown that the sheet was comprised of Taylor–Görtler vortices. However, Ramasamy et al. [22] only examined the region of the sheet near the blade tip and also only at early wake ages (i.e., $\zeta < 6^\circ$). Furthermore, these latter studies [22, 36–38, 64, 65] have only examined the wake sheet for rotors operating out of ground effect. The current work builds on the work performed by Ramasamy et al. [65] by performing high resolution measurements in the wake of a rotor to better characterize the development and evolution of the wake sheet.

1.5.4 Brownout Simulations

It has been previously mentioned that the problem of rotorcraft brownout has partly motivated the present work. While experiments have been preformed toward gaining a better understanding of brownout [3, 26, 32], a significant amount of computational work has also been performed with the goal of being able to simulate the problem of

brownout [29, 66–73]. On one hand, numerical simulations can represent full-scale rotor geometries that are not limited by the geometric constraints and dual-phase scaling issues that are faced with laboratory experiments [49]. On the other hand, the complexity associated with the dual-phase modeling requires varying levels of assumptions and mathematical approximations to be made. Computational fluid dynamic (CFD) techniques have been used to model the rotor wake flows, most often using Eulerian grid-based methods based on the Reynolds-Averaged Navier–Stokes (RANS) equations [66, 70, 74, 75]. Kalra et al. [74] simulated the flow field generated by a laboratory scale rotor operating in ground effect using a RANS method. Their simulations showed good agreement with the measurements of Lee et al. [2]. However, to accurately resolve the vortical nature of the flow field generated by the rotor, as well as preserve the vorticity to old wake ages, require extremely fine grids with complex meshing strategies, which usually makes the use of such techniques computationally expensive. The high computational cost of these methods limits the geometric scale of the rotor (i.e., small-scale rotors) that can be simulated, as well as the flight conditions (i.e., steady, non-maneuvering flight) they operate under [74, 75]. Furthermore, RANS methods require turbulence models to provide closure to the governing equations, and these models are developed based on assumptions that are not necessarily representative of the flow field induced by a rotor, either in the single-phase or dual-phase flow environments.

Compared to Eulerian grid-based methods, Lagrangian-based vortex methods [76–78] require significantly less computational expense and are capable of indefinitely preserving the vorticity in the wake. Syal et al. [72, 73, 79–81] used a free vortex method and a particle tracking method to simulate the generation of a brownout cloud. While

showing reasonable correlation of full-scale brownout dust clouds using free vortex methods [82, 83], these methods sacrifice some fidelity to achieve the significant reductions in computational cost compared to RANS approaches. For example, vortex based methods are inviscid, and therefore, require an empirical model to represent the boundary layer flow at the ground. Furthermore, to save computational expense, the vortex sheets are typically tracked for less than 30° of wake age, after which they are assumed to be rolled up into an outboard tip vortex, which may not be a correct assumption. Therefore, it is necessary to determine if the wake sheet significantly affects the development and evolution of the rotor wake, as well as the near-wall flow over the ground plane.

One of the main challenges involved in simulating the problem of brownout is properly modeling the mobilization and entrainment of the sediment particles that result from the action of the rotor wake on the sediment bed. Many factors play a role in the initial mobilization and entrainment of sediment particles, such as surface shear stresses, fluctuations in the flow velocity, and discrete turbulent events. However, classic semi-empirical sediment transport models (i.e, those of Bagnold and Shao and Lu [30, 84]) do not account for the various effects found in rotor wake flow fields, such as unsteadiness in the flow, concentrated regions of discrete vorticity, and turbulent events. To understand how particles become mobilized, it is necessary to fully understand how the tip vortices and wake sheet influence the near-wall flow field, and only then can proper assumptions be made in the development of better particle entrainment models.

1.6 Objectives of the Current Work

To understand the significance of the trailed wake sheet as it may affect the problem of brownout, a detailed study of the structure and evolution of the wake sheet in the flow field induced by a rotor is required, this goal being the primary objective of the present work. As previously explained, few experiments have documented the detailed structure and evolution of the wake sheet from a rotor blade, and there are no detailed measurements of the wake sheet at older wake ages or where it may interact with a ground plane. However, recent advances in instrumentation have now allowed measurements of the rotor wake to be made with unprecedented levels of spatial resolution. Therefore, a goal of the present work was to quantify, with the necessary fidelity, the structure, evolution, and development of the wake sheet for a rotor that was operating both out of ground effect and in ground effect. The motivation was to obtain a better understanding of the effects the wake sheet as it might affect the problem of brownout, i.e., to examine in detail how the wake sheet evolves through the rotor flow and affects the near-wall flow region at the ground. It will be shown that the present work has revealed details of the evolution, structure, and development of the wake sheets that were hitherto unknown.

1.7 Organization of the Dissertation

The problem of brownout has been introduced in the present chapter, which has partly motivated the present study. An in-depth survey of previous work on brownout, fixed-wing tip vortex measurements, rotary-wing tip vortex measurements, and rotary-wing wake sheet measurements has been conducted. The limitations that were associated

with previous flow measurements of the inboard wake sheet have been discussed. These limitations has lead to a discussion of the primary motivation of the current work, which was to measure wake sheet trailed from a rotor that was operating both out of ground effect and in ground effect with the necessary resolution to better understand its behavior. For the present study, the effects of blade twist were also examined to document the effects on the formation and evolution of the vortical wake sheets and the associated blade tip vortices.

Chapter 2 gives a comprehensive description of the equipment and the experimental techniques that were utilized to characterize the flow fields (i.e., high-speed flow visualization and phase-resolved particle image velocimetry) and rotor performance.

Chapter 3 discusses, in detail, the results obtained in terms of flow field characterization, velocity field measurements, and rotor performance measurements. First, the rotor performance measurements are presented for the rotors with the untwisted and twisted blades operating in hover at different heights above the ground. Then, the flow field measurements taken with the rotor operating out of ground effect are discussed. It is here that the detailed structure, development, and evolution of the wake sheet is exposed. Furthermore, this section also documents the detailed interactions between the wake sheet and newly formed tip vortex as they convect in the wake below the rotor. The corresponding measurements performed with the rotor operating in ground effect are then discussed.

Finally, Chapter 4 gives the conclusions from the present study, and suggests additional avenues of research that could be conducted. For example, the wake sheets trailed from both the untwisted and twisted blades were found to be comprised of small pairs of counterrotating Taylor–Görtler vortices. These sheets were also found to significantly

affect the near-wall flow field and, therefore, would be expected to significantly affect the processes of particle mobilization and entrainment.

Chapter 2

Description of the Experiments

2.1 Introduction

To help provide a better understanding of the intricate three-dimensional, unsteady flow field produced below a hovering rotor, detailed flow visualization and particle image velocimetry experiments were performed with the rotor operating both in and out of ground effect. This chapter describes the experimental setup, the equipment used, the experimental techniques and processes, and the challenges involved in undertaking these types of experiments.

2.2 Rotor System

The measurements were conducted using a two-bladed teetering rotor system with rectangular blades. The rotor had a radius of 0.408 m (16 inches), and the blades had a mean chord of 44.5 mm (1.752 inches), as shown in Fig. 2.1. A NACA 2415 airfoil was used throughout the blade length. The rotor was powered by a motor capable of producing up to 4.5 hp and 19.5 ft-lb of torque. A combination thrust/torque cell was used to measure the thrust produced and the torque needed for of the rotor system. The accuracy of the balance was ± 0.005 lb and ± 0.00041 ft-lb in thrust and torque, respectively. Flow measurements were performed with the rotor operating both in ground effect

and out of ground effect in the hovering state, as shown in Figs. 2.2 and 2.3, respectively. For the present experiments, the rotor was operated at a rotational frequency of 35 Hz (2,100 rpm), yielding a blade tip speed of 89.72 ms^{-1} (294.37 fts^{-1}), corresponding to a nominal tip Mach number and chord Reynolds number of approximately 0.26 and 266,077, respectively.

Two blade sets were tested to examine the effects of blade twist on the development of the rotor wake: 1. A baseline untwisted blade, 2. A twisted blade with -17° of linear twist from the rotational axis to tip. The blades were made of a Carbon-filled Nylon 12 material that provided the necessary tensile and flexural strength while maintaining a relatively low weight. For the out of ground effect experiments, each blade was tested at two blade loading coefficients, C_T/σ, of 0.053 and 0.08, which were selected to represent representative helicopter rotor operations at low and high thrust conditions, respectively. However, only the higher thrust condition (i.e., $C_T/\sigma = 0.08$) was tested with the rotors operating in ground effect.

It was necessary to design a rotor hub with a mechanism that allowed the blade pitch to be varied. Figure 2.4 shows a detailed view of the rotor hub, which allowed the collective blade pitch, θ_0, to be continuously varied between -15° and 25°. The teetering hinge design could accommodate either the one-bladed or two-bladed rotor configuration, a counterweight being used in the case of the one-bladed rotor.

For these experiments, the rotor shaft was mounted horizontally with the rotor blades rotating in a vertical plane. To simulate ground effect conditions, a circular ground plane was used. Performance measurements were taken out of ground effect and with the rotor plane situated at heights of $z/R = 1.5$, 1.0, and 0.5 above the ground; see Fig. 2.5.

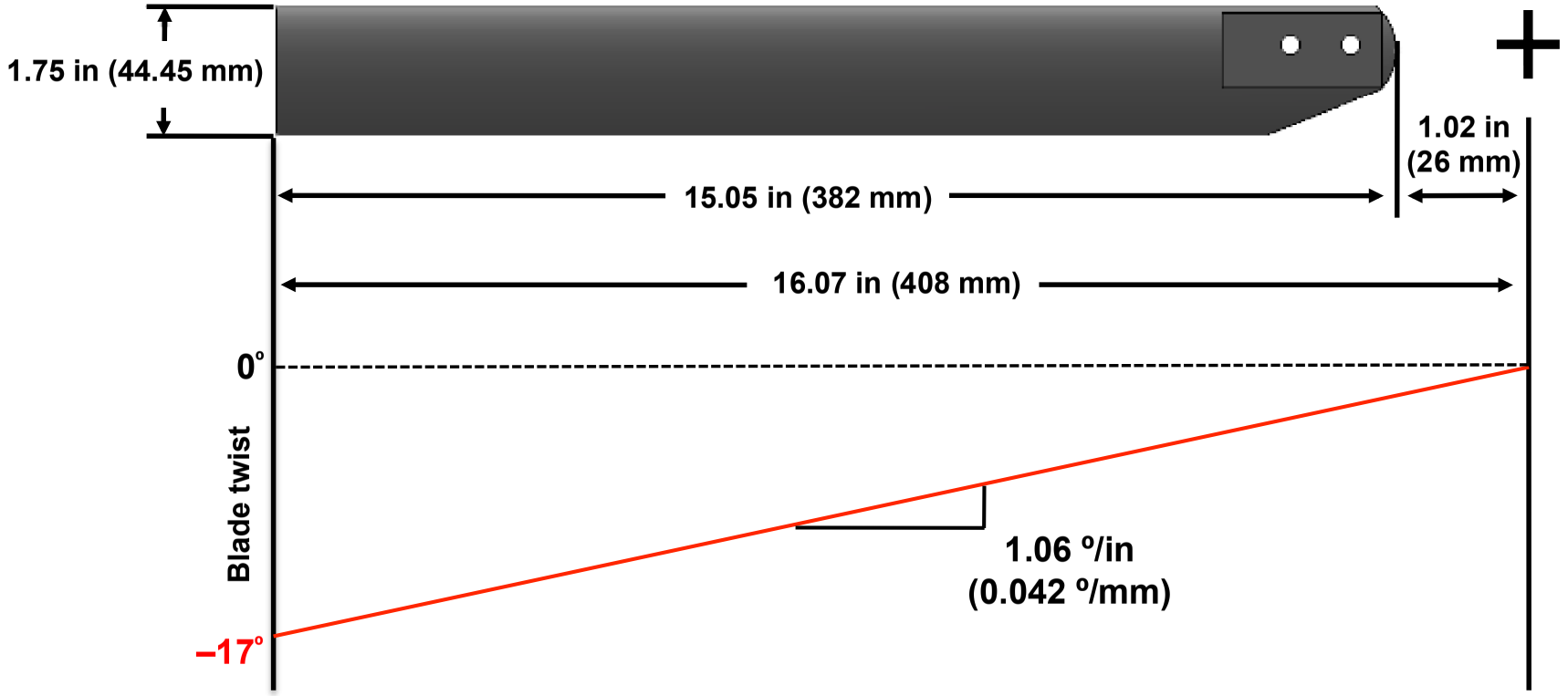

Figure 2.1: Rectangular rotor blade that was tested, showing the dimensions and twist rate.

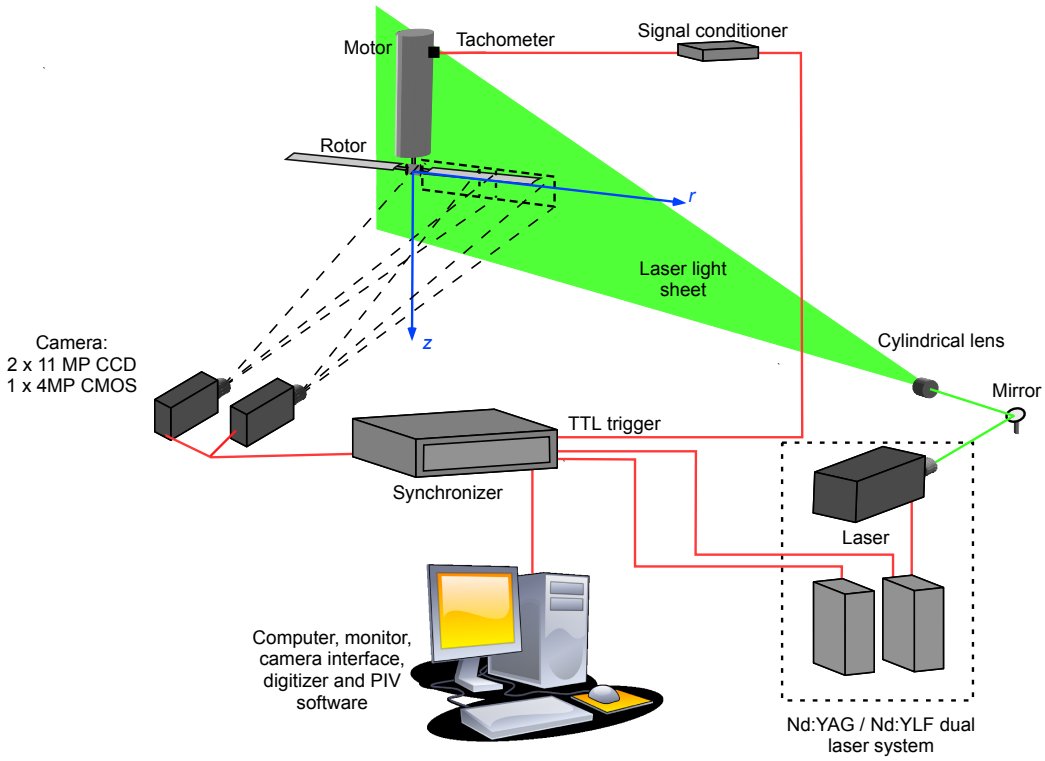

Figure 2.2: Schematic showing the experimental setup used to obtain flow field measurements in the wake of the rotor when operating out of ground effect.

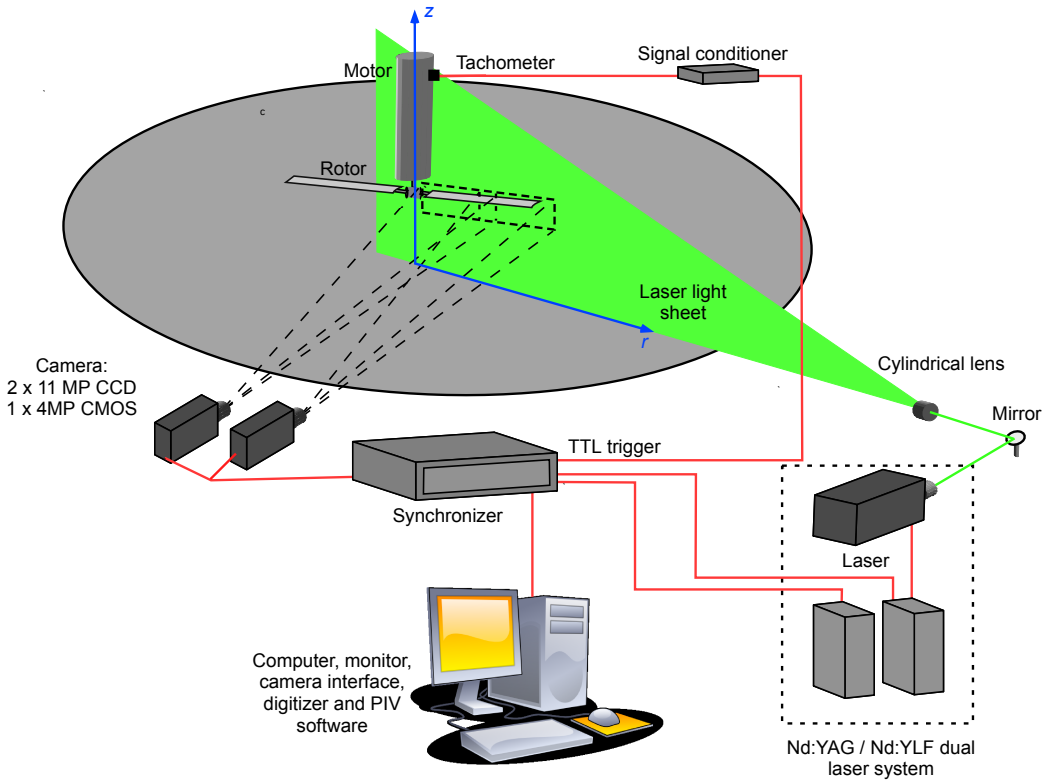

Figure 2.3: Schematic showing the experimental setup used to obtain flow field measurements in the wake of the rotor when operating in ground effect.

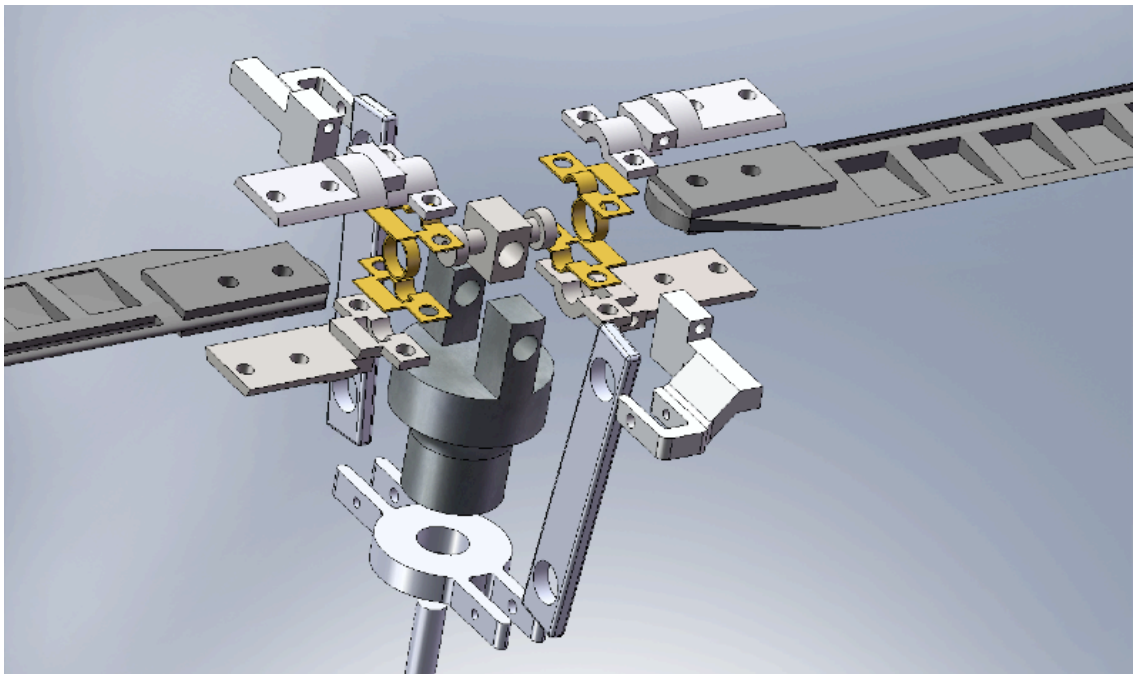

Figure 2.4: Drawing showing all the individual parts that comprised the rotor hub.

For the particle image velocimetry (PIV) and flow visualization (FV) measurements, a laser light sheet was aligned to be perpendicular to the plane traced out by the rotor blade tips or tip path plane (TPP). Cameras (discussed later) were positioned with their viewing axis being orthogonal to the plane of the laser light sheet; see Figs. 2.2 and 2.3. The cameras were focused to the desired regions of interest (ROI), as discussed later in Section 2.5.4. While the lasers an cameras used varied between the PIV and FV measurements, the setup was the same for both, as discussed in detail later in Sections 2.5.3 and 2.5.2.

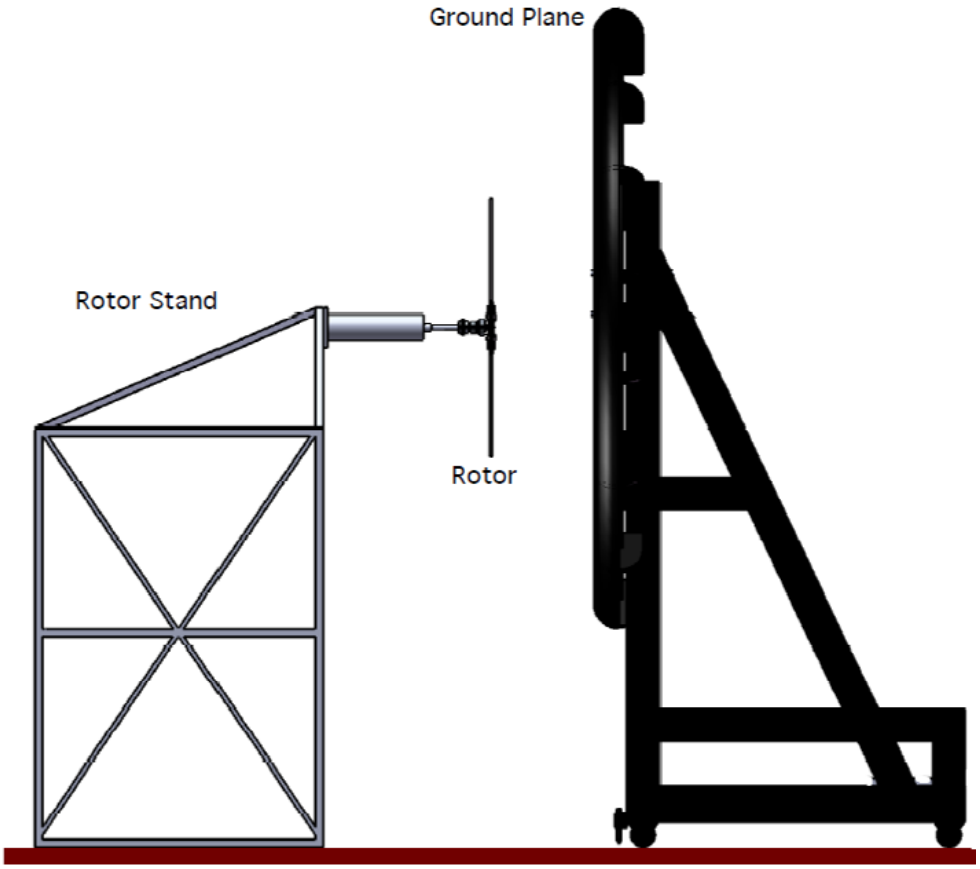

Figure 2.5: Schematic showing a side-view of the rotor and ground plane when the rotor was operated in ground effect.

2.3 Performance Measurements

Performance measurements were taken to determine the thrust generated and power required by the rotor, both in ground effect (i.e., z/R of 0.5, 1.0, and 1.5) and also out of ground effect, (i.e., $z/R = \infty$). Because the rotor shaft was mounted horizontally, the combined load/torque cell experienced a bending moment, so a load cell was selected that could measure up to 500 lb of thrust and 500 in-lb of torque. A 32 bit analogue-to-digital (A/D) converter was used to convert the output voltage from the load cell into a discretely sampled digital signal. Although the output voltage from the cell was relatively small, the high sensitivity of the A/D converter allowed it to read the output signals with low levels of amplification, which also minimized the potential of electrical interference and noise; a low-pass filter was used to remove any remaining high frequency noise that may have been present. The thrust and torque resolution (i.e., $\pm$0.005 lb and $\pm$0.00041 ft-lb, respectively) of the combined load/torque cell in terms of C_T and C_Q gave values of $\pm 4.38\text{x}10^{-6}$ (i.e., 0.06% of the peak measured thrust coefficient) and $\pm 2.74\text{x}10^{-7}$ (i.e., 0.04% of the peak measured torque coefficient), respectively.

To determine the relationship between the output voltage and the applied loads, a calibration was performed by using reference weights. The relationship between output voltage and applied torques was determined using reference weights suspended at known distances from the axis of rotation. Thrust and torque tares were also measured (i.e, with the hub rotating without the rotor blades), and these tares were subsequently removed from the measured balance values. Because both the thrust and power coefficients, C_T and C_P, were dependent on the air density, a laboratory grade barometer and thermometer

were utilized to measure the temperature and pressure and so calculate the local air density using the properties of the international standard atmosphere (ISA). Daily changes in air density required periodic adjustments of the collective pitch on the rotor system to maintain a constant value of C_T/σ

2.4 Ground Plane

Figure 2.6 shows the circular ground plane used for the rotor in ground effect measurements. This plane had a diameter that was twice the rotor diameter and was mounted on a gantry, thereby allowing it to be positioned at any desired distance or orientation from the rotor disk plane. For the present work, performance measurements were taken out of ground effect (i.e., with the ground plane removed) and in ground effect at distances of $z/R = 1.5$, 1.0, and 0.5 away from the TPP. Honeycomb flow conditioning screens were located upstream of the rotor, which reduced the measured values of the incoming turbulence levels to less than 0.5% of V_{tip} [23].

Because flow recirculation in a rotor test cell is always a concern, a relatively large test section volume was used (i.e., approximately 48 m^3 or 1,600 ft^3). The ground plane was designed with flow control devices; flow diverters were mounted along the perimeter of the ground plane, which directed the flow downstream and away from the rotor system.

2.5 Particle Image Velocimetry (PIV) System

The experiments utilized both flow visualization (FV) and particle image velocimetry (PIV). While the basic experimental setup was the same in each case, the tests required

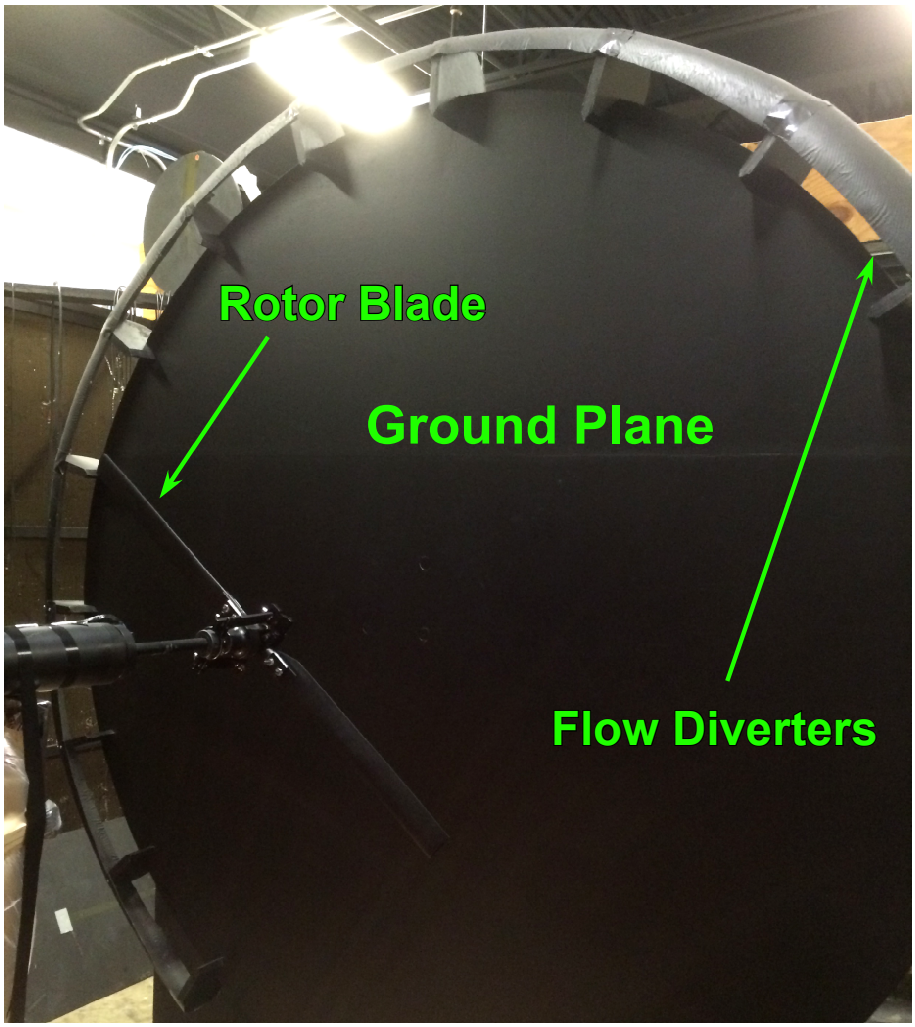

Figure 2.6: Photograph of the rotor and ground plane used in performing the flow measurements.

slightly different types of equipment (i.e., different lasers, cameras, etc.). In each case, the primary laser beam was reflected off a high intensity mirror and though convex and spherical lenses. The convex lens converted the laser beam to a light sheet, and the spherical lens thinned the sheet in the desired region of interest (ROI). From previous research with these lenses [58], it is known that the light sheet is about 1 mm thick at its waist. The cameras were oriented with their imaging axis aligned so that they were orthogonal to the light sheet, focused to the desired regions of the flow, and synchronized to the laser frequency. The process of synchronizing the laser and camera is discussed later in detail in Section 2.5.3.

PIV was used because it could measure the flow field non-intrusively, other than for seeding. The main advantage of PIV was the ability to measure the flow velocity over an entire plane at an instant in time. For PIV, the flow was seeded with sub-micron tracer particles ($\approx 0.2\mu$m) that were illuminated twice over a short time interval (Δt), which was on the order of microseconds. A pair of images (image pair) was thus generated from the Mie scattering from the tracer particles. The resulting image pair was then sub-divided into thousands of smaller interrogation windows of base-2 dimensions (i.e., 16x16, 32x32, 64x64 pixels, etc.) [85]. For each interrogation area, a defined cross-correlation algorithm (i.e., direct, fast Fourier transform, Hart, Rohalay-Hart, etc.) was used to calculate the pixel displacements (between the two images) of the seed particles in the x and y directions, e.g., Δx, Δy, respectively. Upon completion of the cross-correlation, the correlation peak was estimated based on a curve fit to the correlation signal using a defined method (i.e., bilinear curve fit, three-point Gaussian, parabolic fit, centroid, etc.), which provided the displacement of the particles to sub-pixel accuracy [58]. For the

present work a Gaussian method was used.

A fast Fourier transform (FFT) algorithm was used to perform the cross-correlation in the frequency domain before converting back to the spatial domain [86, 87]. The correlated pixel displacement (Δx, Δy) in an interrogation area was then used to calculate the local velocity vectors using the equation

$$(u, v) = \frac{(\Delta x, \Delta y)}{M \Delta t} \tag{2.1}$$

where M is the image magnification and is defined by

$$M = \frac{h_i}{h_o} \tag{2.2}$$

where h_i is the camera imaging array size and h_o is the object size. For the current experiments, the magnification factors, M, were determined using a scale to be 0.11 for the larger fields of view and 0.28 for the smaller fields of view (discussed later in Section 2.5.4). The correlation procedure was repeated for all the interrogation areas in the desired ROI, as shown for a typical vortex flow in Fig. 2.7. For the present measurements, a signal-to-noise ratio of 2.0 was imposed.

The interrogation windows used were 16-by-16 pixels in size, which yielded the necessary spatial resolution to resolve the velocity gradients in the vortex cores and trailed vortex sheets. For the cross-correlations, an image deformation method with a 50% overlap was used, which increased the accuracy of the measurements without sacrificing spatial resolution [88]. This deformation method also better resolved the high velocity gradients present in the wake of a rotor. Because the image deformation method was recursive in nature, the interrogation window sizes were decreased from an initial size of 32-by-32 pixels to the final size of 16-by-16-pixels.

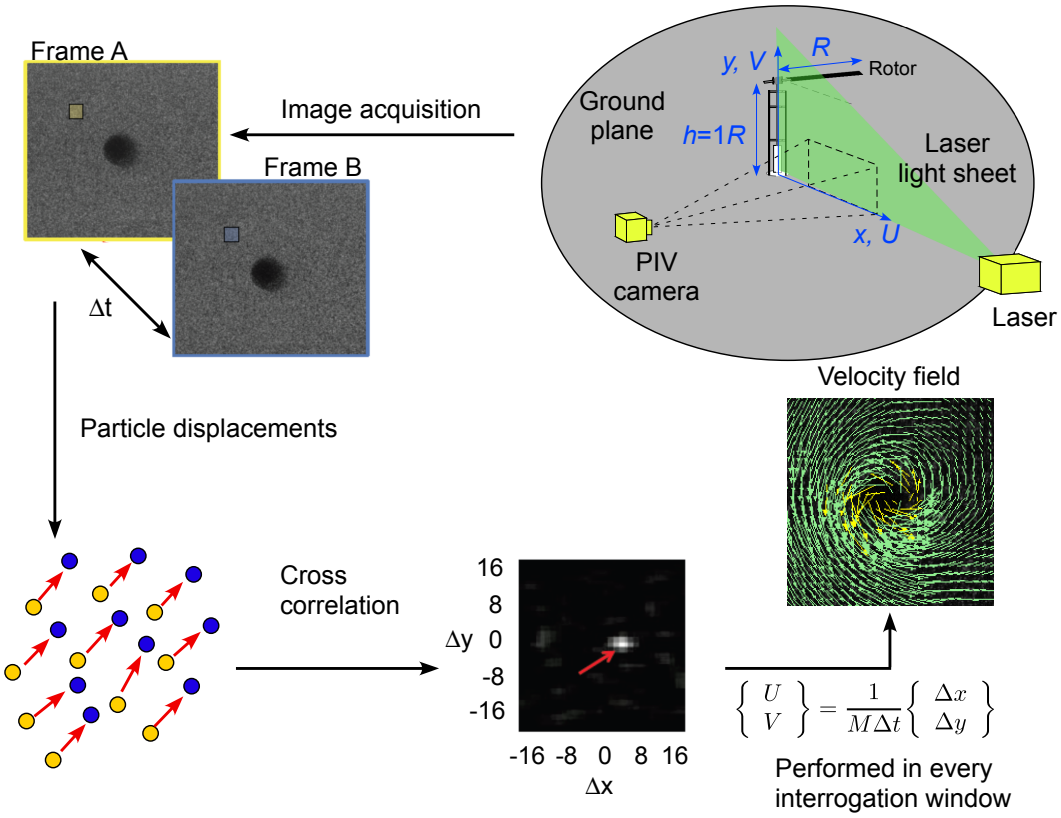

Figure 2.7: Schematic of the basic algorithm used in the PIV analysis.

After the entire image had been correlated the spurious vectors were identified using a local median validation based on the 3-by-3 neighboring vectors. The spurious vectors were replaced by interpolated vectors from the neighboring 3-by-3 vectors and images containing more than 5% spurious vectors were removed from further analysis; in practice, the rejected images were typically less than 2% of the total acquired.

2.5.1 Seeding of the Flows

Seed particles were produced by combining mineral oil and pressurized nitrogen then heating it until the mixture vaporized. As the vaporized mixture interacted with the

ambient air, it rapidly cooled and condensed into a dense white fog. From a calibration [22], 95% of the seed particles were between 0.2 μm in diameter. Particles of 0.2 μm are known to give minimal particle tracking errors in the velocity fields and velocity gradients found in rotor wakes at this scale [89].

For the FV, a series of ducts were used to introduce seed at strategic points into the flow field. This latter approach allowed the seed to be entrained into the desired flow structures such as the tip vortices, producing concentrated bands of seed particles in the images. While FV required larger amounts of seed to better highlight the important flow structures, the PIV experiments needed a fairly sparse quantity of more uniformly dispersed seed particles. Dispersing the seed in this manner allowed individual particles to be identified in the PIV images, thereby providing better cross-correlations between the image pairs.

2.5.2 Time-Resolved Flow Measurements

FV measurements in the rotor wake were performed using a high-speed flow measurement system. This system allowed the temporal evolution of the wake to be documented as it was trailed from each of the rotor blades. This system also allowed the individual vortical flow structures and other turbulent eddies to be tracked in time as they were convected downstream into the far wake of the rotor when it was operating out of ground effect, and into the flow region along the ground plane where the rotor was operating in ground effect.

The time-resolved flow measurement system comprised two main components a

laser and camera. A dual diode-pumped Nd:YLF laser was used, which consisted of a power unit, chiller, and laser head. The power unit provided power to the laser head as well as controlling the laser settings (i.e., individual laser energy, shutter, repetition rate, etc.). The chiller unit cooled distilled water to a temperature of 26°F before pumping it through the laser head to remove the heat that was generated. The laser head was capable of producing two separate laser beams, one from each of the dual cavities, at a wave length of 527 nm. A system of high intensity mirrors was utilized to direct the two laser beams out of a single aperture on the front of the laser head. Each beam could be generated at a maximum rate of 10,000 pulses per second (pps). However, the maximum energy per pulse (10 mJ) was achieved only for rates up to 2,000 pps.

The camera used to perform FV experiments was a high-speed Phantom v641 fitted with an 85 mm lens set to an f-stop of 1.8. The Phantom v641 has a 2,560 x 1,600 pixel complementary metal oxide semiconductor (CMOS) sensor, which provided a maximum spatial resolution of 4 Mp per image. At full resolution, the camera was capable of capturing image pairs at a rate of 750 frames-per-second (fps), or individual images at 1,500 fps. For the current experiments, the camera was set to capture at a frequency of 750 Hz; this frame rate provided the best illumination and spatial resolution in the desired ROI, in addition to providing the temporal resolution necessary to track the individual flow structures that were present in the rotor wake. A high-speed controller was used to digitally synchronize the laser pulses to the camera frame rate, this controller being connected to a computer work station that was used to operate the entire system.

2.5.3 Phase-Resolved flow Measurements

PIV experiments were performed using a phase-resolved system (PR-PIV) with higher spatial resolution, which allowed the rotor wake to be examined with good detail (i.e., greater than 1,500 measurement points per unit radius). However, the disadvantage of this system was that it could only acquire data at a sub-multiple of the rotor frequency, so the individual flow structures could not be continuously tracked in time throughout the flow. However, although the flow features could not be continuously tracked, the time-resolved FV results were used to target locations of the rotor wake for more detailed measurements.

The PR-PIV system used a dual flashlamp pumped Nd:YAG laser. Similar to the system used for FV, a universal power supply provided power to the laser head and controlled the laser settings (i.e., individual laser energy, shutter, repetition rate, etc.). The power supply was a single integrated cooling and electronic (ICE) unit, which provided a compact design that allowed the laser system to be quickly repositioned for each ROI. Deionized water was cooled in the ICE before being pumped through the laser head to remove any excess heat. The laser head contained two Nd:YAG lasers fitted into a single ruggedized monoblock. High intensity mirrors were incorporated to direct the two laser beams out a single aperture. The beams had a wavelength of 532 nm and the laser was capable of firing at a maximum rate of 15 pulses per second with an energy of 200 mJ/pulse.

The cameras used were high-resolution cameras. Each camera had a 4008-by-2672 pixel resolution charge-coupled device (CCD) sensor, providing a maximum spatial resolution of 11 Mp per image. The camera operated at 4.2 frames per second (fps) cor-

responding to 2.1 image pairs per second. However, for the current measurements the cameras were operated at 1.2 fps to provide increased buffer time between successive flow realizations. Given the same region of interest and interrogation window size, this system yielded images of the flow field that were 2.75 times the spatial resolution that was possible when using the high-speed PIV system.

Because the rotational frequency of the rotor (35 Hz) was greater than the maximum imaging rate of the system (2 Hz), electronics and software were used to synchronize the rotation of the rotor and with the imaging system. An infra-red (IR) sensor, mounted just above the rotor shaft, provided the trigger. The one-per-rev output signal was converted into a transistor-transistor logic (TTL) square-wave pulse before being read into a timing hub. The timing hub could to be operated in five different modes, namely, continuous, gated, triggered, re-triggered, and rate change. For the present experiments, the timing hub was operated in re-triggered mode, which gave a TTL signal that pulsed approximately every seventh rotor revolution. The timing hub could also modify the TTL signal with a phase delay that allowed the rotor flow field to be imaged at any desired blade azimuthal position, ψ_b, shown in Fig. 3.11. Modifying the phase delay permitted the documentation of the flow as a function of "wake age" i.e., $\zeta = \psi_b + i(360^\circ/N_b)$ where $i = 0$, 1, 2, etc. The wake age is a measure of the time since the vortex was generated, in terms of the angular displacement (degrees of rotor rotation) of the corresponding blade. For the current experiments 500 PIV image pairs were taken at wake age increments ($\Delta\zeta$) of 30°, and some smaller increments at earlier wake ages.

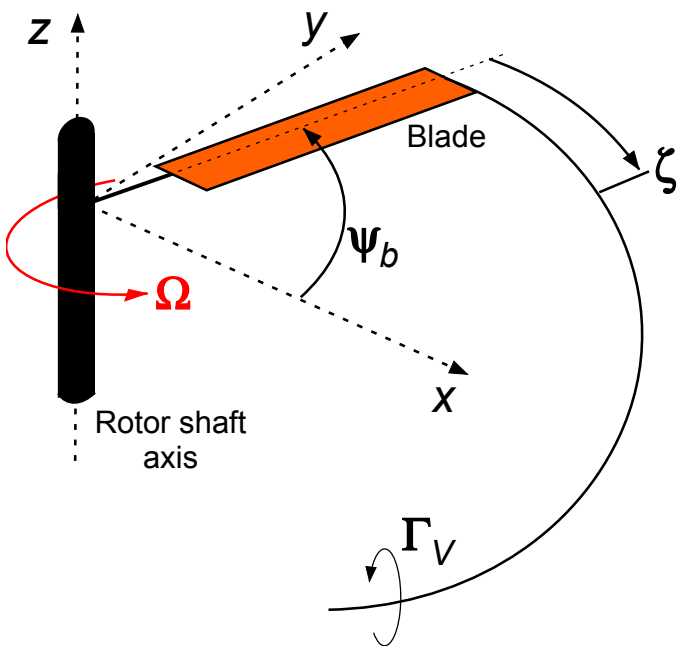

Figure 2.8: Definition of wake age of a vortex filament trailed from a rotor blade and blade azimuth position.

2.5.4 Regions of Interest

Figures 2.9 and 2.10 shows the primary regions of interest (ROIs) where PIV was performed with the rotor operating out of ground effect and in ground effect, respectively. To obtain the measurement resolution necessary to resolve the structure of the wake sheet, multiple regions of interest (ROIs) were required. Because the wake generated by a rotor can be aperiodic, instantaneous measurements taken in different ROIs cannot be easily compared unless they are taken at the same time. Therefore, two 11 Mp cameras were mounted adjacent to each other with a 60 mm overlap in their field of view, as shown in Fig. 2.9. As previously discussed in Section 2.5, the cameras were aligned with their imaging axis being orthogonal to the light sheet such that the two-components of the in-plane velocity could be measured. Using two cameras to measure the flow field at the

same time allowed the temporally correlated images from each camera to be mosaiced together. Each camera had an initial ROI of 270-by-180 mm (0.66-by-0.44 R), so that the total field of view achieved after mosaicing was 480-by-180 mm (1.18-by-0.44 R). An additional ROI (approximately 102-by-68 mm or 0.26-by-0.17 R) with higher resolution (on the order of 3,000 measurement points per radius) was used to identify the behavior of the tip vortices and vortex sheets. A laser pulse separation time of 6 μs was used in ROIs 1 and 2, and and 2 μs in ROI 3.

The rotor in ground effect PIV measurements were performed using the two-bladed rotor and with the untwisted and twisted blades, respectively. The rotor was placed at a height of one rotor radius (z/R = 1.0) from the ground plane, and each blade set was tested at a representative operating condition of C_T/σ = 0.08. The blade pitch was readjusted to achieve this operating thrust. The rotor in ground effect experiments were also performed using the same cameras and setup discussed earlier in this section, yielding the same field of view as the rotor out of ground effect experiments. Four additional ROIs were used to track wake sheets and tip vortices as they were convected toward the ground and were entrained into the developing flow over the surface of the ground plane; see Fig. 2.10.

2.5.5 Flow Measurement Challenges

There are many challenges associated with performing PIV, as well as unique challenges associated with performing PIV in rotor induced flow fields. For the present work these challenges included: data processing and storage, image mosaicing and system alignment, solid body surface reflections, and analysis techniques associated with grid-

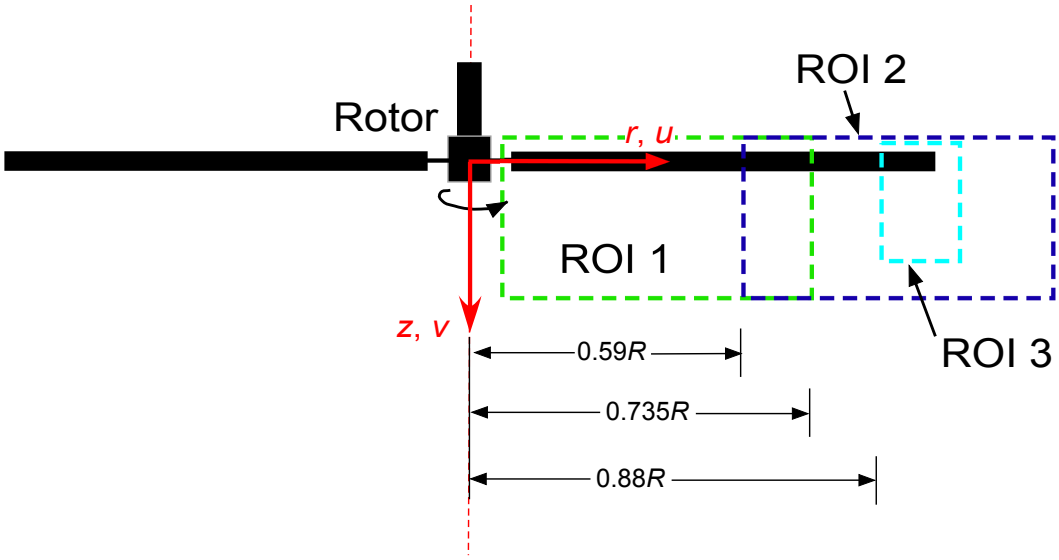

Figure 2.9: Regions in the wake generated by the rotor hovering out of ground effect where velocity field measurements were obtained using PIV.

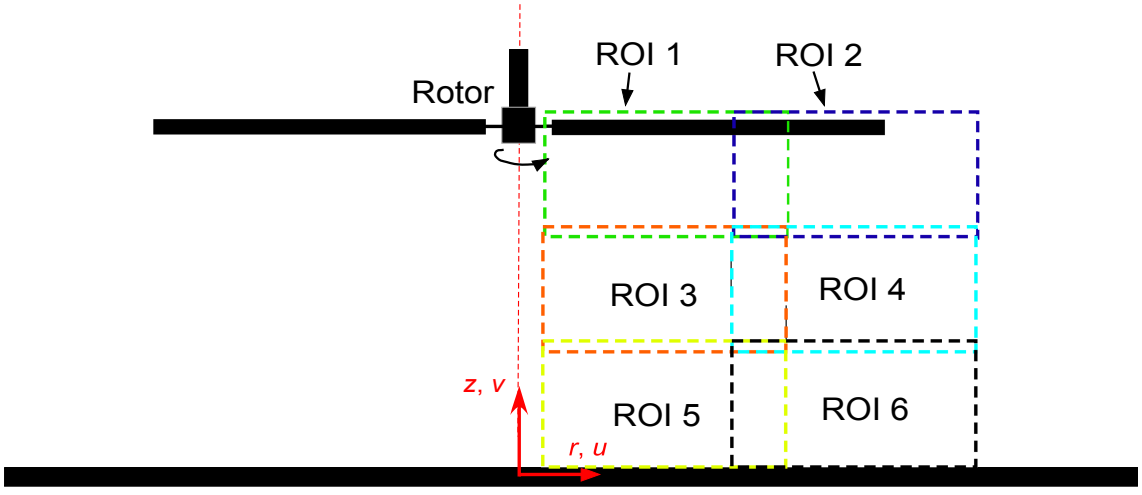

Figure 2.10: Regions in the wake generated by the rotor hovering in ground effect where velocity field measurements were obtained using PIV.

ding and masking near solid boundaries.

The high resolution of the cameras (11 Mp) used for the current work presented new challenges in data processing and storage. Previous experiments with this rotor system used primarily 4 Mp cameras to perform flow field measurements [23, 48, 90], which generated raw image files that were on the order of 8 MB each. Whereas, the 11 Mp cameras used in the current work generated raw image files that were on the order of 20 MB each; see Fig. 2.11. The higher resolution of the 11 Mp cameras also significantly increased the average processing time per run from around 4 hours for the 4 Mp cameras to greater than 24 hours for the 11 Mp cameras. The increase in camera resolution yielded a total processing time of approximately 23 months and required more than 5 TB of storage. To accommodate the large data storage requirements a Drobo data storage system was selected. The Drobo system comprised 8 hard drive ports and provided hot swappable drive capability with dual-disk redundancy. Using 3 TB hard drives the Drobo system provided over 16 TB of data storage capability.

As previously discussed in Section 2.5.4, two cameras were used to measure the flow field and the temporally correlated images from each camera were mosaiced together. The mosaicing process introduced new challenges in system alignment, as well as in determining the necessary overlap region between the two ROIs. Because the ROIs were combine together small misalignments in the each camera were exacerbated at the mosaicing line. Therefore, it was necessary to ensure that the cameras were the same distance from the light sheet, aligned orthogonal to the light sheet, and the light sheet was vertical. Because the two ROis were being mosaiced together the amount of image overlap needed to be determined; see Fig. 2.9. The overlap region was selected such that

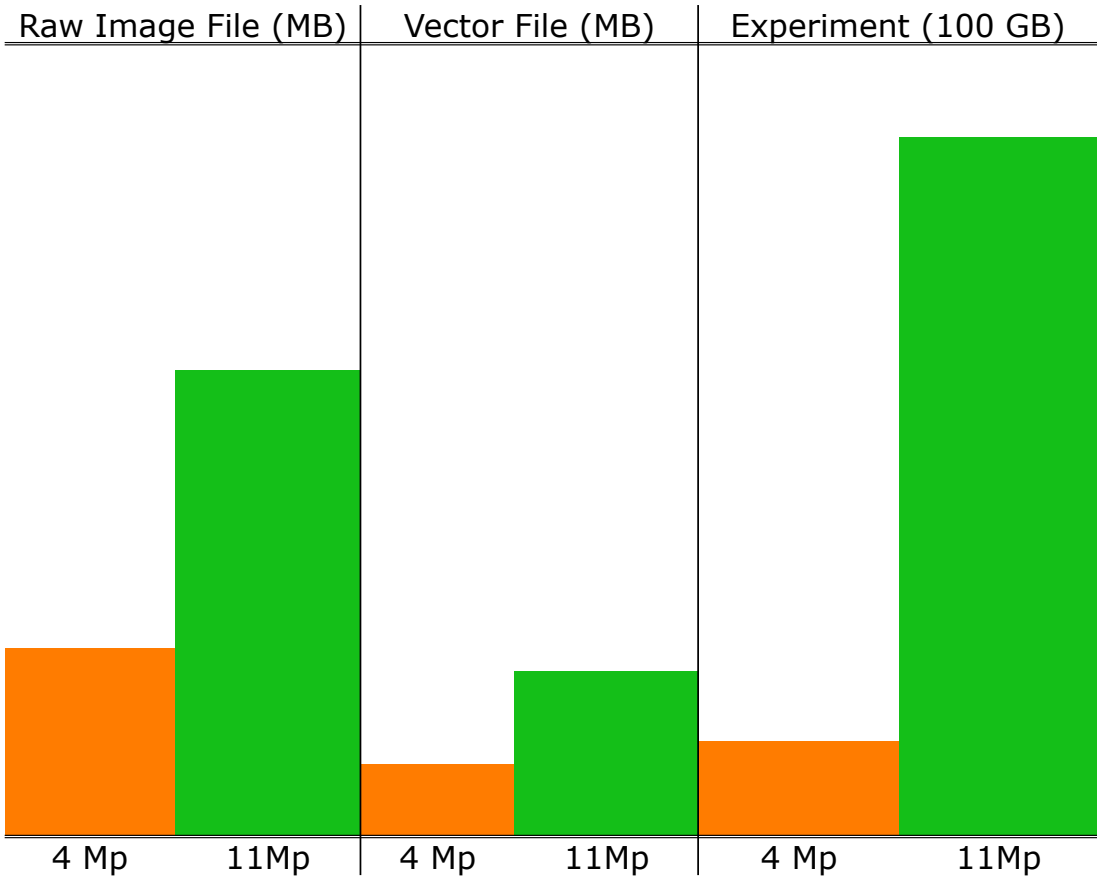

Figure 2.11: Comparison of data storage requirements associated with an increase in camera resolution from 4 Mp to 11 Mp.

a spatial point of commonality could be identified without sacrificing too much of the overall field of view. For the current work an overlap of 60 mm was selected.

When the laser light reflects off a solid surface, the resulting intensity can be significantly higher than the Mie scattering from the seed particles in the flow, making it difficult to obtain good cross-correlations with the PIV image pairs. An example of this latter issue is shown in Fig. 2.12a. Several techniques were implemented to reduce or eliminate these surface reflections, namely, paint selection, judicious alignment of the laser sheet relative to the ground plane, and periodic cleaning of the ground plane to remove any oil from the condensed seed particles; see Fig. 2.12b. While several different types of paint were evaluated, only flat black paint was effective in reducing the surface reflections. Laser alignment also resulted in a substantial reduction in surface reflections. Specifically, the light sheet was aligned such that the ground plane bisected the light sheet, resulting in the centerline of the light sheet being parallel to the surface of the ground plane. Although this laser alignment method resulted in some of the laser light sheet energy being lost below the ground plane, it still provided the necessary illumination in the desired ROI.

An additional challenge associated with performing PIV near solid boundaries arises from the spatial misplacement of the velocity vector because the interrogation window overlaps the boundary interface. Because PIV algorithms naturally place the vectors at the center of the interrogation window, if the window overlaps the boundary the correlation window will not coincide with the center of the window; see Fig. 2.13. Therefore, it would be necessary to adjust the spatial location of the correlated vector such that its final location coincided with the center of the correlated region [91]. To alleviate this issue the bottom of the first correlation windows were anchored to the boundary, and defined such

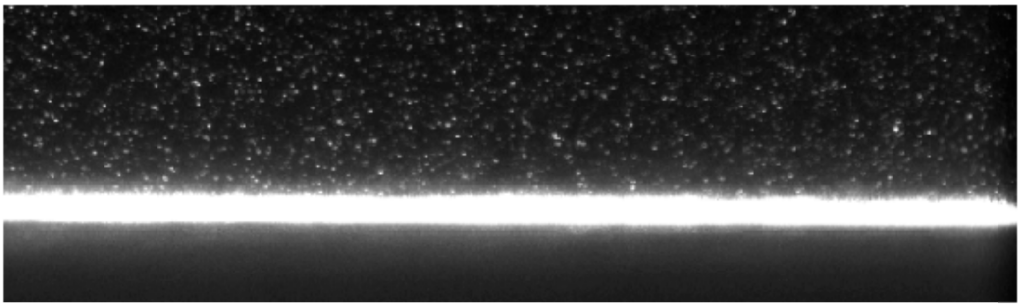

(a) Before

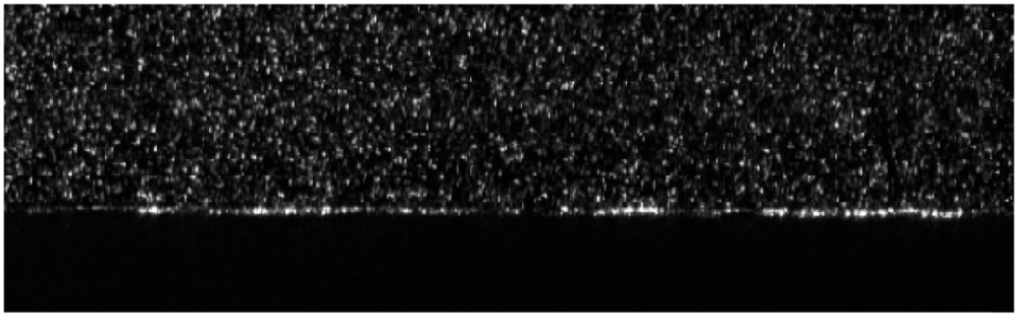

(b) After

Figure 2.12: Reflections off the ground plane (a) before and (b) after the implementation of reduction techniques.

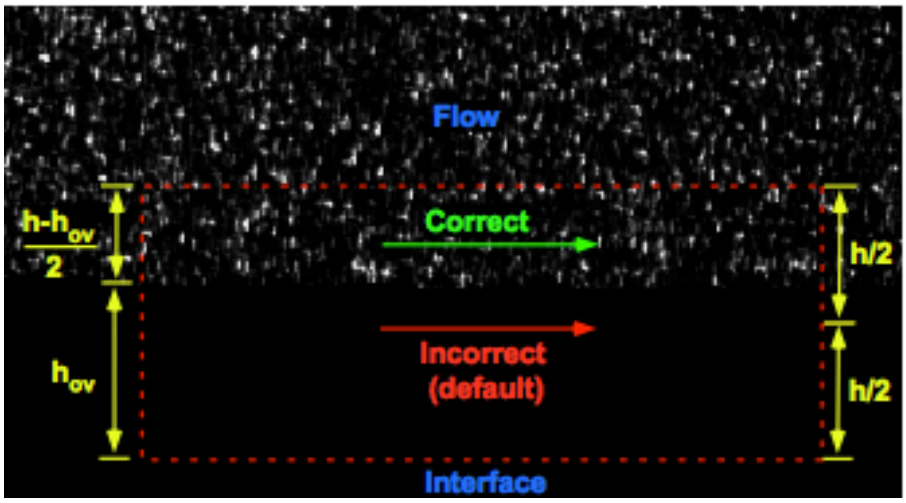

Figure 2.13: Relocation of correlated vector when the interrogation windows overlap the interface.

that no windows overlapped the boundary.

2.6 Uncertainties in the Measurements

Sources of uncertainty in the flow measurements using PIV include tracking errors of the tracer particles, background noise, interrogation window size, pulse separation time, and laser light reflections. Because the seed particles do not perfectly follow the flow, errors in the velocity field measurements can arise. However, the seed particles used in the present work were such that these errors were relatively small [89].

Background noise was a result of noise in the camera signal, and manifested as artificial intensities in the raw image that can produce erroneous correlations. To limit such errors, a minimum signal-to-noise ratio of 2.0 (i.e., higher than previous PIV measurements [3, 23, 26, 58]) was used to assess the validity of each vector.

Because the seed particles are assumed to have linear motion between image frames,

flow curvature and shearing is always a concern when performing PIV in flow fields with significant vorticity concentrations To minimize such errors the pulse separation time was chosen to be as small as possible while maintaining the necessary particle displacement to obtain good correlations, i.e., a displacement of about one-quarter the interrogation window size.

As previously discussed in Section 2.5.4, an image deformation method was implemented to removed the errors that were associated with large velocity gradients [88]. Laser light reflections can obscure the tracer particles in the raw images, resulting in a loss of signal or erroneous velocity vectors.

The components of the uncertainty in the velocity field measurements were determined using the method discussed by Ramasamy and Leishman [58] and Lazar et al. [92]. A breakdown of the error associated with the current measurements, as well as the corresponding uncertainty in the measured velocity field, is shown in Table 2.1. The total propagated uncertainty in the flow velocity measurements was estimated using the equation

$$\Delta U = \sqrt{\left(\Delta\varepsilon_a \frac{\partial U}{\partial a}\right)^2 + \left(\Delta\varepsilon_{\Delta t} \frac{\partial U}{\partial \Delta t}\right)^2 + \left(\Delta\varepsilon_M \frac{\partial U}{\partial M}\right)^2 + \left(\Delta\varepsilon_c \frac{\partial U}{\partial c}\right)^2} \tag{2.3}$$

where ε_a, $\varepsilon_{\Delta t}$, ε_M, and ε_c correspond to the uncertainties in the particle acceleration, pulse separation time, magnification factor, and particle curvature. The estimated uncertainty in the measured velocity fields was determined to be 1.5% in the mosaiced ROI and 1.0% in the blade tip ROI, as summarized in Table 2.1.

Table 2.1: Errors associated with the PIV measurements and the uncertainty in the measured velocity field.

	Mosaiced ROIs	Blade Tip ROI
Diffraction limited minimum image diameter, d_{diff}, μm	4.04	6.68
Particle image diameter, d_τ, μm	4.04	6.68
Random error, σ_{rand}, μm	0.28	0.334
Acceleration uncertainty, ε_a	1.24	0.350
Curvature uncertainty, ε_c	0.0034	0.0012
Magnification uncertainty, ε_M	0.00775	0.0095
Pulse separation time uncertainty, $\varepsilon_{\Delta t}$	0.00017	0.0005
Uncertainty, % of the peak velocity	1.5	1.0

2.7 Summary

The present chapter has discussed the experimental setup and procedures used to make the various measurements. The main components of the experimental setup included the rotor system, a load cell, and the various flow field measurement systems (i.e., PIV). This chapter has also discussed the technical challenges involved in performing the measurements, as well as the errors associated with the PIV measurements and the resulting uncertainty in the velocity field data.

As discussed in Section 2.2, the rotor system used was a two-bladed teetering rotor design with rectangular blades. Tests were conducted on: 1. A baseline untwisted blade, and 2. A twisted blade with -17° of linear twist from the rotational axis to tip. Flow field measurements were performed both out of ground effect and in ground effect with the rotor in the hovering state. For the out of ground effect flow measurements, each rotor was tested at two blade loading coefficients, namely C_T/σ, of 0.053 and 0.08. However, for the in ground effect flow field measurements, only the higher blade loading coefficient was tested.

Performance sweeps (i.e., thrust and power measurements, as discussed in Section 2.3) were performed with the rotor hovering out of ground effect and in ground effect at three rotor heights. Sections 2.5.2 and 2.5.3 have discussed the experiments performed, which used both FV and PIV.

The technical challenges associated with performing PIV measurements near solid boundaries were discussed in Section 2.5.5. Several techniques were implemented to mitigate or eliminate these issues. Specifically, surface treatment and judicious alignment

of the laser relative to the ground plane were used to limit the reflections.

As discussed in Section 2.6, uncertainties in the PIV flow field measurements can arise from particle tracking errors, background noise, interrogation window size, and laser pulse separation time. The interrogation window size, laser pulse separation time, and seed particle size were judiciously chosen to minimize such errors. For the present work, the estimated uncertainty in the measured velocity field was found to be 1.5, and 1.0 % of the peak velocity in the larger and smaller ROIs, respectively.

Chapter 3

Results and Discussion

3.1 Introduction

As discussed in Chapter 1, the wake generated by a hovering rotor is comprised of vortices trailed from the blade tips as well as wake sheets trailed from along the span of each rotor blade. The details of the formation and roll-up of the vortical wake behind a rotor blade is directly related to the distribution and magnitude of the aerodynamic loads that are produced along the blade span, i.e., the distribution of bound circulation and the circulation gradient. Specifically, the blade twist, operating disk loading and blade loading coefficient and the rotor height above the ground, all significantly affect the distribution of bound circulation over the blade. Therefore, the questions that the current work aimed to answer were:

1. Do the effects of rotor thrust and blade twist (i.e., the thrust distribution over the rotor disk) significantly affect the development and evolution of the tip vortices and the wake sheets as they are convected downstream of a rotor? If so, what were the fluid dynamics that were responsible for these differences?

2. Do any of these effects change when the rotor is hovering in ground effect versus when it is operating away from the ground? If so, what might the implications be on the flow environment that is produced at the ground and the potential effects on

the problem of brownout?

3. Does blade twist have an affect on the flow near the ground after the dominant flow features (i.e., the tip vortices and wake sheets) have been convected and aged significantly in the downstream wake? In other words, do the trailed wake sheets persist in the flow to older wake ages and so contribute significantly to the flow environment near the ground plane?

The present study has examined the formation and evolution of the wake sheets and associated blade tip vortices that were generated by a rotor with untwisted and twisted blades. The rotor was operated both out of ground effect and in ground effect, as previously described in Chapter 2.

3.2 Performance Measurements

The measured power coefficient, C_P, versus the ideal power coefficient, $C_{P_{\text{ideal}}}$ is shown in Fig. 3.1 for the rotor operating out of ground effect (i.e., at $z/R = \infty$) and in ground effect (i.e., at z/R of 1.5, 1.0, 0.5, respectively). A least-squares fit to the measured performance data was performed using modified momentum theory [63]. The two-dimensional profile drag on the airfoil sections was assumed to vary according to the drag polar given by

$$C_d = C_{d_0} + C_{d_1}\alpha + C_{d_2}\alpha^2 \tag{3.1}$$

where α is the blade section angle of attack, C_{d_0} is the mean zero-lift profile drag coefficient, and C_{d_1} and C_{d_2} are empirical constants. Using the quadratic profile drag polar, the

integrated profile power coefficient for the rotor, C_{P_0}, can be written as

$$C_{P_0} = \frac{\sigma C_{d_0}}{8} + \left(\frac{2C_{d_1}}{3C_{l_\alpha}}\right) C_T + \left(\frac{4C_{d_2}}{\sigma C_{l_\alpha}^2}\right) C_T^2 \tag{3.2}$$

where σ is the rotor solidity, C_{l_α} is the two-dimensional lift-curve-slope of the airfoil sections (discussed next), and C_T is the rotor thrust coefficient. The total power coefficient, C_P, for the rotor becomes

$$C_P = C_{P_0} + \frac{\kappa C_T^{3/2}}{\sqrt{2}} = \underbrace{\frac{\sigma C_{d_0}}{8} + \left(\frac{2C_{d_1}}{3C_{l_\alpha}}\right) C_T + \left(\frac{4C_{d_2}}{\sigma C_{l_\alpha}^2}\right) C_T^2}_{\text{profile}} + \underbrace{\frac{\kappa C_T^{3/2}}{\sqrt{2}}}_{\text{induced}} \tag{3.3}$$

where κ is the induced power factor that accounts for many nonideal effects (i.e., nonuniform inflow, tip losses, nonideal wake contraction, etc.) [63]. The values of C_{d_0}, C_{d_1}, C_{d_2}, and C_{l_α} were determined from the measured airfoil characteristics given in Ref. 4 (see Fig. 3.2) to be 0.0101, 0.00458, 0.3282, and 5.953, respectively. The induced power factor, κ, was the determined using a least squares fit of Eq. 3.2 to the measured data shown in Fig. 3.1.

At higher values of rotor thrust, the induced losses dominate the power required and the slope of the power coefficient (C_P) versus the ideal power coefficient ($C_{P_{\text{ideal}}}$) line approaches the value of κ. When operating out of ground effect, the induced power factors of the two rotors were determined to be 1.1612 and 1.1336 for the untwisted and twisted blades, respectively. When the rotors were operated at zero thrust, the inboard sections on the twisted blade produced positive thrust (i.e., they operated at a positive angles of attack) whereas the outboard sections produced a negative thrust. Therefore, the values of C_{P_0} measured for the twisted blade were found to be slightly higher than that of the untwisted blade, as shown in Tables 3.1 and 3.2.

The induced power factors, κ, and mean profile drag coefficient, C_{d_0}, determined for the three rotor heights off the ground as well as out of ground effect are given in Tables 3.1 and 3.2. It is interesting to note that both blade sets produced an increase in the induced power factor as the rotor was moved from out of ground effect operation to a rotor height of $z/R = 1.5$. However, as z/R was decreased further, the induced power factor for the untwisted blade was seen to decrease; see Table 3.1. For $z/R \leq 1.0$ the induced power factor for the untwisted blade was just less than 1.0, which indicated that the ground decreased the induced losses associated with hovering flight. While the induced power factor for the rotor with the twisted blades also decreased as z/R decreased, the performance gains were less pronounced as compared to the untwisted blades; see Table 3.2.

One measure of rotor efficiency is the value of the figure of merit (FM) as given by

$$FM = \frac{C_{P_{\text{ideal}}}}{C_P} \tag{3.4}$$

where C_P is the actual power required to hover and $C_{P_{\text{ideal}}}$ is the ideal power required to hover and is defined by the equation

$$C_{P_{\text{ideal}}} = \frac{C_T^{3/2}}{\sqrt{2}} \tag{3.5}$$

where C_T is the rotor thrust coefficient, as before. Figure 3.3 shows the variation of the values of FM for the rotor with untwisted and twisted blades as a function of the blade loading coefficient, C_T/σ, for the each of the operating conditions tested. As expected, decreasing the rotor height above the ground resulted in an increase in the values of FM (see Fig. 3.3) and a decrease in the power required to hover at a given thrust (see Fig. 3.4). The rotor with untwisted blades experienced the most significant increase in the peak values of FM, which increased by approximately 20% relative to the out of ground effect

Operating state	OGE	$r/R = 1.5$	$r/R = 1.0$	$r/R = 0.5$
Induced power factor, κ	1.1612	1.1732	0.9104	0.7739

Table 3.1: Induced power factor and mean profile drag coefficient for the rotor with untwisted blades when operated at various heights above the ground.

Operating state	OGE	$r/R = 1.5$	$r/R = 1.0$	$r/R = 0.5$
Induced power factor, κ	1.1336	1.1494	1.1278	1.0361

Table 3.2: Induced power factor and mean profile drag coefficient for the rotor with twisted blades when operated at various heights above the ground.

values; see Fig. 3.3a. Conversely, the twisted blades exhibited a much less significant increase in the values of the FM from the maximum out of ground effect (i.e., FM = 0.55) to the maximum in ground effect (i.e., $FM \approx 0.65$), as shown in Fig. 3.3b. On one hand, the increased efficiency of the rotor with the untwisted blades in ground effect can most likely be attributed to changes in the inflow distribution resulting from the presence of the ground. On the other hand, the addition of twist to the blade modified the inflow distribution and, therefore, the presence of the ground most likely had less of an effect on the inflow distribution. These effects are discussed later from the perspective of the flow field measurements.

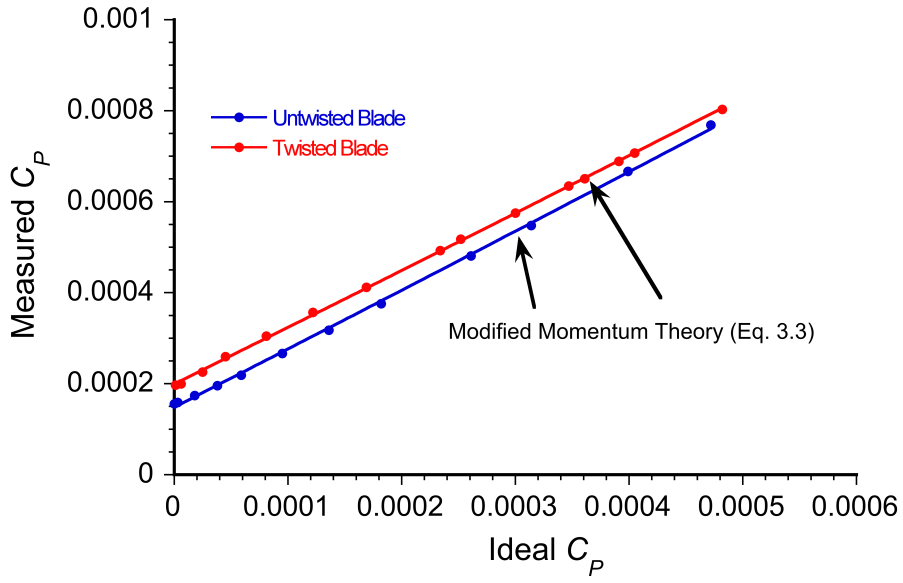

(a) Out of ground effect

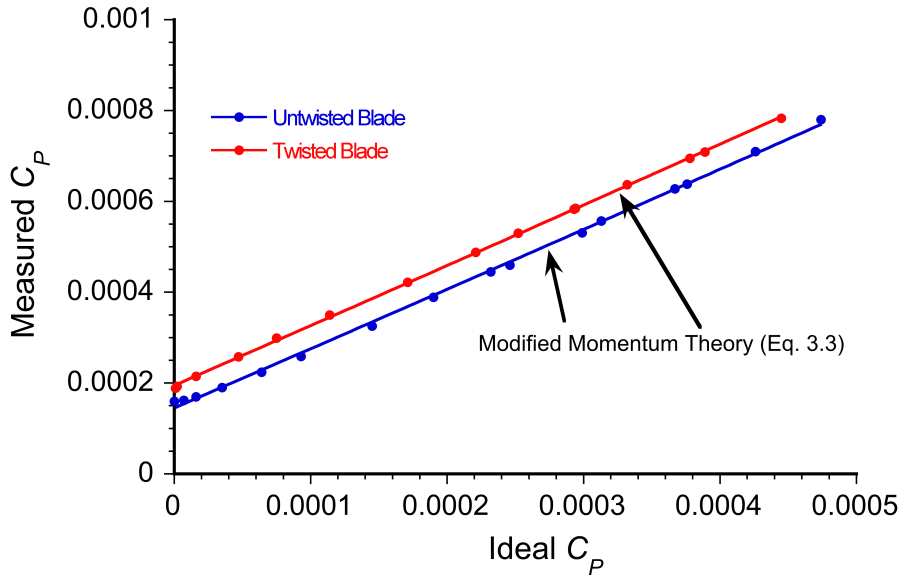

(b) In ground effect at $z/R = 1.5$

Figure 3.1: Plot of the measured power coefficient versus ideal power coefficient for each rotor operated operated: (a) Out of ground effect ($z/R = \infty$); (b) $z/R = 1.5$; (c) $z/R = 1.0$; and (d) $z/R = 0.5$.

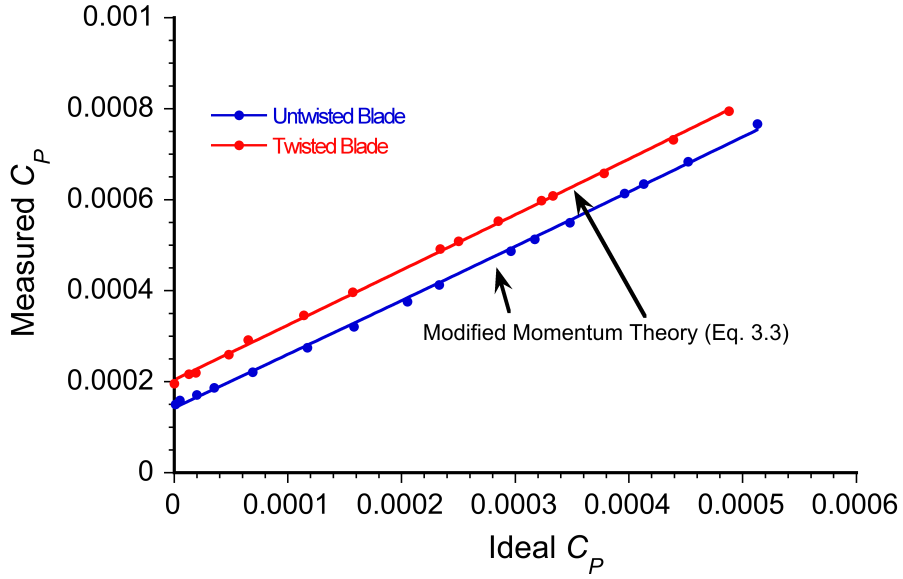

(c) In ground effect at $z/R = 1.0$

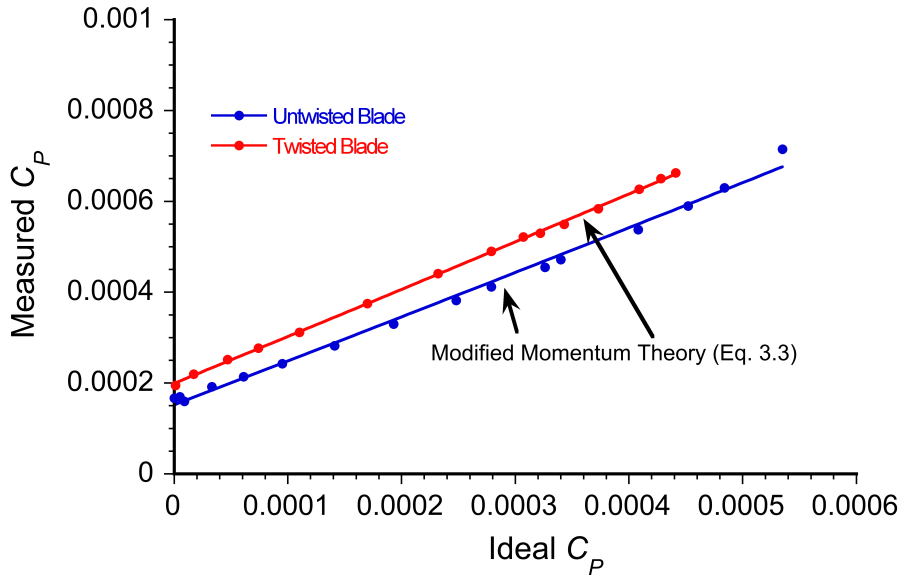

(d) In ground effect at $z/R = 0.5$

Figure 3.1: (Cont'd) Plot of the measured power coefficient versus ideal power coefficient for each rotor operated : (a) Out of ground effect ($z/R = \infty$); (b) $z/R = 1.5$; (c) $z/R = 1.0$; and (d) $z/R = 0.5$.

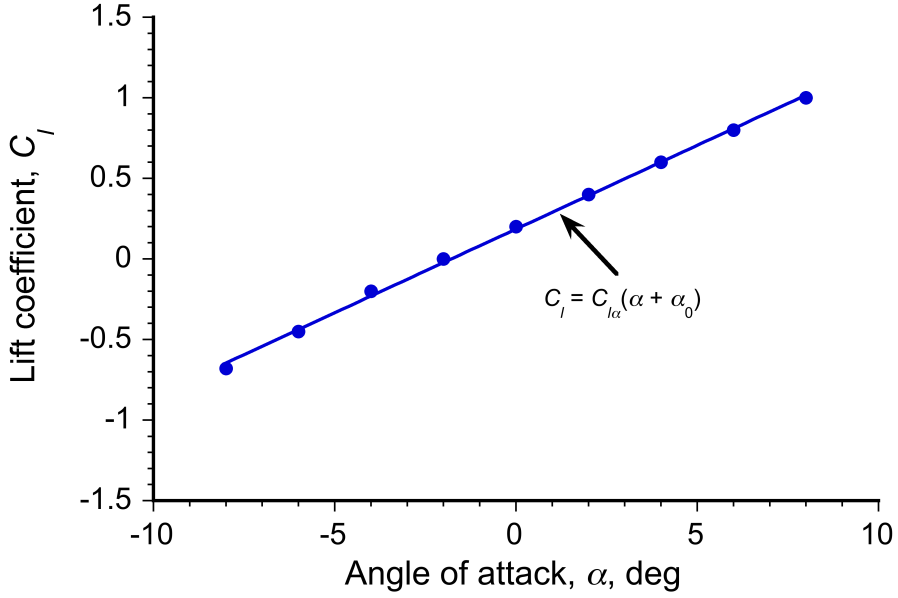

(a) Lift coefficient

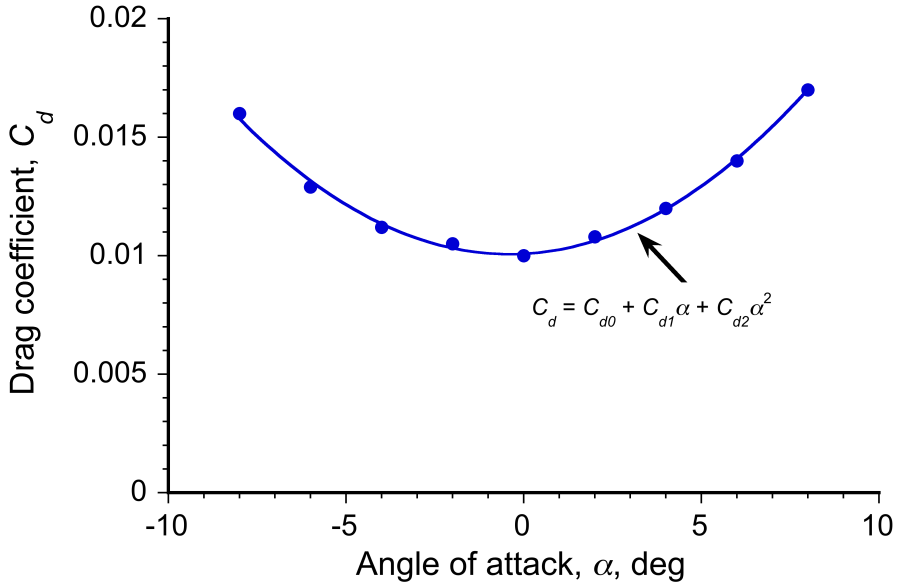

(b) Drag coefficient

Figure 3.2: Plot showing the measured values of the lift and drag coefficients versus angle of attack in the low angle of attack regime. Data from Ref. 4.

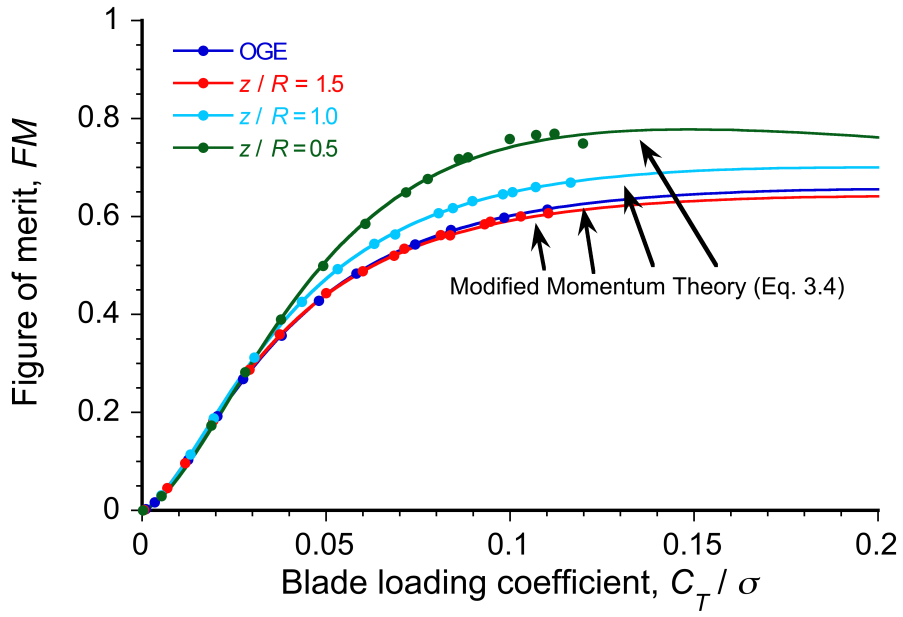

(a) Untwisted blade

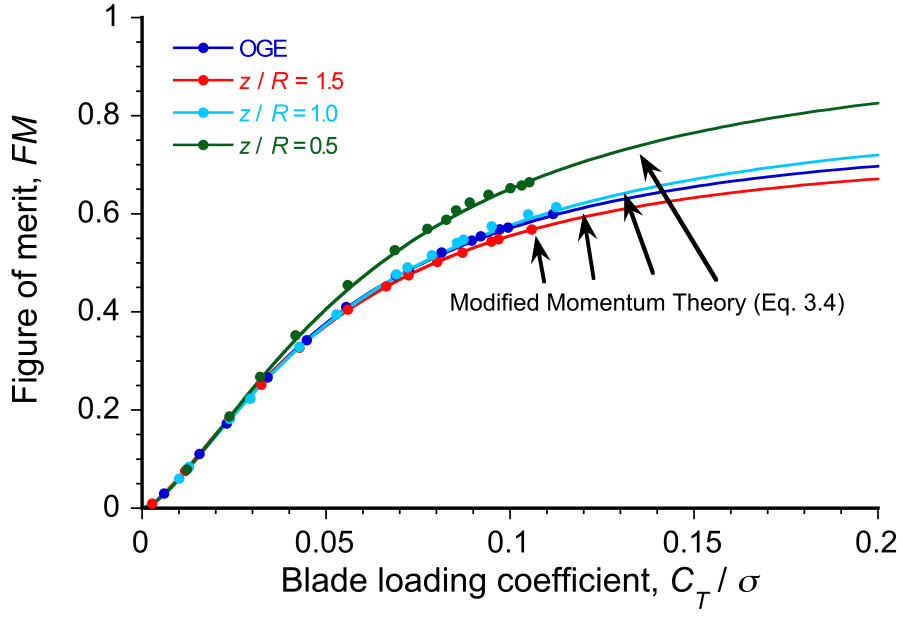

(b) Twisted blade

Figure 3.3: Plot of the figure of merit versus blade loading coefficient for different rotor heights above the ground for a rotor with: (a) Untwisted blades and (b) Twisted blades.

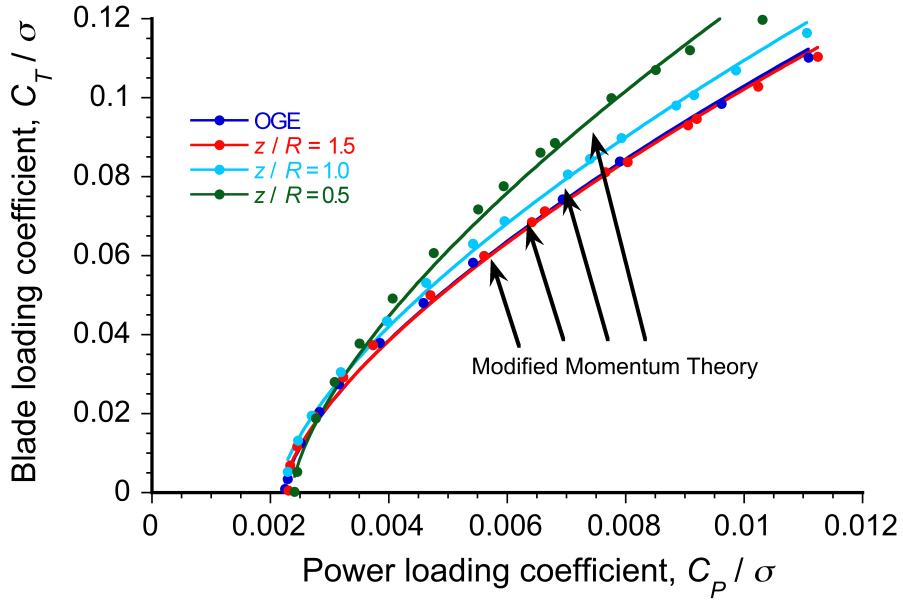

(a) Untwisted blade

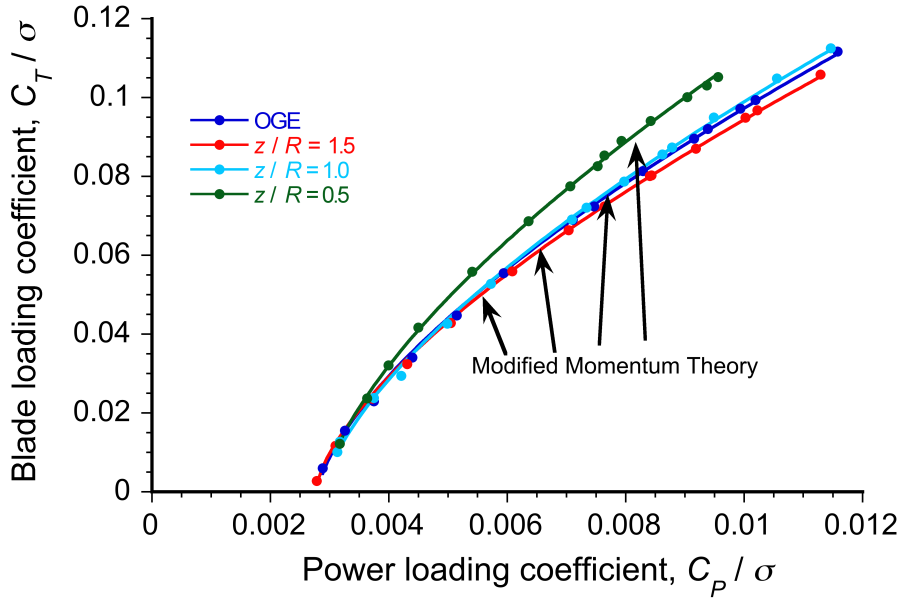

(b) Twisted blade

Figure 3.4: Plot of the power loading coefficient versus blade loading coefficient for different rotor heights above the ground for a rotor with: (a) Untwisted blades and (b) Twisted blades.

3.3 Out of Ground Effect Flow Field Measurements

While an examination of the flow field produced by a rotor operating in ground effects is critical to better understanding the problem of brownout, analyzing the flow field generated by a rotor operating out of ground effect can yield significant insight into the initial development and evolution of the wake sheets and the tip vortices.

3.3.1 Flow Visualization

To obtain good flow visualization (FV), the seed was judiciously introduced into the flow in concentrated bands to highlight the primary flow structures. Figures 3.5 and 3.6 show representative FV images for each blade set and at each blade loading coefficient, with the reference blade in this case being at $\psi_b \approx 30^\circ$, i.e., the blade had just passed through the light sheet. The FV images showed that the untwisted and twisted blades produced qualitatively similar flow fields, with a dominant vortex being trailed from the blade tip and an associated wake sheet being trailed behind the entire blade. Notice that the nominally helicoidal rotor wake intersected the laser light sheet at wake age increments of $\Delta\zeta = (360^\circ/N_b)$, which corresponded to wake ages of $\zeta = \psi_b + i\,(360^\circ/N_b)$ where $i = 0$, 1, 2, etc. For the present case, a rotor with two blades (N_b = 2) at a blade azimuth angle of approximately 30° ($\psi_b \approx 30^\circ$), this condition corresponded to wake ages of ζ = 30°, 210°, 390°, etc.

The blade tip vortices can be identified by the presence of darker almost circular regions in the FV, which arises from the small but finite centrifugal and Coriolis forces that act upon the seed particles. However, these darker regions are not completely devoid

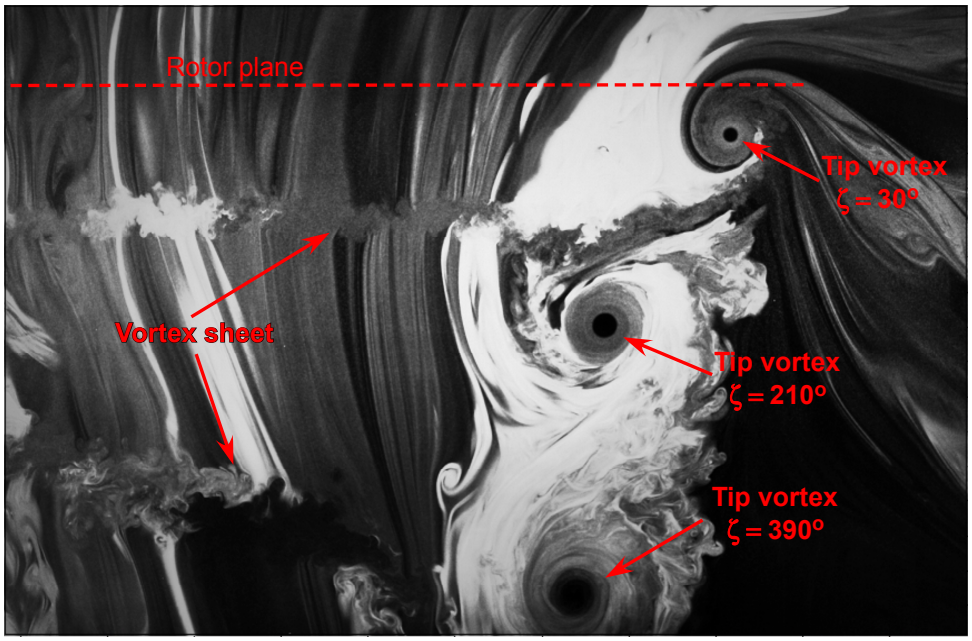

(a) Untwisted blade, $C_T/\sigma = 0.053$

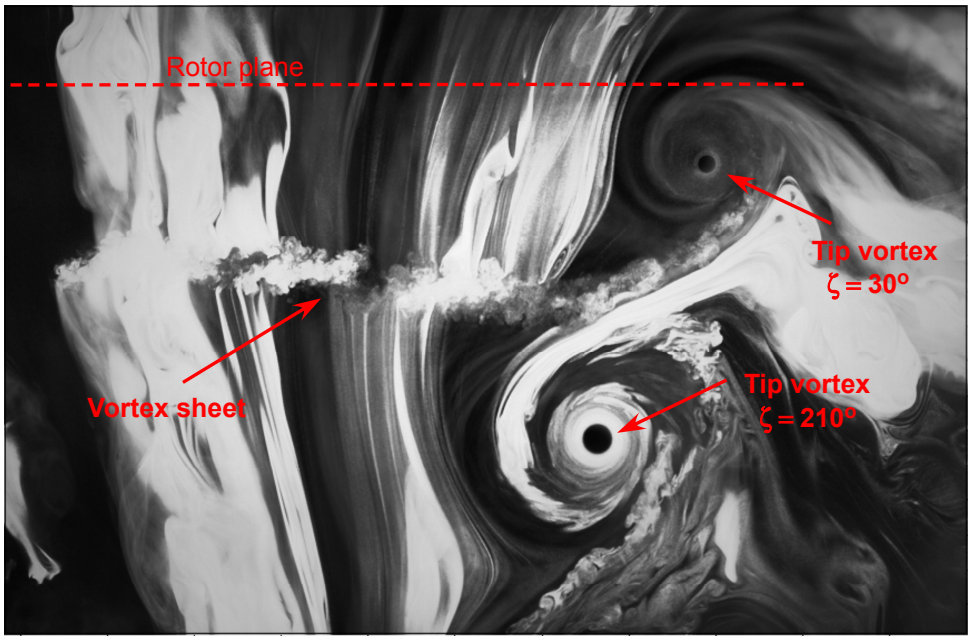

(b) Untwisted blade, $C_T/\sigma = 0.080$

Figure 3.5: Representative flow visualization images at two rotor thrusts taken in the rotor wake near the tip of the untwisted blades at a blade reference angle of $\psi_b \approx 30°$: (a) $C_T/\sigma = 0.053$; (b) $C_T/\sigma = 0.080$.

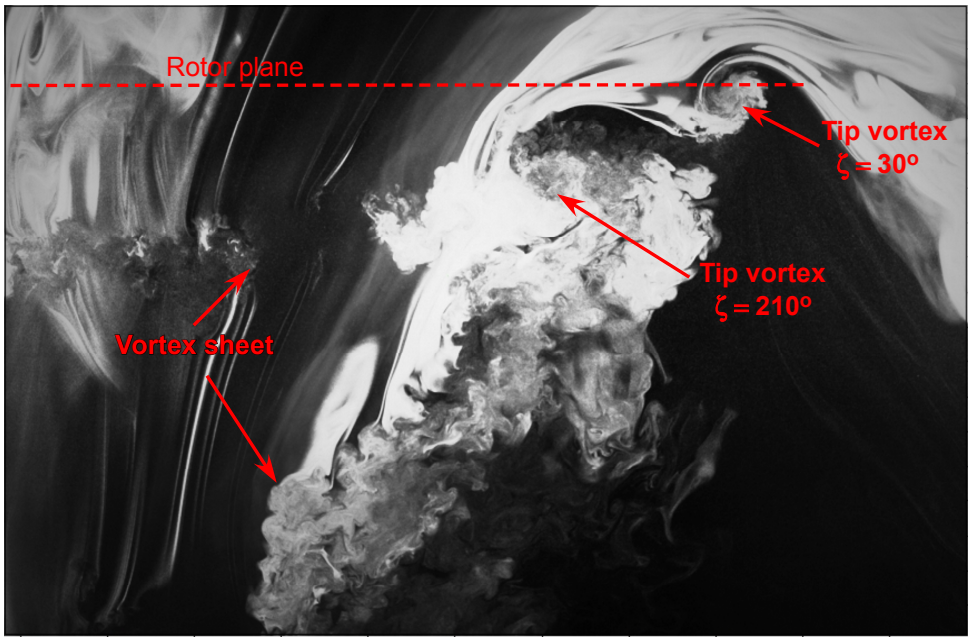

(a) Twisted blade, $C_T/\sigma = 0.053$

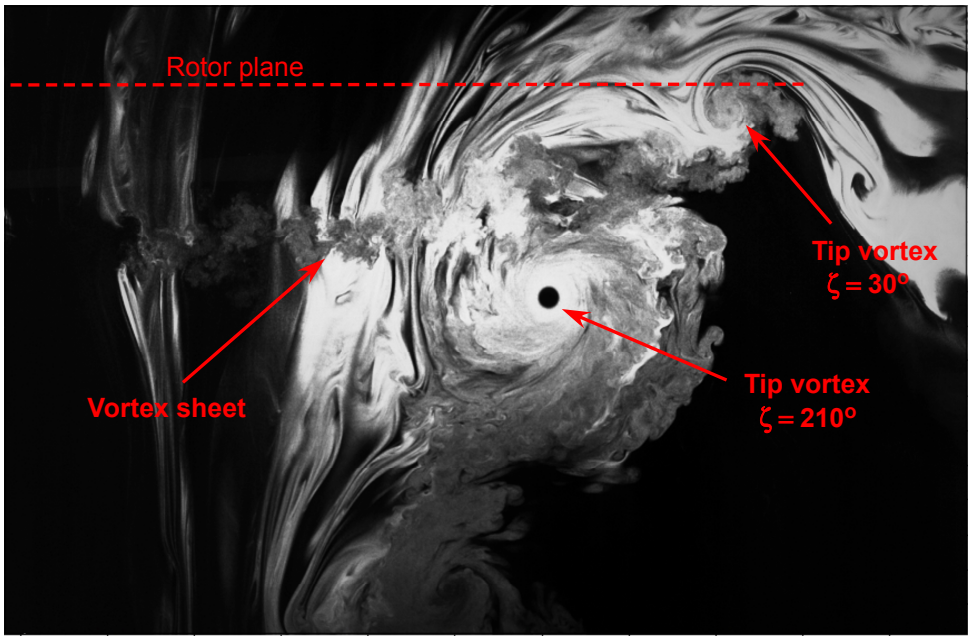

(b) Twisted blade, $C_T/\sigma = 0.080$

Figure 3.6: Representative flow visualization images at two rotor thrusts taken in the rotor wake near the tip of the twisted blades at a blade reference angle of $\psi_b \approx 30°$: (a) $C_T/\sigma = 0.053$; (b) $C_T/\sigma = 0.080$.

of seed particles, which allowed PIV measurements to be obtained. Furthermore, the radial dimensions of the darker regions do not necessarily reflect changes in the local flow structure or vortex strength because seeding can vary between FV images. The wake sheets, which are of primary interest in the present work, can be easily identified by the shear layer (i.e., discontinuities in the smoke streaklines) that form initially almost parallel to the trailing edge of the blades. While these shear layers are often referred to as a wake sheet, strictly speaking a "wake sheet" is only obtained when the vorticity lies in a surface of zero thickness. Nevertheless, it is convenient for further discussion to refer to this flow feature as a wake sheet.

The FV results also indicated that the tip vortices produced by the untwisted blades rolled-up almost immediately behind the trailing edge, and could be considered fully-formed at a wake age as early as $\zeta = 3^\circ$. However, the tip vortices produced by the twisted blades appeared to take somewhat longer to roll-up, and not until $\zeta \approx 15^\circ$ to 20° did they appear to have fully-formed. Although the rotor was operated at the same thrust and C_T/σ, the differences in the vortex roll-up seen in the flow visualization may be a consequence of the changes in the loading distributions produced over the tip region of each blade set.

The structure and behavior of the wake sheets are of particular interest in the present work, which as mentioned previously appeared as shear layers that were trailed behind the full span of each of the blades. At the most basic level, these shear layers are formed as a consequence of the merging of the boundary layers off the upper and lower surfaces of the blades. Furthermore, these sheets contained an initial vortical strength (i.e., distribution of circulation strength) that was related to the magnitude and spanwise gradient of lift

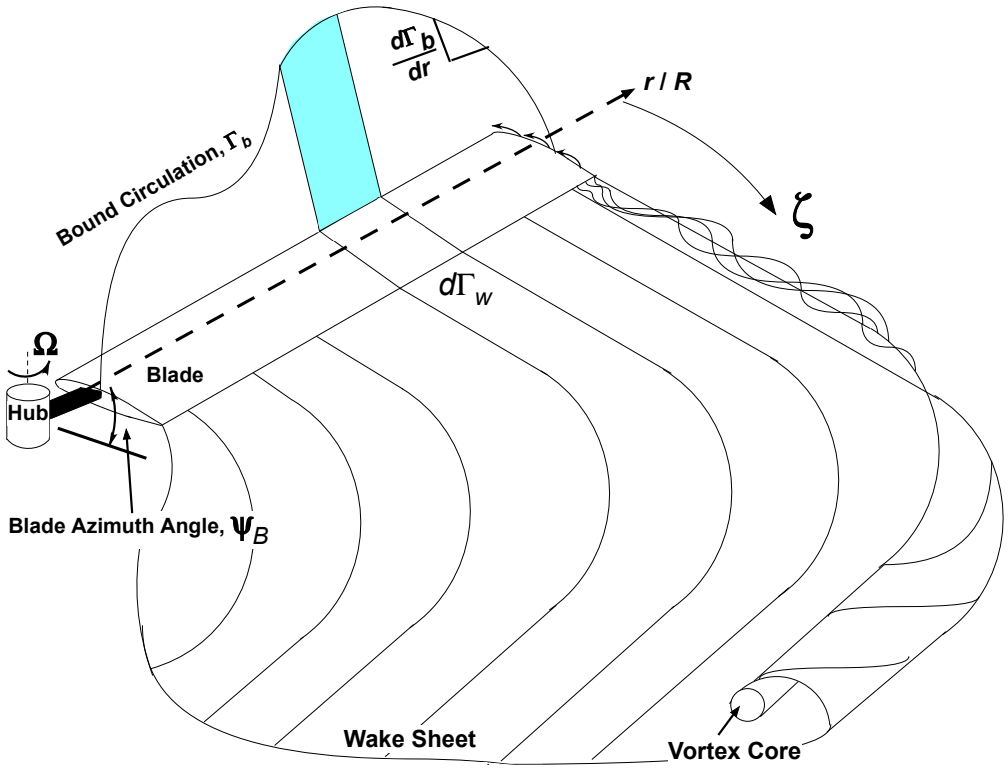

Figure 3.7: Schematic showing the nature of the bound circulation distribution along the rotor blade and the corresponding flow features trailed into the wake by a rotor.

(i.e., the "bound" circulation) over the blade, as shown in Fig. 3.7. The spanwise gradient of lift can be reconciled with classical lifting-line theory, which states that the trailed circulation strength, $d\Gamma_w$, is proportional to the local circulation gradient [93], i.e.,

$$d\Gamma_w = \left(\frac{\partial \Gamma_b}{\partial r}\right) dr \tag{3.6}$$

where $\partial\Gamma_b/\partial r$ is the local circulation gradient along the rotor blade and dr is the radial distance over which the change in circulation occurs.

Initially, the wake sheets were trailed directly behind the entire blade span (see Fig. 3.5 and 3.6), however, the subsequent behavior of the wake sheets depend on many factors. Specifically, as the sheets and tip vortices convected in the nonuniform flow

below the rotor disk they experienced various forms of distortions; see Figs. 3.5 and 3.6. Furthermore, a comparison of Figs. 3.5 and 3.6 showed that the wake sheets produced by the rotor with twisted blades appeared to be significantly thicker and more turbulent than the sheets produced by the untwisted blades.

As previously documented by Landgrebe [36–38], the wake sheets produced by a rotor with untwisted blades convect relatively non-uniformly, with the fastest axial convection being near the blade tip. The faster axial convection below the tip region caused the portion of the sheet below the blade tip to assume a pronounced downward orientation relative to the rotor TPP, as shown in Fig. 3.5. The wake sheets produced by the untwisted blades were also seen to take on two different slopes (i.e., a negative slope inboard and positive slope outboard) at a local point on the sheet; this latter effect occurred as a consequence of the local interactions of the sheet with the adjacent tip vortex. Conversely, the wake sheets produced by the twisted blade were observed to convect more uniformly, resulting in the portion of the sheet near the tip assuming an upward orientation relative to the rotor TPP; see Fig. 3.6.

The FV results also showed that turbulent eddies originating from the vortical sheet underwent a process of stretching and relaminarizaton as they were entrained into the tip vortex cores. This behavior was a consequence of the high rotational flow accelerations found in the core region [53, 55, 56], which suppressed the creation of turbulence and can even lead to rotational stratification of existing turbulence. The FV shown in Figs. 3.5 and 3.6 confirms that a smooth, eddy-free, almost laminar flow existed in the vortex core regions. Ramasamy & Leishman [58], studied the foregoing behavior in terms of a rotational stratification effect using a Richardson number (i.e., a measure of the ratio of

turbulence produced or consumed inside the vortex to the turbulence produced by shear). The Richardson number can be written as

$$Ri = \frac{\left(\frac{2V_\theta}{r^2}\right)\frac{\partial\left(V_\theta r\right)}{\partial r}}{\left(r\frac{\partial\left(V_\theta/r\right)}{\partial r}\right)^2} \tag{3.7}$$

where r is the radial distance from the vortex core, and $V_\theta(r)$ is the swirl velocity profile. Ultimately, if the local Richardson number is above the threshold (i.e., $Ri \approx Re_v^{1/4}$) turbulence cannot form [55, 56, 58]. The ability of the tip vortex core to remain above the threshold (i.e., maintain a laminar core) helps to explain why the tip vortices persisted to older wake ages and significant downstream distances compared to the vortices contained in the wake sheet (as discussed in more detail later in Section 3.3.2.3).

For the rotor with the twisted blades when it was operated at the lower value of C_T/σ (i.e., 0.053), it was interesting to note the lack of coherent tip vortices after about one rotor revolution (i.e., for $\zeta \geq 360^\circ$). Figure 3.8 shows a time-history of the wake produced behind the twisted blade at this condition for wake ages of approximately 125° to 215°. By ζ = 125°, the tip vortex appeared to have fully rolled-up and had begun to convect axially downward in the rotor wake. However, because the tip vortex remained closer to the TPP of the rotor, as the following blade passage occurred (see Fig. 3.8b) it directly interacted with the tip vortex, as detailed in Fig. 3.8c. Such direct or head-on interactions of the blade with a tip vortex (i.e., a form of perpendicular blade vortex interaction or BVI) caused the rapid diffusion of the vorticity in the vortex core. Consequently, in this case no distinguishable vortices were present in the rotor wake after approximately one rotor revolution (i.e, for $\zeta \geq 360^\circ$); see Fig. 3.8d.



(a) $\zeta = 125^\circ$



(b) $\zeta = 155^\circ$

Figure 3.8: Flow visualization time-history of a tip vortex trailed from the rotor with the twisted blades operating at $C_T/\sigma = 0.053$ showing the consequences of the direct interaction of the trailed tip vortex with the following blade.



(c) $\zeta = 185^\circ$



(d) $\zeta = 215^\circ$

Figure 3.8: (Cont'd) Flow visualization time-history of a tip vortex trailed from the rotor with the twisted blades operating at $C_T/\sigma = 0.053$ showing the consequences of the direct interaction of the trailed tip vortex with the following blade.

3.3.2 Particle Image Velocimetry (PIV)

3.3.2.1 Wake Displacements

Figures 3.9 and 3.10 quantify the locations of the tip vortices and the wake sheets as a function of wake age for each rotor at each of the values of C_T/σ. The results showed that the wake sheets produced by the untwisted blades convected faster below the blade tip region, with very little axial convection of the sheets near the blade root. In this case, the more linear spanwise downwash distribution in the wake below the rotor was the source of this non-uniform convection, which also resulted in a smaller axial distance between the wake sheets; see Fig. 3.9. However, because the rotor with the twisted blades produced a more uniform velocity distribution in the wake (discussed next) the sheets convected more uniformly, resulting in larger axial distances between adjacent sheets, as shown in Fig. 3.10.

Notice from Figs. 3.9 and 3.10 that a wave-like perturbation was formed on the wake sheets shortly after they were trailed from the blades. This perturbation was more pronounced on the sheets produced by the twisted blades, and initially grew relatively quickly in amplitude as the sheet aged; see Figs. 3.10a and 3.10b. However, as the sheets convected further axially downward in the wake, they were stretched by the non-uniform velocity field (discussed quantitatively next), which appeared to suppress any additional growth in the wave amplitude. Furthermore, the wake sheets trailed by the untwisted blades were seen to take on two distinct slopes relative to the TPP (i.e., negative inboard and positive outboard), as discussed previously and shown in Fig. 3.9. Figure 3.10a also shows that at the lower value of C_T/σ, the tip vortices produced by the twisted blades

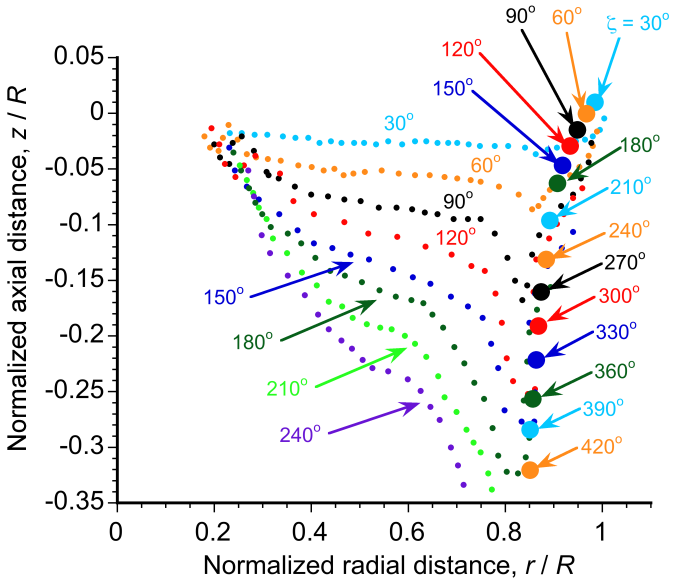

(a) Untwisted blade, $C_T/\sigma = 0.053$

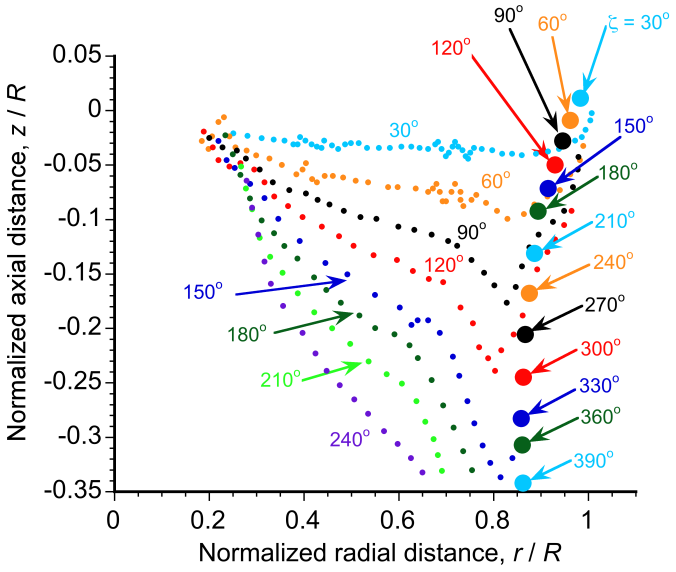

(b) Untwisted blade, $C_T/\sigma = 0.080$

Figure 3.9: Plot of the axial and radial locations of the wake sheets and tip vortices for the rotor with the untwisted blades: (a) $C_T/\sigma = 0.053$; (b) $C_T/\sigma = 0.080$.

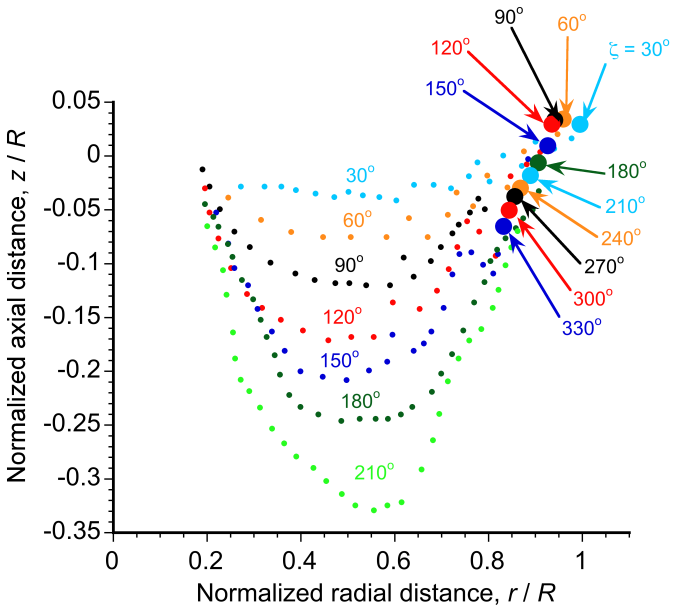

(a) Twisted blade, $C_T/\sigma = 0.053$

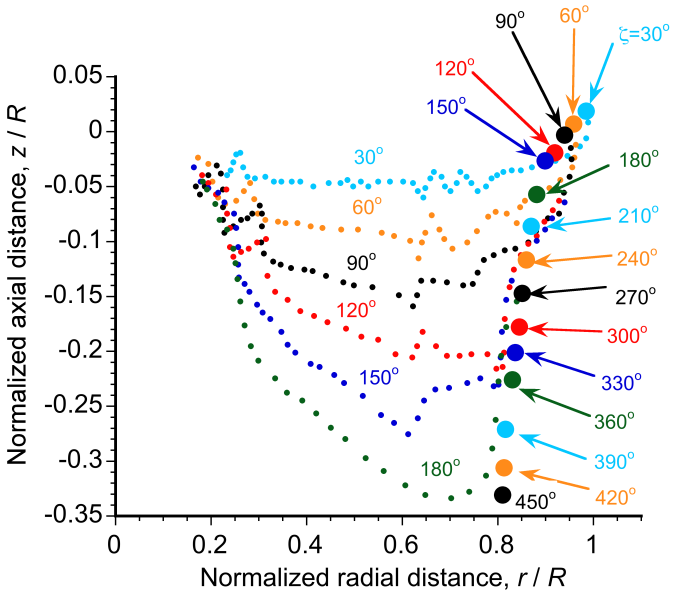

(b) Twisted blade, $C_T/\sigma = 0.080$

Figure 3.10: Plot of the axial and radial locations of the wake sheets and tip vortices for the rotor with the twisted blades: (a) $C_T/\sigma = 0.053$; (b) $C_T/\sigma = 0.080$.

were convected axially more slowly than for the other cases, the outcome being that it caused the following blade to collide with the tip vortex at early wake ages, a behavior previously discussed and shown in Fig. 3.8.

The radial and axial positions of the center of the vortex core (determined using the Q-criterion and discussed in Appendix B) as a function of wake age are summarized in Fig. 3.10a. It is clear from Fig. 3.11a that the wake produced by the rotor with the twisted blades contracted radially inward significantly more than the untwisted blades. While the radial position of the tip vortices varied with both blade twist and rotor thrust, smaller variations were seen in the axial position of the tip vortices, which was a direct consequence of the differences in the axial convection velocities; see Fig. 3.11b. Notice that, the rate at which the vortices convected axially (i.e, the slope of the curves in Fig. 3.11b) was seen to increase suddenly after the passage of the following blade, similar to the results first observed by Landgrebe [36–38] and Kocurek & Tangler [39], as well as other investigators. It is interesting to note that the vortices produced by the rotor with twisted blades (when operating at the higher value of C_T/σ) convected axially at approximately the same rate as the vortices produced by the untwisted blades (when operating at the lower value of C_T/σ), which was a consequence of the differences in the spanwise downwash distribution in the wake (discussed next).

3.3.2.2 Averaged Velocity Field Measurements

Figures 3.12 and 3.13 show the time-averaged velocity fields in the wake of each of the rotors with untwisted and twisted blades, respectively. The results confirmed that

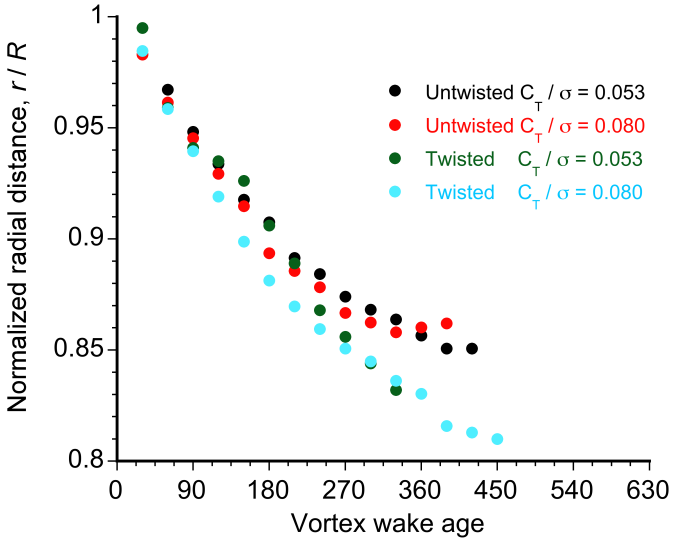

(a) Normalized radial distance

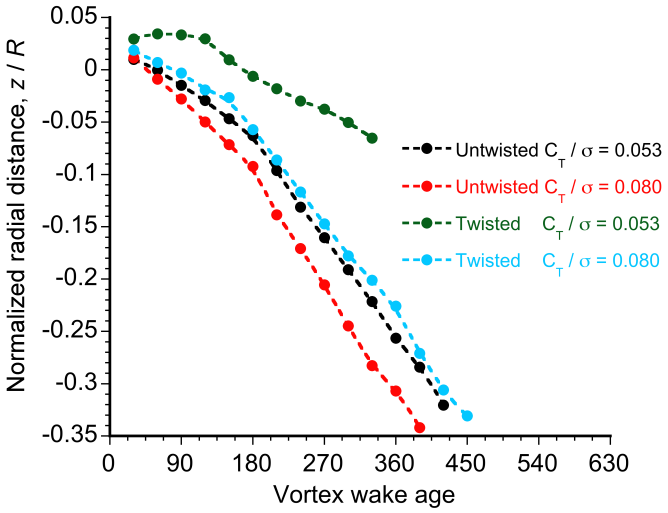

(b) Normalized axial distance

Figure 3.11: Summary of the radial and axial tip vortex locations in the rotor wake as a function of wake age, ζ, for the rotors with the untwisted and twisted blades: (a) Normalized radial distance; (b) Normalized axial distance.

the twist of the blade significantly affected the distribution of the axial velocity in the downstream wake. Notice that in each case, the rotor wake initially contracted and so the velocity of the slipstream increased with distance downstream from the rotor disk, as would be expected based on conservation of mass within the slipstream boundaries. The contraction of the wake also affected the axial displacement of the wake sheets. As previously discussed in Section 2.5.5, any abrupt change in the velocities seen at the upper boundary between the mosaiced measurements are erroneous and are an artifact of local blade surface reflections in the PIV images, which cannot be completely avoided.

The axial flow velocities in the wake below the rotor with the twisted blades was found to be more uniformly distributed, with the highest values occurring around mid-span; see Fig. 3.13. Conversely, the untwisted blades produced a velocity distribution that was biased toward the blade tip, with the lowest axial velocities being found inboard of mid-span. As noted by Landgrebe [36–38], an increase in the slipstream velocities at higher values of rotor thrust (i.e., those associated with the increase of the rotor disk loading) lead to the tip vortices and wake sheets both being convected axially more quickly in the downstream wake. As a consequence, the helical pitch was increased between adjacent turns of the rotor wake. As shown in Ref. 44, a higher helical pitch decreases the susceptibility of the downstream wake to the development perturbations and instabilities because fewer interactions occur between adjacent turns of the vortex wake.

The flow velocities induced in the wake are, of course, directly related to the circulation strength of the vortices. Namely, a higher circulation strength would be expected to produce higher flow velocities. Bhagwat and Leishman [60] showed that the initial circulation strength of the tip vortices was approximately 70% of the estimated peak bound

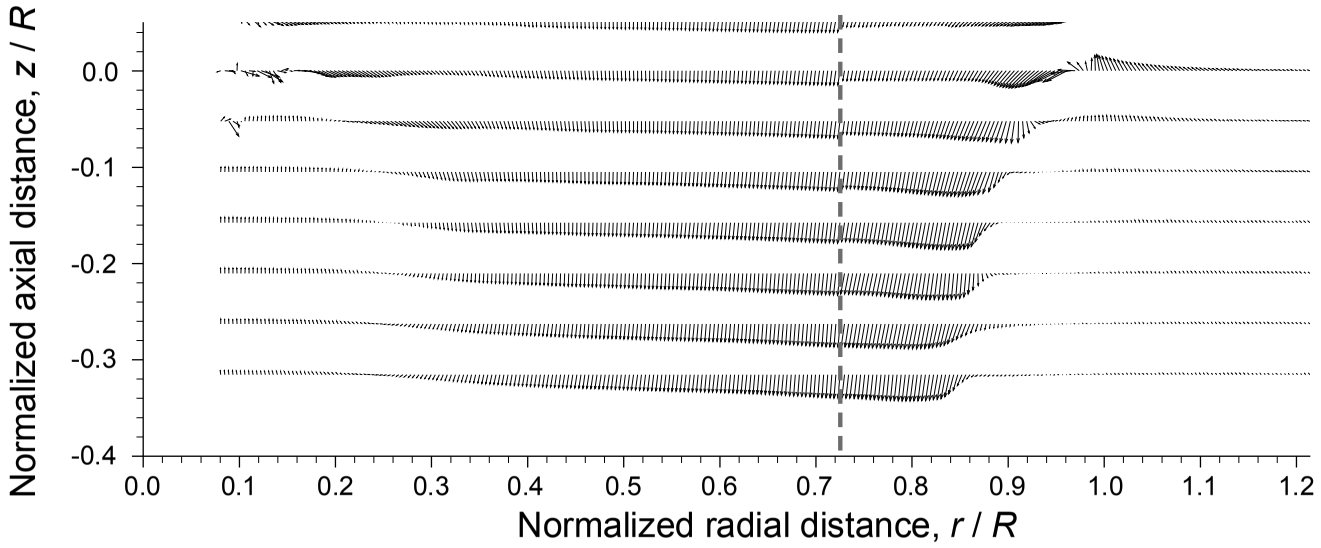

(a) Untwisted blade, $C_T/\sigma = 0.053$

Figure 3.12: Measured time-averaged spanwise velocity distribution at varying axial locations in the wake trailed below the rotor with the untwisted blades: (a) $C_T/\sigma = 0.053$; (b) $C_T/\sigma = 0.080$.

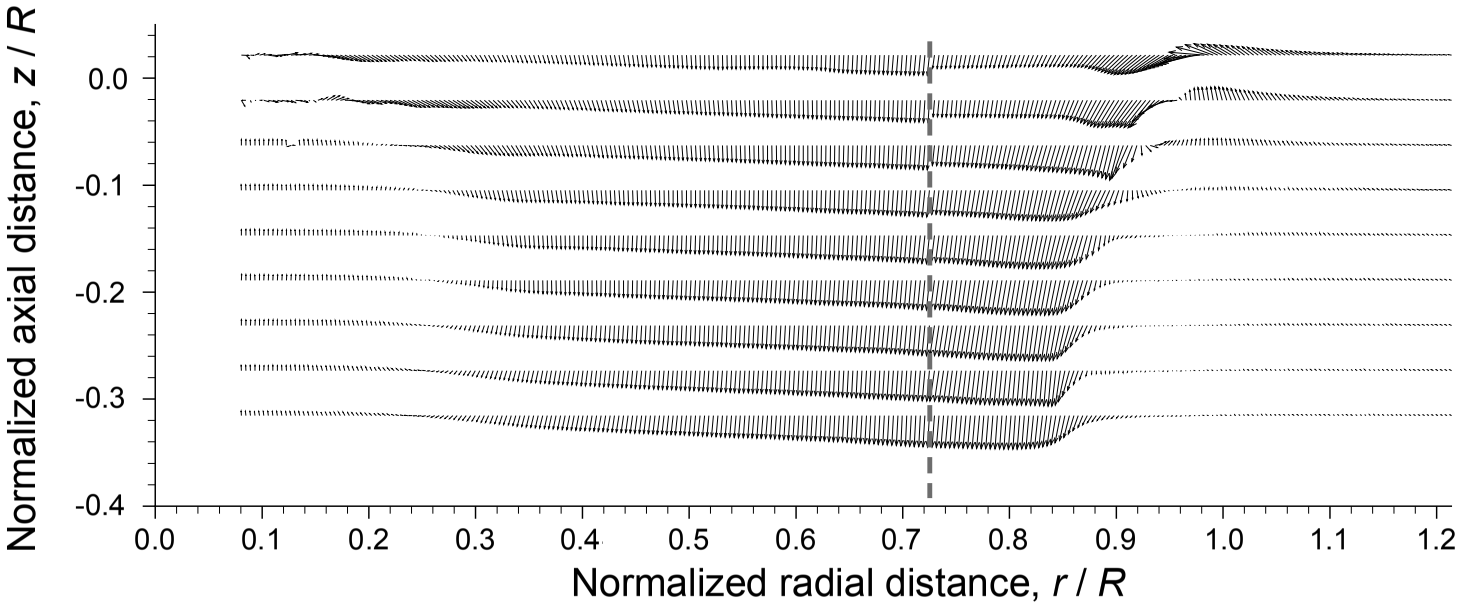

(b) Untwisted blade, $C_T/\sigma = 0.080$

Figure 3.12: (Cont'd) Measured time-averaged spanwise velocity distribution at varying axial locations in the wake trailed below the rotor with the untwisted blades: (a) $C_T/\sigma = 0.053$; (b) $C_T/\sigma = 0.080$.

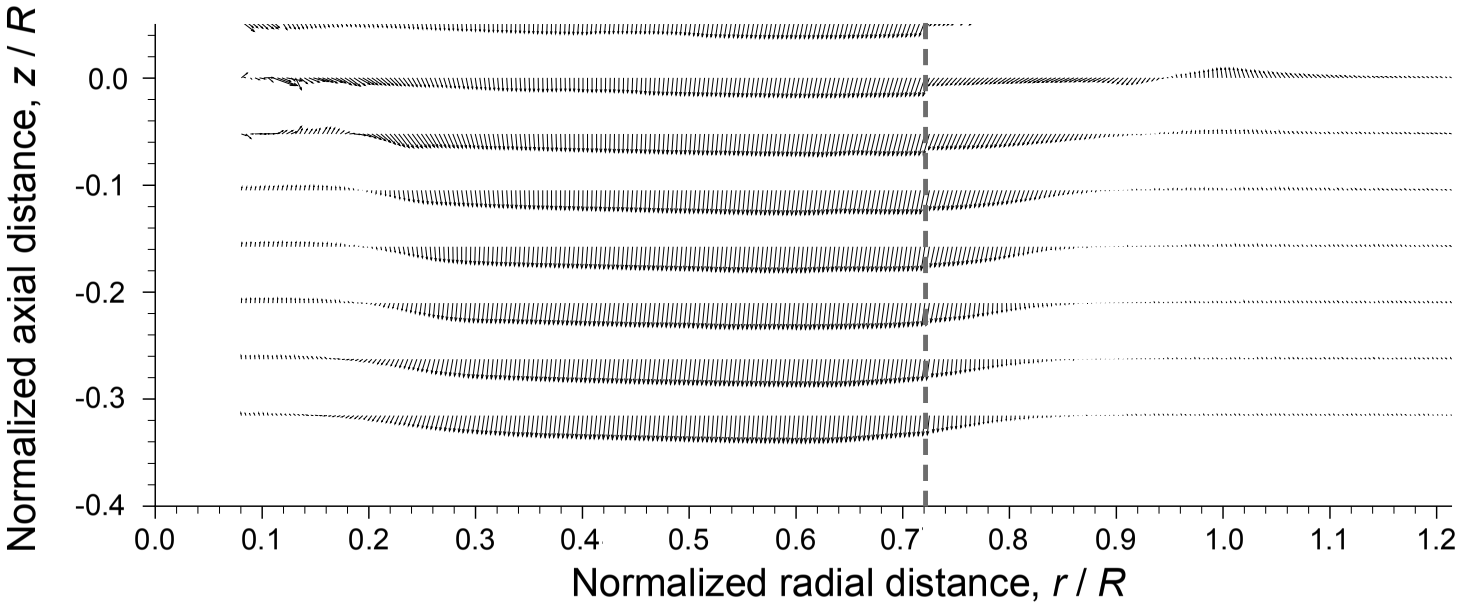

(a) Twisted blade, $C_T/\sigma = 0.053$

Figure 3.13: Measured time-averaged spanwise velocity distribution at varying axial locations in the wake trailed below the rotor with the twisted blades: (a) $C_T/\sigma = 0.053$; (b) $C_T/\sigma = 0.080$.

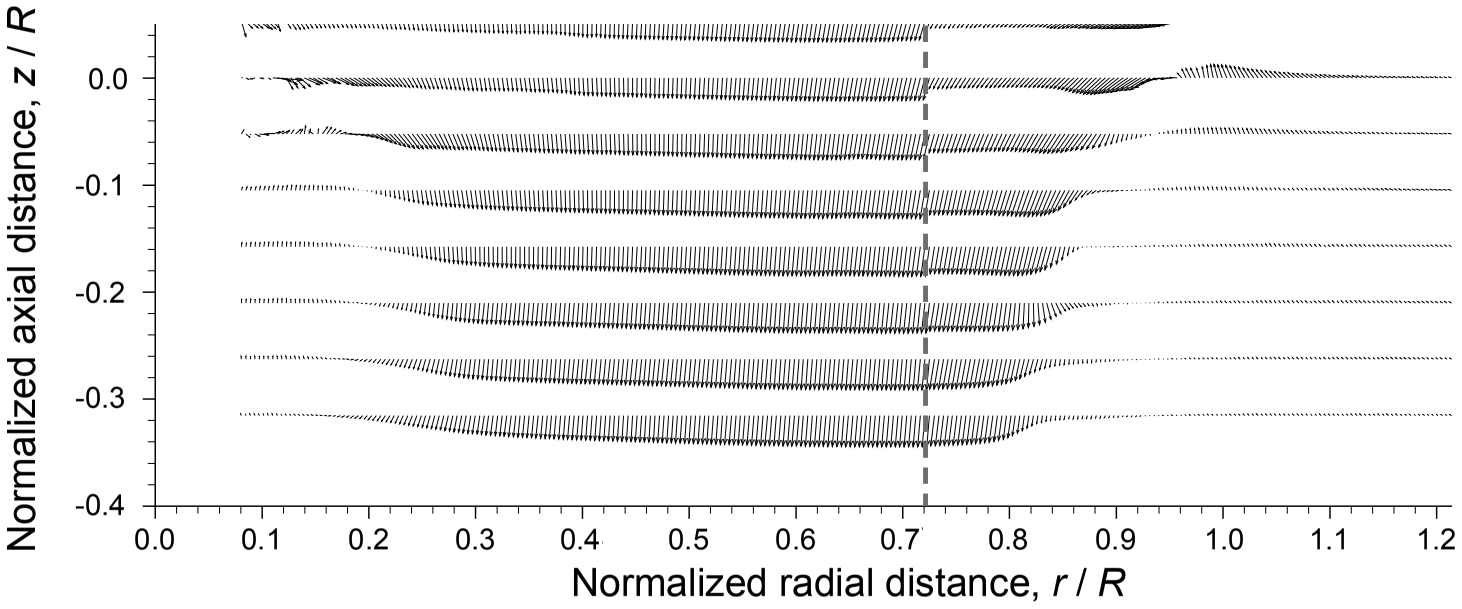

(b) Twisted blade, $C_T/\sigma = 0.080$

Figure 3.13: (Cont'd) Measured time-averaged spanwise velocity distribution at varying axial locations in the wake trailed below the rotor with the twisted blades: (a) $C_T/\sigma = 0.053$; (b) $C_T/\sigma = 0.080$.

circulation on the blades. While it is possible to measure the bound circulation along the span of the blade [60], there are many challenges involved in doing so. However, the results obtained using a model (in this case a free-vortex method) can provide a good estimate of the distribution of bound circulation on the blade and can also help to explain the nature of some of the wake measurements shown in the present work.

Figure 3.14 shows the spanwise distribution of bound circulation for the rotors with the untwisted and twisted blades at the two thrust conditions, as calculated using the free-vortex method [94]. A comparison of the results given in Fig. 3.14 indicated that the addition of blade twist off-loaded the blade tip region and also reduced the peak value of bound circulation, the calculated peak bound circulation along the twisted blade being approximately 75% of the peak bound circulation along the untwisted blade, which is consistent with experimental measurements. Therefore, the tip vortices produced by the rotor with the twisted blades would be expected (based on the free-vortex method) to contain 25% less circulation than the corresponding tip vortices produced by the untwisted blades.

This latter conclusion is supported by the PIV results shown in Figs. 3.15 and 3.16, which show the total flow velocities in the wake produced below the two rotors at a reference blade azimuth angle of $\psi_b = 10^\circ$. The tip vortices produced by the rotor with the untwisted blades induced significantly higher local flow velocities compared to the vortices produced by the twisted blade. As previously discussed, the tip vortices produced by the rotor with the untwisted blades when operating at the lower thrust condition were convected axially through the flow somewhat faster than the vortices produced by the twisted blades and were, therefore, below the rotor TPP when the following blade passage

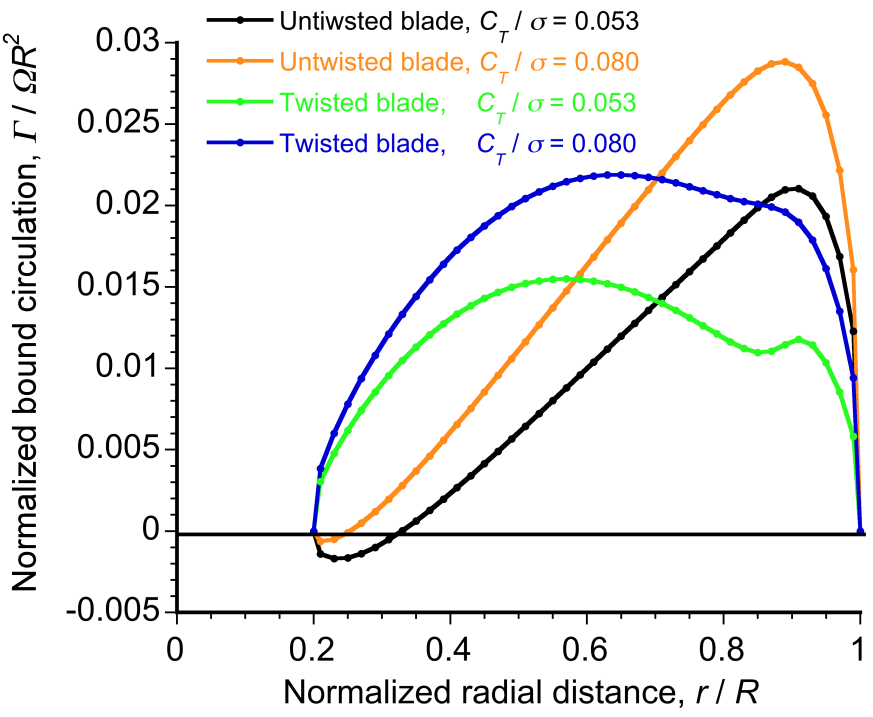

Figure 3.14: Predictions of the spanwise distributions of bound circulation for the untwisted and twisted blades at each rotor thrust condition using a free-vortex method.

occurred, as discussed previously in Section 3.3.1. The faster axial convection allowed the vortices produced by the untwisted blade to persist in the wake to significantly older wake ages (i.e., to $\zeta > 450°$) compared to the twisted blades (to $\zeta \leq 360°$), a behavior that affected the overall structure of the developing wake; see Fig. 3.15a and 3.16a. The persistence of the tip vortices produced by the rotor with the untwisted blades would also be expected to significantly affect the flow field near the ground.

As previously discussed, the differences seen between the two blade sets can be attributed to changes in their loading distribution (i.e., to the bound circulation on the blade), specifically the offloading of the tip region of the twisted blade; see Fig. 3.14. While differences in the wake flows between the two blade sets were found to be somewhat less at the higher rotor thrust, some differences were still apparent inboard near the blade root where the twisted blades produced relatively higher flow velocities; see Fig. 3.16. Specifically, in the downstream contracted wake the flow velocities were noted to be significantly higher when using the twisted blades. Furthermore, in this case the flow near the root of the blade appeared to be more turbulent and also showed the signature of a more concentrated region of vorticity that was indicative of a root vortex, which is discussed further in Section 3.3.2.3.

3.3.2.3 Vorticity in the Wake

Previous work has shown that the wake sheets trailed behind a rotor blade consist of small pairs of counterrotating vortices [22], which are usually called Taylor–Görtler or T–G vortices [95]. These T–G vortex pairs can be seen in Figs. 3.17 and 3.18 by the red

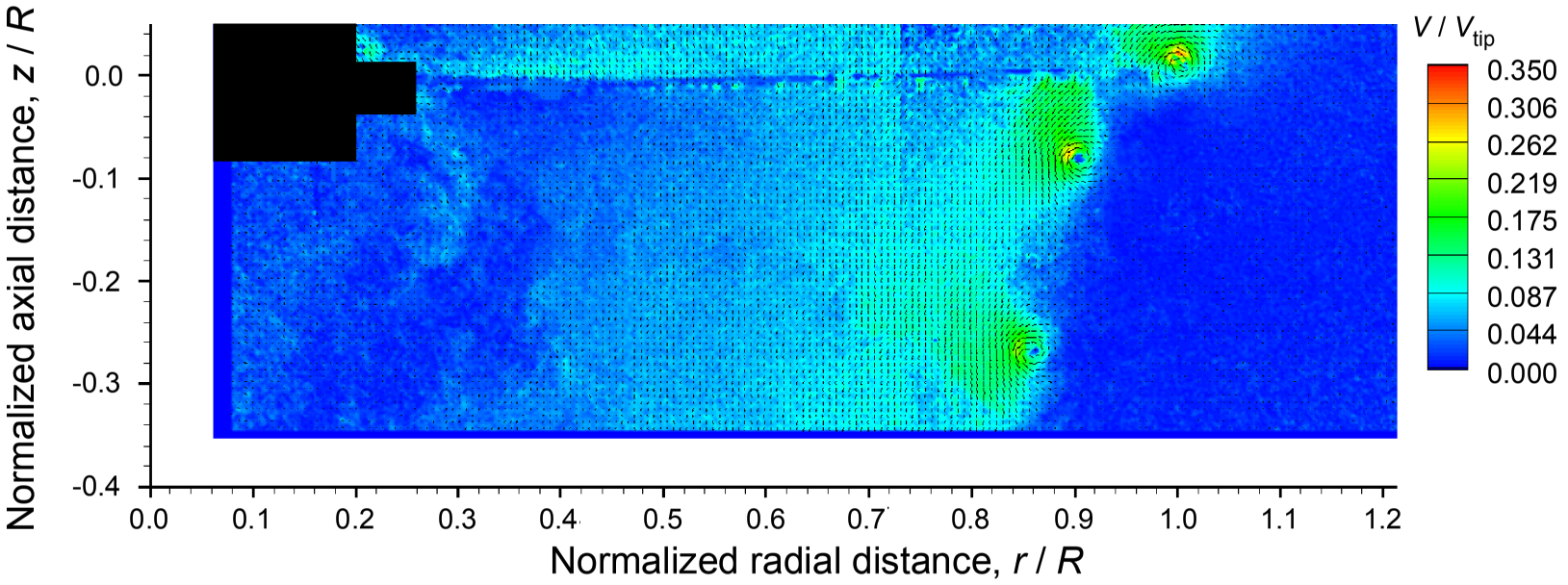

(a) Untwisted blade, $C_T/\sigma = 0.053$

Figure 3.15: Contours of the normalized total flow velocity for the rotor with the untwisted blades at a blade azimuth angle of $\psi_b = 10°$: (a) $C_T/\sigma = 0.053$; (b) $C_T/\sigma = 0.080$

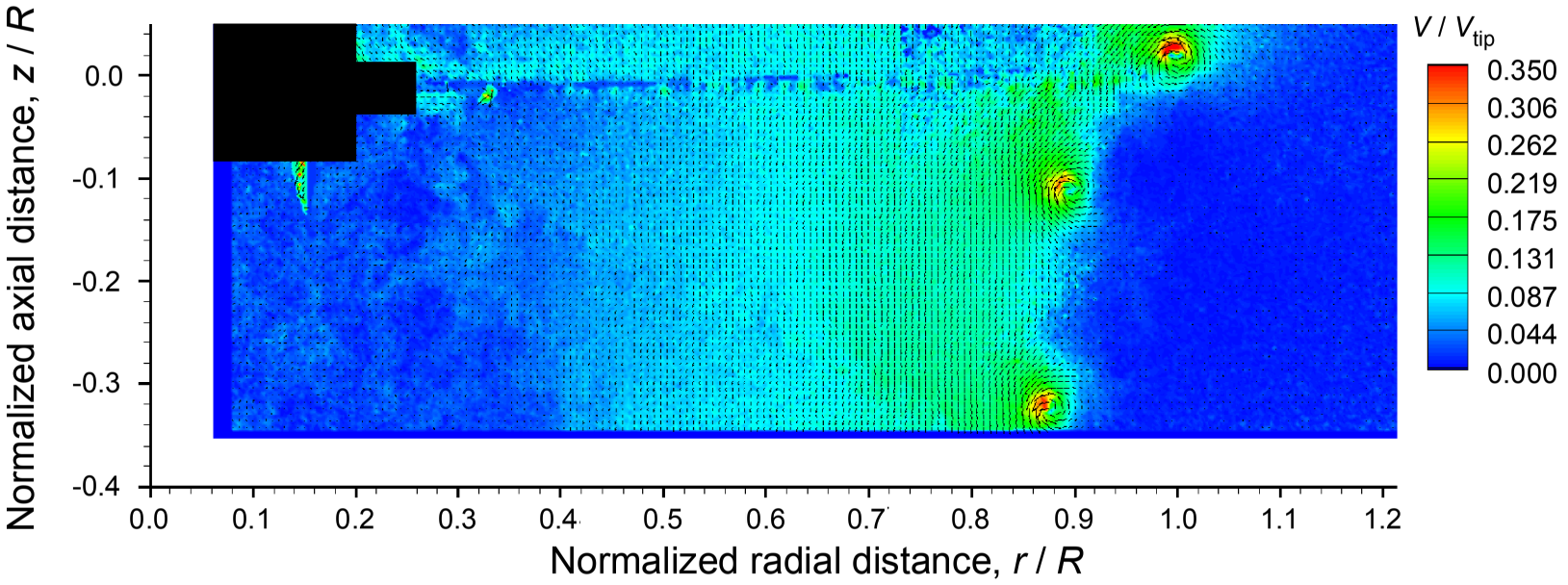

(b) Untwisted blade, $C_T/\sigma = 0.080$

Figure 3.15: (Cont'd) Contours of the normalized total flow velocity for the rotor with the untwisted blades at a blade azimuth angle of $\psi_b = 10°$: (a) $C_T/\sigma = 0.053$; (b) $C_T/\sigma = 0.080$.

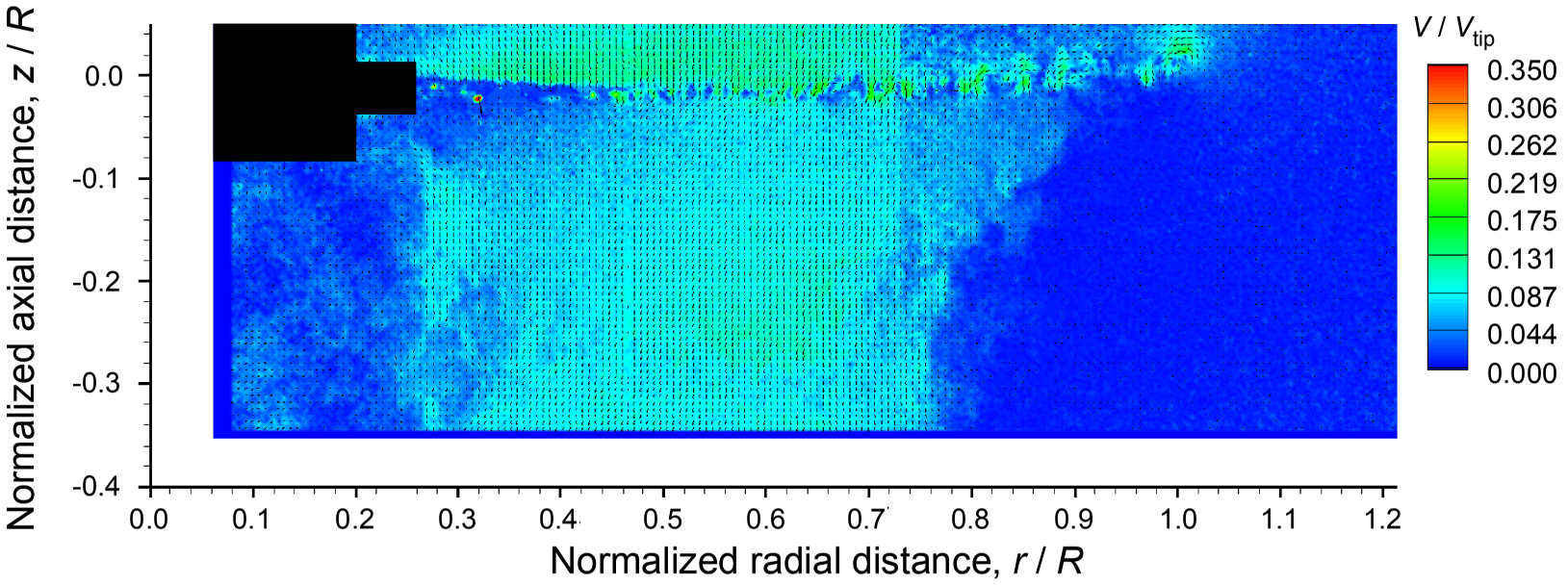

(a) Twisted blade, $C_T/\sigma = 0.053$

Figure 3.16: Contours of the normalized total flow velocity for the rotor with the twisted blades at a blade azimuth angle of $\psi_b = 10°$: (a) $C_T/\sigma = 0.053$; (b) $C_T/\sigma = 0.080$.

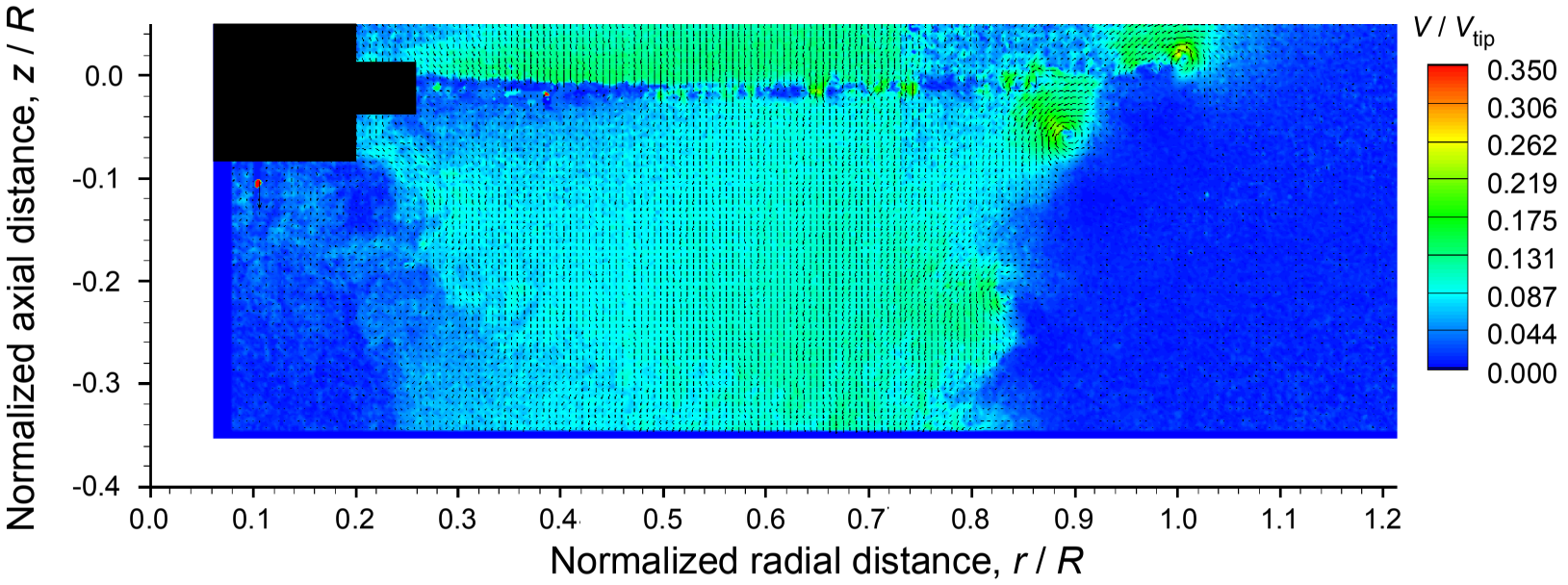

(b) Twisted blade, $C_T/\sigma = 0.080$

Figure 3.16: (Cont'd) Contours of the normalized total flow velocity for the rotor with the twisted blades at a blade azimuth angle of $\psi_b = 10°$: (a) $C_T/\sigma = 0.053$; (b) $C_T/\sigma = 0.080$.

and blue vorticity contours, i.e., vorticity of clockwise and counterclockwise rotations, respectively. Notice that the much larger regions of concentrated vorticity indicate the presence of the tip vortices.

The signatures of the tip vortices trailed by the twisted blades can be seen in Fig. 3.18, and the vortices remain in close proximity to the wake sheet. Locally high induced velocities in the wake sheet, resulting from the closer proximity of the tip vortices to the sheet can lead to an increased susceptibility to vortex–wake sheet interactions. These interactions can significantly affect the subsequent behavior of the wake sheet. Conversely, the tip vortices produced by the untwisted blades convected axially further in the wake, thereby minimizing the interactions between the wake sheet and the previously trailed tip vortex.

Compared to the rotor with untwisted blades, the twisted blades were noted to produce a significantly more intense wake sheet containing stronger vorticity and a higher total circulation (of similar overall magnitude to that the tip vortex). Lifting-line theory [93] shows that the distribution of circulation trailed into the wake will depend on the spanwise circulation gradient along the rotor blade, as previously shown in Eq. 3.6. The addition of blade twist biases the production of more lift and circulation further inboard (see Fig. 3.14) and it is, therefore, expected that more circulation will be initially trailed into the wake sheet rather than rolling up into the tip vortex. However, the instantaneous vorticity contours shown in Figs. 3.17 and 3.18 were found to be significantly different to the mean values of vorticity because of the presence of the T–G vortex pairs. Furthermore, the measurements indicated that in most cases one of each T–G pair was actually somewhat stronger than the other.

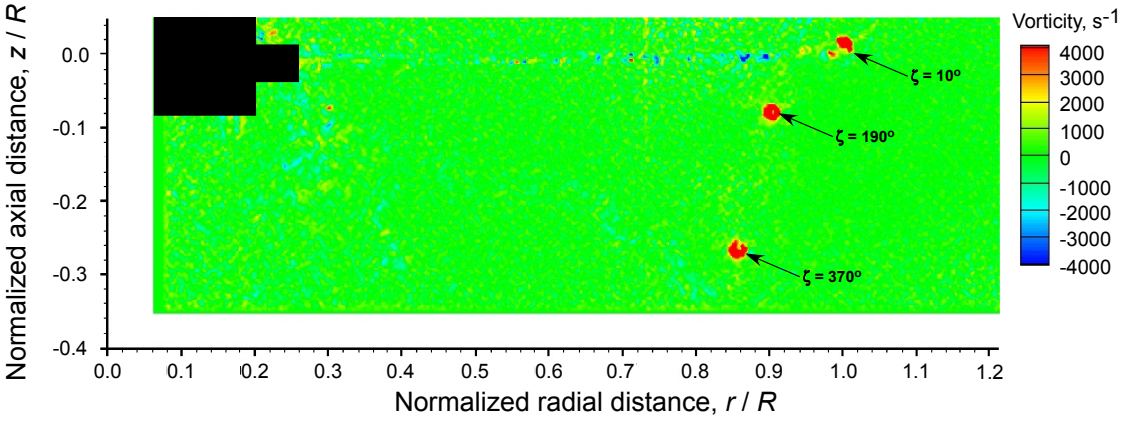

(a) Untwisted blade, $C_T/\sigma = 0.053$

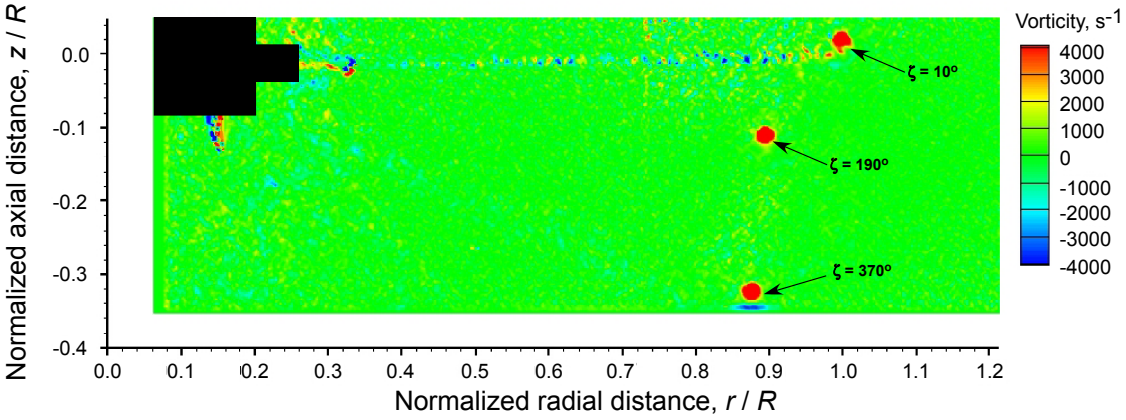

(b) Untwisted blade, $C_T/\sigma = 0.080$

Figure 3.17: Contours of instantaneous vorticity in the wake below the rotor with the untwisted blades at $\psi_b = 10°$: (a) $C_T/\sigma = 0.053$; (b) $C_T/\sigma = 0.080$.

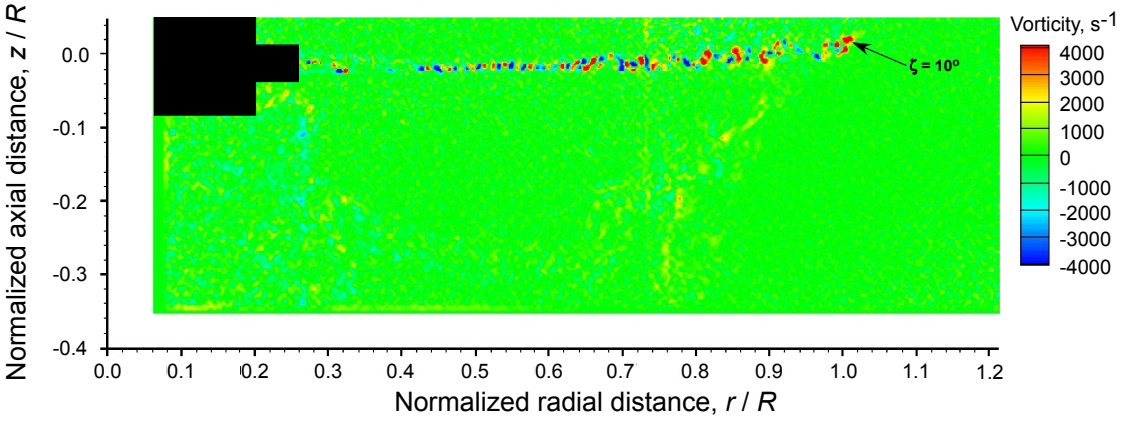

(a) Twisted blade, $C_T/\sigma = 0.053$

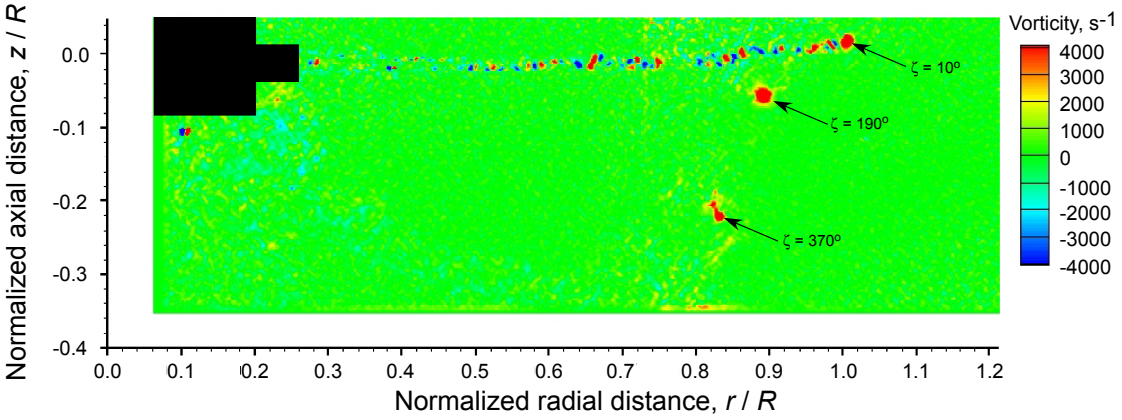

(b) Twisted blade, $C_T/\sigma = 0.080$

Figure 3.18: Contours of instantaneous vorticity in the wake below the rotor with the twisted blades at $\psi_b = 10°$: (a) $C_T/\sigma = 0.053$; (b) $C_T/\sigma = 0.080$.

An ensemble phase-average of the vorticity where the blade was at $\psi_b = 30^\circ$ is shown in Figs. 3.19 and 3.20, with the tip vortices and wake sheets being identified by concentrations of vorticity and a thin band of vorticity, respectively. Figure 3.19 shows that the wake sheet was comprised of vorticity of entirely opposite sign to that of the tip vortex, except for the outboard region. The sign of the mean vorticity contained in the wake sheet followed the expected distribution of bound circulation along the blade; see Fig. 3.14. Similar results can also be seen in the wake produced by the twisted blades, as shown in Figs. 3.20a and 3.20b, with the outboard 40% of the sheet containing the same sign of vorticity as the tip vortex and the inboard 60% of the sheet containing vorticity of the opposite sign.

Notice that compared to the untwisted blades, the twisted blades (at both the higher and lower rotor thrust conditions) produced a notable region of vorticity near the blade root (i.e., what might be referred to as a root vortex). It is also interesting to note the presence of a region of concentrated positive vorticity in the wake sheet near 65% span of the twisted blade, as shown in Fig. 3.20a and 3.20b. The circulation here was unexpected because this location is near to the point of the expected maximum bound circulation on the blade, where the circulation gradient will be lower (i.e., the circulation trailed into the wake should be lower), as shown in Fig. 3.14.

While the wake sheet contained relatively larger amounts of concentrated vorticity at the early wake ages (i.e., for $\zeta \leq 30^\circ$), this initial vorticity was found to quickly diffuse as it convected downstream; see Fig. 3.21. By $\zeta = 15^\circ$ in this case, the concentrated regions of vorticity in the wake sheet had already degenerated into smaller turbulent eddies. After $\zeta = 30^\circ$, the initial vorticity was seen to have diffused even further into turbulence,

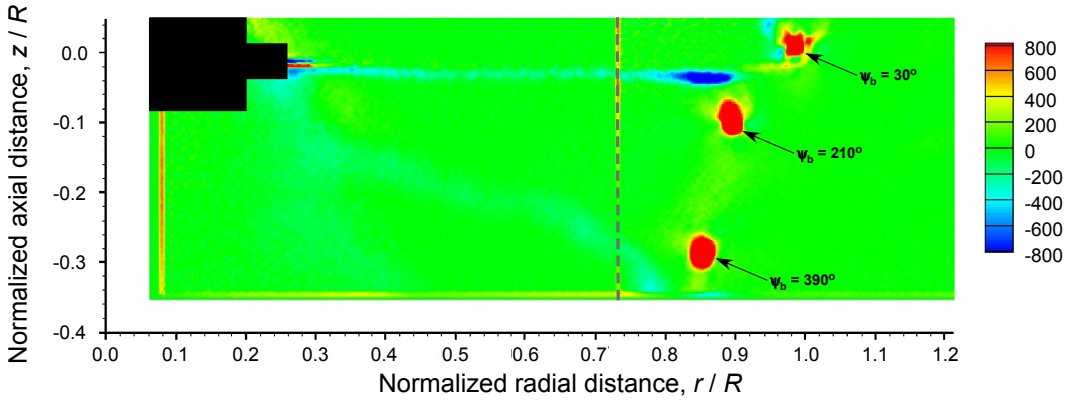

(a) Untwisted blade, $C_T/\sigma = 0.053$

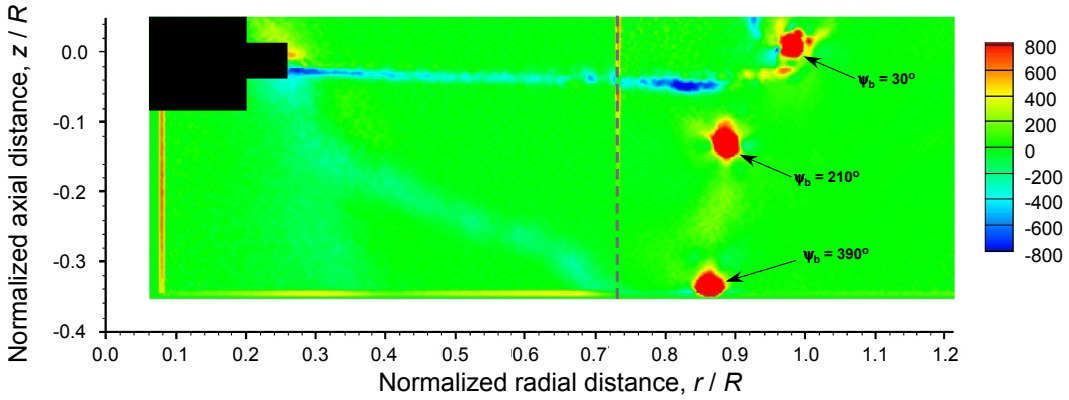

(b) Untwisted blade, $C_T/\sigma = 0.080$

Figure 3.19: Contours of mean vorticity for the rotor with the untwisted blades at $\psi_b = 30^\circ$ for: (a) $C_T/\sigma = 0.053$; (b) $C_T/\sigma = 0.080$.

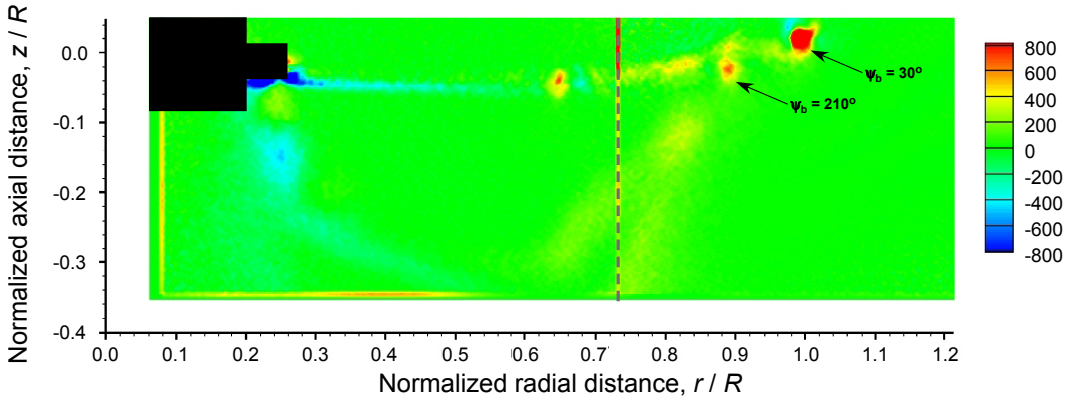

(a) Twisted blade, $C_T/\sigma = 0.053$

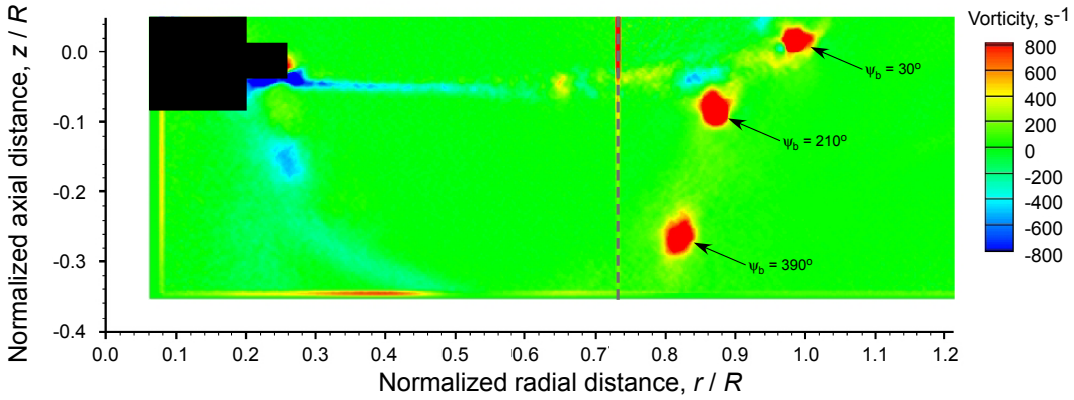

(b) Twisted blade, $C_T/\sigma = 0.080$

Figure 3.20: Contours of the mean vorticity for the rotor with the twisted blades at $\psi_b = 30^\circ$ for: (a) $C_T/\sigma = 0.053$; (b) $C_T/\sigma = 0.080$.

and only the outboard part of the wake sheet contained discernible vorticity, as shown in Fig. 3.21c. However, the turbulence that comprised the sheet was found to persist to much older wake ages in the downstream wake.

3.3.2.4 Blade Tip Region

Regions of interest (ROIs) 1 and 2 allowed the development of the wake sheets to be examined along the entire span of the blade. However, a single ROI in the blade tip region (i.e., ROI 3) allowed the development of the wake sheet and the associated tip vortex to be examined in detail, specifically to document the evolving turbulent nature of the wake sheet. The PIV images in this region contained over 70,000 measurement points, corresponding to over 3,000 points per unit rotor radius in the radial direction.

Figures 3.25 and 3.26 show contours of instantaneous (phase-resolved) vorticity and the corresponding velocity vectors in the wake sheet for the rotor with the untwisted and twisted blades, respectively. As previously noted, the wake sheet produced by both blade sets was comprised of concentrated regions of counterrotating T–G vortices that generated significant affected the local velocity. However, it can be seen from Fig. 3.26 that the twisted blade produced a stronger wake sheet, as indicated by the higher local levels of vorticity. These high levels of vorticity further inboard suggest that the bound circulation on the twisted blade was biased further inboard in comparison to that found on the untwisted blade, an outcome also seen previously using the free-vortex method, as shown in Fig. 3.14.

While the wake sheets appear to contribute significant overall turbulence to the de-

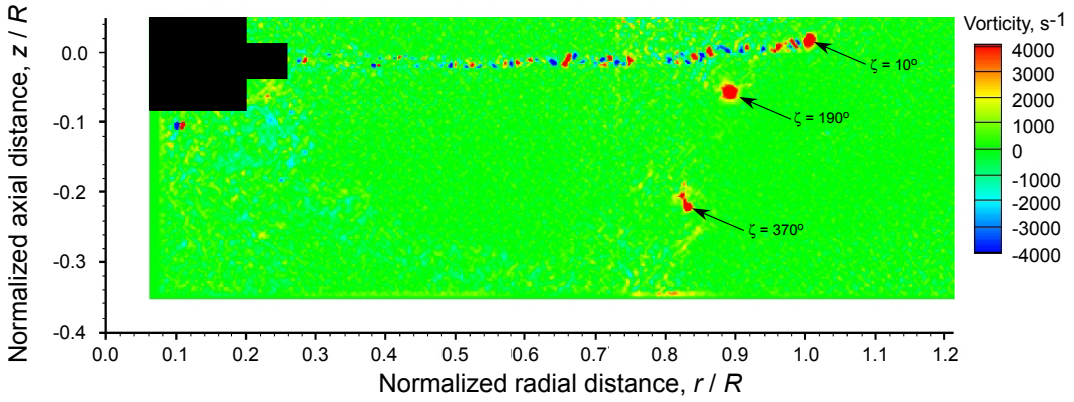

(a) $\psi_b = 10^\circ$

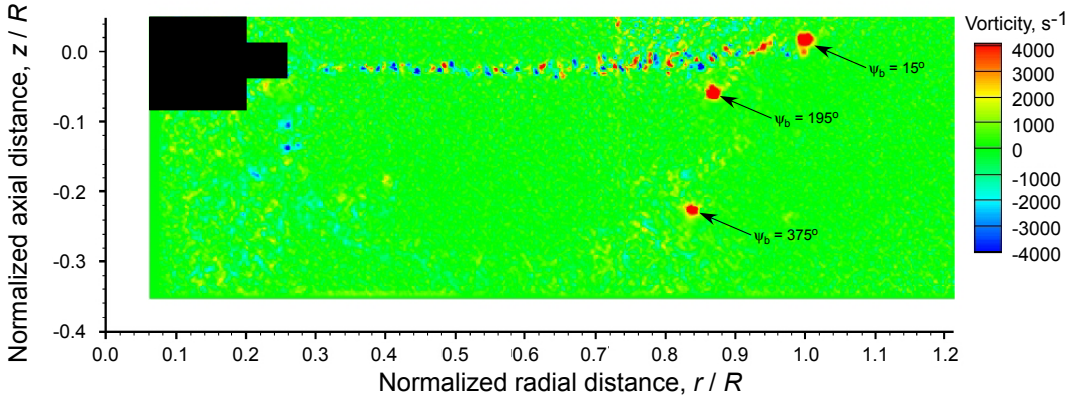

(b) $\psi_b = 15^\circ$

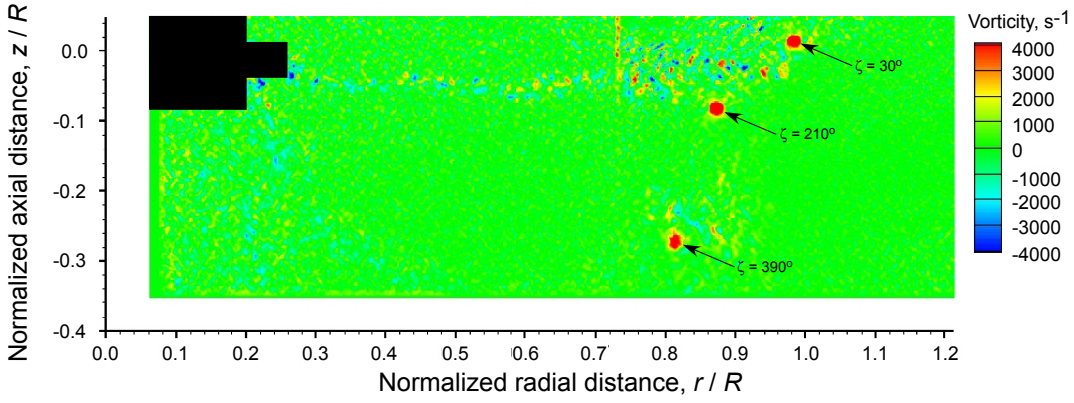

(c) $\psi_b = 30^\circ$

Figure 3.21: Representative contours of instantaneous vorticity showing the development of the wake sheet behind the rotor: (a) $\psi_b = 10^\circ$; (b) $\psi_b = 15^\circ$; (c) $\psi_b = 30^\circ$.

veloping wake, it was not possible to statistically quantify the turbulence because of the aperiodic nature of the wake. For example, the four realizations of the phase-resolved instantaneous vorticity in Figs. 3.25 and 3.26 show that each time the wake sheet intersected the laser sheet the location of the vorticity and turbulence relative to the blade (i.e., a fixed coordinate system) was slightly different. The aperiodic nature of a rotor wake is well known and has been studied in great detail [48, 57, 61, 96]. Methods for collocating dominant flow structures (such as the tip vortices) to determine the local turbulence statistics have been developed [48, 58, 97]. However, in the case of the wake sheet, which contains a broad spatial distribution of vorticity, such collocation techniques cannot be so easily applied. Therefore, local turbulence statistics for the wake sheet, as in the manner that has been developed for tip vortices are difficult to acquire.

The transition of the initial vorticity in the sheet to turbulence is of considerable interest because it affects the dynamics of the wake sheet and the possible participation of the sheet in the longer-term development of the tip vortex. The initial vorticity in the sheets were found to diffuse rapidly as they was convected in the wake, as shown in Figs. 3.28 and 3.27. By $\zeta = 30^{\circ}$, the initial vorticity had already begun to diffuse into smaller scale eddies and turbulence. However, because the rotor with twisted blades initially produced a somewhat more concentrated wake sheet, the vorticity in this case persisted to somewhat older wake ages.

Unlike the tip vortices, which were approximately circular regions of concentrated vorticity, the majority of the T–G vortices contained in the wake sheet had more irregular shapes. However, it was possible to identify a few T–G vortices that were approximately circular regions of vorticity; see Fig. 3.22. The higher resolution achieved in the current

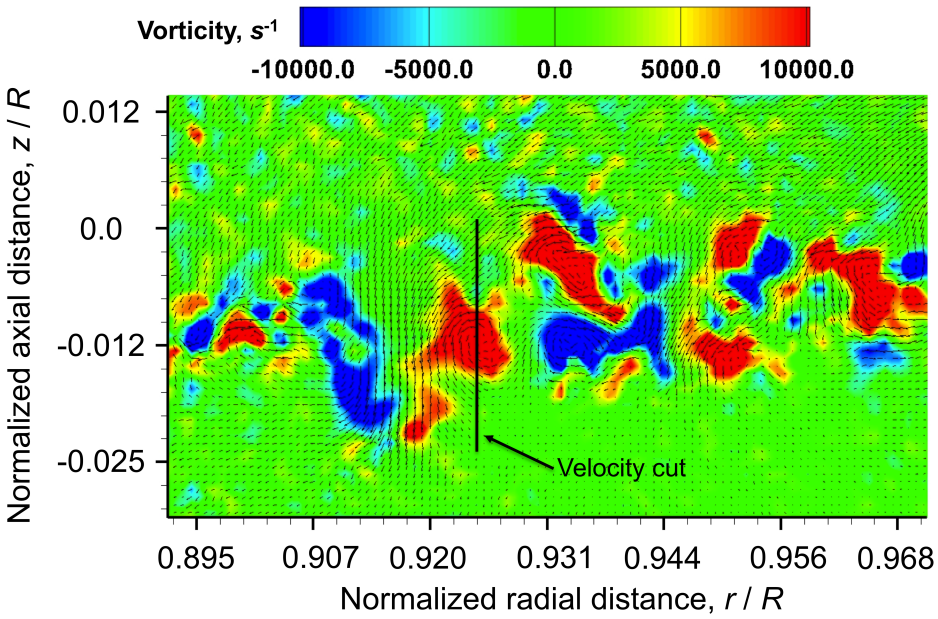

Figure 3.22: Contours of instantaneous vorticity and corresponding flow velocity vectors near the tip of the rotor with the twisted blades at a blade azimuth angle of $\zeta = 3°$.

experiments yielded approximately 10–15 measurement points across the dimensions of most of the T–G vortices, which allowed their velocity profiles to be extracted.

By making a vertical cut through a roughly circular region of vorticity in the sheet (as shown in Fig. 3.22) a swirl velocity profile was acquired, as shown in Fig. 3.23. However, because of the aperiodic nature of the flow (as previously discussed) it was not possible to measure the mean characteristics (i.e., turbulence statistics, swirl velocity profile, vortex core size, etc.) in the wake sheet and only instantaneous profiles could be obtained. Therefore, to generate an approximate "average" swirl velocity profile (i.e.,

devoid of large velocity fluctuations) a least-squares fit of the measurements were made using the Vatistas et al. [5] model, as shown in Fig. 3.23. In this model the tangential (or swirl) velocity, V_θ, is defined as

$$V_\theta(\bar{r}) = \left(\frac{\Gamma_v}{2\pi r_c}\right) \frac{\left(\frac{r}{r_c}\right)}{\left(1+\left(\frac{r}{r_c}\right)^{2n}\right)^{\frac{1}{n}}} \tag{3.8}$$

where Γ_v is the circulation contained in the vortical element, r_c is the radius of the core, r is the distance from the core, and n is an integer value. A value of $n = 2$ (an algebraic approximation to the Lamb-Oseen model) was selected in this case because it provided the best fit to the measured swirl velocity gradient in the core.

Using the fitted swirl velocity profile, it was possible to obtain the Richardson's number. As previously given in Eq. 3.24, the Richardson's number (Ri) is a ratio of the turbulence produced or consumed inside the vortex to the turbulence produced by shear [53, 55, 56]. For a Richardson's number above $Ri \approx Re_v^{1/4}$ turbulence cannot form [55, 56, 58]. Figure 3.24 shows the variation of the Richardson's number with the normalized distance from the core for wake ages of 3° and 9°. It is shown here that at relatively early wake ages (i.e., $\zeta = 3°$) more than 75% of the core region was above the $Re_v^{1/4}$ threshold. However, as the sheet convected in the wake, the portion of the core region above the threshold rapidly decreased. By $\zeta = 9°$ less than 40% of the core was above the threshold. Because only a small portion was above the threshold, this vortical element was expected to rapidly diffuse into small scale turbulence, as can be seen in Fig. 3.21 It is important to note that these calculations were performed for the wake sheet produced by the rotor with twisted blades and as previously discussed, the twisted blades produced significantly stronger wake sheets compared to the sheets produced by the untwisted blades. Therefore,

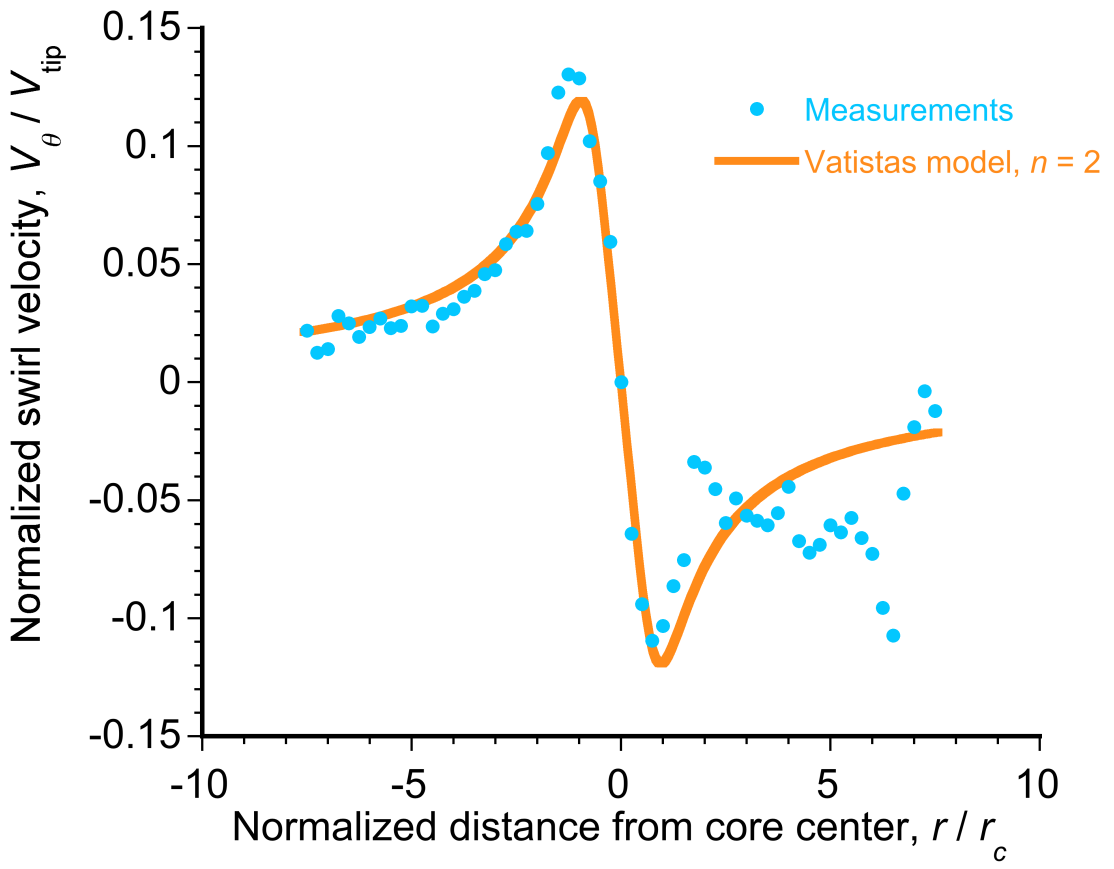

Figure 3.23: Measured swirl velocity profile for a single vortical element contained in the wake sheet as produced by the twisted blades at $\zeta = 3°$ and the corresponding Vatistas et al. vortex model (Ref 5).

the vortical elements contained in the wake sheets produced by the rotor with untwisted blades would be expected to diffuse into smaller scale turbulence somewhat faster than those produced by the twisted blades.

This persistence of the vorticity (and the associated self-induced velocity field) also led to the development of a wave-like perturbation in the wake sheet of larger amplitude, as shown previously in Fig. 3.10. Such a wave-like perturbation was seen to form in the wake sheets produced by both the untwisted and the twisted blades. Even on the basis

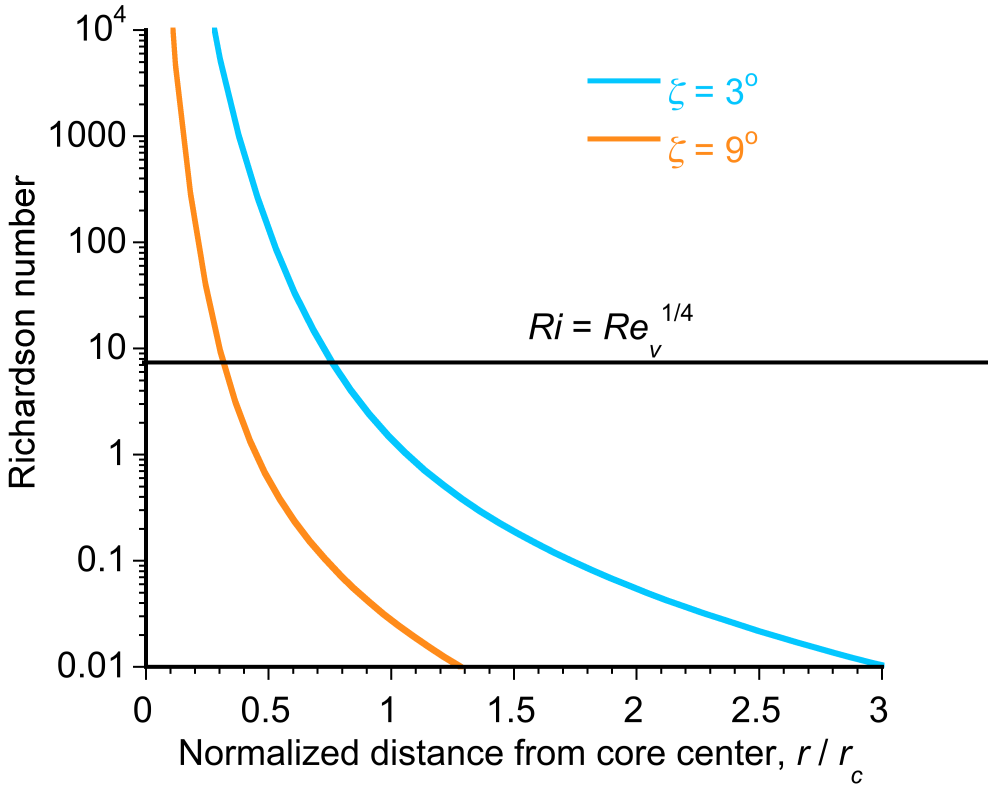

Figure 3.24: Variations in the local Richardson's number with distance from the vortex core for vortices in the wake sheet produced by the rotor with twisted blades for $\zeta = 3^\circ$ and $\zeta = 9^\circ$.

of inviscid arguments, the generally unstable nature of the wake sheet arises from the local self-induced velocities that are formed within the sheet; see Fig. 3.31d. Because the wake sheets are not completely planar and have non-uniform distributions of vorticity, the amplitude of the wave on the sheet has a tendency to grow rather quickly within a few degrees of blade rotation.

Figures 3.29 through 3.32 show contours of the instantaneous vorticity field with the corresponding velocity vectors being superimposed. While these images are not temporally correlated, they are still representations of the flow fields that were produced at the respective wake ages. Figures 3.29 and 3.30 show how the wake sheet convected faster relative to its associated tip vortex. Furthermore, it can be seen that the relative intensity of the vortices contained in the wake sheet decreased rapidly as they convected in the wake, and by $\zeta = 9^\circ$ the initial vorticity in the sheet was significantly diffused, as shown in Figs. 3.29d and 3.30d. The twisted blades, however, produced more intense wake sheets that merged into the tip vortex, as shown in Figs. 3.31 and 3.32. Changes to the downwash distribution below the rotor (see Figs. 3.12 and 3.13) also caused the sheet to convect more slowly in the tip region, thereby allowing a longer interaction with its associated tip vortex.

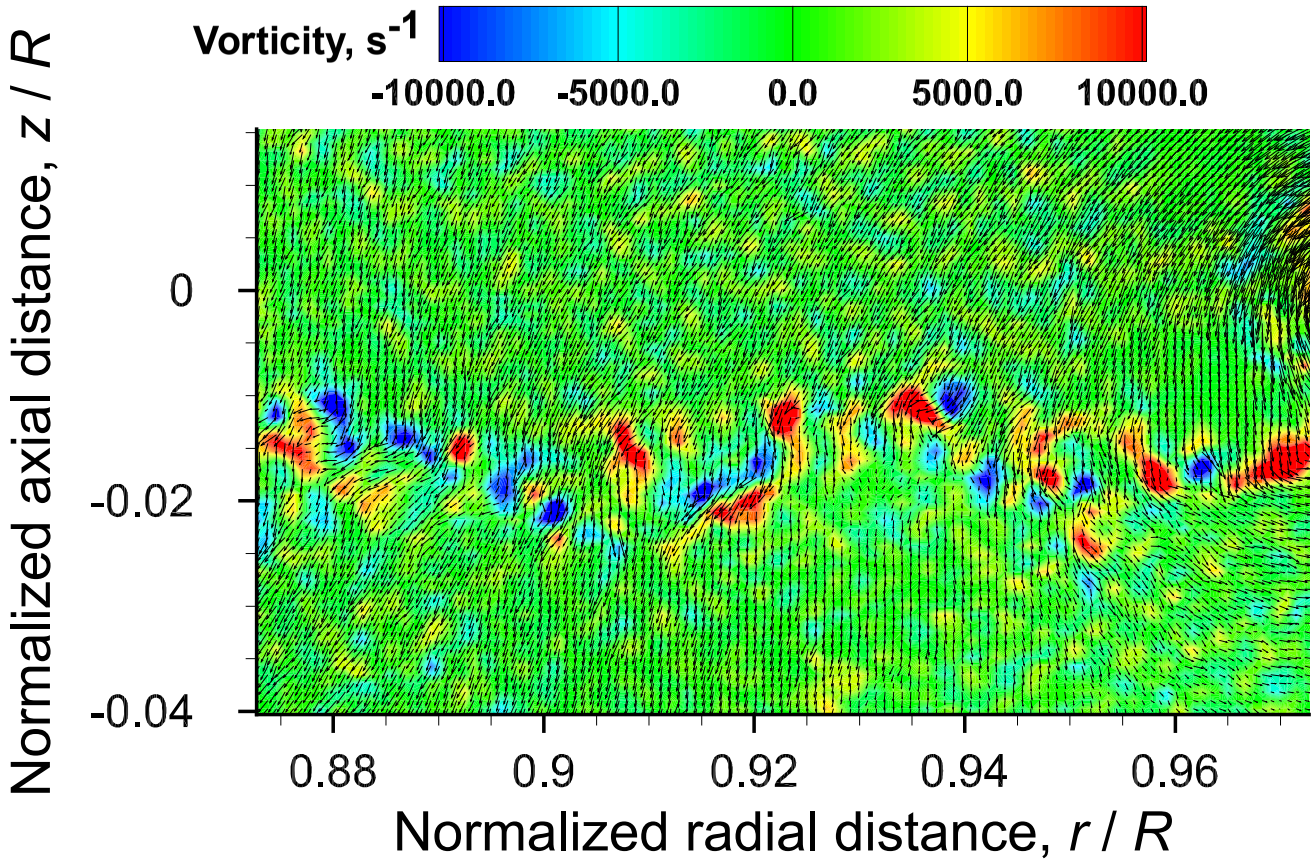

(a) First realization

Figure 3.25: Phase-resolved instantaneous vorticity realizations at $\zeta = 6^\circ$ for the rotor with the untwisted blades showing the aperiodic nature of the wake sheet: (a) First realization; (b) Second realization; (c) Third realization; (d) Fourth realization.

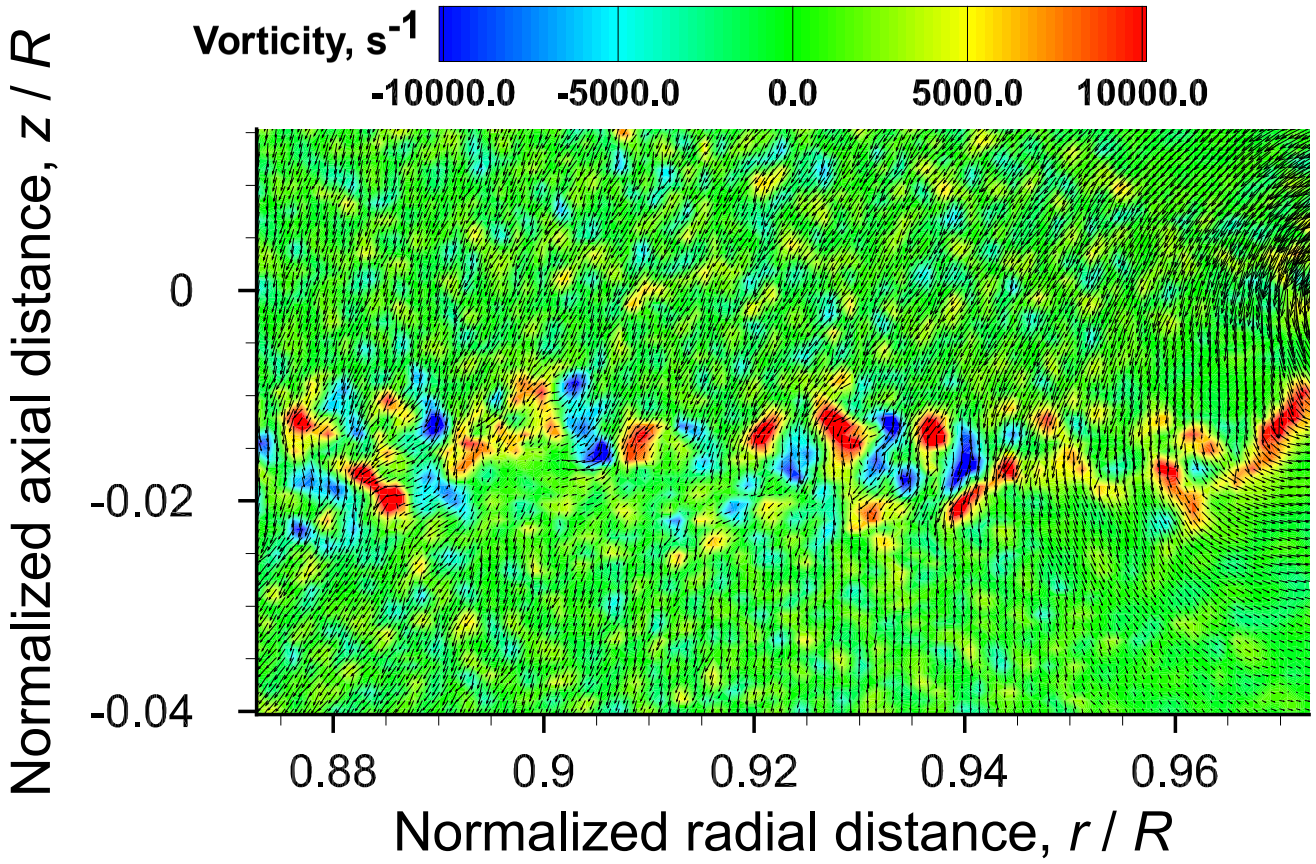

(b) Second realization

Figure 3.25: (Cont'd) Phase-resolved instantaneous vorticity realizations at $\zeta = 6^{\circ}$ for the rotor with the untwisted blades showing the aperiodic nature of the wake sheet: (a) First realization; (b) Second realization; (c) Third realization; (d) Fourth realization.

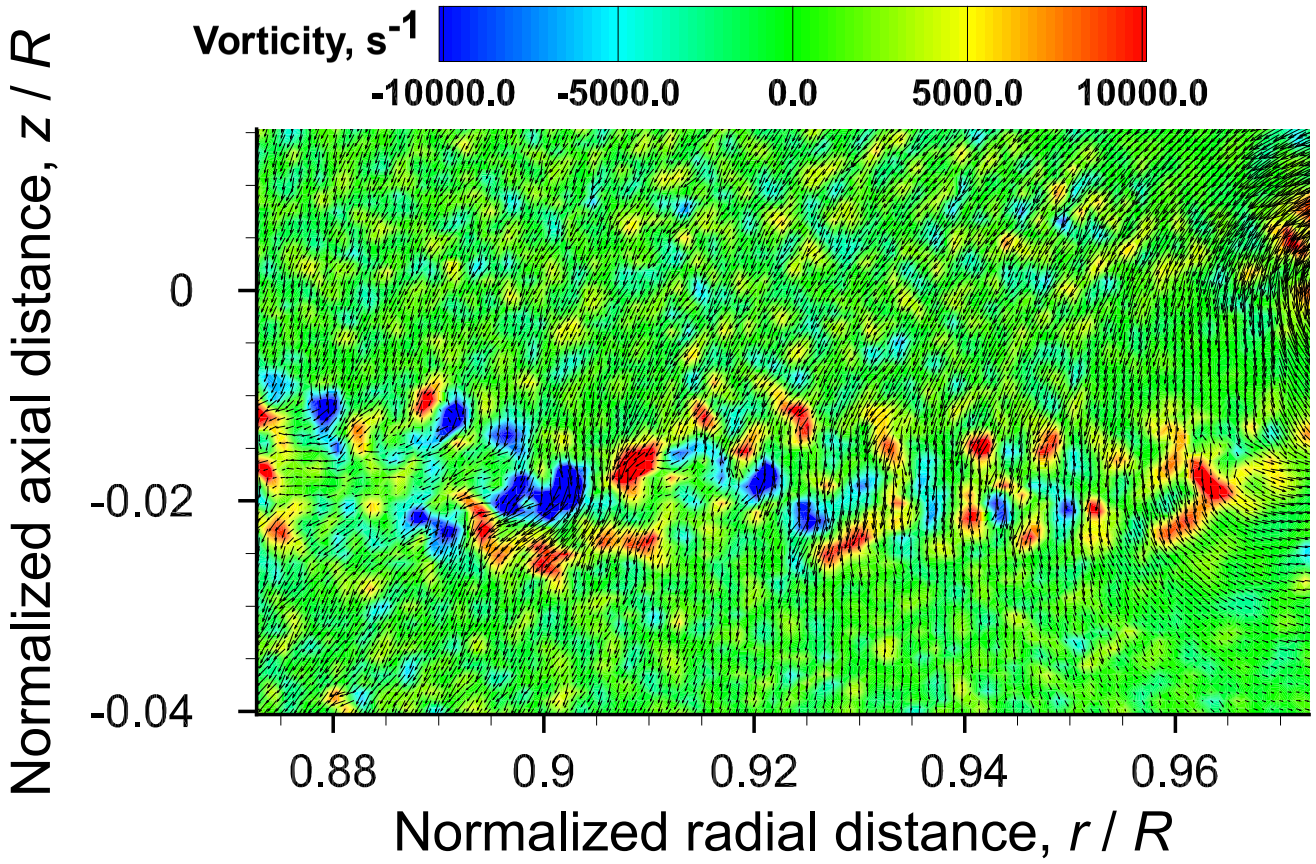

(c) Third realization

Figure 3.25: (Cont'd) Phase-resolved instantaneous vorticity realizations at $\zeta = 6^\circ$ for the rotor with the untwisted blades showing the aperiodic nature of the wake sheet: (a) First realization; (b) Second realization; (c) Third realization; (d) Fourth realization.

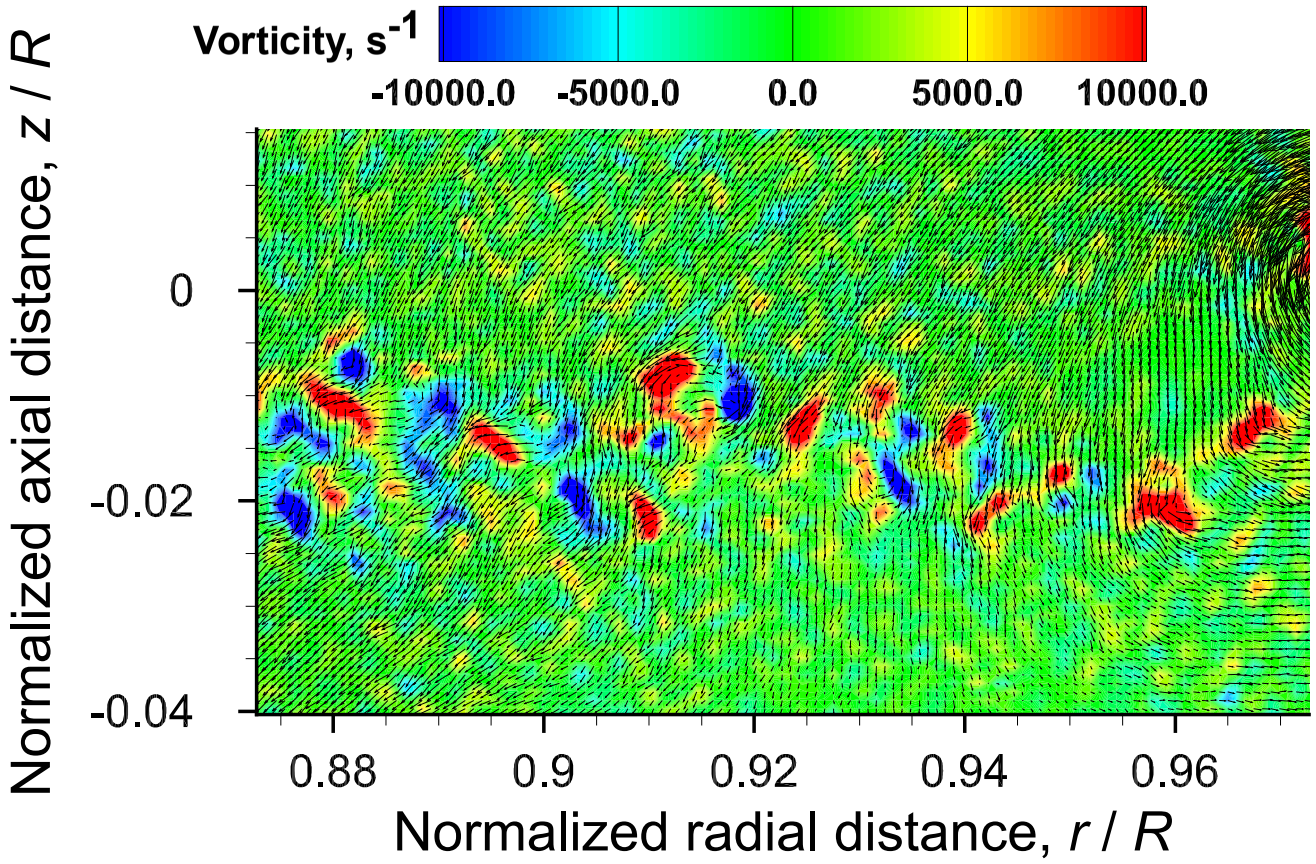

(d) Fourth realization

Figure 3.25: (Cont'd) Phase-resolved instantaneous vorticity realizations at $\zeta = 6^{\circ}$ for the rotor with the untwisted blades showing the aperiodic nature of the wake sheet: (a) First realization; (b) Second realization; (c) Third realization; (d) Fourth realization.

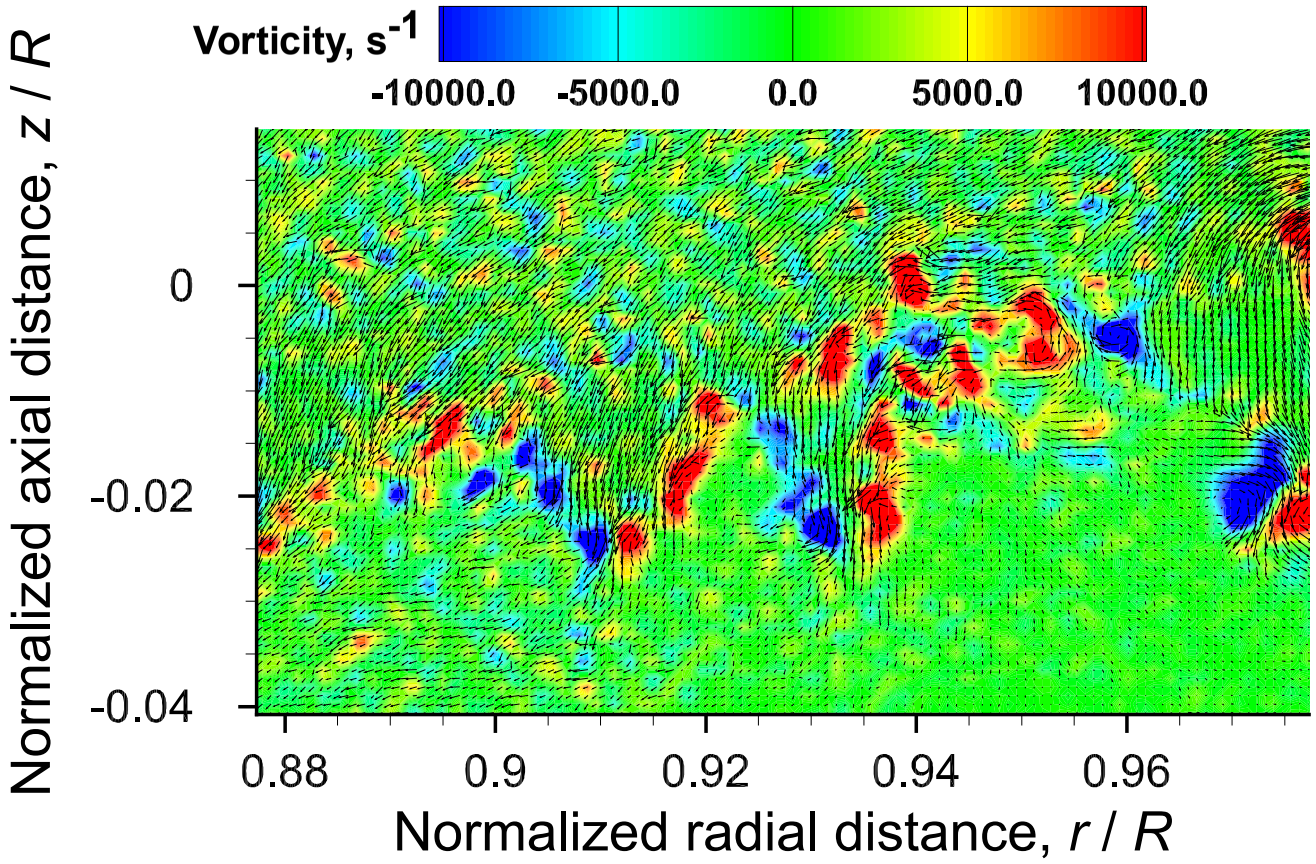

(a) First realization

Figure 3.26: Phase-resolved instantaneous vorticity realizations at $\zeta = 6^\circ$ for the rotor with the twisted blades showing the aperiodic nature of the wake sheet: (a) First realization; (b) Second realization; (c) Third realization; (d) Fourth realization.

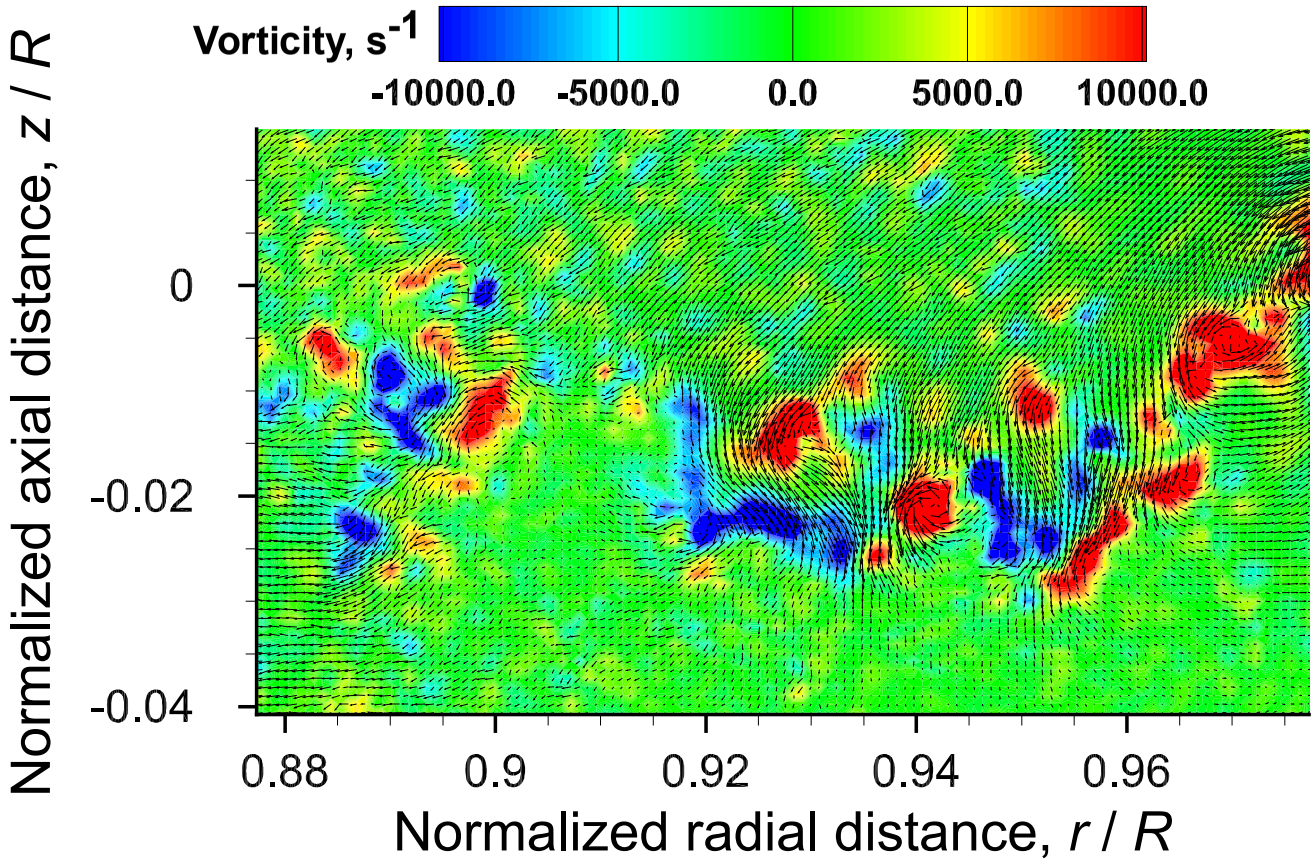

(b) Second realization

Figure 3.26: (Cont'd) Phase-resolved instantaneous vorticity realizations at $\zeta = 6^\circ$ for the rotor with the twisted blades showing the aperiodic nature of the wake sheet: (a) First realization; (b) Second realization; (c) Third realization; (d) Fourth realization.

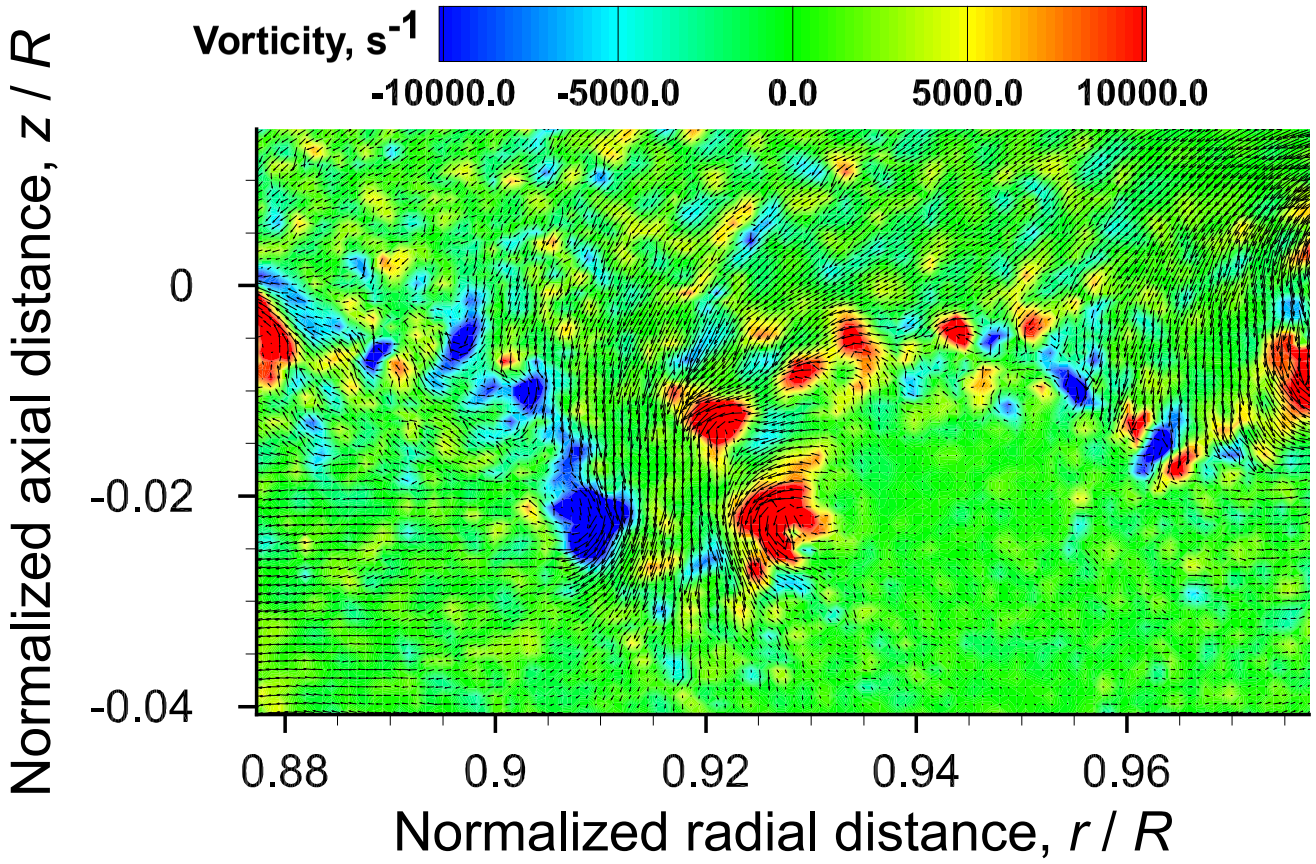

(c) Third realization

Figure 3.26: (Cont'd) Phase-resolved instantaneous vorticity realizations at $\zeta = 6^\circ$ for the rotor with the twisted blades showing the aperiodic nature of the wake sheet: (a) First realization; (b) Second realization; (c) Third realization; (d) Fourth realization.

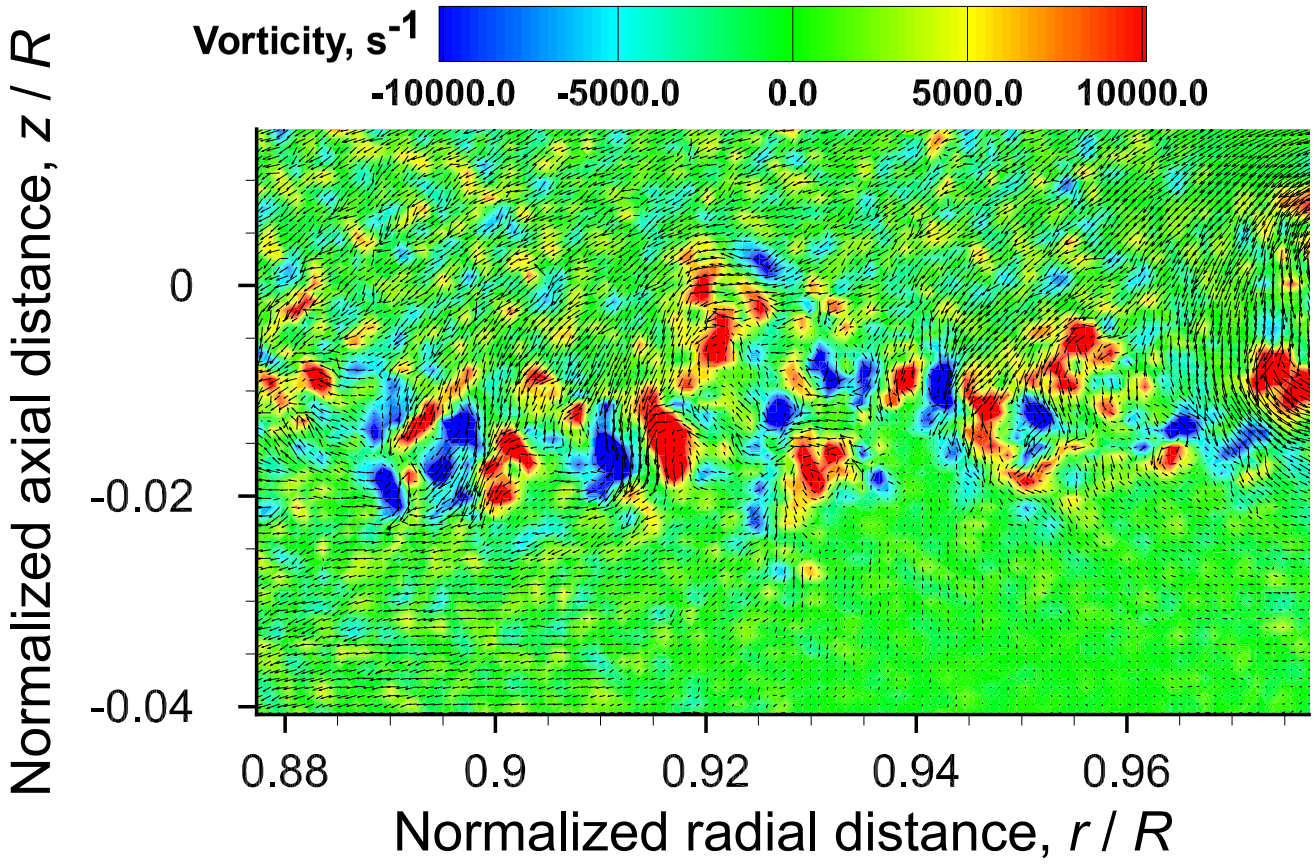

(d) Fourth realization

Figure 3.26: (Cont'd) Phase-resolved instantaneous vorticity realizations at $\zeta = 6^\circ$ for the rotor with the twisted blades showing the aperiodic nature of the wake sheet: (a) First realization; (b) Second realization; (c) Third realization; (d) Fourth realization.

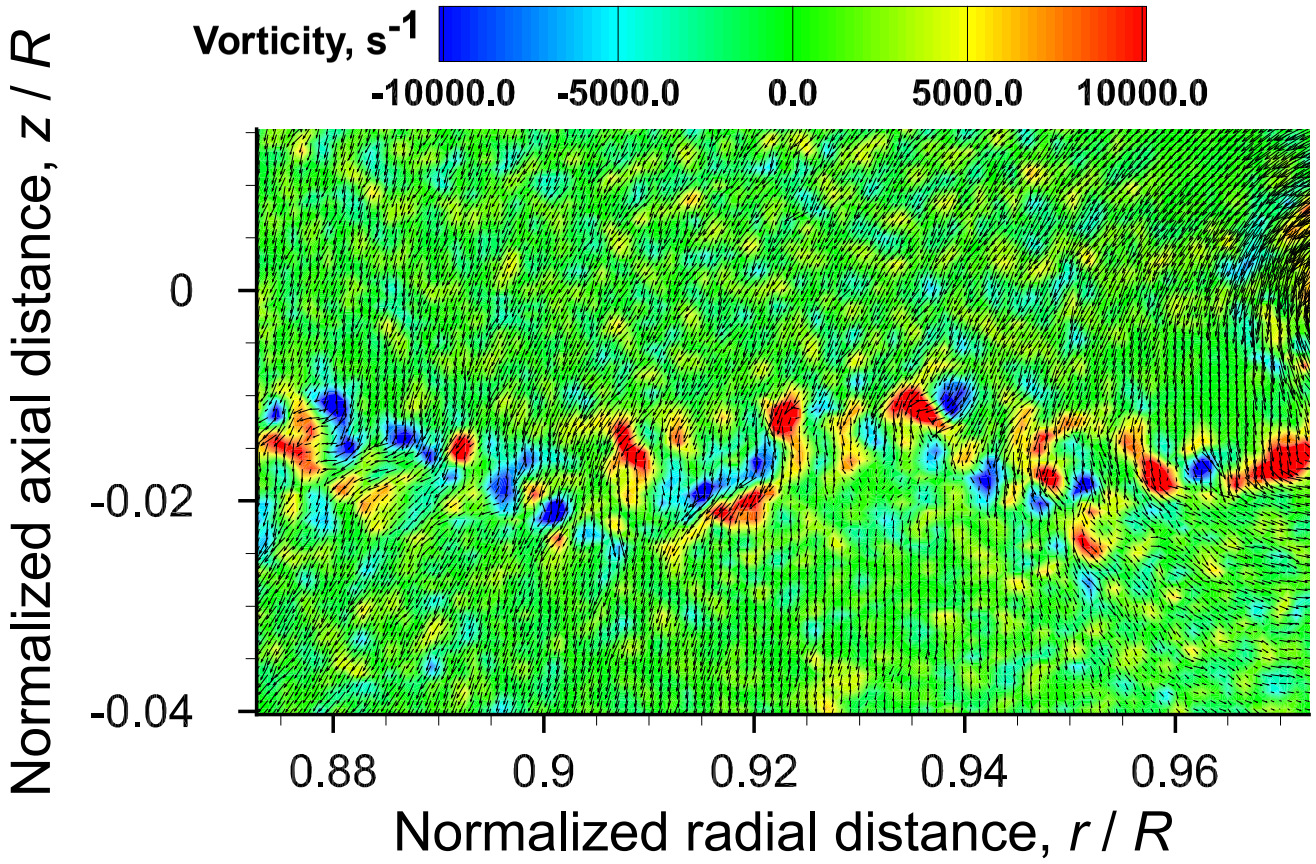

(a) $\zeta = 6°$

Figure 3.27: Contours of instantaneous vorticity in the wake generated by the rotor with untwisted blades operating at $C_T/\sigma = 0.08$ for: (a) $\zeta = 6°$; (b) $\zeta = 30°$.

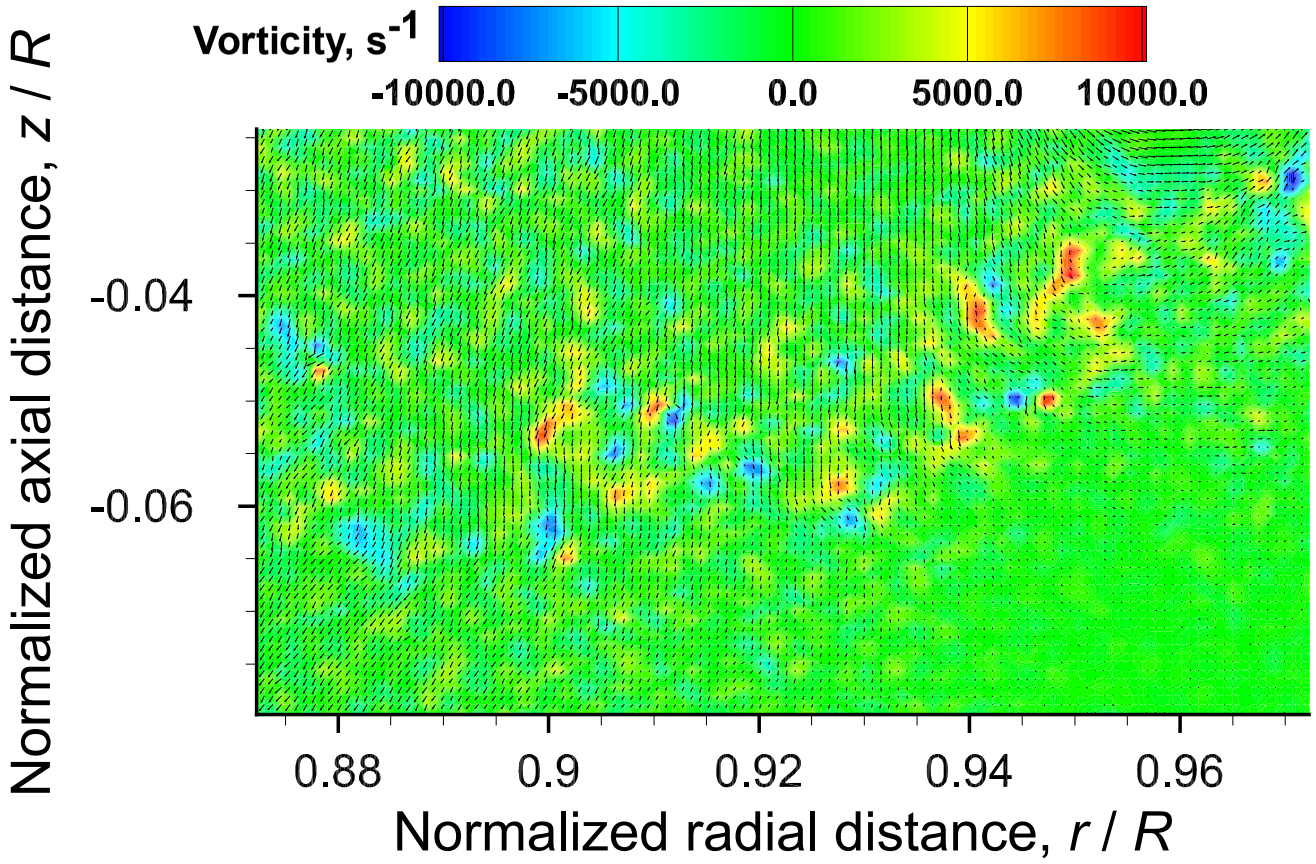

(b) $\zeta = 30°$

Figure 3.27: (Cont'd) Contours of instantaneous vorticity in the wake generated by the rotor with untwisted blades operating at C_T/σ = 0.08 for: (a) $\zeta = 6°$; (b) $\zeta = 30°$.

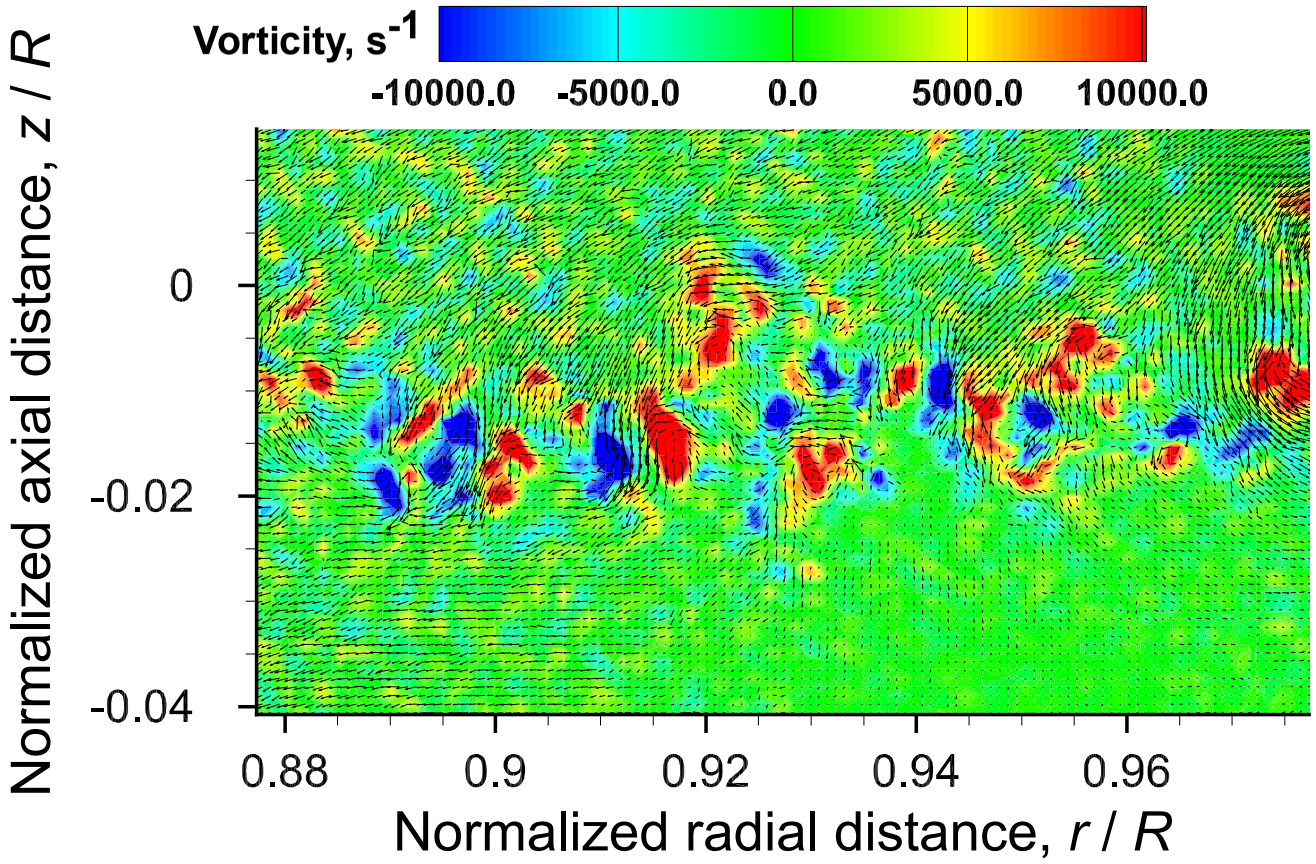

(a) $\zeta = 6°$

Figure 3.28: Contours of instantaneous vorticity in the wake generated by the rotor with twisted blades operating at $C_T/\sigma = 0.08$ for: (a) $\zeta = 6°$; (b) $\zeta = 30°$.

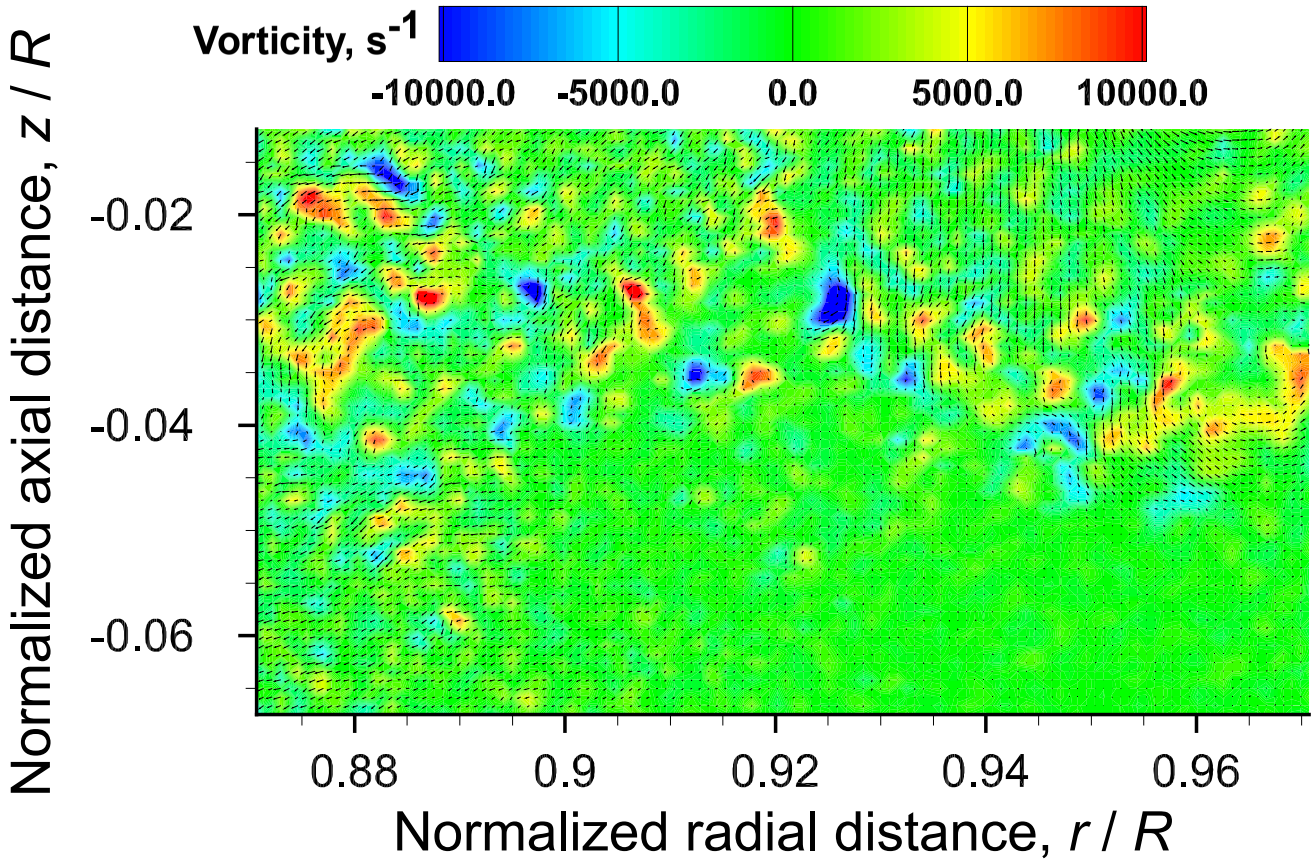

(b) $\zeta = 30°$

Figure 3.28: (Cont'd) Contours of instantaneous vorticity in the wake generated by the rotor with twisted blades operating at C_T/σ = 0.08 for: (a) $\zeta = 6°$; (b) $\zeta = 30°$.

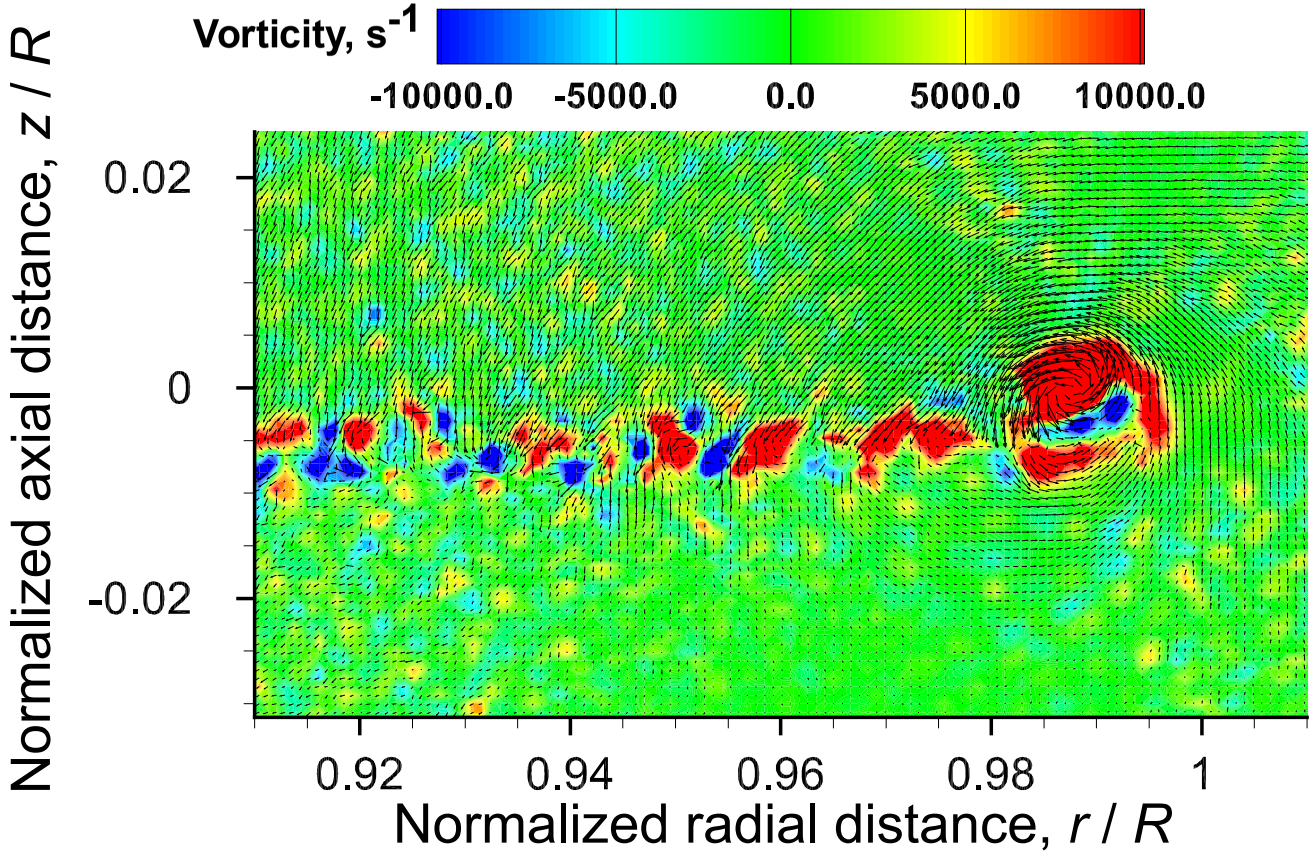

(a) $\zeta = 0^\circ$

Figure 3.29: Contours of instantaneous vorticity near the tip of the untwisted blade at the low thrust condition (i.e., $C_T/\sigma = 0.053$): (a) $\psi_b = 0^\circ$; (b) $\psi_b = 3^\circ$; (c) $\psi_b = 6^\circ$; (d) $\psi_b = 9^\circ$.

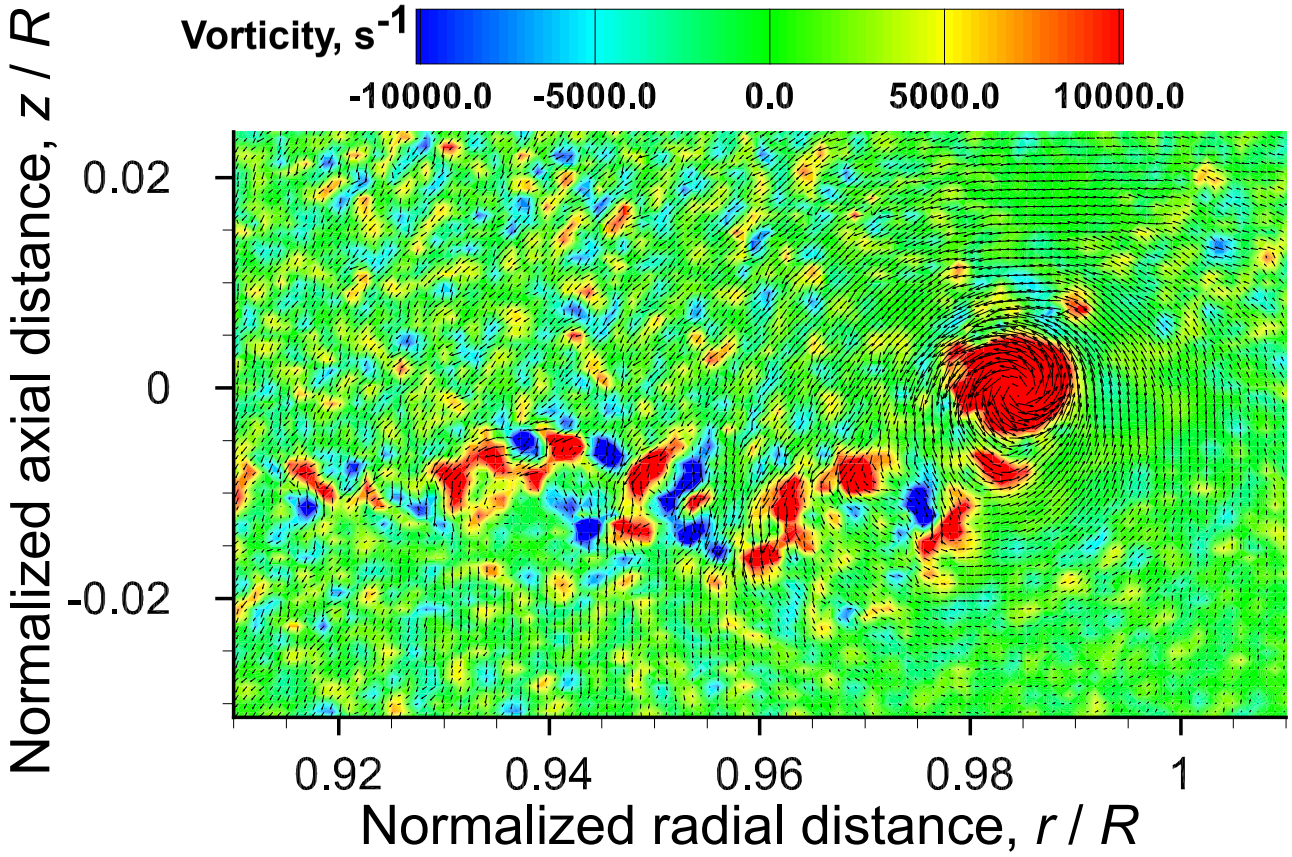

(b) $\zeta = 3^\circ$

Figure 3.29: (Cont'd) Contours of instantaneous vorticity near the tip of the untwisted blade when at C_T/σ = 0.053: (a) $\psi_b = 0^\circ$; (b) $\psi_b = 3^\circ$; (c) $\psi_b = 6^\circ$; (d) $\psi_b = 9^\circ$.

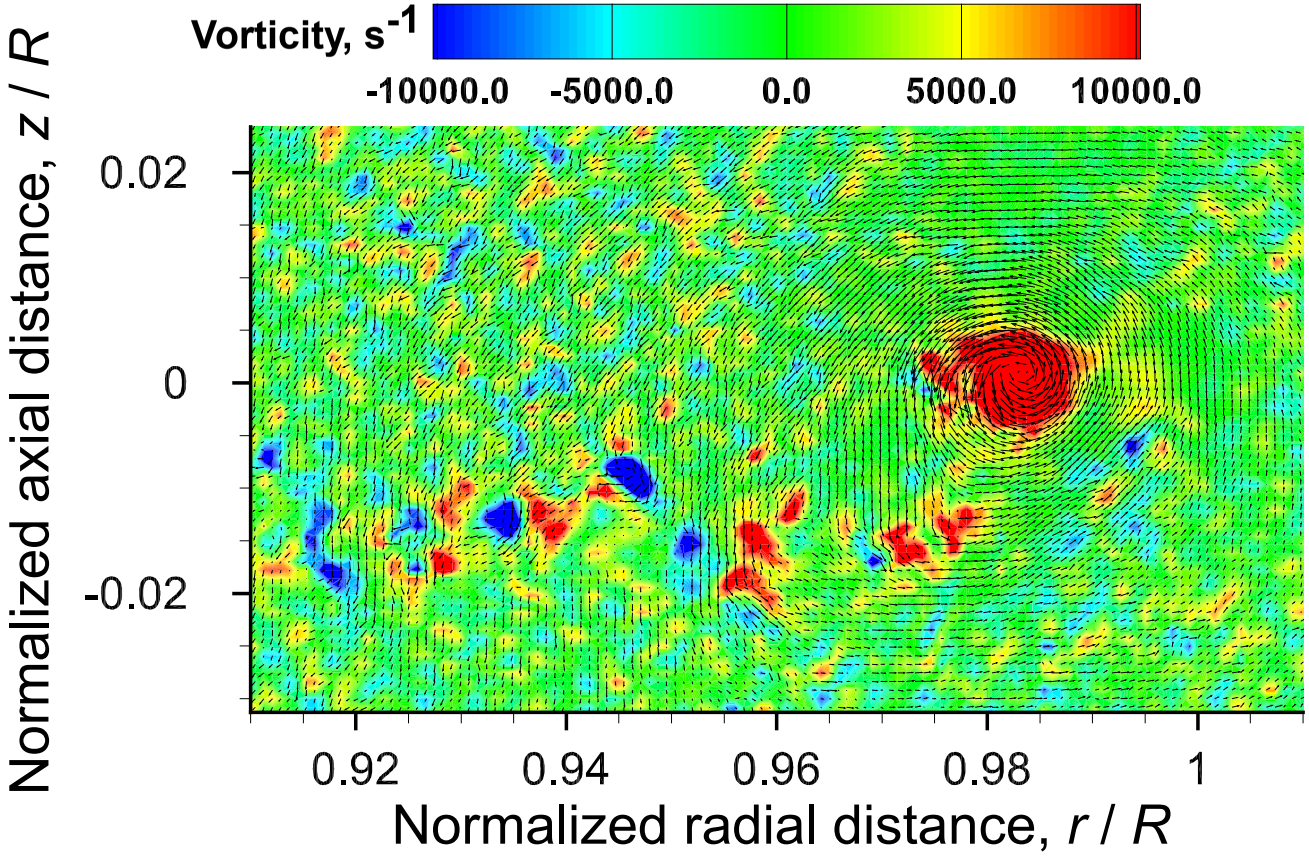

(c) $\zeta = 6^\circ$

Figure 3.29: (Cont'd) Contours of instantaneous vorticity near the tip of the untwisted blade at $C_T/\sigma = 0.053$: (a) $\psi_b = 0^\circ$; (b) $\psi_b = 3^\circ$; (c) $\psi_b = 6^\circ$; (d) $\psi_b = 9^\circ$.

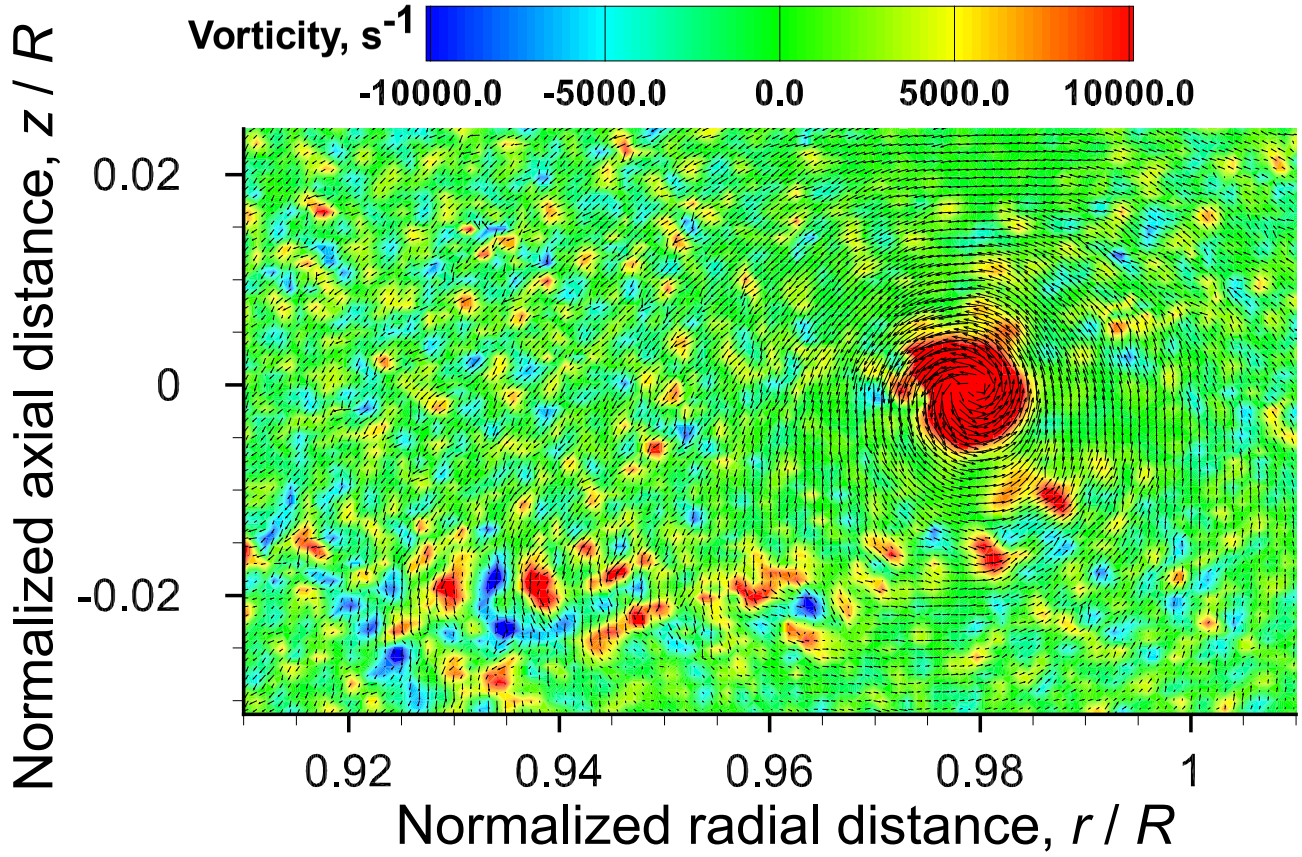

(d) $\zeta = 9^\circ$

Figure 3.29: (Cont'd) Contours of instantaneous vorticity near the tip of the untwisted blade at $C_T/\sigma = 0.053$: (a) $\psi_b = 0^\circ$; (b) $\psi_b = 3^\circ$; (c) $\psi_b = 6^\circ$; (d) $\psi_b = 9^\circ$.

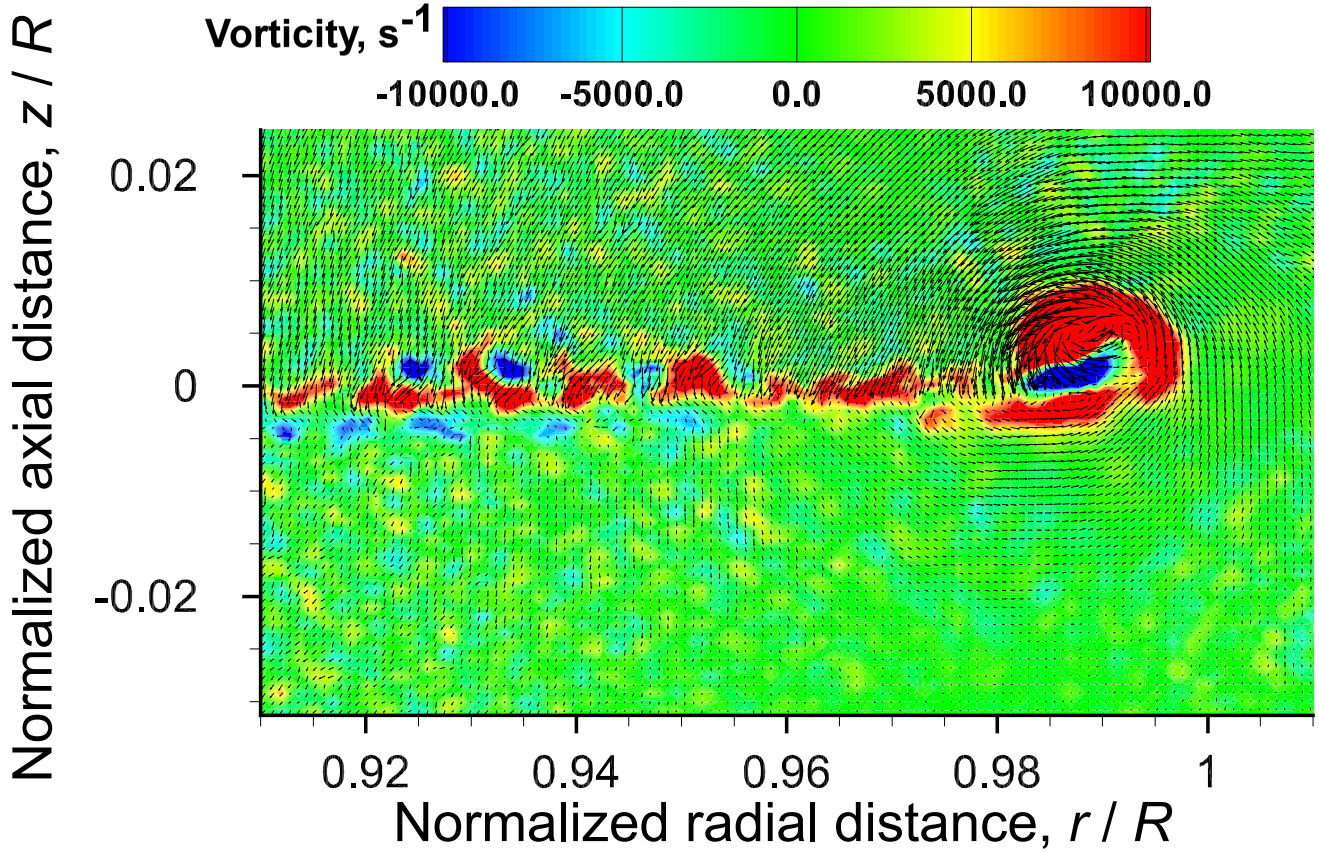

(a) $\zeta = 0^\circ$

Figure 3.30: Contours of instantaneous vorticity near the tip of the untwisted blade at $C_T/\sigma = 0.080$: (a) $\psi_b = 0^\circ$; (b) $\psi_b = 3^\circ$; (c) $\psi_b = 6^\circ$; (d) $\psi_b = 9^\circ$.

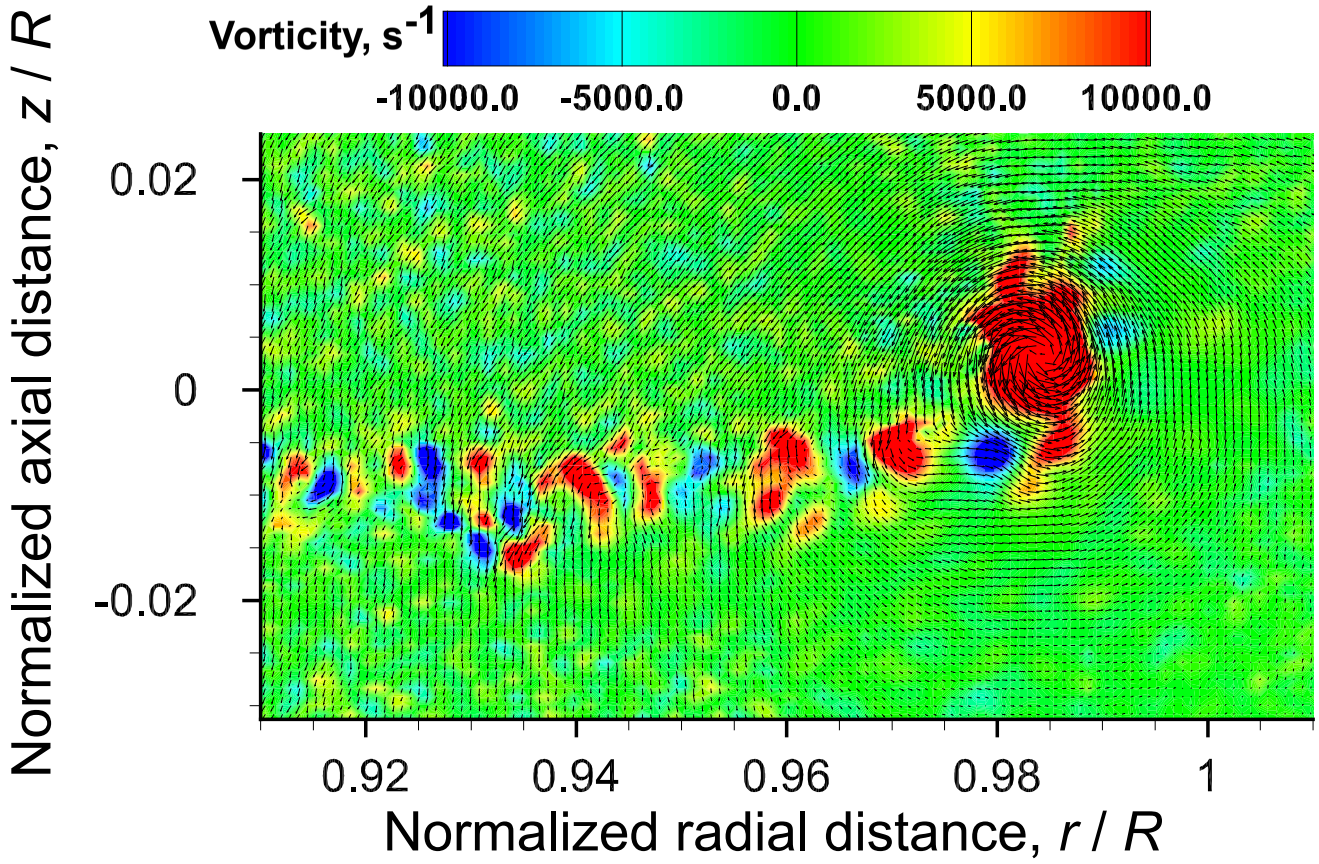

(b) $\zeta = 3^\circ$

Figure 3.30: (Cont'd) Contours of instantaneous vorticity near the tip of the untwisted blade at $C_T/\sigma = 0.080$: (a) $\psi_b = 0^\circ$; (b) $\psi_b = 3^\circ$; (c) $\psi_b = 6^\circ$; (d) $\psi_b = 9^\circ$.

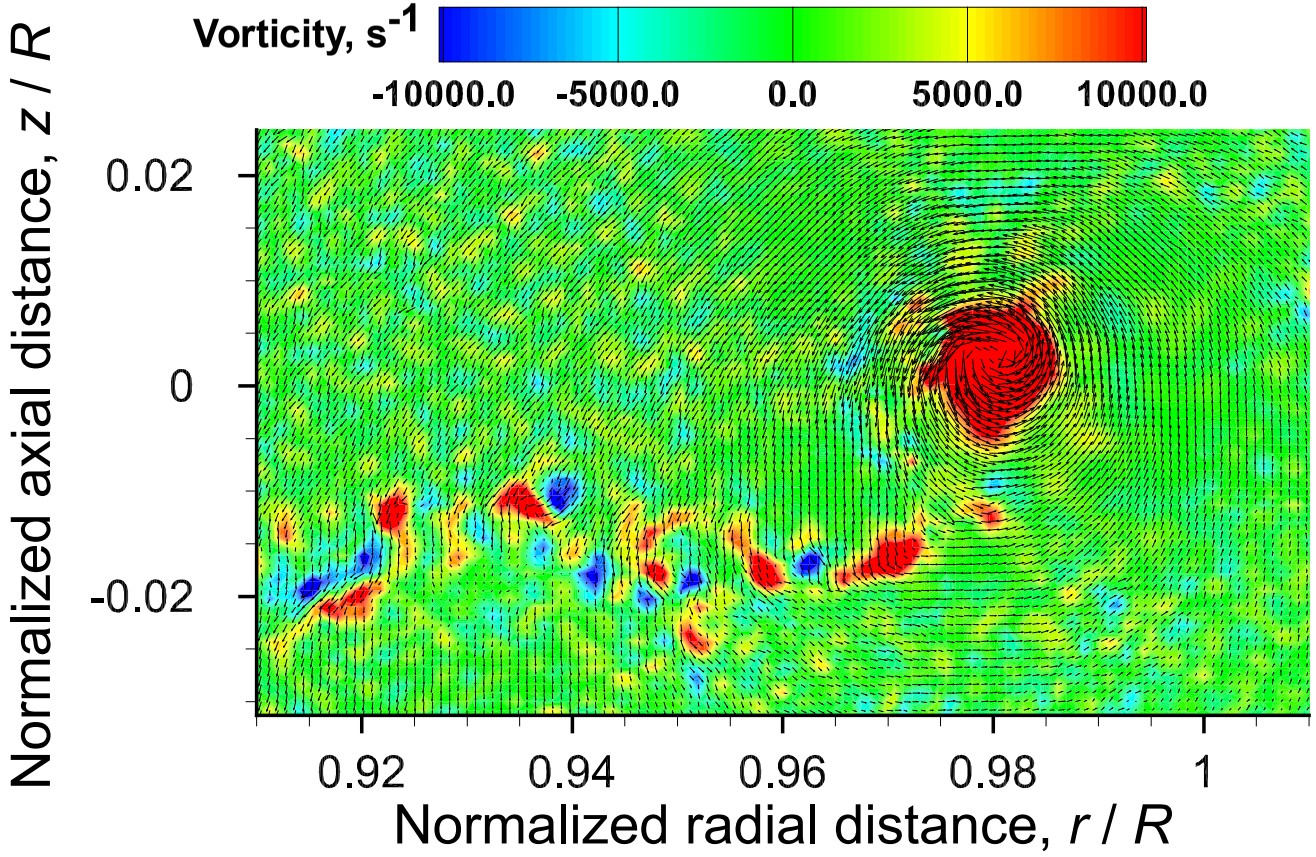

(c) $\zeta = 6^\circ$

Figure 3.30: (Cont'd) Contours of instantaneous vorticity near the tip of the untwisted blade at $C_T/\sigma = 0.080$: (a) $\psi_b = 0^\circ$; (b) $\psi_b = 3^\circ$; (c) $\psi_b = 6^\circ$; (d) $\psi_b = 9^\circ$.

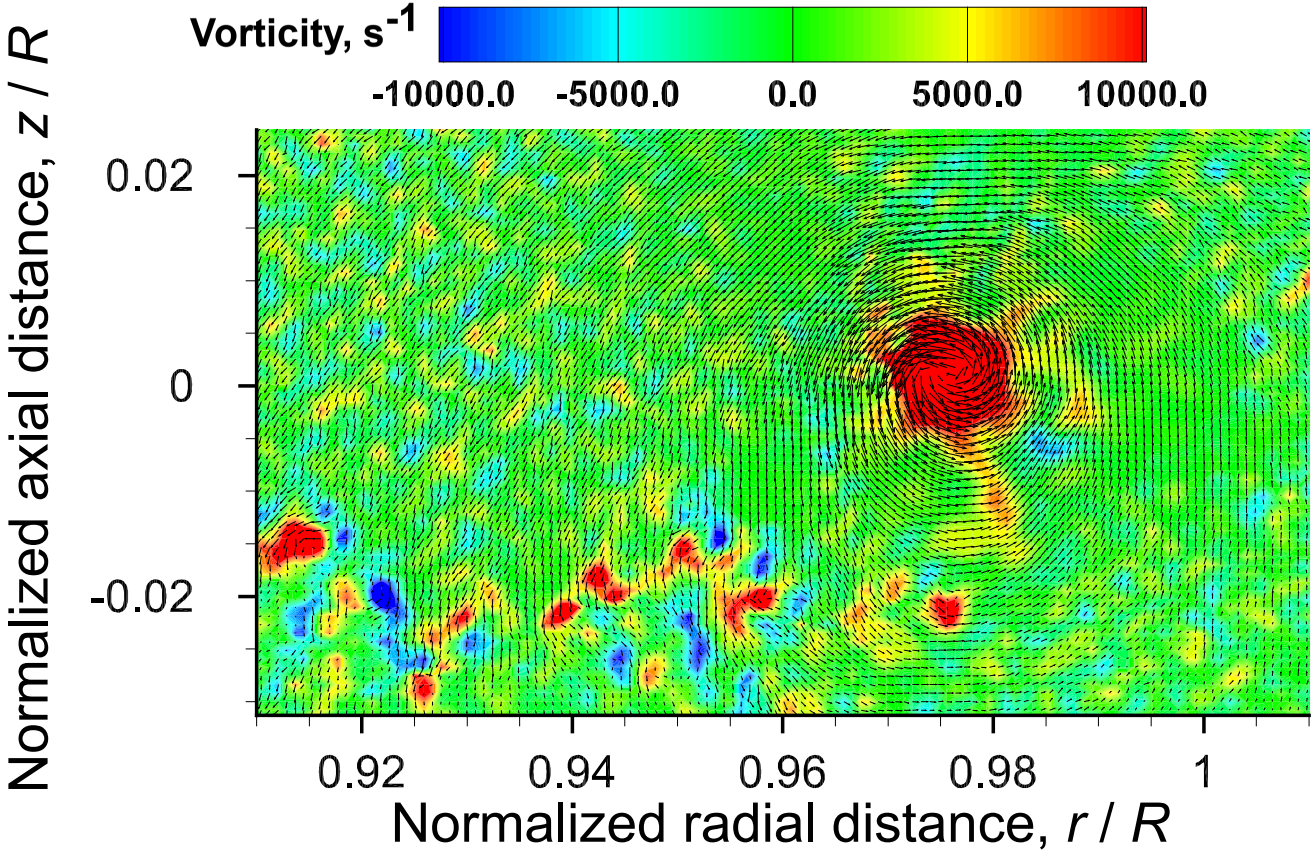

(d) $\zeta = 9^\circ$

Figure 3.30: (Cont'd) Contours of instantaneous vorticity near the tip of the untwisted blade at $C_T/\sigma = 0.080$: (a) $\psi_b = 0^\circ$; (b) $\psi_b = 3^\circ$; (c) $\psi_b = 6^\circ$; (d) $\psi_b = 9^\circ$.

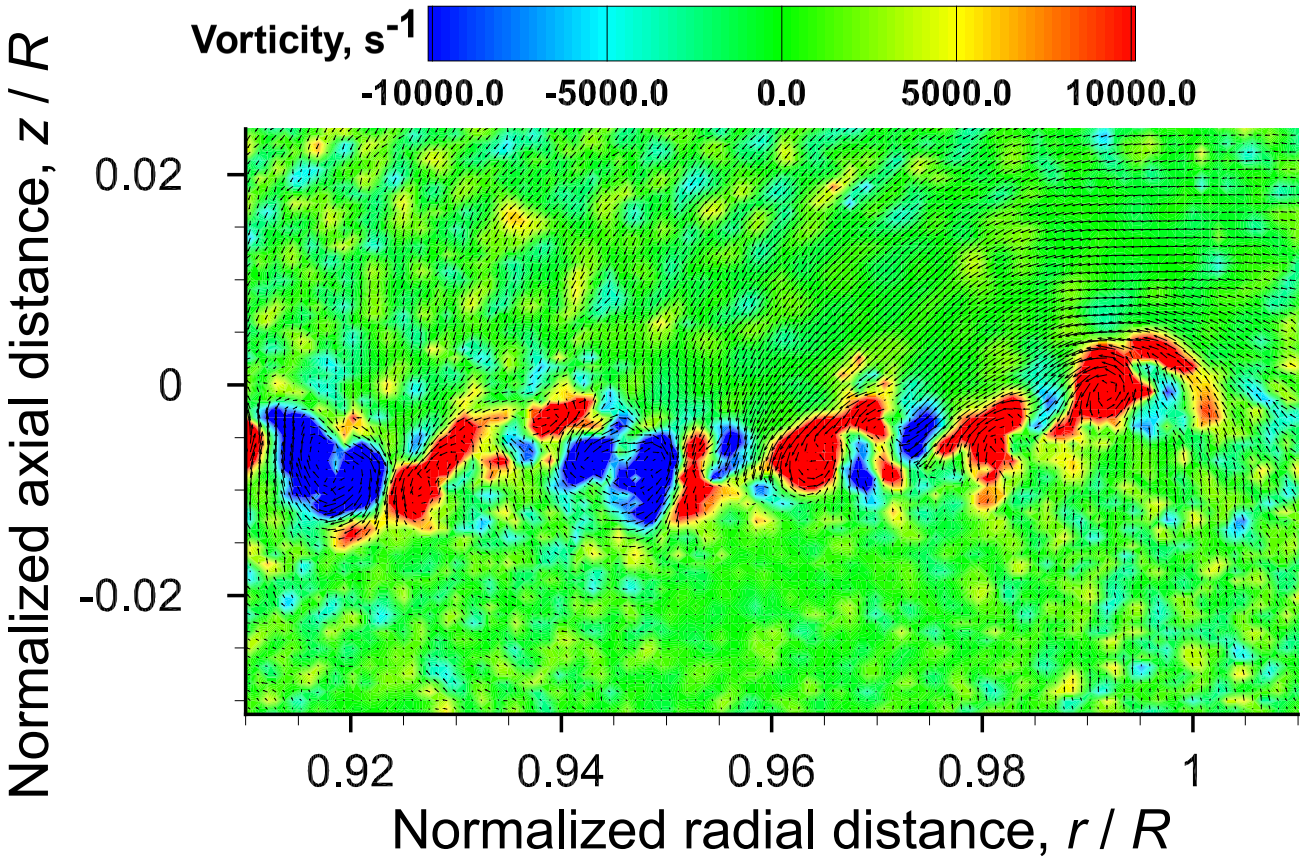

(a) $\zeta = 0^\circ$

Figure 3.31: Contours of instantaneous vorticity near the tip of the twisted blade at $C_T/\sigma = 0.053$: (a) $\psi_b = 0^\circ$; (b) $\psi_b = 3^\circ$; (c) $\psi_b = 6^\circ$; (d) $\psi_b = 9^\circ$.

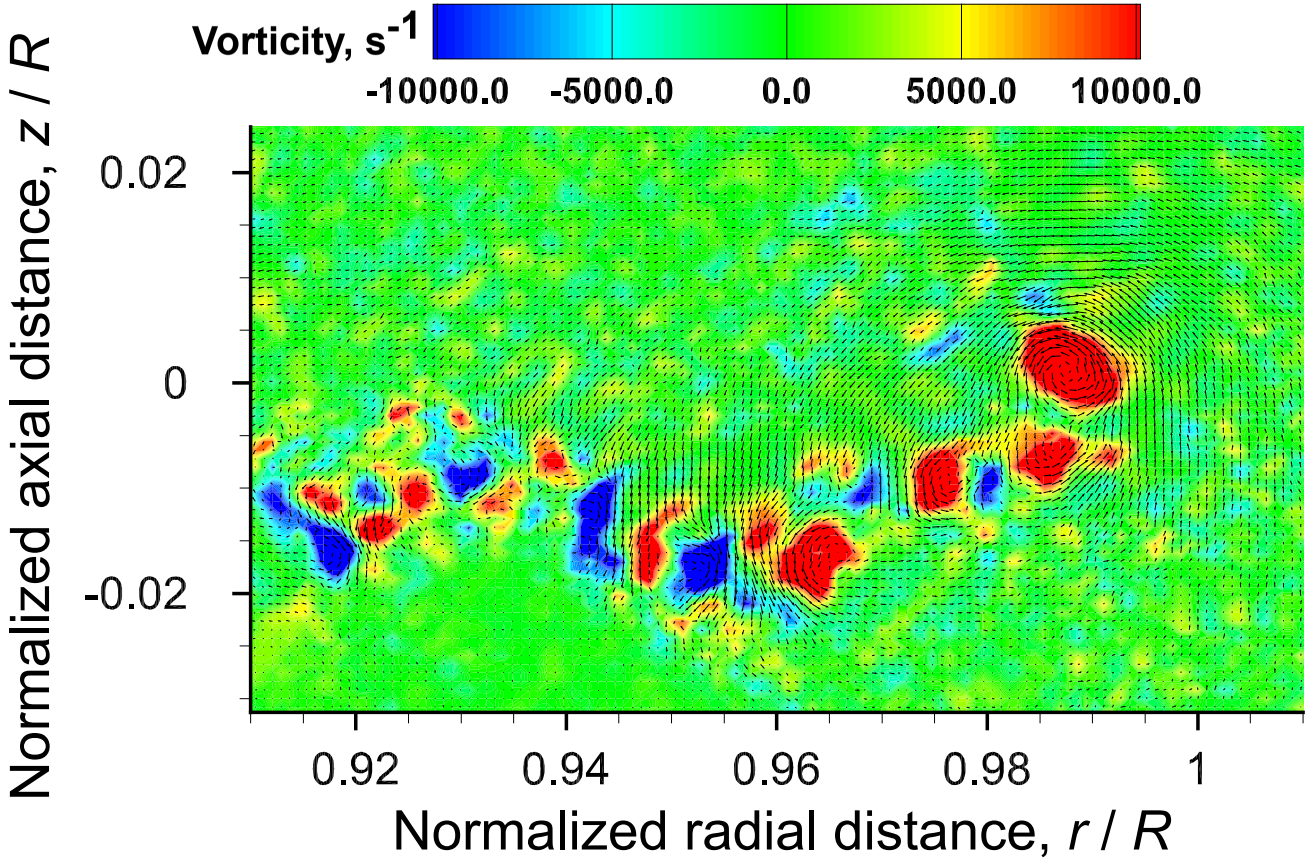

(b) $\zeta = 3^\circ$

Figure 3.31: (Cont'd) Contours of instantaneous vorticity near the tip of the twisted blade at $C_T/\sigma = 0.053$: (a) $\psi_b = 0^\circ$; (b) $\psi_b = 3^\circ$; (c) $\psi_b = 6^\circ$; (d) $\psi_b = 9^\circ$.

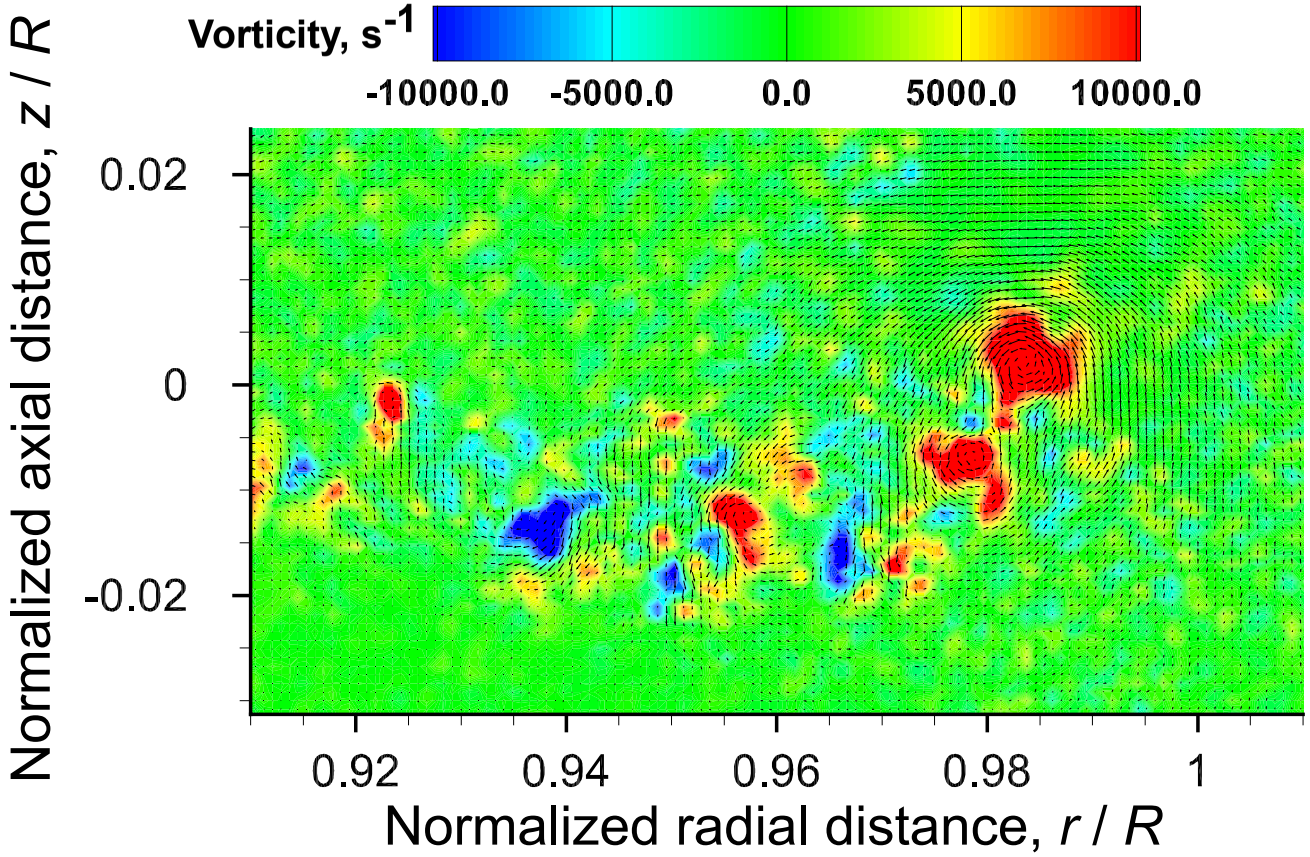

(c) $\zeta = 6^\circ$

Figure 3.31: (Cont'd) Contours of instantaneous vorticity near the tip of the twisted bladeat $C_T/\sigma = 0.053$: (a) $\psi_b = 0^\circ$; (b) $\psi_b = 3^\circ$; (c) $\psi_b = 6^\circ$; (d) $\psi_b = 9^\circ$.

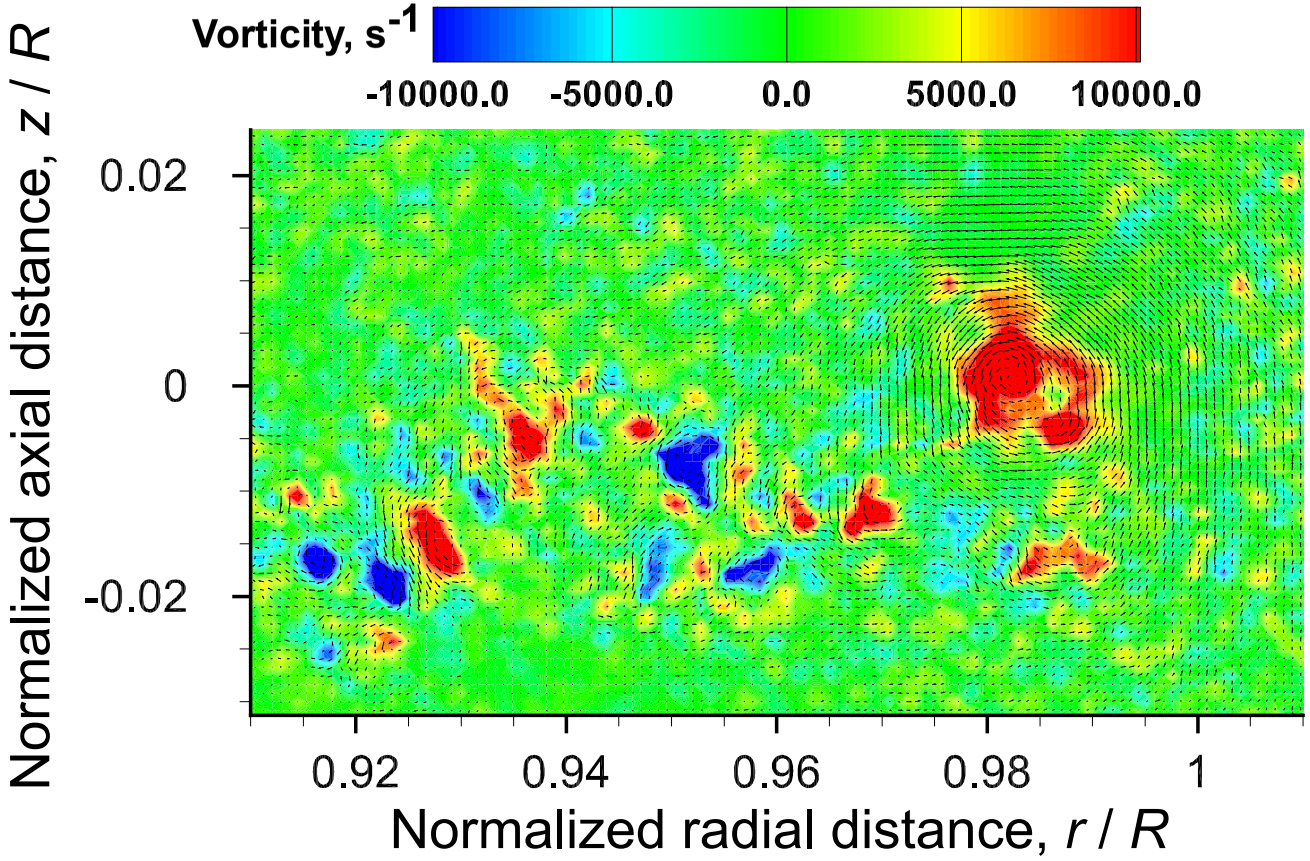

(d) $\zeta = 9^\circ$

Figure 3.31: (Cont'd) Contours of instantaneous vorticity near the tip of the twisted blade at $C_T/\sigma = 0.053$: (a) $\psi_b = 0^\circ$; (b) $\psi_b = 3^\circ$; (c) $\psi_b = 6^\circ$; (d) $\psi_b = 9^\circ$.

The rotor with the twisted blades produced a similar behavior to the untwisted blades, and at both the higher and lower values of C_T/σ. However after $\zeta = 9°$, in this case the sheet was seen to be entrained into the tip vortex as well as into another (secondary) dominant vortex that had formed in the region of the sheet near the blade tip, as shown in Fig. 3.32d. The formation of this secondary vortex was particularly interesting, and was likely a consequence of changes in the bound circulation along the blade span from the addition of blade twist (discussed previously in Section 3.3.2.2), which should have resulted in a shallower circulation gradient at the blade tip, as predicted by the free-vortex method and shown in Fig. 3.14. These two vortices (i.e., the main tip vortex and the secondary vortex at the end of the wake sheet) then begin to pair and merge together, as shown in Fig. 3.32d.

Figures 3.29 through 3.32 show that the roll-up of the tip vortices with the corresponding wake sheet was a process that did not occur immediately upon being trailed from the rotor blade. In fact, Figs. 3.31d and 3.32d show that tip vortex trailed from the rotor with the twisted blades did not appear to be fully developed, even at a somewhat older wake age of $\zeta = 9°$.

To investigate the roll-up process further, the circulation of the primary vortex (i.e., tip vortex) and each individual wake sheet vortex was calculated from the PIV measurements. Details of this circulation calculation are given in Appendix A. To quantify the roll-up process, it was necessary to develop a metric characterizing the evolution of the primary vortex. It would be expected that a fully developed tip vortex would contain the total circulation trailed from the outboard portion of the blade. Therefore, in the present work the circulation of the primary vortex was normalized by the total circulation out-

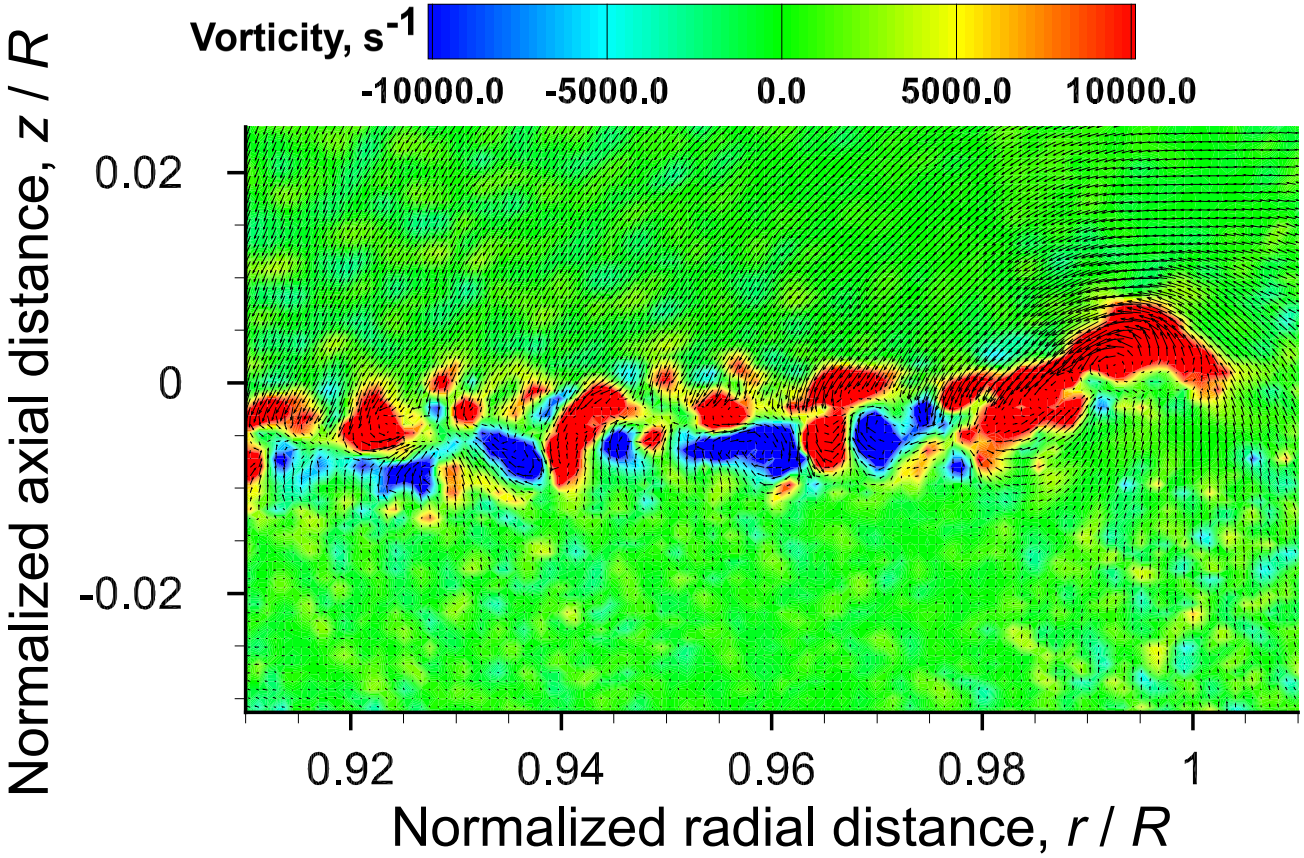

(a) $\zeta = 0^\circ$

Figure 3.32: Contours of instantaneous vorticity near the tip of the twisted blade at $C_T/\sigma = 0.080$: (a) $\psi_b = 0^\circ$; (b) $\psi_b = 3^\circ$; (c) $\psi_b = 6^\circ$; (d) $\psi_b = 9^\circ$.

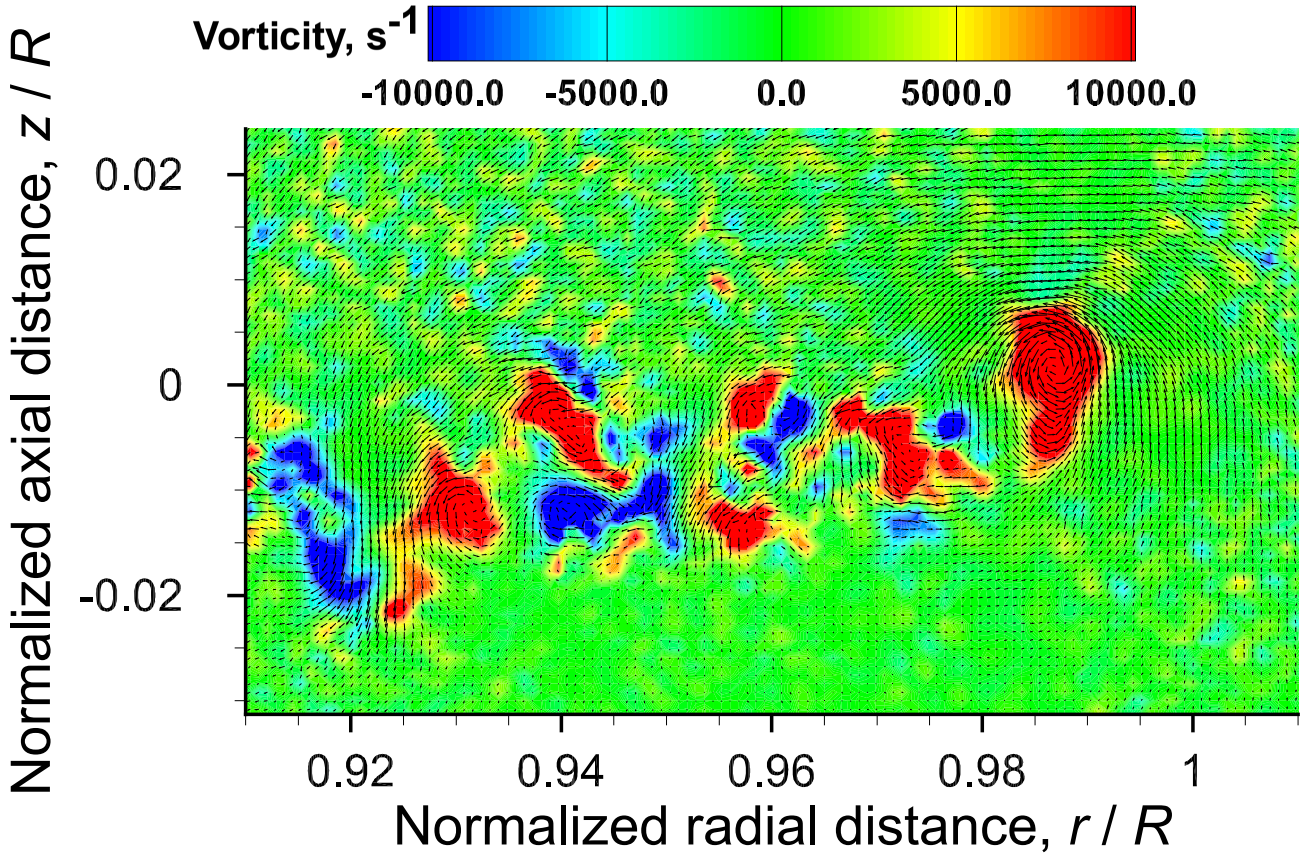

(b) $\zeta = 3^\circ$

Figure 3.32: (Cont'd) Contours of instantaneous vorticity near the tip of the twisted blade at $C_T/\sigma = 0.080$: (a) $\psi_b = 0^\circ$; (b) $\psi_b = 3^\circ$; (c) $\psi_b = 6^\circ$; (d) $\psi_b = 9^\circ$.

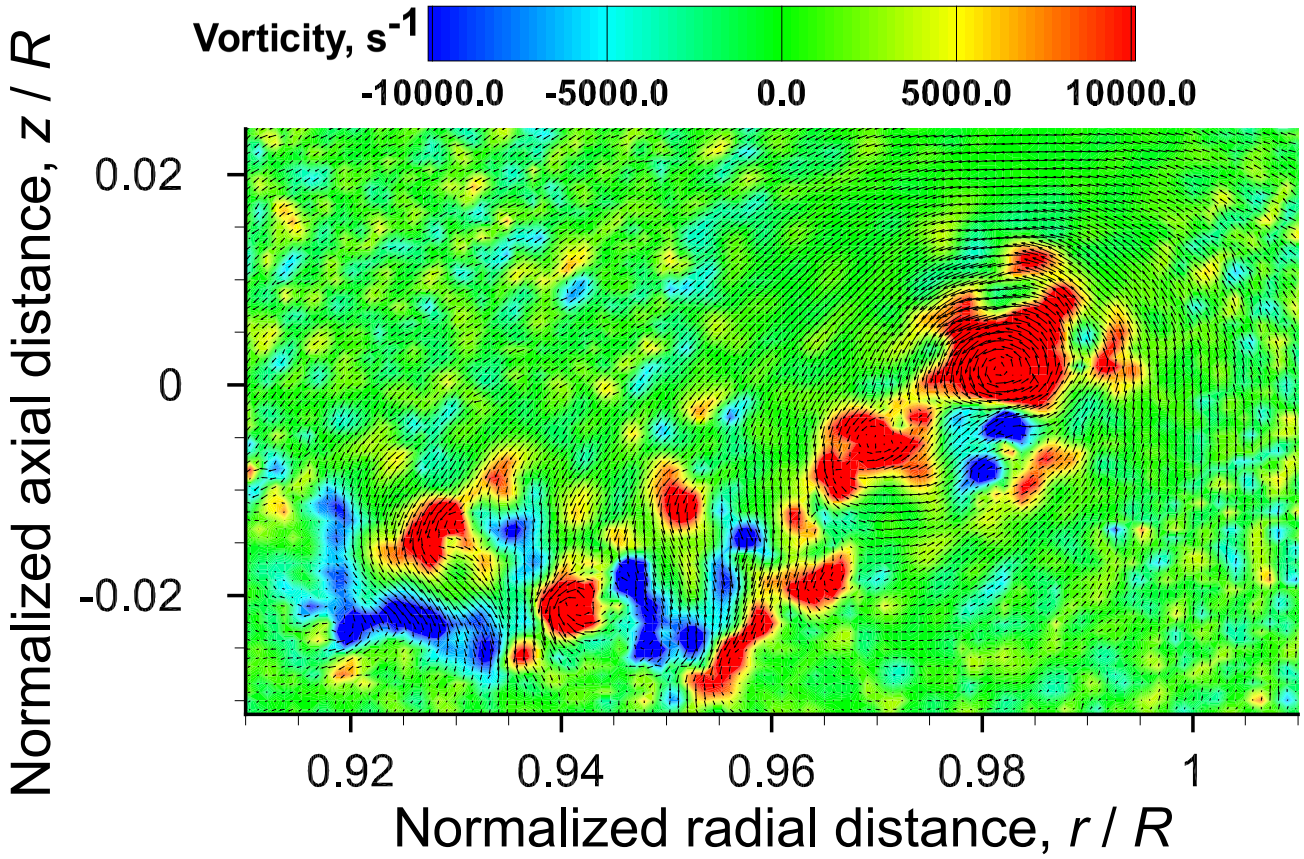

(c) $\zeta = 6^\circ$

Figure 3.32: (Cont'd) Contours of instantaneous vorticity near the tip of the twisted blade at $C_T/\sigma = 0.080$: (a) $\psi_b = 0^\circ$; (b) $\psi_b = 3^\circ$; (c) $\psi_b = 6^\circ$; (d) $\psi_b = 9^\circ$.

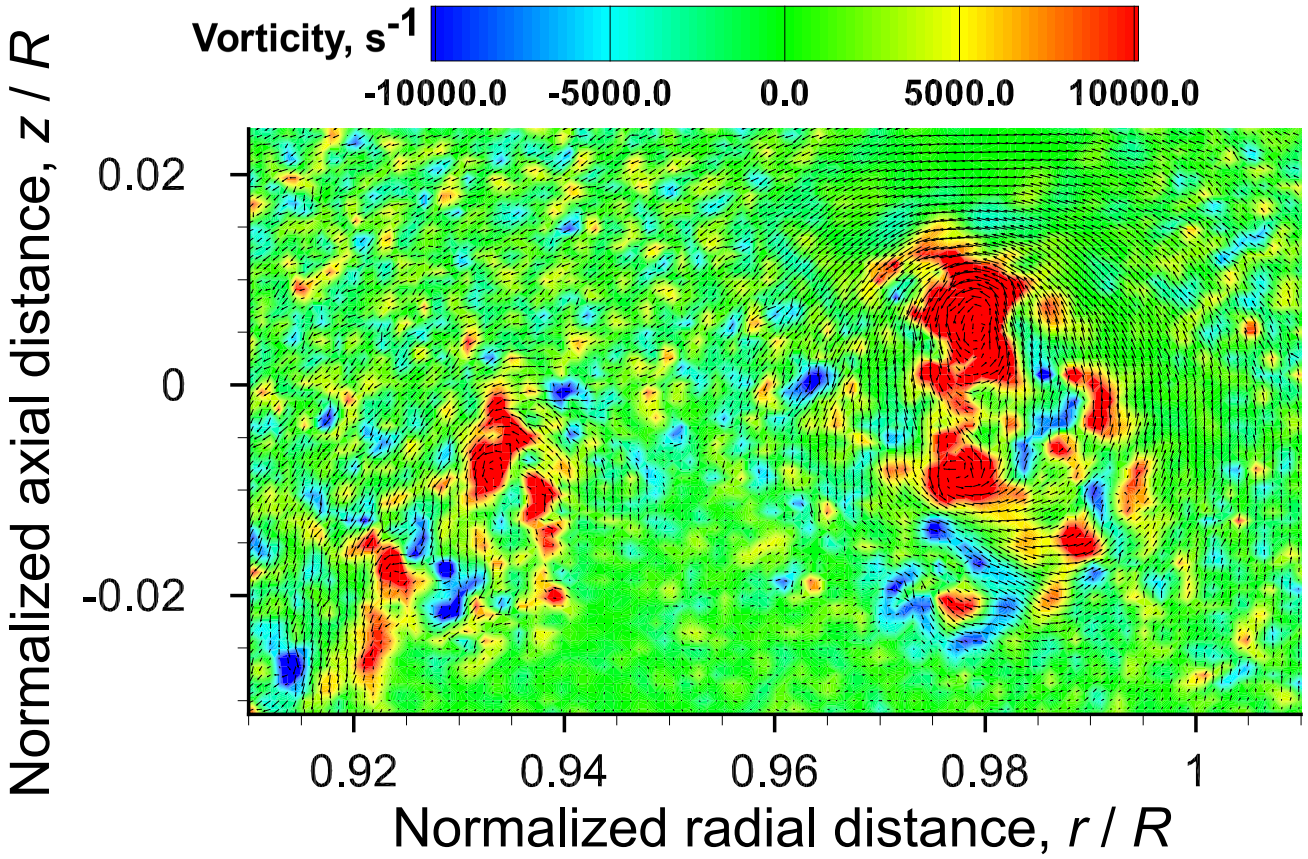

(d) $\zeta = 9^\circ$

Figure 3.32: (Cont'd) Contours of instantaneous vorticity near the tip of the twisted blade at $C_T/\sigma = 0.080$: (a) $\psi_b = 0^\circ$; (b) $\psi_b = 3^\circ$; (c) $\psi_b = 6^\circ$; (d) $\psi_b = 9^\circ$.

board of $r/R = 0.85$, which is plotted as a function of wake age in Fig. 3.34.

Notice that for the untwisted blade, the primary vortex (i.e., the tip vortex) contained more than 86% of the total outboard circulation by a wake age of 3°, and more than 95% by a wake age of 9°, i.e., it could be considered fully rolled up by that point. The primary vortex trailed by the twisted blade, however, contained 63% of the total circulation by $\zeta = 3°$ (approximately 25% less than the untwisted blade) and only 70% of the total circulation by a wake age of 9°. In fact, the circulation in the primary vortex trailed from the twisted blade did not reach over 90% of the total circulation until a wake age of 60° was reached. Therefore, it is clear that the tip vortex produced by twisted blade took considerably longer to roll-up than the tip vortex produced by the untwisted blade, which is most likely related to the differences in the distributions of bound circulation along the blades, as shown in Fig. 3.14.

Figure 3.33 shows the representative variation in the peak swirl velocity and vortex core radius as a function of wake age for a rotor operating in ground effect. The peak swirl velocity was found to be very sensitive to small changes in the structure of the vortex filament (see Fig. 3.33a) and variations in the peak swirl velocity began to manifest as the vortex filaments interacted with the ground. In particular, as the vortex began to interact with the ground the swirl velocities were significantly reintensified as the vortex filament was stretched along its length.

The stretching of the vortex filaments was also reflected in the variation of the vortex core size with wake age; see Fig. 3.33b. Initially, the trailed vortices grew (logarithmically) with wake age, however, as the vortices began to interact with the ground the vortex filament was stretched, which caused the growth of the core size to be reversed, i.e., the

core size decreased with further increases in wake age. As found with the peak swirl velocities, the core radius of the tip vortices changed very little at older wake ages (i.e., $\zeta \geq 420^\circ$), which was because diffusion and reintensification were more in equilibrium.

The evolution of the wake sheet and its contribution to the total circulation contained in the near tip region of the flow was also examined. Because the wake sheet was comprised of T–G vortices of both positive (i.e., the same sign as the tip vortex) and negative circulation, it was necessary to isolate their total contribution to the final circulation in the fully developed rotor wake. Therefore, the total positive and negative circulation of the tip vortex and outboard portion of the wake sheet was plotted as a function of wake age, which is shown in Fig. 3.35.

Figure 3.35 shows that at early wake ages the rotor with twisted blades produced a wake sheet that contained a substantial amount of negative circulation (i.e., Γ_N and the blue markers), on the order of one-sixth that of the total positive circulation (i.e., Γ_P and red markers). Conversely, the rotor with untwisted blades produced a wake sheet with significantly lower negative circulation. Furthermore, the total negative circulation contained in the outboard portion of the wake sheet decreased with increasing wake age, with very little negative circulation remaining by $\zeta > 15^\circ$. The total positive circulation also decreased as the tip vortex and wake sheet aged in the flow, as also shown in Fig. 3.35. If at a given wake age the negative circulation is assumed to be completely rolled up into the tip vortex, then the decrease in the total positive circulation closely matches the measured decrease in total negative circulation at subsequent wake ages. In particular, it was possible to predict the total positive circulation at a later wake age by summing the total measured positive and negative circulations at the previous wake age.

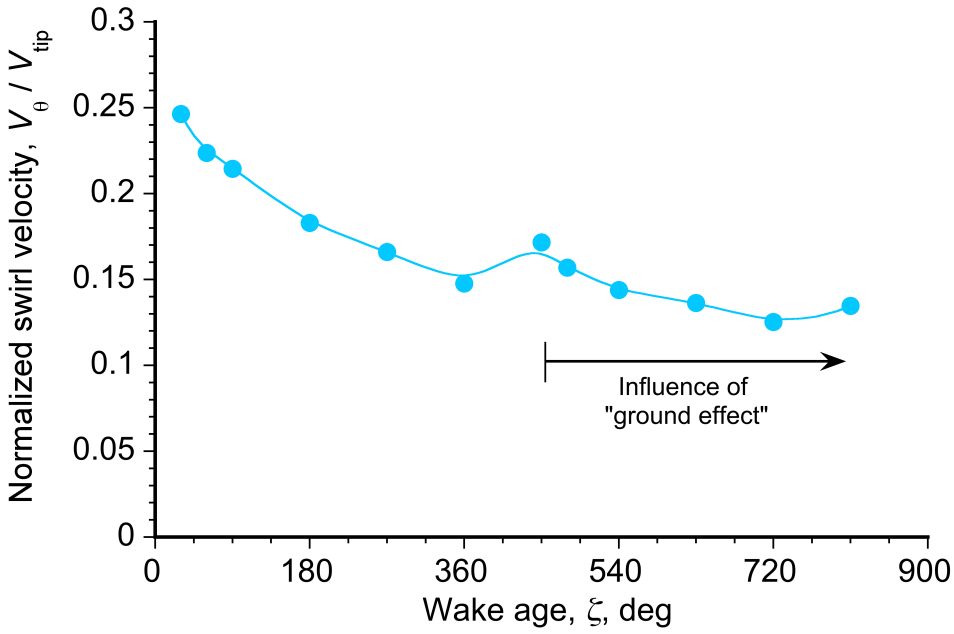

(a) Peak swirl velocity

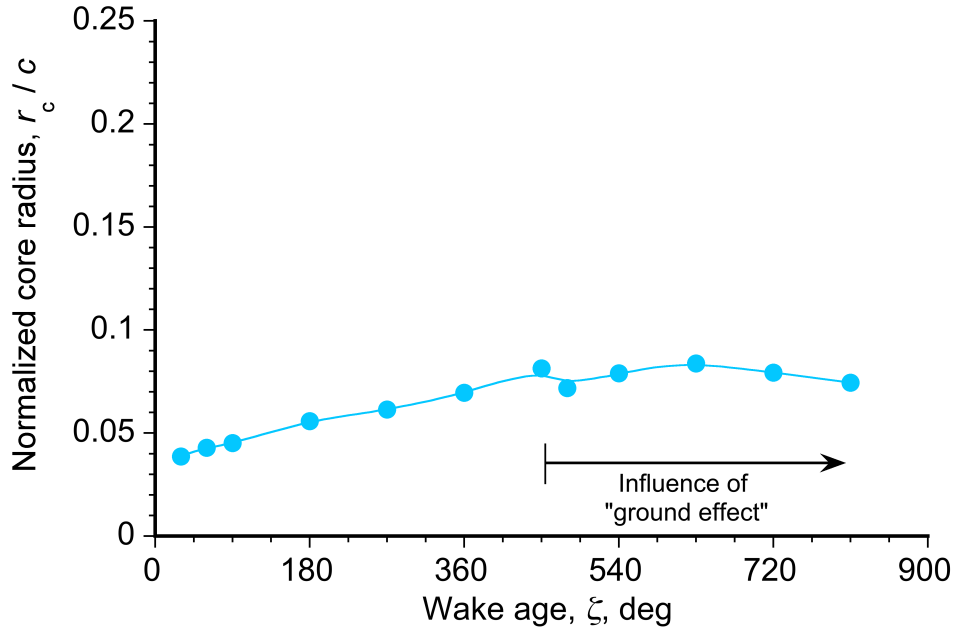

(b) Vortex core size

Figure 3.33: Representative tip vortex characteristics a function of wake age for a rotor operating in ground effect: (a) Peak swirl velocity; (b) Vortex core size.

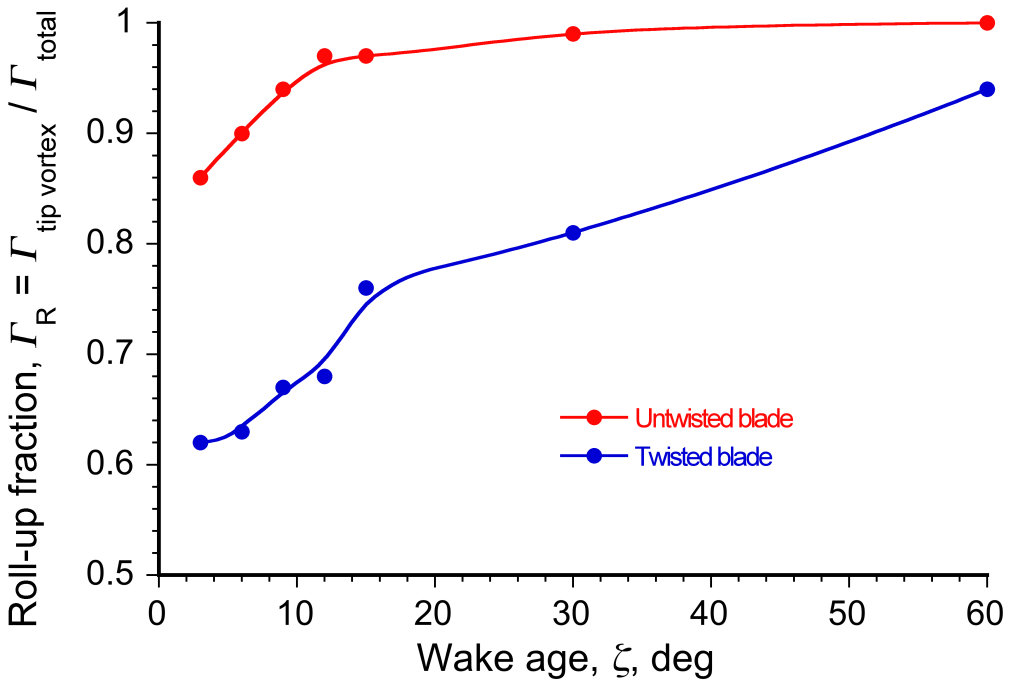

Figure 3.34: Plot of the measured peak circulation in the tip vortex versus wake age normalized by the total circulation in the outboard portion of the wake sheet.

The predicted positive circulation (i.e., $\Gamma_{Predicted}$ and the green markers in Fig. 3.35) for both the untwisted and twisted blades at $\zeta \geq 6^\circ$ closely matched the corresponding measured positive circulation (see Fig. 3.35), indicating that outboard portion of the wake sheet had a significant influence on the development and evolution of the tip vortex. Furthermore, the tip vortex produced by the twisted blade was affected significantly more by the wake sheet than the tip vortex produced by the untwisted blade, with the total positive circulation decreasing by almost one-third.

Most of these latter observations are consistent with the findings of Duraisamy et al. [98], who showed using measurements and CFD modeling (RANS) that as a vortex is trailed from the blade tip a smaller region of negative vorticity is formed, which is

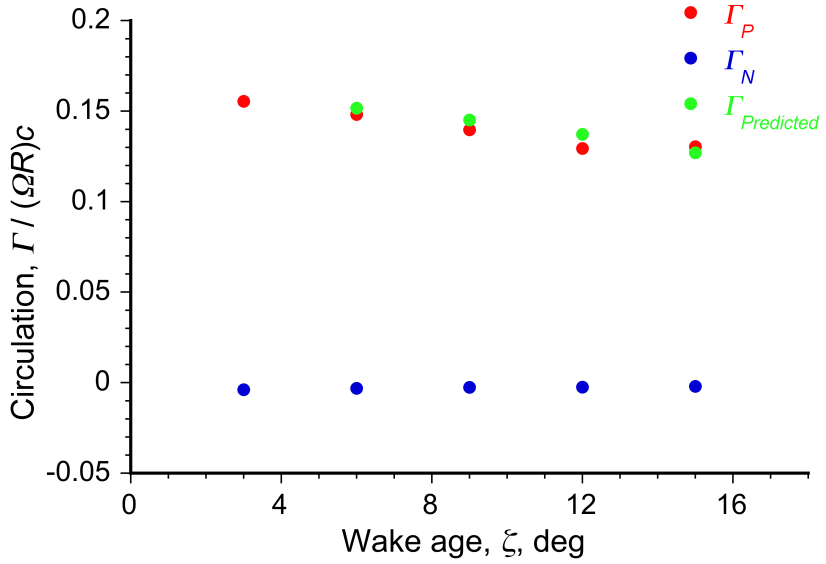

(a) Untwisted blade

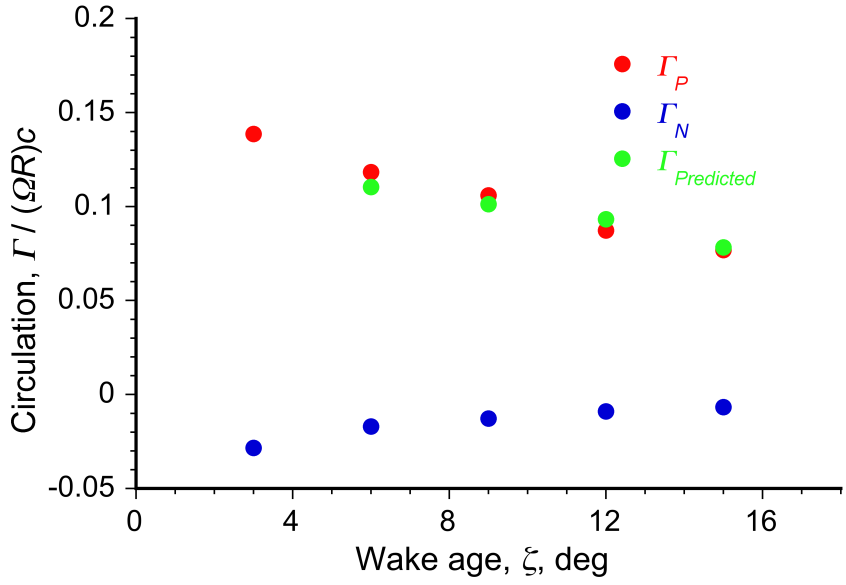

(b) Twisted blade

Figure 3.35: Plot showing the total positive, negative, and predicted circulation trailed from the tip region of the: (a) Untwisted blade; (b) Twisted blade.

surrounded by a band of positive vorticity, i.e., of the same sign as the tip vortex. The present results also found that counter vorticity is produced by the untwisted blades, as shown in Figs. 3.29a and 3.30a. The region of counter vorticity may be a consequence of the interaction of the newly formed tip vortex with the upper surface of the blade, as also pointed out by Duraisamy et al. [98]. As the vortex rolls up, it can be expected to induce a strong adverse pressure gradient on the upper surface of the blade, which will then cause the boundary layer to grow in thickness. Eventually, as the adverse pressure gradient builds, vorticity of opposite sign to the tip vortex (i.e., negative) is shed from the boundary layer. As shown in Figs. 3.29a and 3.30a, this region of negative vorticity was seen in this case only for the untwisted blades.

The PIV measurements that were conducted in the present research have given significant new insight into the flow field induced by a hovering rotor and its downstream wake behavior. In particular, the relatively high spatial resolution of the measurements compared to prior work [22, 23, 48, 61, 90, 98, 99] allowed for the formation and evolution of the wake sheet trailed from the inner part of the blade to be quantified with an unprecedented level of fidelity.

To better demonstrate the improvements in measurement fidelity, the simulated effects of measurement resolution on the ability to resolve the wake sheet are shown in Figs. 3.36 and 3.37. Figure 3.36 shows instantaneous contours of axial (slipstream) velocity in the same ROI using three effective measurement resolutions, the lower resolutions being simulated by degrading the vector density. While the general features of the flow were retained as the resolution was degraded from 11 Mp (Fig. 3.36c) to 4 Mp (Fig. 3.36b), such as that used in Ref. 22, 23, 48, 61, 90, 98, 99, and then to 2 Mp

(Fig. 3.36a), such as that used in Ref. 64, the lower measurement resolutions resulted in a non-physical smearing of the velocity field. More importantly, however, the reduction in measurement resolution also significantly affected the ability to resolve velocity gradients and so the estimated levels of vorticity in the flow, as shown in Fig. 3.37, which correspond to the measurements of the flow velocities shown in Fig. 3.36. Because of the small scale vorticity and relatively high velocity gradients that are present in the wake sheets laid down by the rotor, a reduction in the measurement resolution from 11 Mp to 4 Mp (see Figs. 3.37c and 3.37b, respectively) greatly affected the ability to resolve the flow, and a further reduction in the measurement resolution to 2 Mp resulted in only the tip vortex being resolved, as shown in Fig. 3.37a.

The foregoing results suggest that that to properly resolve the velocity gradients in the overall flow field that is generated generated by a hovering rotor, and thereby also obtain good measurements of derived flow quantities such as vorticity and turbulence, it will be necessary to strive for at least 3,000 measurement points per unit radius. This goal certainly requires high resolution cameras, but image storage and PIV processing time also become important issues. Such spatial resolutions are also challenging to obtain with current computational methods, even with CFD methods like RANS, but future advances in processing capability and memory will eventually make these resolutions possible. Meantime, the present measurements set resolution standards for which CFD methods can aspire to reach.

The out of ground effect measurements presented in this section have provided significant insight into the initial structure, development, and evolution of the wake sheets trailed from the inboard parts of the rotor blades. Furthermore, the interaction of the

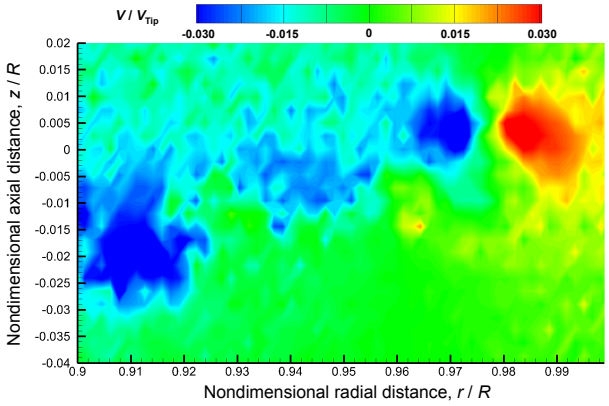

(a) 2 Mp camera

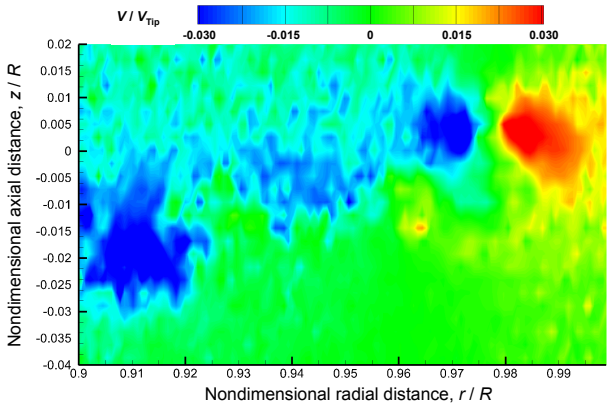

(b) 4 Mp camera

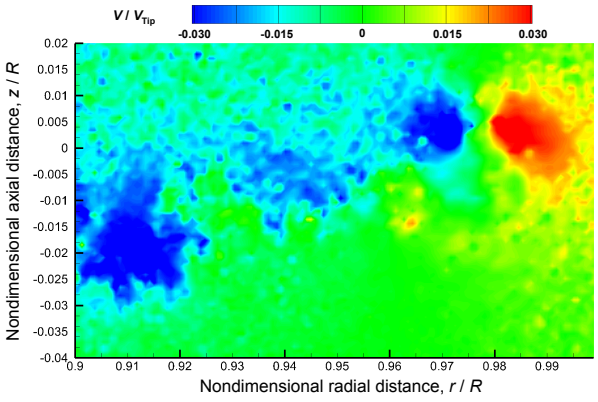

(c) 11 Mp camera

Figure 3.36: Example of the affect of camera resolution on the ability to resolve the axial velocity induced by the wake sheet: (a) 11 Mp camera; (b) 4 Mp camera; (c) 2 Mp camera.

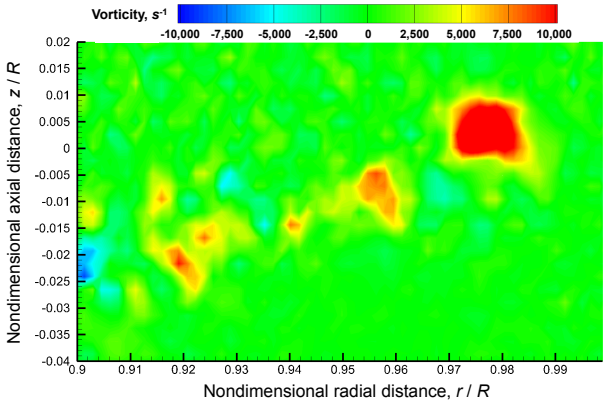

(a) 2 Mp camera

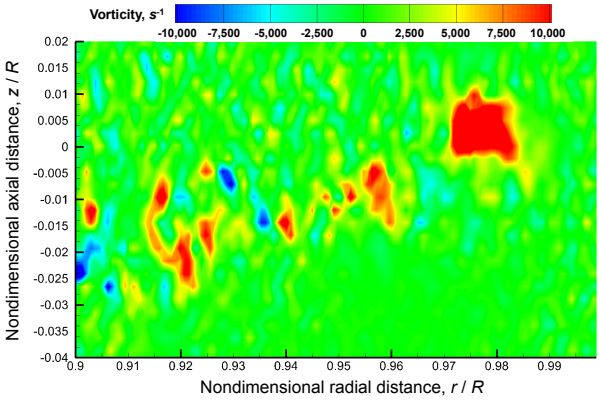

(b) 4 Mp camera

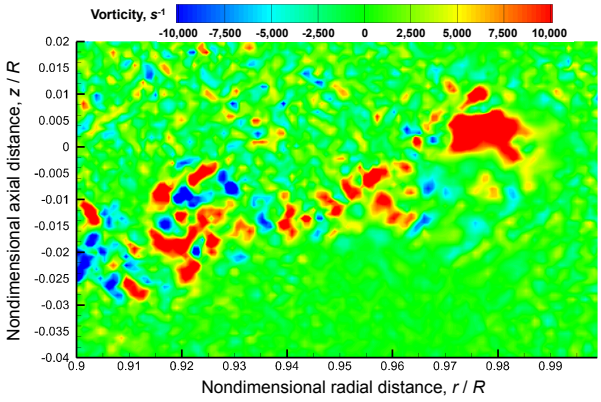

(c) 11 Mp camera

Figure 3.37: Example of the affect of camera resolution on the ability to resolve the vorticity contained in the wake sheet: (a) 11 Mp camera; (b) 4 Mp camera; (c) 2 Mp camera.

wake sheets with the newly formed blade tip vortices, as well as the roll-up process, has been quantified. While significant insight has been gained into the initial formation and evolution of both the blade tip vortices and wake sheets, the problem of brownout is a rotor in ground effect problem. Therefore, additional measurements of the flow field induced by a rotor hovering in ground effect were required, which are presented in the next section.

3.4 In Ground Effect Flow Field Measurements

By carefully examining the wake generated by the rotor when operating out of ground effect it has helped to quantify the effect of blade loading coefficient (i.e., C_T/σ) and blade twist on the characteristics of the rotor wake, such as the tip vortices and wake sheets. However, because the problem of brownout occurs when a rotor is operating in ground effect, measurements were also taken with the rotor operating over a ground plane, in this case with the rotor TPP at a representative height of one rotor radius above the ground (i.e., $z/R = 1.0$). These latter measurements have helped to quantify the effects of blade twist on the evolution and development of the flow as it reached the ground and, particularly, the participation of the wake sheet as it influenced the developing flow over the ground surface.

3.4.1 Particle Image Velocimetry

3.4.1.1 Wake Displacements

Similar to the approach described in Section 3.3.2.1, the PIV data were analyzed to quantify the rotor wake behavior in ground effect operation. Figure 3.38 documents the locations of the tip vortices and the wake sheets as a function of wake age for both blade sets when the rotor was operating at $C_T/\sigma = 0.08$. The results showed that the wake sheets trailed from the untwisted blades convected axially faster near the blade tip region, whereas near the root the wake sheets convected more slowly. The non-uniform convection of the wake sheets was caused by the more linear spanwise distribution of

downwash in the wake below the rotor that had the untwisted blades. In contrast, the more uniform axial velocity distribution in the wake of the rotor with the twisted blades resulted in the wake sheets convecting more uniformly in the downstream wake; see Fig. 3.38b.

For a rotor when it is operating in ground effect, it is convenient to use a reference frame that is located at the ground and coincident with the rotor shaft axis, which for the current work was referred to as a ground based reference frame; see the schematic in Fig. 3.39b. In this reference frame, the location z/R = 1 and r/R = 1 corresponded to the position of the rotor blade tip at a blade azimuth angle of ψ_b = 0°. However, when the rotor is operated out of ground effect (i.e., $z/R = \infty$) a ground based reference frame could not be used. Therefore, a reference frame located coincident with the rotor shaft and in the plane of rotation of the rotor disk (i.e., a rotor based reference frame) was used, as shown in Fig. 3.39a. In a rotor based reference frame, a position of z/R = 0 and r/R = 1 corresponded to the position of the rotor blade tip at ψ_b = 0°. Because the reference frame varied depending on operating state of the rotor (i.e., out of ground effect or in ground effect), the measurements obtained for the rotor in ground effect (i.e., in a ground based reference frame) were converted to a rotor based reference frame by using the equations $r_R = r_G$ and $z_R = z_G - z$, where r_R and z_R are the radial and axial coordinates, respectively, in the rotor based reference frame, r_G and z_G are the radial and axial coordinate, respectively, in the ground based reference frame, and z is the height of the rotor above the ground (i.e., for the current work $z = R$).

The locations of the tip vortices and wake sheets (in the rotor based reference frame) as a function of wake age are shown in Fig. 3.40 for the rotor with the untwisted blades, when it was operating both out of ground effect and in ground effect. The results showed

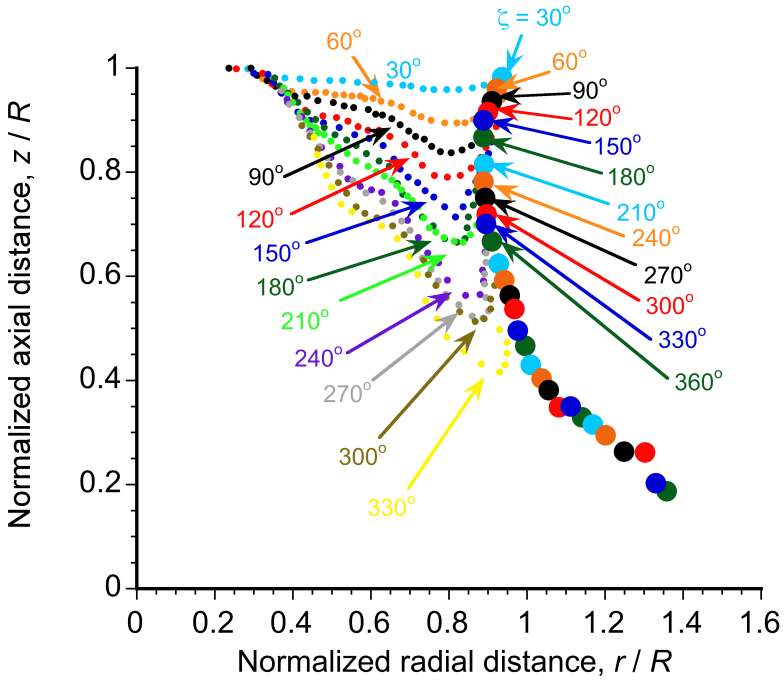

(a) Untwisted blade

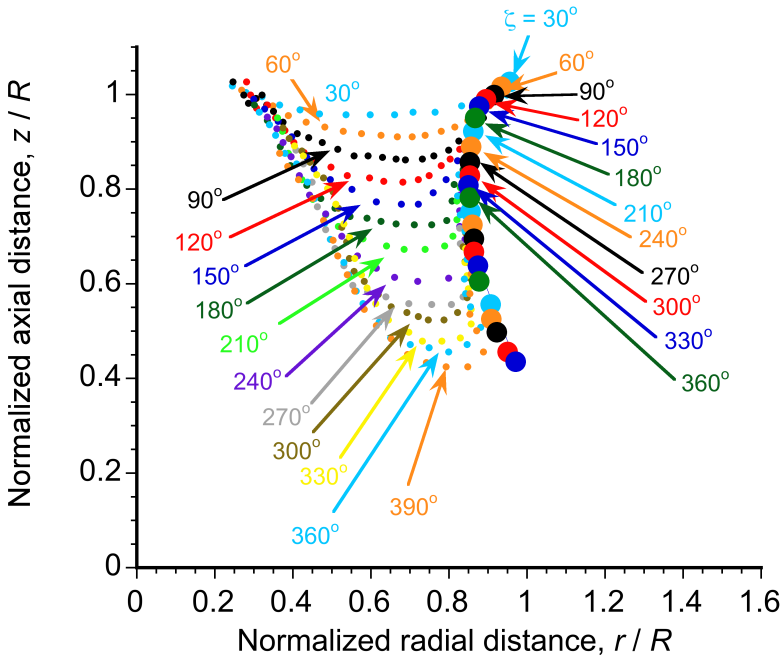

(b) Twisted blade

Figure 3.38: Plot of the axial and radial locations of the wake sheets and tip vortices when operating in ground effect with: (a) Untwisted blades; (b) Twisted blades.

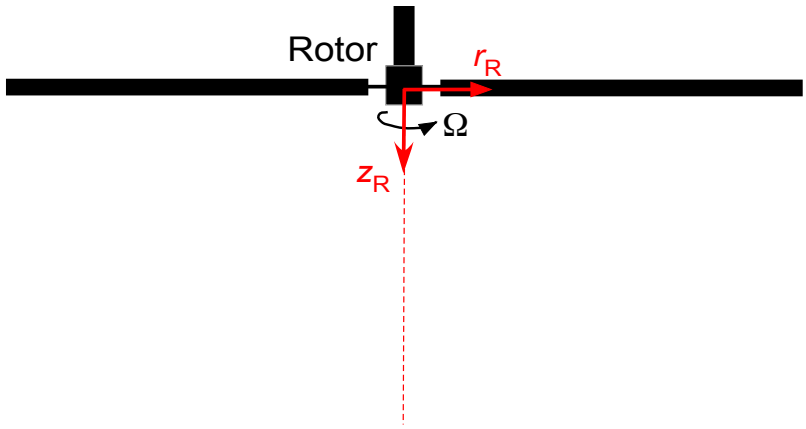

(a) Rotor based reference frame

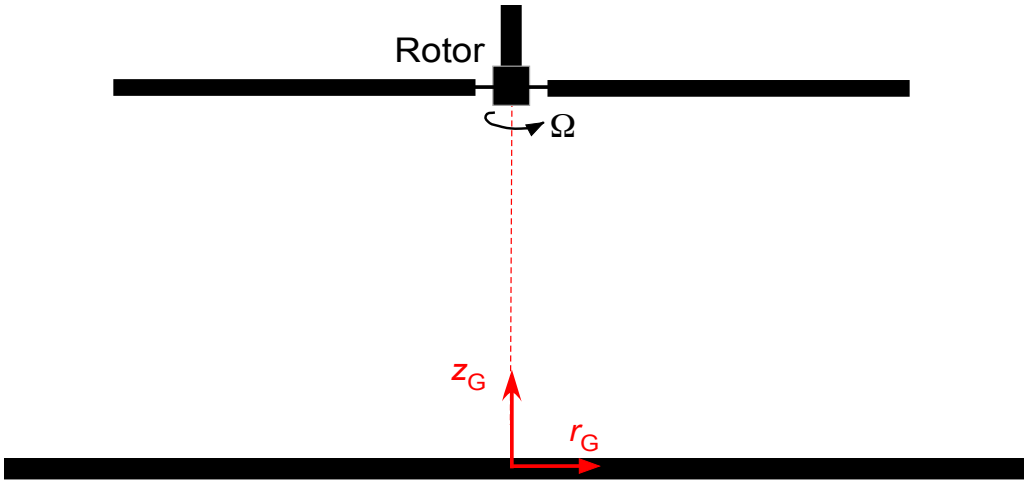

(b) Ground based reference frame

Figure 3.39: Schematic showing the reference frames used for the rotor when operating: (a) Out of ground effect; (b) In ground effect.

that the non-uniform convection of the wake sheets was qualitatively similar for both operating conditions, with the quickest axial convection occurring in the wake outboard of $r/R = 0.6$; see Fig. 3.40. However, the behavior of the wake sheets was significantly affected by the presence of the ground. As discussed previously in Section 3.3.2.1, when the untwisted blade set was operated out of ground effect, the wake sheets were seen to take on two different slopes relative to the rotor disk (i.e., a negative slope inboard and positive slope outboard) as they convected in the wake, as shown in Fig. 3.40a. Figure 3.40b shows that the wake sheets trailed from the untwisted blades in ground effect also took on two different slopes as they convected in the wake below the rotor. However, in this case the slopes on the inboard (i.e., negative) and outboard (i.e., positive) sections of the sheet were significantly shallower; see Fig. 3.40.

Notice from Fig. 3.40 that at early wake ages (i.e., for $\zeta \leq 120^\circ$) the wake sheets trailed from the rotor the with untwisted blades convected axially at approximately the same rates. However, after $\zeta = 120^\circ$, the wake sheets from the untwisted blades convected axially slower below the rotor when it was operating in ground effect. For example, on one hand Fig. 3.9 shows that at a wake age of $\zeta = 180^\circ$ only the inboard 75% of the wake sheet was above $z/R = -0.35$ for the rotor operating out of ground effect. On the other hand, when the rotor was operated in ground effect the entire wake sheet remained above $z/R = -0.35$ until a wake age of $\zeta \geq 210^\circ$ was reached. In this case, the slower axial convection was because of the presence of the ground, which modified the spanwise downwash distribution in the wake below the rotor.

As discussed previously in Section 3.3.2.1, when the rotor was operated out of ground effect a wave-like perturbation formed on the wake sheets shortly after they were

trailed from the untwisted blade; see Fig. 3.40a. However, as the sheet convected axially below the rotor it was stretched, which effectively suppressed any additional growth in the wave amplitude. From an examination of Fig. 3.40b, it can be see that when the rotor was operated in ground effect, no wave-like perturbation was observed to form on the sheet. In this case, the radial stretching of the wake because of the presence of the ground appeared to be the source of the change in the behavior of the wake sheet. Figure 3.40b shows that as the wake sheet convected below the rotor it was stretched axially, however the expansion of the rotor wake also caused the sheet to stretch radially. In this case, the combination of both axial and radial stretching of the sheet appeared to completely suppress the tendency to form of any wave-like instabilities, as shown in Fig. 3.40b.

Figure 3.40 shows that at early wake ages (i.e., for $\zeta \leq 210^\circ$) when the rotor with the untwisted blades was in ground effect and out of ground effect, the radial and axial locations of the tip vortices below the rotor were very similar. However, the interaction of the wake with the ground caused it to expand radially outward. This expansion could be seen in the change of the radial position of the tip vortices at older wake ages (i.e., for $\zeta \geq 210^\circ$); see Fig. 3.40b. For example, at a wake age of $\zeta = 390^\circ$, the radial location of the tip vortex trailed from the rotor in ground effect was approximately $0.05R$ further outboard as compared to the out of ground effect case, as shown in Fig. 3.40. Furthermore, Fig. 3.40b shows that the axial convection rate of the tip vortices was also affected by the presence of the ground. Specifically, for $\zeta \geq 330^\circ$ the tip vortices trailed from the rotor when out of ground effect convected approximately $0.03R$ further in the wake below the rotor than the corresponding tip vortices in ground effect; see Fig. 3.40.

Figure 3.41 shows the locations of the tip vortices and wake sheets (in the rotor

based reference frame) as a function of wake age for the rotor with twisted blades when it was operating both out of ground effect and in ground effect. The results showed that the wake sheets convected more uniformly in the wake below the rotor because of the more uniform spanwise velocity distribution; see Fig. 3.41. However, as with the rotor the with untwisted blades, the wake sheets trailed from the rotor with twisted blades convected axially slower than the corresponding out of ground effect case; see Fig. 3.41. Furthermore, for the rotor with untwisted blades (see Fig. 3.40a), the presence of the ground resulted in the suppression of the wave-like perturbation on the wake sheets, as shown in Fig. 3.41b.

Compared to the rotor with twisted blades when operating out of ground effect, the tip vortices were noted to convect axially slower for $\zeta \geq 180^\circ$ compared to when the rotor was operating in ground effect; see Fig. 3.41. For example, at a wake age of $\zeta = 450^\circ$ the tip vortex trailed from the rotor when out of ground effect convected axially approximately 5% of the rotor radius further in the wake than the corresponding tip vortex trailed in ground effect, as shown in Fig. 3.41. As previously discussed in Section 3.3.2.1, a lower helical pitch increased the susceptibility of the downstream wake to develop perturbations and instabilities [44].

Figure 3.42 shows the radial and axial locations of the vortex cores as a function of wake age produced by the untwisted and twisted blades when the rotor was operated in ground effect. Because the tip vortices convected along the slipstream boundary their positions represent the wake boundary. Examination of Fig. 3.42a shows that the wake generated by the rotor with the twisted blades contracted radially significantly more than the wake from the untwisted blades (i.e., $r/R \approx 0.08$). Specifically, the wake produced

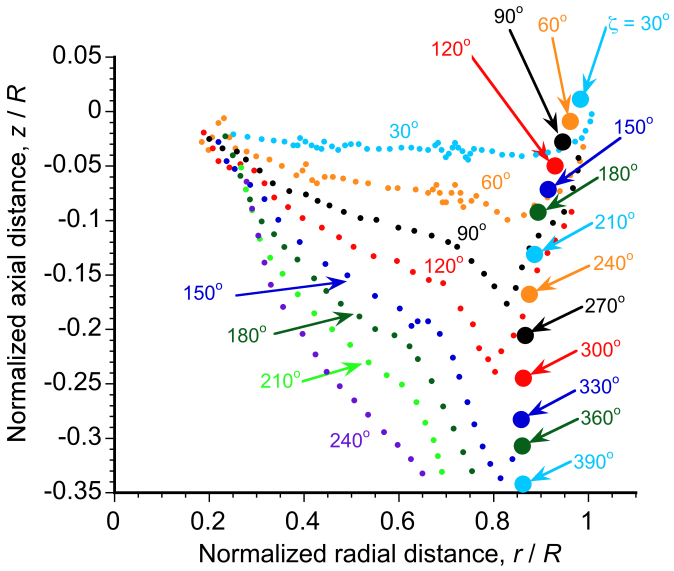

(a) Out of ground effect, ($z/R = \infty$)

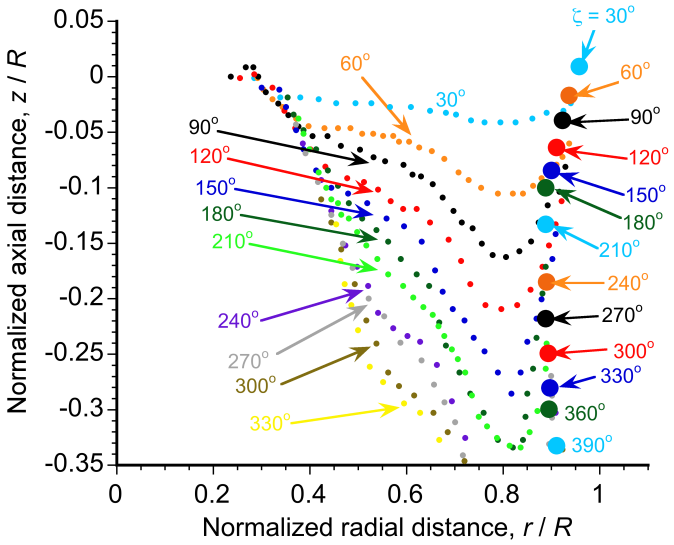

(b) In ground effect, $z/R = 1.0$

Figure 3.40: Plot of the axial and radial locations (using a rotor based reference frame) of the wake sheets and tip vortices in ROIs 1 and 2 using a rotor based reference frame for the rotor with untwisted blades operated: (a) Out of ground effect ($z/R = \infty$); (b) In ground effect ($z/R = 1.0$).

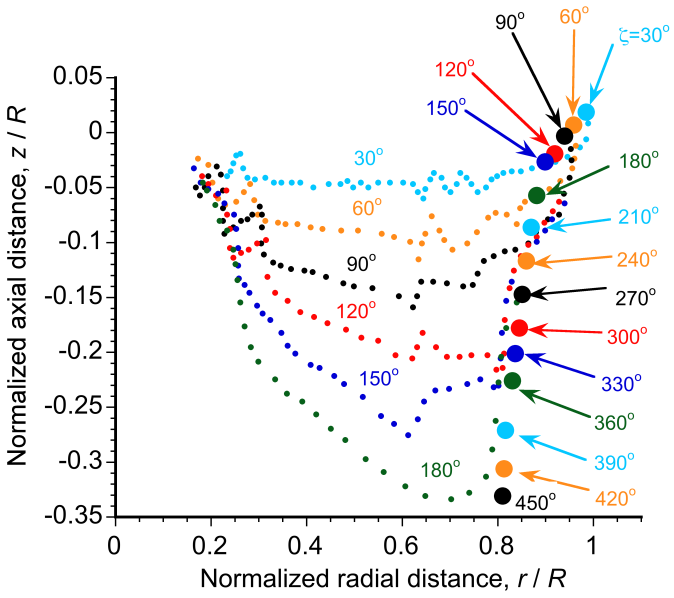

(a) Out of ground effect, $(z/R = \infty)$

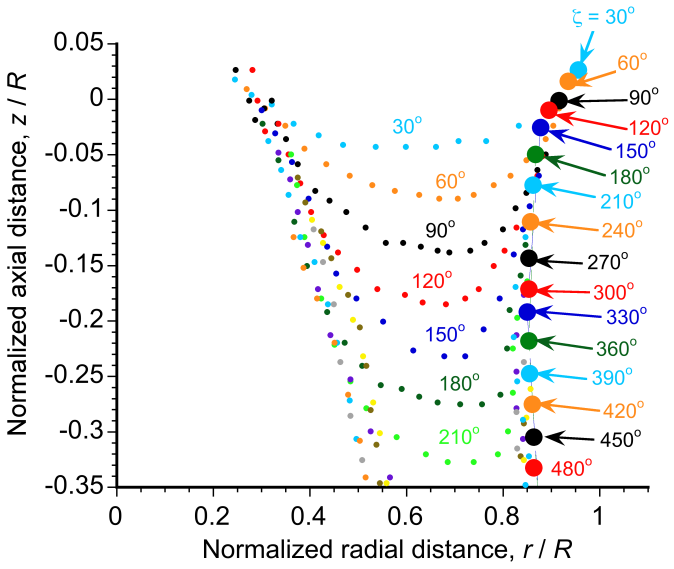

(b) In ground effect, $z/R = 1.0$

Figure 3.41: Plot of the axial and radial locations (for a rotor based reference frame) of the wake sheets and tip vortices in ROIs 1 and 2 for the rotor with the twisted blades operated: (a) Out of ground effect $(z/R = \infty)$; (b) In ground effect $(z/R = 1.0)$.

by the twisted blades did not begin to expand radially until $\zeta \approx 420^\circ$, whereas the wake produced by the untwisted blades began expanding as early as $\zeta \approx 330^\circ$; see Fig. 3.42a. While the radial position of the tip vortices varied significantly with blade twist, the axial locations (shown in Fig. 3.42b) indicated smaller variations between the blade sets. Before the first blade passage occurred, the vortices produced by the rotor with twisted blades convected axially slower (i.e, a shallower slope of the curves in Fig. 3.42b) than the corresponding tip vortices produced by the untwisted blades. However, the rate at which the vortices convected axially was increased after the passage of the following blade [36–39], which resulted in the tip vortices convecting at approximately the same rate (i.e., the curves shown in Fig. 3.42b had similar slopes).

3.4.1.2 Averaged Velocity Field Measurements

Figures 3.44 and 3.45 show the time-averaged velocity fields in ROIs 1–4 (Fig. 2.10) for the rotor with the untwisted and twisted blades, respectively. The results confirmed that the velocity distributions in the rotor wake were significantly affected by blade twist. Notice in Figs. 3.12 and 3.45 that the wakes produced by the both the untwisted and twisted blades contracted radially at first, which caused the magnitudes of the velocities in the rotor wake to increase. However, as the wake interacted with the ground it began to expand and also turn radially outward, going from a primarily downward axial flow to a primarily outward radial flow. Figures 3.44 and 3.45 show that as the wake expanded, the magnitude of the velocity in the downstream wake decreased, which affected the convection of wake sheets and tip vortices (see Figs. 3.40 and 3.41). It is important to note

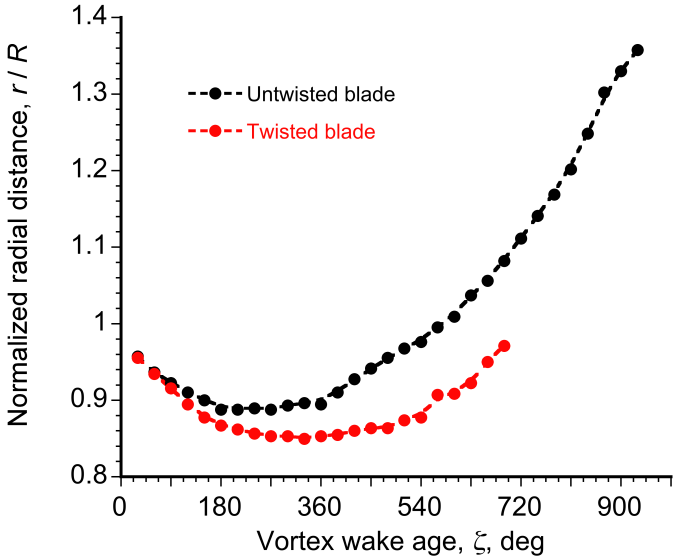

(a) Normalized radial distance

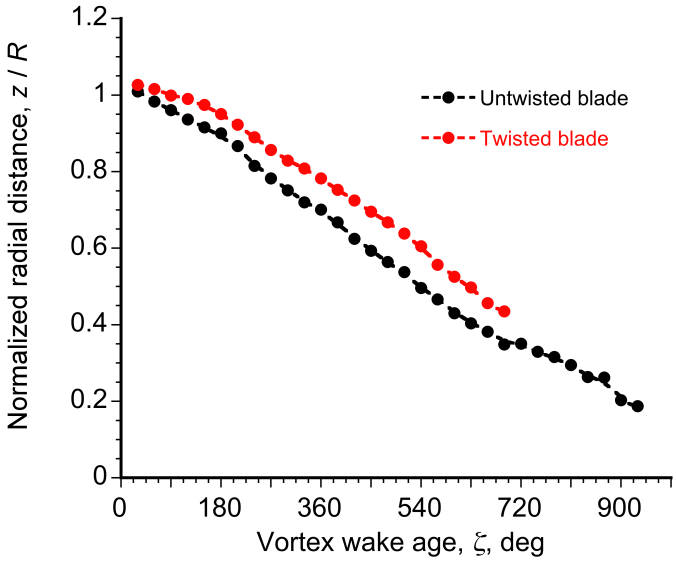

(b) Normalized axial distance

Figure 3.42: Summary of the tip vortex locations (using a ground based reference frame) in the rotor wake as a function of wake age, ζ, for the rotors with the untwisted and twisted blades: (a) Normalized radial distance; (b) Normalized axial distance.

that the spanwise velocity profiles in ROIs 5 and 6 were not shown in Figs. 3.44 and 3.45 because in these regions the flow was primarily in the radial direction. The flow fields in ROIs 5 and 6 will be discussed in more detail next.

Notice from Fig. 3.45 that the spanwise velocity distribution in the wake below the rotor with twisted blades was more uniformly distributed, with the highest flow velocities occurring around the midspan of the blade. Conversely, the untwisted blade produced the highest velocities toward the blade tip region; see Fig. 3.44. Because the twisted blade produced higher velocities closer to the rotor shaft, it would be expected to change the structure of the near-wall flow. This latter conclusion is supported by the PIV results in Figs. 3.46 and 3.47, which show background contours of the time-averaged velocity fields in ROIs 5 and 6 (as shown in Fig. 2.10) for the rotor with the untwisted and twisted blades, respectively. To better show the development of the flow along the ground, only every 30th measured vector is shown in the radial direction.

On examination of Figs. 3.46 and 3.47, an inner and outer slipstream boundary are visible. The outer slipstream boundary separated mostly the quiescent flow outside the rotor wake from the relatively higher velocity flow inside the rotor wake, whereas the inner slipstream boundary separated the higher and lower flow velocity regions inside the rotor wake, a schematic of this being shown in Fig. 3.43. For the rotor with the untwisted blades, the more linear spanwise velocity distribution (shown in Fig. 3.44) resulted in the inner slipstream boundary impinging on the ground plane at a radial position of $r/R \approx 1.0$, as shown in Fig. 3.46. Conversely, the more uniform spanwise velocity distribution in the wake below the twisted blades (shown in Fig. 3.45) resulted in the inner slipstream boundary impinging on the ground at a significantly closer radial location (i.e., $r/R \approx$

0.85); see Fig. 3.47.

Outboard of the radial point where the inner slipstream boundary impinged on the ground, the velocity of the near-wall flow was seen to increase rapidly; see Figs. 3.46 and 3.47. Therefore, the impingement of the inner slipstream boundary at a closer radial location with the rotor with the twisted blades would be expected to result in higher flow velocities along the ground plane closer to the rotor. This conclusion was supported by the velocity contours in Figs. 3.46 and 3.47, which showed that the rotor with the twisted blades produced significantly higher flow velocities outboard of $r/R = 1.2$ than the corresponding velocities from the rotor with the untwisted blades.

Previous research [3,26,49] has shown that as a rotor wake interacted with a ground plane, the average flow in the near-wall region had the potential to mobilize sediment particles. Namely, if the velocity in the near-wall flow exceeded some threshold velocity (i.e., the minimum flow velocity or equivalent shear stress required to mobilize the sediment) then the particles would become entrained into the flow. The process of particle mobilization begins with the heavier particles rolling along the sediment bed, disturbing other particles along their path. Some of these particles may encounter upward flow fluctuations and begin saltating. Therefore, it would be expected that the the higher flow velocities found in the near-wall flow produced by the rotor with the twisted blades would mobilize sediment closer to the rotor. The mobilization of sediment closer to the rotor would be expected to exacerbate the problem of brownout [6, 7].

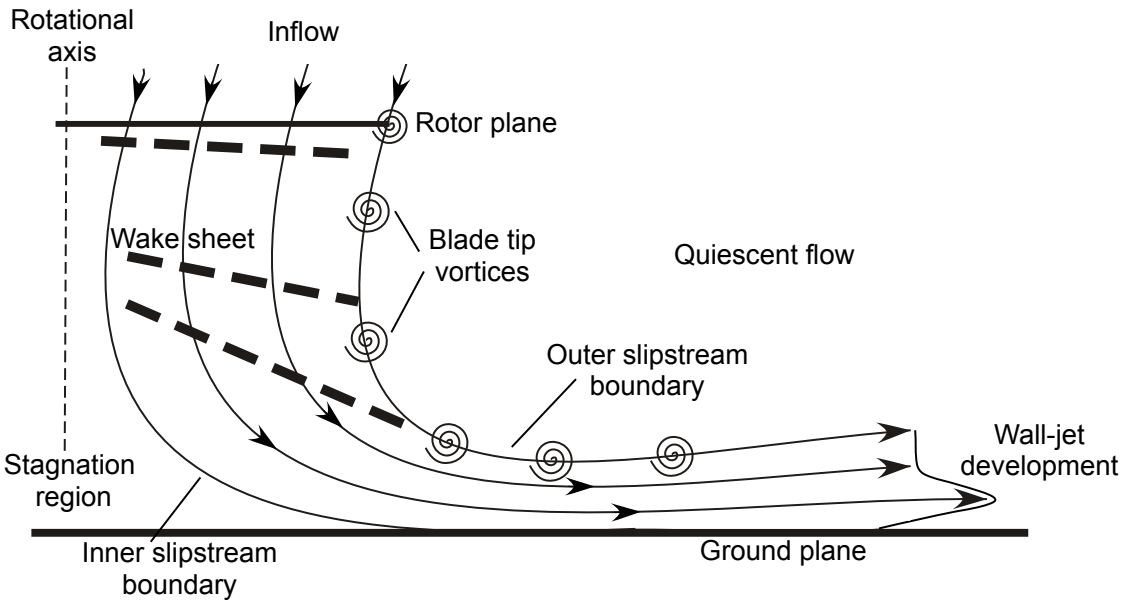

Figure 3.43: Schematic showing the wake generated by a rotor operating in ground effect.

3.4.1.3 Instantaneous Flow Field Measurements

Figures 3.48 and 3.49 show representative instantaneous flow realizations of the total flow velocities in the wake produced below the two rotors at a reference blade azimuth angle of $\psi_b = 30°$. The tip vortices produced by the rotor with the untwisted blades were found to induce significantly higher local flow velocities compared to the twisted blade. However, the most significant differences in the flow velocities were observed inboard, where the twisted blade produced substantially higher magnitudes as well as larger fluctuations; see Fig. 3.49.

As previously discussed in Section 3.3.2.3, the wake sheets trailed behind both rotor blades consisted of T–G vortex pairs [95]. These T–G vortices can also be seen in Figs. 3.50 and 3.51, which show contours of instantaneous vorticity corresponding to the total velocity contours in Figs. 3.48 and 3.49. The T–G vortex pairs are identified

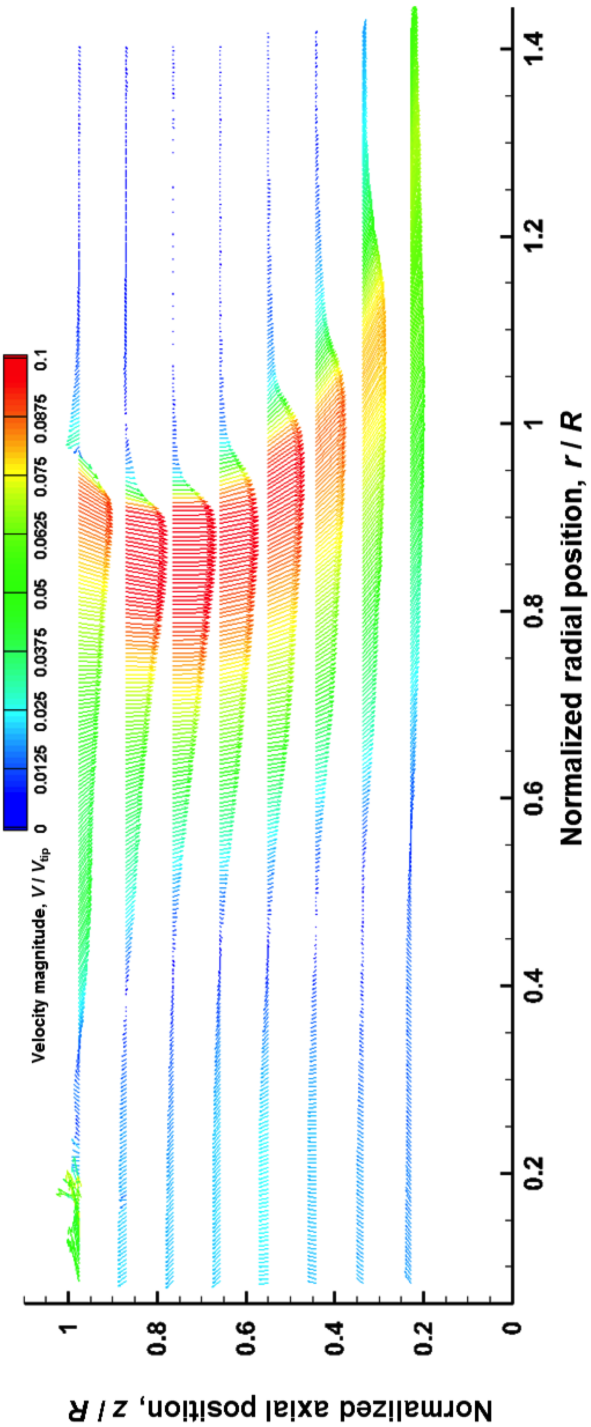

Figure 3.44: Measured time-averaged spanwise velocity distribution at varying axial locations in ROIs 1–4 for the rotor with untwisted blades when operated at $z/R = 1.0$ off the ground plane.

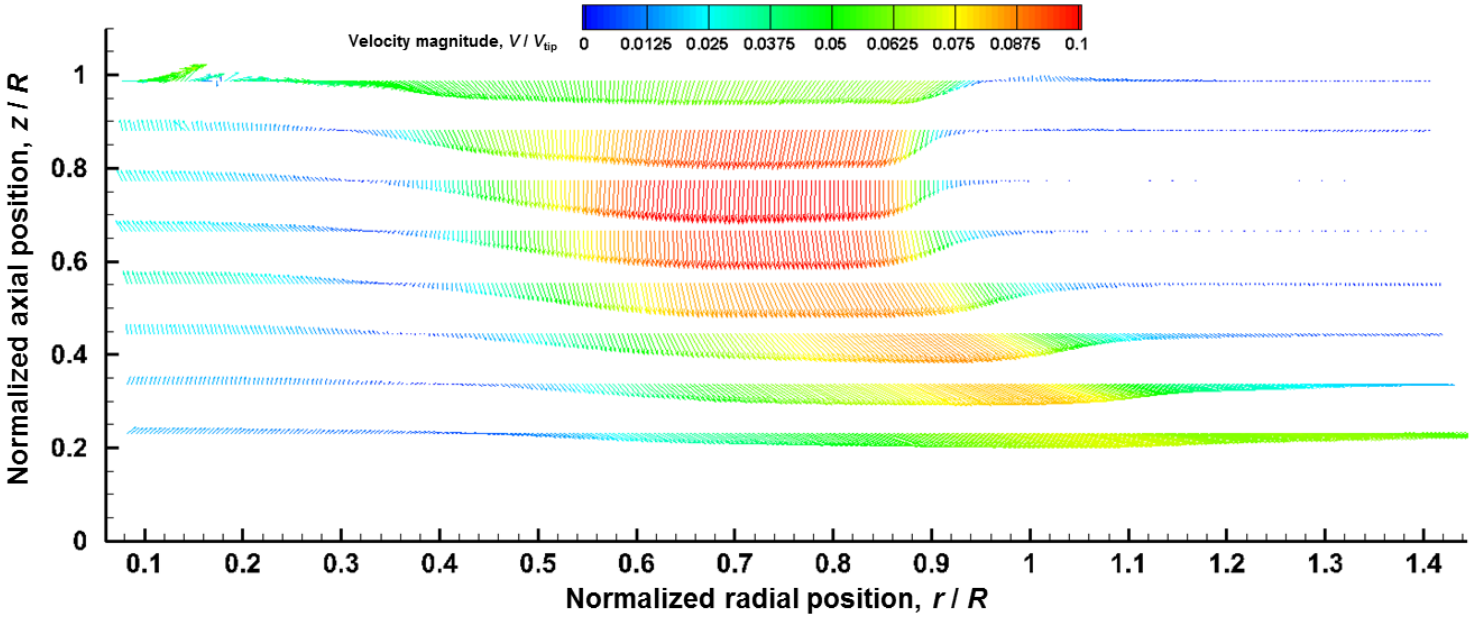

Figure 3.45: Measured time-averaged spanwise velocity distribution at varying axial locations in ROIs 1–4 for the rotor with twisted blades when operated at z/R = 1.0 off the ground plane.

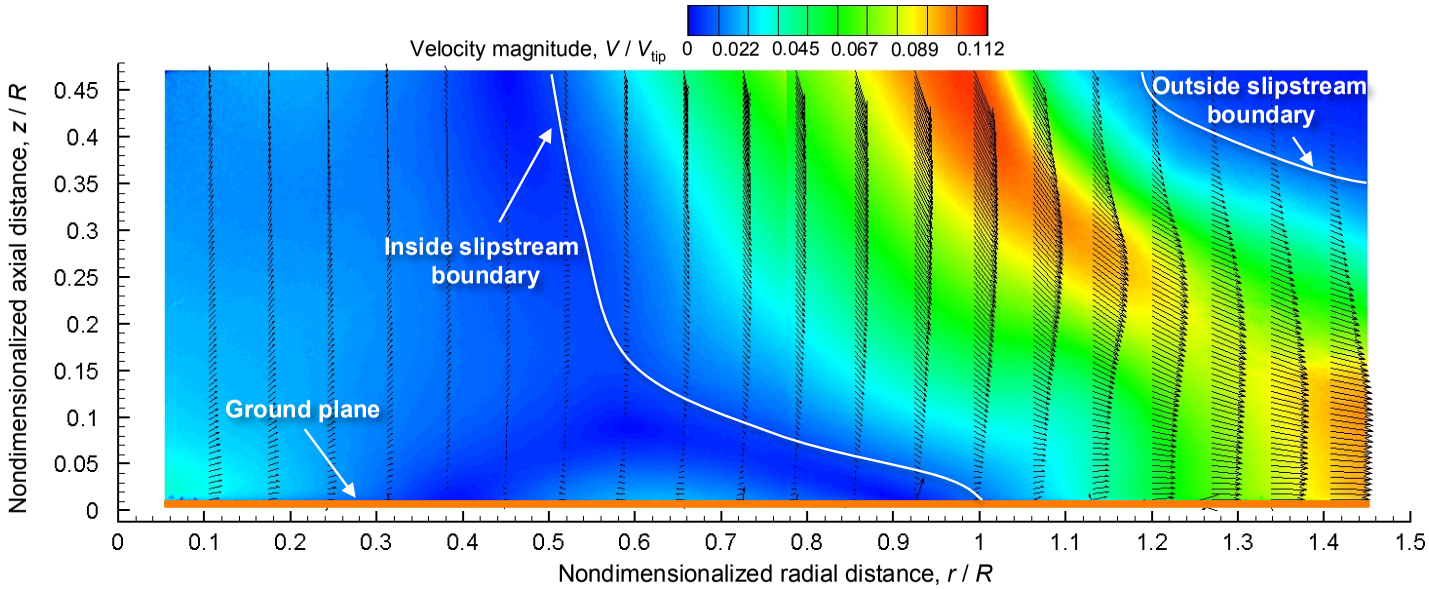

Figure 3.46: Measured time-averaged velocity distribution at varying radial locations in ROIs 5 and 6 for the rotor with the untwisted blades.

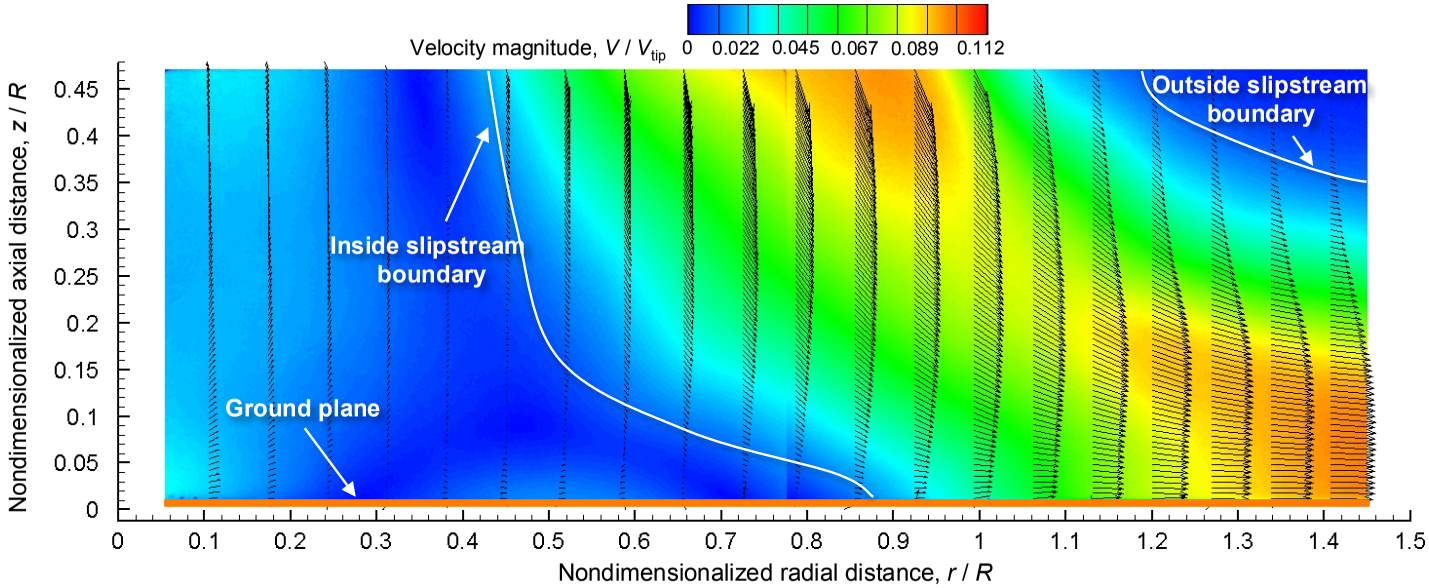

Figure 3.47: Measured time-averaged velocity distribution at varying radial locations in ROIs 5 and 6 for the rotor with the twisted blades.

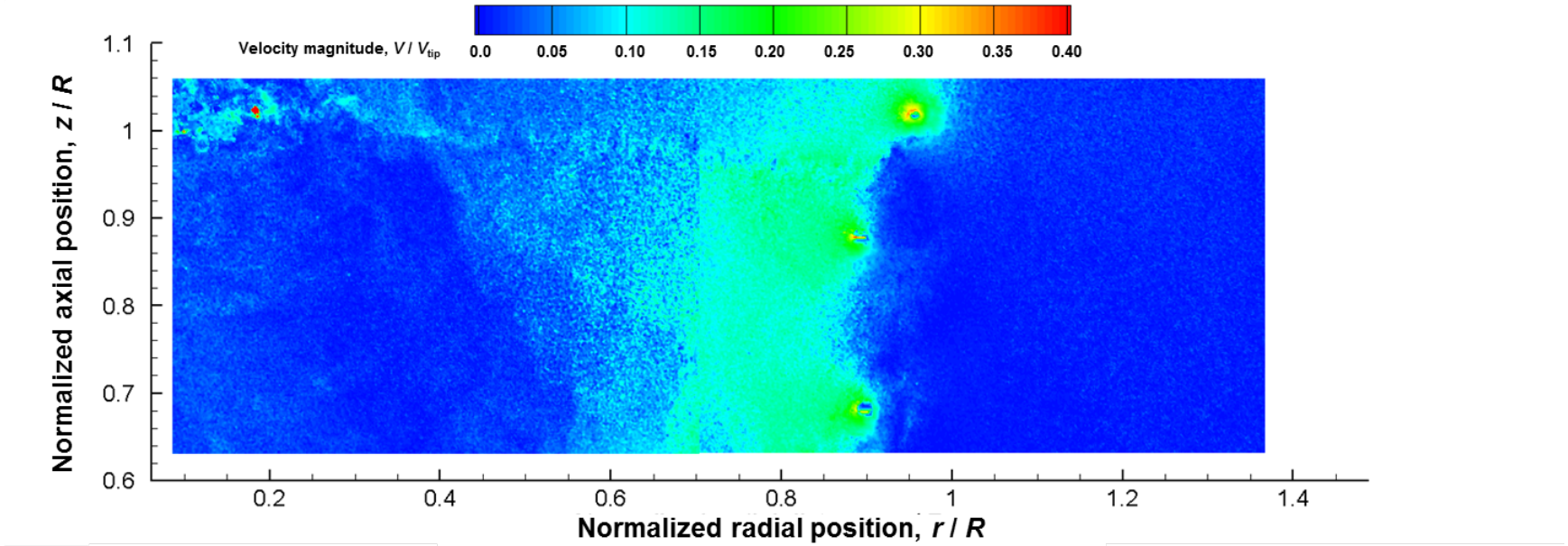

Figure 3.48: PIV measurements of the instantaneous realization of the flow field in ROIs 1 and 2 for the rotor with the untwisted blades at a blade azimuth angle $\psi_b = 30°$. Background contours are of velocity magnitude.

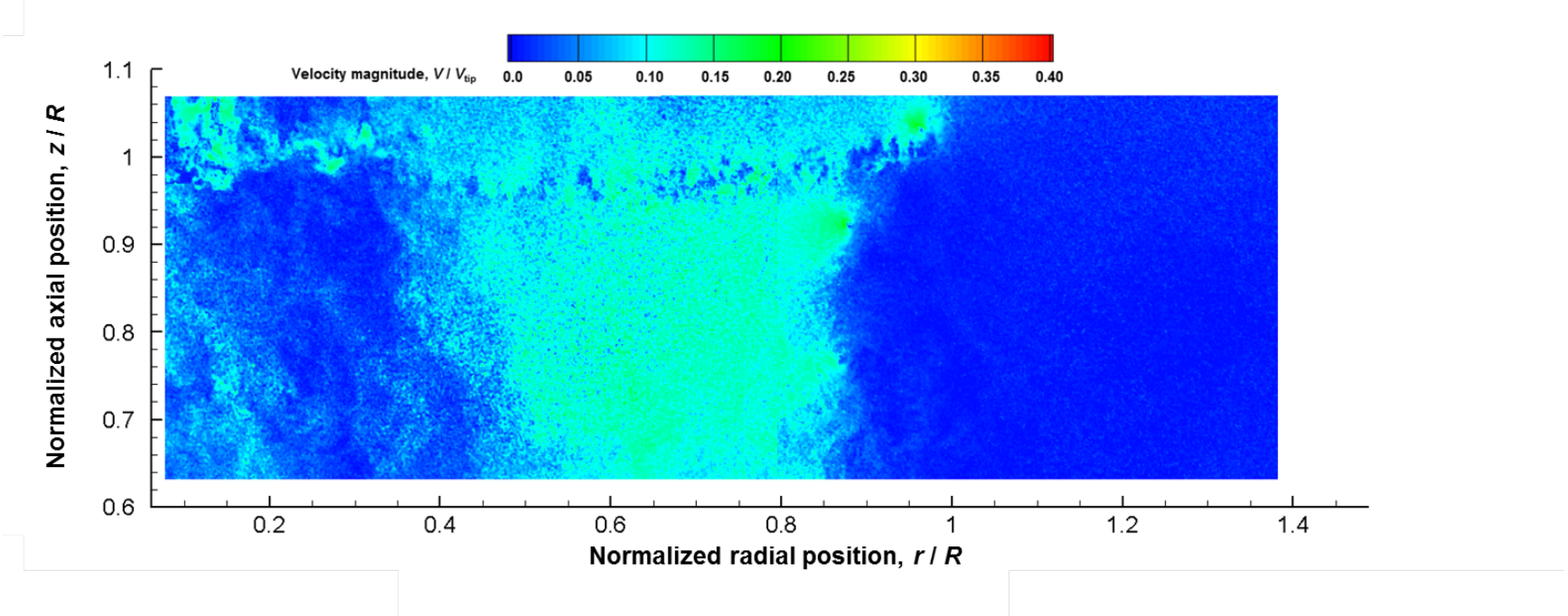

Figure 3.49: PIV measurements of the instantaneous realization of the flow field in ROIs 1 and 2 for the rotor with the twisted blades at a blade azimuth angle $\psi_b = 30°$. Background contours are of velocity magnitude.

by the red and blue vorticity contours, i.e., vorticity of clockwise and counterclockwise rotations, respectively, whereas the larger regions of concentrated vorticity were the tip vortices.

Compared to the rotor with untwisted blades, the twisted blades were noted to produce a wake sheet that contained more concentrated regions of vorticity. As previously discussed in Section 3.3.2.2, the use of blade twist tends to bias the bound circulation further inboard (see Fig. 3.14), which based on classical lifting-line theory [100], would be expected to trail more circulation into the wake sheet rather than it rolling up into the tip vortex.

When operating out of ground effect, the wake sheets trailed from both rotors were observed to quickly diffuse as they convected downstream in the rotor wake (discussed previously in Section 3.3.2.3 and shown in Fig. 3.21), with only smaller scale vorticity remaining after $\zeta = 30^{\circ}$. However, Figs. 3.50 and 3.51 show that when the rotor was operated in ground effect, the wake sheets trailed from both the untwisted and twisted blades contained regions of concentrated vorticity to much older wake ages.

As discussed previously in Section 3.4.1.2, sediment mobilization would be expected to occur when the near-wall flow velocities and corresponding shear stresses exceed the necessary threshold condition. These mobilized particles then have a tendency to saltate. However, the work by Johnson et al. [26] and Sydney et al. [3] documented that the uplift of most of the particles around a rotor was caused by the blade tip vortices interacting with the sediment bed. Specifically, the particles within the saltation layer were easily entrained by the upwash velocities induced by the tip vortices. Therefore, it was concluded that the generation of a brownout cloud was likely the result of both the

formation of a saltation layer initiated by the rotor downwash, as well as by the interaction of the blade tip vortices with that saltation layer.

Because the problem of brownout is linked to the structure of the near-wall vorticity, Figs. 3.52 and 3.53 show representative instantaneous realizations of the vorticity in ROIs 5 and 6 for both blade sets at a reference blade azimuth angle of $\psi_b = 30°$. A considerable amount of small scale vorticity in the wakes was observed inboard of the inner slipstream boundary (i.e., for $r/R \leq 0.6$). As previously discussed in Section 3.3.2.3, in ground effect the small scale vorticity that comprised the wake sheets was found to persist in the wake to older wake ages. Therefore, it would be expected that the small scale vorticity seen in Figs. 3.52 and 3.53 was conveyed there by the sheets. Furthermore, because the twisted blade initially trailed a more intense wake sheet (discussed in Section 3.3.2.3), the vorticity in the near-wall flow would be expected to have higher magnitudes as compared to the corresponding untwisted blade, as shown in Figs. 3.52 and 3.53.

As previously discussed, the formation of a brownout cloud results from the interaction of the tip vortices with the saltation layer along the ground [3, 26]. Specifically, the mobilized sediment along the ground becomes "trapped" in the higher velocities induced by the vortices and is suspended around the rotor. Therefore, the question becomes, how does the vorticity in the near-wall flow (as shown in Figs. 3.52 and 3.53) affect the wall-normal velocities?

To help answer this question, contours of the wall-normal velocity in ROIs 5 and 6 are shown in Figs. 3.54 and 3.55 for the untwisted and twisted blades, respectively. The tip vortices are identified in Figs. 3.54 and 3.55 by the red (upwash) and blue (downwash) pairs. While the tip vortices induced strong upwash velocities and, therefore, would

have the potential to uplift large amounts of previously mobilized sediment particles, the smaller scale vorticity (shown in Figs. 3.52 and 3.53) also induced significant upwash velocities, and also closer to the rotor; see Figs. 3.54 and 3.55.

As discussed previously and shown in Figs. 3.52 and 3.53, the convection of the wake sheets to the ground introduced a significant amount of vorticity into the near-wall flow field (see Figs. 3.54 and 3.55). It would be expected that the fluctuating velocities associated with the wake sheets could uplift sediment particles, and so will be a contributing mechanism to the problem of brownout. Without the flow fluctuations induced by the wake sheet, it is likely that the saltation layer would develop further downstream and, therefore, the initial uplift of particles would be further away from the rotor.

The impingement point of the inner slipstream boundary would also be expected to affect sediment mobilization and uplift. As discussed previously in Section 3.4.1.2, with the twisted blades the inner slipstream boundary impinged on the ground plane closer to the rotor, which would be expected to result in higher flow velocities along the ground closer to the rotor. The higher flow velocities is likely to cause sediment to be mobilized closer to the rotor, resulting in the earlier formation of a saltation layer. Therefore, the combination of the earlier formation of a saltation layer and the velocity fluctuations associated with the wake sheets (and the tip vortices) would be expected to uplift and suspend particles significantly closer to the rotor. It remains to be seen, however, if indeed this would be the actual outcome. Further studies using a ground plane covered with a mobile sediment bed and dual-phased flow measurements would provide further insight into this problem.

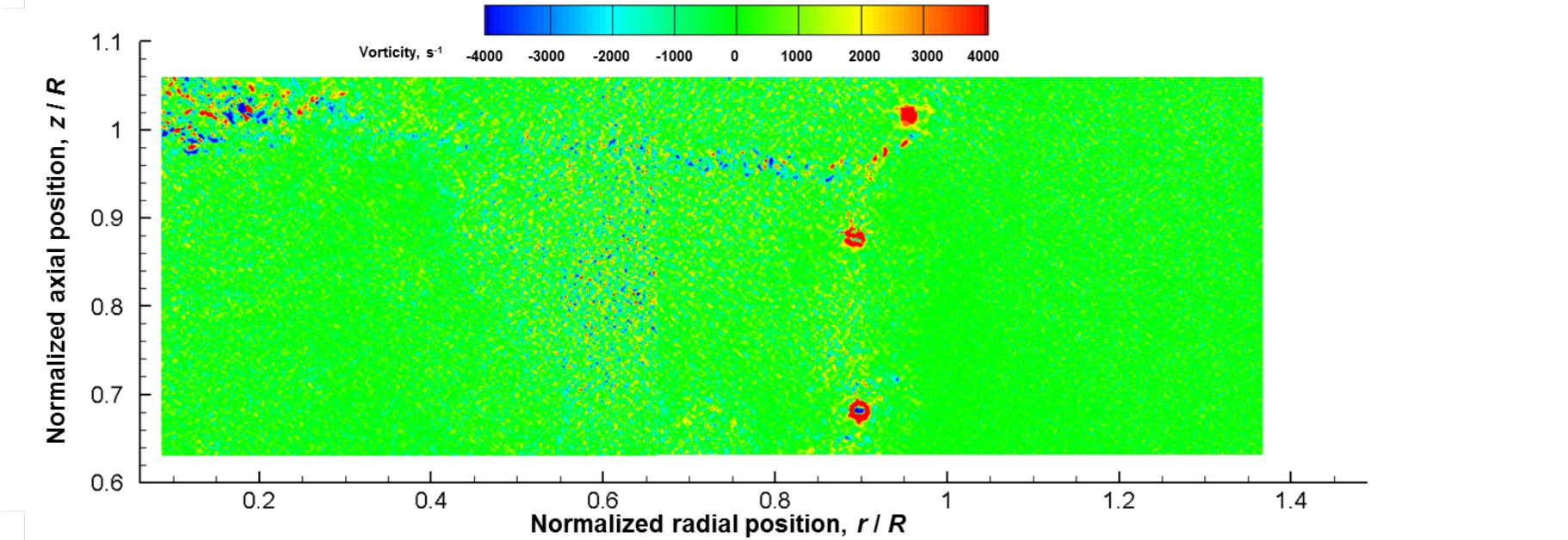

Figure 3.50: Instantaneous realization of the flow field in ROIs 1 and 2 for the rotor with the untwisted blades at a blade azimuth angle $\psi_b = 30°$. Background contours are of vorticity.

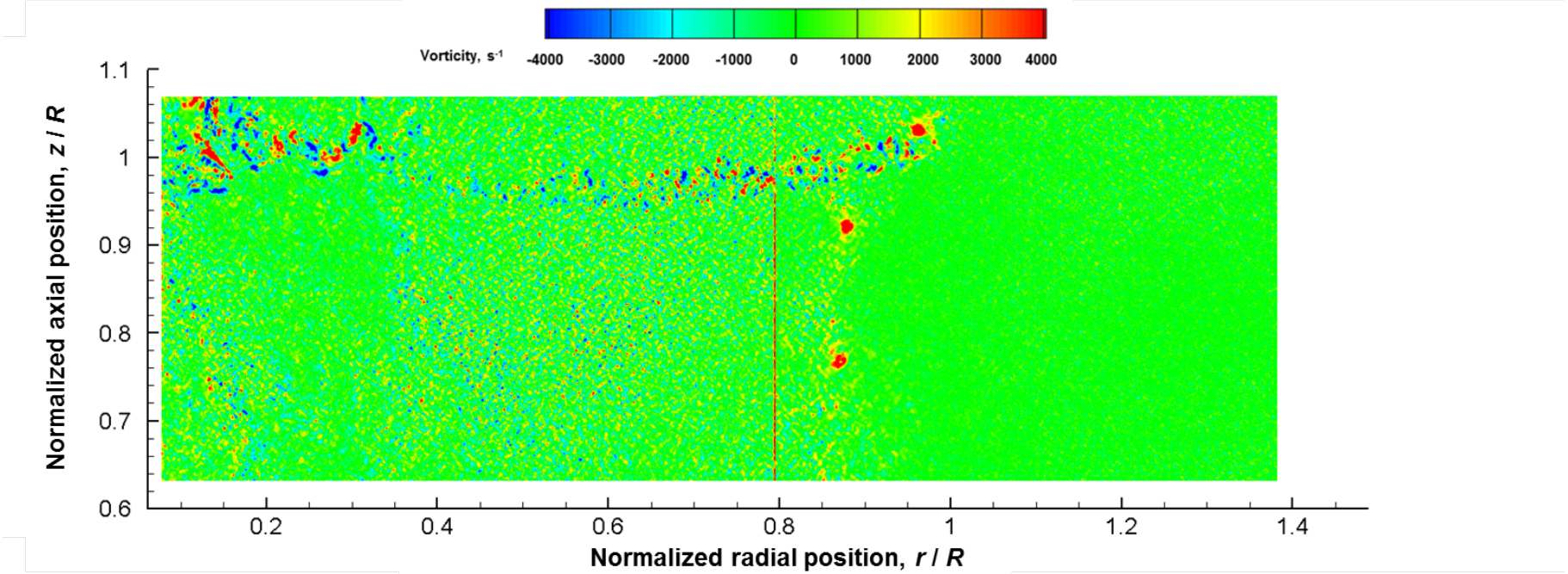

Figure 3.51: Instantaneous realization of the flow field in ROIs 1 and 2 for the rotor with the twisted blades at a blade azimuth angle ψ_b = 30°. Background contours are of vorticity.

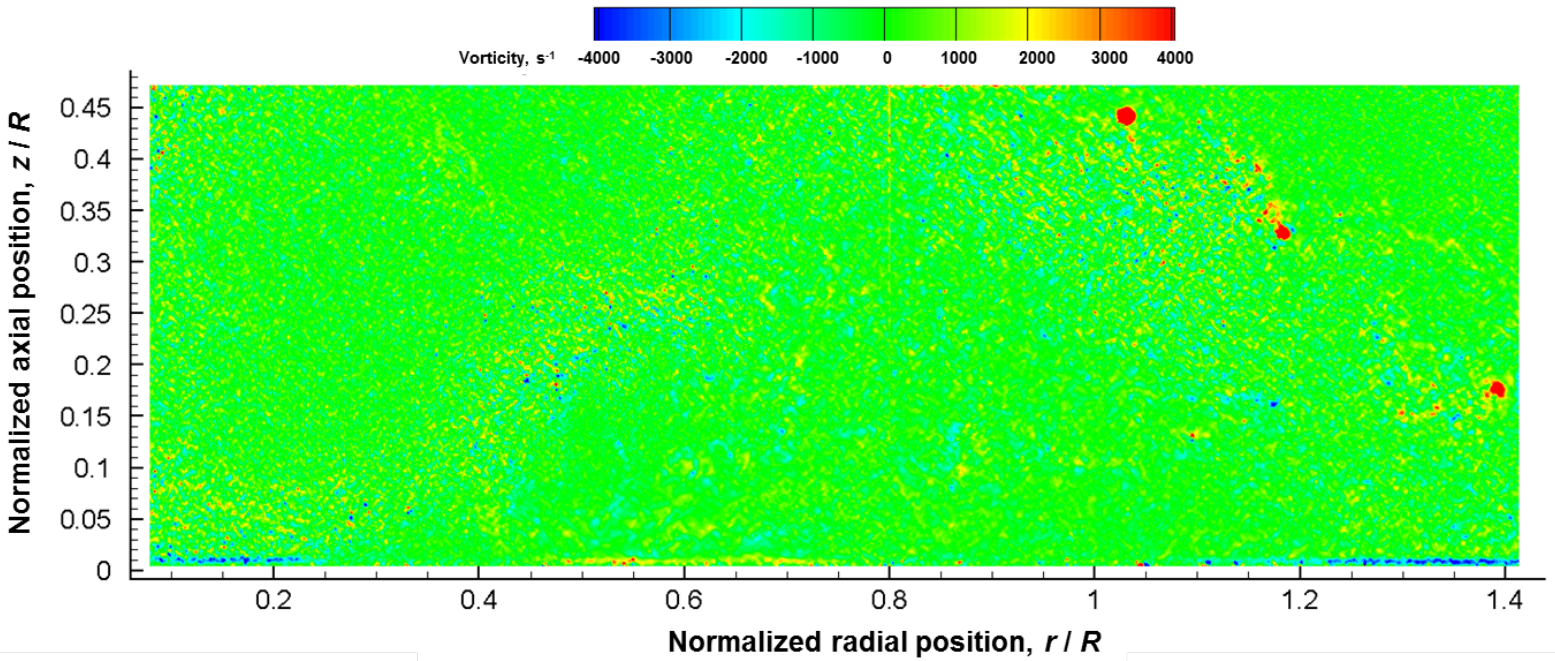

Figure 3.52: Instantaneous realization of the flow field in ROIs 5 and 6 for the rotor with the untwisted blades at a blade azimuth angle $\psi_b = 30°$. Background contours are of vorticity.

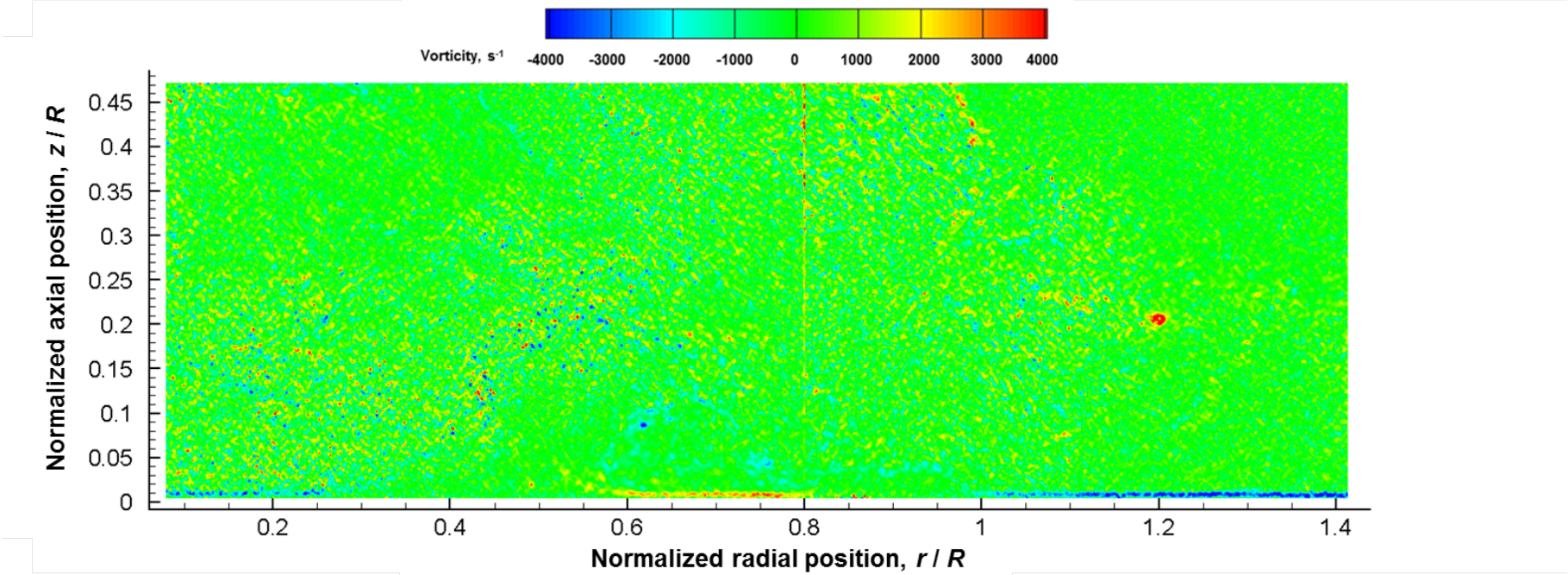

Figure 3.53: Instantaneous realization of the flow field in ROIs 5 and 6 for the rotor with the twisted blades at a blade azimuth angle ψ_b = 30°. Background contours are of vorticity.

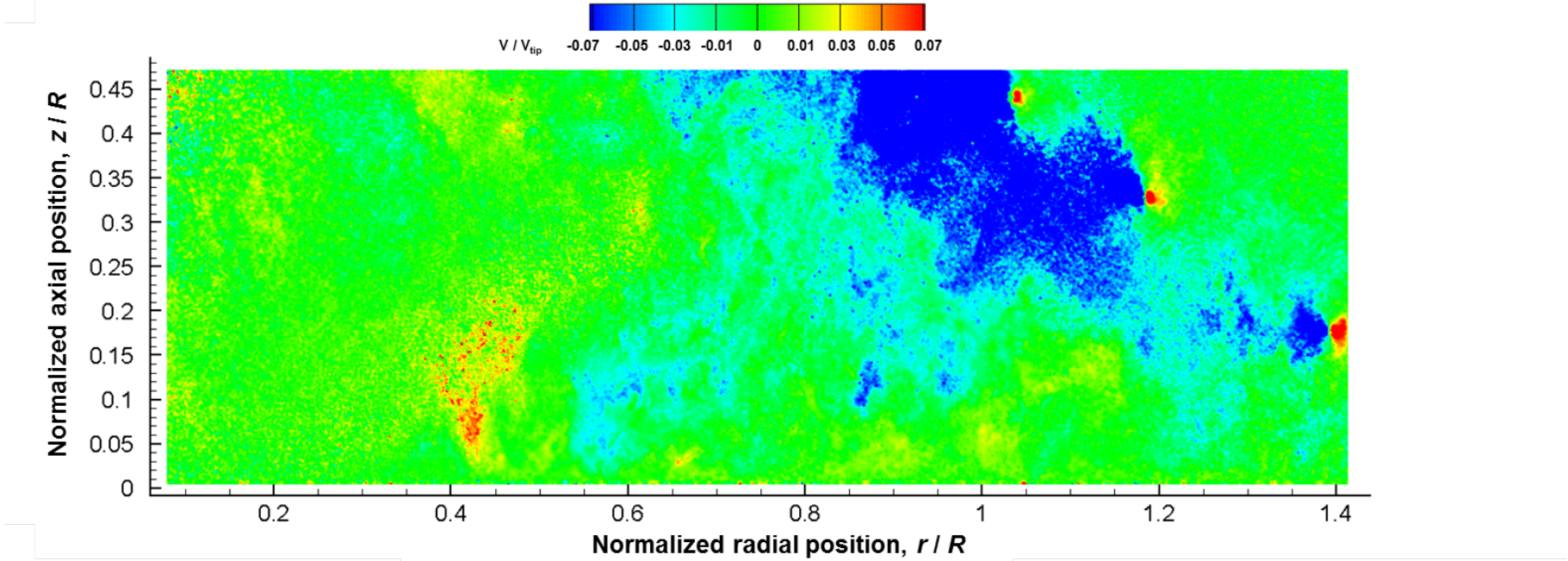

Figure 3.54: Instantaneous realization of the flow field in ROIs 5 and 6 for the rotor with the untwisted blades at a blade azimuth angle $\psi_b = 30°$. Background contours are of the wall-normal velocity.

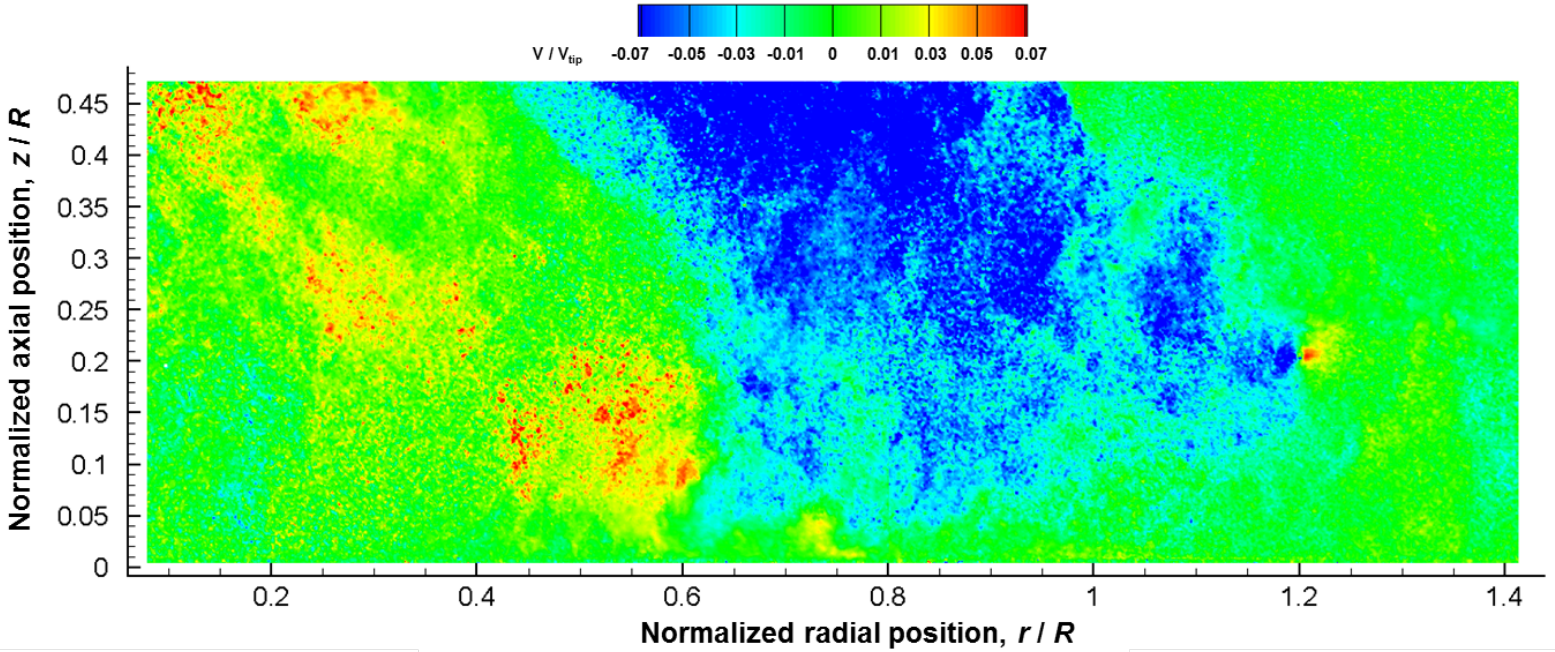

Figure 3.55: Instantaneous realization of the flow field in ROIs 5 and 6 for the rotor with the twisted blades at a blade azimuth angle ψ_b 30°. Background contours are of the wall-normal velocity.

Chapter 4

Conclusions

4.1 Conclusions

Detailed flow visualization and phase-resolved particle image velocimetry experiments were conducted on a two-bladed rotor that was operated in the hovering state, both out of ground effect and in ground effect. The measurements were complemented by rotor performance measurements (i.e., thrust and power as function of blade pitch angle) for several rotor heights off the ground. A specific goal of the work was to better understand the fluid dynamics of the turbulent wake sheets and their interactions with the blade tip vortices as they were laid down by the rotor blades.

A rotor system with two different blade sets were tested: 1. A baseline untwisted blade, 2. A twisted blade with -17° of linear twist measured from the rotational axis out to blade tip. For the out of ground effect experiments, each blade set was tested at two blade loading coefficients of 0.053 and 0.08, although only the higher loading condition was tested with the rotors operating in ground effect. Flow field measurements with high spatial resolution were made along the span of the blades, as well as in the vortex roll up region at the blade tip. Similar measurements were performed with the rotor operating in ground effect, but in this case additional measurements were made in intermediate zones between the rotor and the ground where the wake began to distort under the presence of the ground plane, as well as in the immediate near-wall region at the ground plane.

The following conclusions have been drawn from the research that was conducted:

1. Decreasing the rotor height above the ground resulted in a significant increase in the effective rotor efficiency, i.e., an increase in the power loading and effective values of the figure of merit of the rotor relative to operations out of ground effect. As the rotor height above the ground was decreased, the rotor with untwisted blades experienced the most significant increase in efficiency compared to the rotor with the twisted blades. This increased efficiency was shown to occur because of changes in the magnitude and distribution of the inflow induced at the blades because of the presence of the ground plane.

2. The wake sheets were found to contain relatively large amounts of concentrated vorticity at early wake ages just after they were formed behind the blades. In particular, the rotor with the twisted blades was found to produce somewhat stronger wake sheets compared to the untwisted blade. The instantaneous vorticity trailed into the wake sheets was shown to be comprised of small pairs of counterrotating vortices of unequal strength. However, the phase-averaged vorticity contained in the wake sheet followed the gradient of bound circulation along the blade as would be expected based on outcomes from classic lifting-line theory. The concentrated vorticity contained in the sheets quickly diffused as they were convected in the wake, but the small scale vorticity and turbulence in the sheets persisted to relatively old wake ages, even as far as the ground plane.

3. The breakdown of the wake sheet from regions of concentrated vorticity to that of small scale vorticity and turbulence was quantified in terms of a Richardson's

number. An examination of the variation in the Richardson's number across the core of a vortical element contained in the wake sheet at a relatively early wake ages showed that the majority of the core was above the laminar threshold and, therefore, would be expected to be laminar. However, by a wake age of $\zeta = 9^\circ$ less than half the core was above the threshold, which coincided with the transition of the vortical characteristics of the wake sheet into smaller scale vorticity and turbulence.

4. The use of blade twist was shown to modify the spanwise distribution of flow velocities in the rotor wake, resulting in a more uniform spanwise downwash distribution. On one hand, this more uniform downwash distribution resulted in the wake sheets being convected more uniformly and the tip vortices experiencing slower axial convection velocities. On the other hand, the rotor with the untwisted blades generated a more linear spanwise downwash distribution, which resulted in a much more non-uniform convection of the wake sheets, this effect also causing the axial spacing between successive turns of the sheets to be reduced.

5. The structure of the wake below the rotor disk was significantly affected by blade twist, with the slipstream boundary contracting more for the rotor with the twisted blades. Furthermore, the radial position of the tip vortices was shown to vary with both blade twist and rotor thrust. However, the axial locations showed smaller variations, which were associated with the differences in the axial convection velocity. Furthermore, the wake produced by the rotor with the twisted blades was found to impinge on the ground further inboard (i.e., closer to the rotor) than the corresponding wake produced by the untwisted blades. This outcome resulted in higher

flow velocities being produced on the ground plane closer to the rotor. Such differences could also be expected to change the nature of the brownout problem, i.e., the processes of sediment mobilization and uplift.

6. At early wake ages, sinusoidal wave-like disturbances were seen to form on the wake sheets, with the most significant perturbations being produced on the sheets laid down by the rotor with the twisted blades. This wave initially grew in magnitude as it developed in the wake, but the wave amplitude was limited as the sheet convected axially and was stretched by the velocity gradients in the downstream wake. However, when the rotors were operated in ground effect, this wave-like perturbation was not observed to form. In this case, the radial stretching of the wake sheet under the presence of the ground was the source of the change in the behavior, which suppressed the natural tendency of the sheet to develop waves.

7. The tip vortex from the untwisted blade was found to roll up significantly earlier than the corresponding vortex trailed from the twisted blade. Once fully rolled up, the tip vortices from the untwisted blades were found to contain more circulation compared to the twisted blades. These differences can be attributed to the differences in the distribution of bound circulation along the different blades and especially the magnitude and distribution of the peak loading near the blade tip.

4.2 Suggestions for Future Work

This dissertation has documented a systematic study into the fluid dynamics of the wake sheets trailed from a rotor, and has provided an improved understanding into the

structure, development and evolution of these wake sheets. The detailed structure of the wake sheet as it interacted with a ground plane has also been documented, showing the importance of the vorticity contained in the wake sheets as it influenced the flow developments near the ground. However, there are still several areas of further research and investigation that could be pursued to further the work that has been described in this dissertation.

1. While the vorticity in the wake sheets was weaker compared to that contained in the blade tip vortices, this vorticity contributed significantly to the flow environment at the ground. Therefore, to fully predict the development of the rotor wake, the flow conditions at the ground and the problem of brownout, the vorticity contained in the wake sheets must be properly accounted for. Specifically, from a CFD perspective, grids with the necessary resolution will be required to fully resolve this vorticity, as well as to preserve the vorticity to the relatively old wake ages where the interactions with the ground actually occur. Because of the high spatial resolution of the measurements in the current work, the measurements can be used to help in the validation of new and existing models, as well as to provide insight into the regions of the rotor wake that may require special types of grids.

2. Grid-based RANS methods also require turbulence models to provide closure to the governing equations. However, current models are developed based on assumptions that are not necessarily representative of the flow field induced by a rotor. The present work has resolved the structure of the small scale vortical flows found in the wake induced by a rotor, which was hovering both out of ground effect and in

ground effect. It is possible that these new data can aid in the validation of models that better represent the physical aspects of the flow fields generated by rotors.

3. The current work has also shown that while the outboard portion of the wake sheet becomes rolled up into the developing tip vortex, the inboard sections of the sheet remained as such to relatively older wake ages and, therefore, will affect the downstream wake and near-wall flow field. This observation brings into question the assumption made in most free-vortex methods that the planar wake sheets roll up into an outboard tip vortex after some predetermined wake age. Therefore, there is a need to determine the effect this assumption has on the modeling of the near-wall flow field as well as the overall development of the rotor wake. The measurements made in the present work may also aid in the validation and development of improved free-vortex wake models.

4. While the high spatial resolution measurements obtained in the present work has provided significant insight into the structure of the wake sheets and their interactions with the tip vortices, these interactions are rather complex and not easily generalized, i.e., they depend not only on the blade shape but also the specific operating state of the rotor, i.e., the rotor thrust, blade loading coefficient, tip speed, etc. With the current rate of advancement of measurements technology it may soon be possible to obtain a full time-history of the development and interaction of the wake sheets and tip vortices while also maintaining the necessary spatial resolution to fully resolve the small scale vortical structures contained in the sheets. Such an ability would yield significant further insight into the development and evolution of

the rotor wake, as well as perhaps the problem of brownout if dual-phase (including the dust) measurements can be performed.

5. The structure and evolution of the wake sheets and their contribution to the near-wall flow field has been quantified in the present work. However, the majority of the dual-phase fluid dynamic research has been preformed on smaller scale laboratory rotors compared to the somewhat larger (albeit still small-scale) rotor used in the current work. There is a clear need to understand how the structure, development, and evolution of the wake sheet scales with rotor size (i.e., blade chord Reynolds number, tip Mach number, vortex Reynolds number, etc.).

6. While the ability to quantify the turbulence contained in the wake sheet would provide further insight into the evolution of the rotor wake, the inherent aperiodicity in the wake makes the determination of the turbulence statistics extremely difficult. Therefore, there will be a need to develop new aperiodicity correction techniques that are capable of correcting for the varying spatial aperiodicity of the vortex sheets along their lengths.

7. The current work has documented the fluid dynamics of the wake sheets trailed from a rotor operating both in and out of ground effect, as well as the wake sheets affect on the near-wall flow field. However, the present measurements were unable to quantify the effect the wake sheet might have on sediment mobilization. Although a ambitious task for a rotor even at small-scale, complete dual-phase measurements will be required to quantify the effect of the wake sheet on sediment mobilization and brownout.

Appendix A

Algorithm used to Calculate the Circulation

In previous work [23], the circulation was obtained through the evaluation of a line integral around a path enclosing the flow feature (see Fig. A.1), i.e.,

$$\Gamma_v = \oint \vec{V} \cdot d\vec{s} \tag{A1}$$

where $\vec{V}$ is the velocity field (obtained using PIV) and $d\vec{s}$ is the line segment directed along the path of integration. A rectangular grid was utilized for convenience because it coincided with the PIV grid [23]. For the current measurements this method was not ideal because the vortices varied in size and shape as well as being too closely spaced; see Fig. A.2. However using Stokes' theorem, the line integral of velocity around a closed path can be converted into an area integral of vorticity, i.e.,

$$\Gamma_v = \oint_C \vec{V} \cdot d\vec{s} = \iint_A \vec{\omega} \cdot \vec{n}\, dA \tag{A2}$$

where $\vec{V}$ is the velocity field obtained using PIV, $d\vec{s}$ is the directed line segment, $\vec{\omega}$ is the vorticity field, $\vec{n}$ is a unit normal vector, and dA is an incremental area. The vorticity field was calculated from the gradients of the PIV velocity field using the 4-point central differencing method given by

$$\left(\frac{du}{dx}\right)_n = \frac{-2u_{n-2} - u_{n-1} + u_{n+1} + 2u_{n+2}}{10\Delta x} \tag{A3}$$

$$\left(\frac{du}{dy}\right)_n = \frac{-2u_{n-2} - u_{n-1} + u_{n+1} + 2u_{n+2}}{10\Delta y} \tag{A4}$$

$$\left(\frac{dv}{dx}\right)_n = \frac{-2v_{n-2} - v_{n-1} + v_{n+1} + 2v_{n+2}}{10\Delta x} \tag{A5}$$

$$\left(\frac{dv}{dy}\right)_n = \frac{-2v_{n-2} - v_{n-1} + v_{n+1} + 2v_{n+2}}{10\Delta y} \tag{A6}$$

where u and v are the velocities in the horizontal and vertical directions, Δx and Δy are the distances between adjacent measurement points in the horizontal and vertical directions, and n is the measurement point being evaluated. The calculated velocity gradients were used to determine the vorticity field in the z, r plane using

$$\omega = \frac{dv}{dr} - \frac{du}{dz} \tag{A7}$$

To identify the tip vortices as well as the vortices contained in the wake, a vorticity thresholding method was implemented. This algorithm identified all the points above the given vorticity threshold, and grouped connected points into distinct vortices. Their corresponding circulation was then calculated using the discretized form of Eq. A2 given by

$$\Gamma_v = \iint_A \vec{\omega} \cdot \vec{n}\, dA = \sum_i \sum_j \omega_{ij}\, \Delta r_{ij}\, \Delta z_{ij} \tag{A8}$$

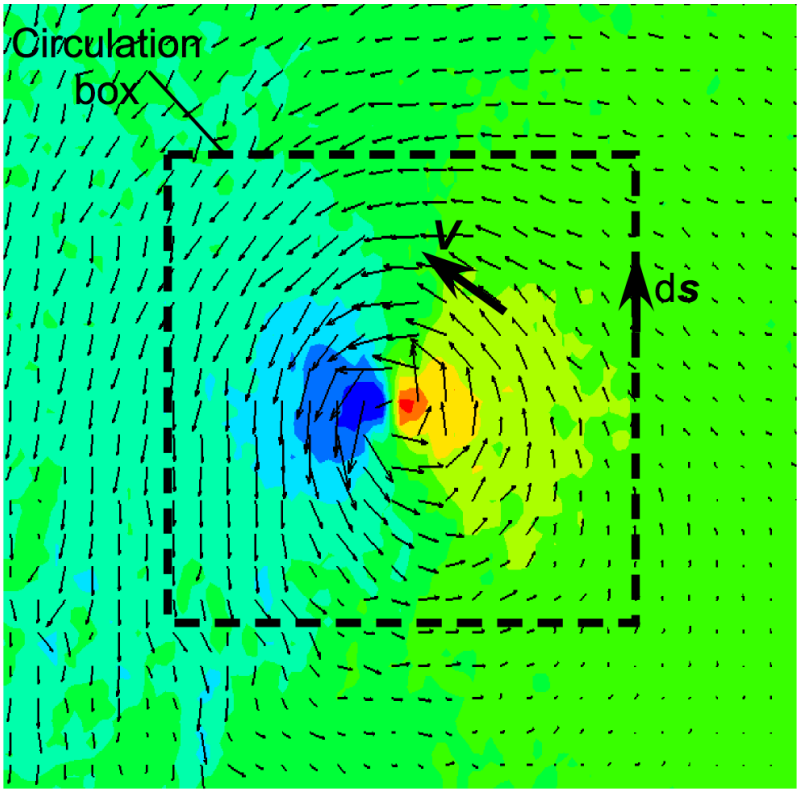

Figure A.1: Path enclosing a tip vortex utilized for evaluating the line integral.

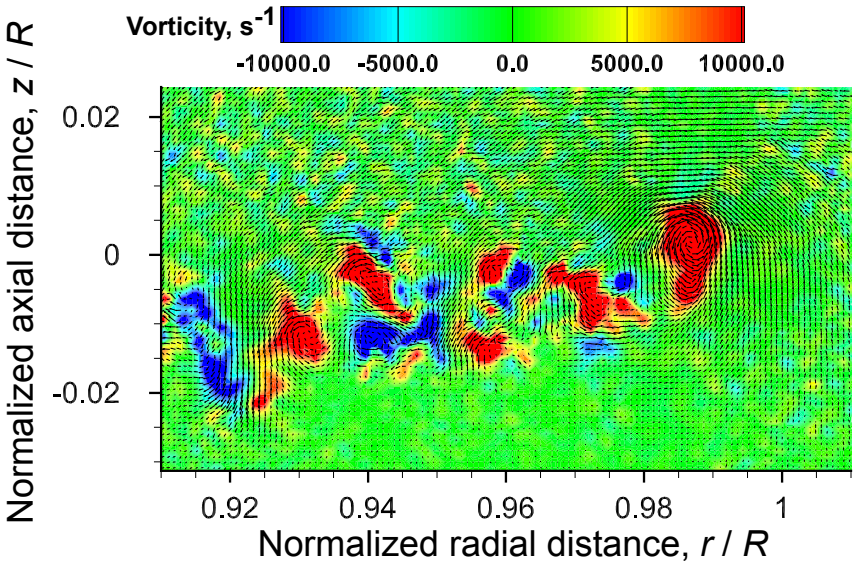

Figure A.2: Contours of instantaneous vorticity near the tip of the twisted blades when operating at $C_T/\sigma = 0.080$.

Appendix B

Q-criterion Algorithm

The Q-criterion is defined as the discriminant of the velocity gradient tensor as given by

$$Q = \frac{1}{4}S^2 - q \tag{B1}$$

where S is the trace of the velocity gradient tensor given by

$$S = \frac{\partial u}{\partial x} + \frac{\partial v}{\partial x} \tag{B2}$$

and q is the determinant of the velocity gradient tensor given by

$$q = \frac{\partial u}{\partial x}\frac{\partial v}{\partial y} - \frac{\partial u}{\partial y}\frac{\partial v}{\partial x} \tag{B3}$$

The velocity gradients were calculated using 4-point central differencing method given by

$$\left(\frac{du}{dx}\right)_n = \frac{-2u_{n-2} - u_{n-1} + u_{n+1} + 2u_{n+2}}{10\Delta x} \tag{B4}$$

$$\left(\frac{du}{dy}\right)_n = \frac{-2u_{n-2} - u_{n-1} + u_{n+1} + 2u_{n+2}}{10\Delta y} \tag{B5}$$

$$\left(\frac{dv}{dx}\right)_n = \frac{-2v_{n-2} - v_{n-1} + v_{n+1} + 2v_{n+2}}{10\Delta x} \tag{B6}$$

$$\left(\frac{dv}{dy}\right)_n = \frac{-2v_{n-2} - v_{n-1} + v_{n+1} + 2v_{n+2}}{10\Delta y} \tag{B7}$$

where u and v are the velocities in the horizontal and vertical directions, Δx and Δy are the distances between adjacent measurement points in the horizontal and vertical directions, and n is the measurement point being evaluated. The calculated gradients were then used

to determine q and S. With the determinant of the velocity gradient tensor and trace of the velocity gradient tensor a value of Q at every measurement point could be determined. Typically, a maximum value of Q corresponded to the center of the vortex core.

Bibliography

[1] Warren, T., Hong, S. C., Yu, C. J., and Rosenzweig, E. L., "Enhanced Erosion Protection for Rotor Blades," 65th Annual Forum Proceedings of the American Helicopter Society, Grapevine, TX, May 27–29, 2009.

[2] Lee, T. E., Leishman, J. G., and Ramasamy, M., "Fluid Dynamics of Interacting Blade Tip Vortices With a Ground Plane," *Journal of the American Helicopter Society*, Vol. 55, No. 2, April 2010, pp. 1–16.

[3] Sydney, A., Baharani, A., and Leishman, J. G., "Understanding Brownout using Near-Wall Dual-Phase Flow Measurements," 67th Annual Forum Proceedings of the American Helicopter Society, Virginia Beach, VA, May 3–5, 2011.

[4] Abbott, I. H., and Von Doenhoff, A. E., *Theory of Wing Sections,* Dover Publications Inc., New York, NY, 1949.

[5] Vatistas, G. H., Kozel, V., and Mih, W. C., "A Simpler Model for Concentrated Vortices," *Experiments in Fluids*, Vol. 11, No. 1, 1991, pp. 73–76.

[6] Tritschler, J., Syal, M., Celi, R., and Leishman, J. G., "A Methodology for Rotor Design Optimization for Rotorcraft Brownout Mitigation," 66th Annual Forum Proceedings of the American Helicopter Society, Phoenix, AZ, May 10–13, 2010.

[7] Tritschler, J., Syal, M., Celi, R., and Leishman, J. G., "The Effect of Number of Blades on Optimum Rotor Design for Brownout Mitigation," Future Vertical Lift Aircraft Design Conference, San Francisco, CA, January 18–20, 2012.

[8] Mapes, P., Kent, R., and Wood, R., "DoD Helicopter Mishaps FY85-05: Findings and Recommendations," U.S. Air Force, Washington, DC April, 2008.

[9] National Transportation Safety Board, NTSB Accident Briefs: LAX01LA283, LAX01LA304, LAX04LA285, SEA05CA173.

[10] Jansen, C., Wennemers, A., and Groen, E., "FlyTact: A Tactile Display Improves a Helicopter Pilots Landing Performance in Degraded Visual Environments," *Haptics: Perception, Devices and Scenarios*, Vol. 502, No. 4, 2008, pp. 867–875.

[11] "Sandblaster 2 Support of See-Through Technologies for Particulate Brownout," Task 1 Technical Report, Sponsored by Defense Advanced Research Projects Agency (DOD) Strategic Technology Office, Issued by U.S. Army Aviation and Missile Command under Contract No. W31P4Q-07-C-0215, MRI Project No. 110565, October 31, 2007.

[12] "Sandblaster 2 Support of See-Through Technologies for Particulate Brownout," Task 5 Final Technical Report, Sponsored by Defense Advanced Research Projects Agency (DOD) Strategic Technology Office, Issued by U.S. Army Aviation and Missile Command under Contract No. W31P4Q-07-C-0215, MRI Project No. 110565, October 31, 2007.

[13] Pickford, M., "Operating Helicopters Safely in a Degraded Visual Environment in Support of Military Operations," Proceedings of the Royal Aeronautical Society Rotorcraft Group Conference, Operating Helicopters Safely in a Degraded Visual Environment, London, UK, June 16 & 17, 2010.

[14] Milluzzo, J., and Leishman, J. G., "Assessment of Rotorcraft Brownout Severity in Terms of Rotor Design Parameters," *Journal of the American Helicopter Society*, Vol. 55, No. 3, October 2010, pp. 032009–1–032009–9.

[15] Leishman, J. G., "Challenges in Understanding the Fluid Dynamics of Brownout: Review and Update," Proceedings of the AHS International Meeting on Advanced Rotorcraft Technology and Safety Operations, Omiya, Japan, November 1–3, 2010.

[16] Knight, M., and Hefner, R. A., "Analysis of Ground Effect on the Lifting Airscrew," NACA TN 835, 1941.

[17] Zbrozek, J., "Ground Effect on the Lifting Rotor," British ARC R&M 2347, 1947.

[18] Cheeseman, I. C., and Bennett, W. E., "The Effect of the Ground on a Helicopter Rotor in Forward Flight," British ARC R&M 3021, 1955.

[19] Fradenburgh, E. A., "The Helicopter and the Ground Effect Machine," *Journal of the American Helicopter Society*, Vol. 5, No. 4, 1960, pp. 26–28.

[20] Hayden, J. S., "The Effect of the Ground on Helicopter Hovering Power Required," American Helicopter Society 32th Annual National V/STOL Forum Proceedings, Washington DC, May 10–12, 1976.

[21] Prouty, R. W., "Ground Effect and the Helicopter," AIAA Paper 85-4034, AIAA/AHS/ASEE Aircraft Design Systems and Operations Meeting, Colorado Springs, CO, October 14–16, 1985.

[22] Ramasamy, M., Johnson, B., and Leishman, J. G., "Turbulent Tip Vortex Measurements Using Dual-Plane Stereoscopic Particle Image Velocimetry," *AIAA Journal*, Vol. 47, No. 8, 2009, pp. 1826–1840.

[23] Milluzzo, J., Sydney, A., Rauleder, J., and Leishman, J. G., "In-Ground-Effect Aerodynamics of Rotors with Different Blade Tips," 66th Annual Forum Proceedings of the American Helicopter Society, Phoenix, AZ, May 10–13, 2010.

[24] Ramasamy, M., and Leishman, J. G., "Interdependence of Diffusion and Straining of Helicopter Blade Tip Vortices," *Journal of Aircraft*, Vol. 41, No. 5, September 2004, pp. 1014–1024.

[25] Ananthan, S., Leishman, J. G., and Ramasamy, M., "The Role of Filament Stretching in the Free-Vortex Modeling of Rotor Wakes," American Helicopter Society International 58th Annual Forum Proceedings, Montréal, Canada, June 11–13, 2002.

[26] Johnson, B., Leishman, J. G., and Sydney, A., "Investigation of Sediment Entrainment Using Dual-Phase, High-Speed Particle Image Velocimetry," *Journal of the American Helicopter Society*, Vol. 55, No. 4, 2010, pp. 1–16.

[27] Curtiss, H. C., Sun, M., Putman, W. F., and Hanker, E. J., "Rotor Aerodynamics in Ground Effect at Low Advance Ratios," *Journal of the American Helicopter Society*, Vol. 29, No. 1, 1984, pp. 48–55.

[28] Nathan, N. D., and Green, R. B., "Measurements of a Rotor Flow in Ground Effect and Visualisation of the Brown-out Phenomenon," American Helicopter Society 64th Annual Forum Proceedings, Montréal, Canada, April 29–May 1, 2008.

[29] Phillips, C., and Brown, R.E., "Eulerian Simulation of the Fluid Dynamics of Helicopter Brownout," *Journal of Aircraft*, Vol. 46, No. 4, July 2009, pp. 1416–1429.

[30] Bagnold, R. A., *The Physics of Blown Sand and Desert Dunes,* Dover Publications, Inc., Mineola, NY, 1941.

[31] Greeley, R., "Saltation Impact as a Means for Raising Dust on Mars," *Planetary and Space Sciences*, Vol. 50, No. 2, February 2002, pp. 151–155.

[32] Rauleder, J., and Leishman, J. G., "Measurements of the Turbulent Flow Environment on the Ground Below a Hovering Rotor," 37th European Rotorcraft Forum, Gallarate, Italy, September 13–15, 2011.

[33] Rauleder, J., and Leishman, J. G., "Measurements of Organized Turbulence in the Dual-Phase Flow Below a Rotor," 38th European Rotorcraft Forum, The Netherlands, September 4–7, 2012.

[34] Drees, J. M., and Hendal, W. P., "The Field of Flow Through a Helicopter Rotor Obtained from Wind Tunnel Smoke Tests," *Journal of Aircraft Engineering*, Vol. 23, No. 266, 1950, pp. 107–111.

[35] Gray, R. B., "An Aerodynamic Analysis of a Single Bladed Rotor in Hovering and Low Speed Forward Flight as Determined from Smoke Studies of the Vorticity Distribution in the Wake," Princeton University Report No. 356, 1956.

[36] Landgrebe, A. J., "An Analytical Method for Predicting Rotor Wake Geometry," *Journal of the American Helicopter Society*, Vol. 14, No. 4, 1969, pp. 20–32.

[37] Landgrebe, A. J., "An Analytical and Experimental Investigation of Helicopter Rotor Performance and Wake Geometry Characteristics," USAAMRDL TR 24, 1971.

[38] Landgrebe, A. J., "The Wake Geometry of a Hovering Rotor and Its Influence on Rotor Performance," *Journal of the American Helicopter Society*, Vol. 17, No. 4, 1972, pp. 2–15.

[39] Kocurek, J. D. and Tangler, J. L., "A Prescribed Wake Lifting Surface Hover Performance Analysis," *Journal of the American Helicopter Society*, Vol. 21, No. 1, 1976, pp. 24–35.

[40] Caradonna, F. X., and Tung, C., "Experimental and Analytical Studies of a Model Helicopter Rotor in Hover," Proceedings of the 7th European Rotorcraft Forum, Garmisch-Partenkirchen, Germany, September 22–25, 1980.

[41] Egolf, T. A., and Landgrebe, A. J., "Helicopter Rotor Wake Geometry and its Influence in Forward Flight, Vol. 1 – Generalized Wake Geometry and Wake Effects in Rotor Airloads and Performance," NACA CR-3726, October 1983.

[42] Lorber, P. F., Stauter, R. C., Pollack, M. J., and Landgrebe, A. J., "A Comprehensive Hover Test of the Airloads and Airflow of an Extensively Instrumented Model Helicopter Rotor," Vol. 1–5, USAAVSCOM TR-D-16 (A-E), October 1991.

[43] Martin, P. B., Bhagwat, M. J., and Leishman, J. G., "Strobed Laser-Sheet Visualization of a Helicopter Rotor Wake," *Journal of Flow Visualization and Image Processing*, Vol. 7, No. 1, 2000, pp. 34–54.

[44] Bhagwat, M. J., and Leishman, J. G., "Stability Analysis of Helicopter Rotor Wakes in Axial Flight," *Journal of the American Helicopter Society*, Vol. 45, No. 3, July 2000, pp. 165–178.

[45] Fradenburg, E. A., "Aerodynamic Factors Influencing Overall Hover Performance," AGARD-CP 111, 1972.

[46] Curtiss, H. C., Erdman, W., and Sun, M., "Ground Effect Aerodynamics," *Vertica*, Vol. 11, No. (1/2), 1987, pp. 29–42.

[47] Light, J. S., and Norman, T., "Tip Vortex Geometry of a Hovering Helicopter Rotor in Ground Effect," American Helicopter Society 45th Annual Forum Proceedings, Boston, MA, May 22–24, 1989.

[48] Ramasamy, M., Johnson, B., Huismann, T., and Leishman, J. G., "Digital Particle Image Velocimetry Measurements of Tip Vortex Characteristics Using an Improved Aperiodicity Correction," *Journal of the American Helicopter Society*, Vol. 54, No. 1, 2009, pp. 1–13.

[49] Baharani, A., "Investigation into the Effects of Aeolian Scaling Parameters on Sediment Mobilization Below a Hovering Rotor," M.s. thesis, Department of Aerospace Engineering, University of Maryland, College Park, MD, 2011.

[50] Tung, C., Pucci, S. L., Caradonna, F. X., and Morse, H. A., "The Structure of Trailing Vortices Generated by Model Helicopter Rotor Blades," NACA TM 81316, 1981.

[51] Hoffman, E. R., and Joubert, P. N., "Turbulent Line Vortices," *Journal of Fluid Mechanics*, Vol. 16, No. 3, 1963, pp. 395–411.

[52] Martin, P. B., and Leishman, J. G., "Trailing Vortex Measurements in the Wake of a Hovering Rotor with Various Tip Shapes," American Helicopter Society 58th Annual Forum Proceedings, Montréal, Canada, June 11–13, 2002.

[53] Bradshaw, P., "The Analogy Between Streamline Curvature and Buoyancy in Turbulent Shear Flows," *Journal of Fluid Mechanics*, Vol. 36, No. 1, March 1969, pp. 177–191.

[54] Holzapfel, A. Hofbauer, T., Gerz, T., and Schumann, U., "Aircraft Wake Vortex Evolution and Decay in Idealized and Real Environments: Methodologies, Benefits and Limitations," Proceedings of the Euromech Colloquium, Munich, Germany, October 4–6, 2000.

[55] Cotel, A. J., and Breidenthal, R. E., "Turbulence Inside a Vortex," *Physics of Fluid*, Vol. 11, No. 10, 1999, pp. 3026–3029.

[56] Cotel, A. J., "Turbulence Inside a Vortex: Take Two," *Physics of Fluid*, Vol. 14, No. 8, 2002, pp. 2933–2934.

[57] Leishman, J. G., Martin, P. B., and Pugliese, G., "High Resolution Trailing Vortex Measurements in the Wake of a Hovering Rotor," *Journal of the American Helicopter Society*, Vol. 48, No. 1, 2003, pp. 39–52.

[58] Ramasamy, M., and Leishman, J. G., "A Generalized Model for Transitional Blade Tip Vortices," *Journal of the American Helicopter Society*, Vol. 51, No. 1, January 2006, pp. 92–103.

[59] Squire, H. B., "The Growth of a Vortex In Turbulent Flow," *Aeronautical Quarterly*, Vol. 16, No. 3, 1965, pp. 302–306.

[60] Bhagwat, M. J., and Leishman, J. G., "Measurements of Bound and Wake Circulation on a Helicopter Rotor," *Journal of Aircraft*, Vol. 37, No. 2, 2000, pp. 227–234.

[61] McAlister, K., "Rotor Wake Development During the First Revolution," *Journal of the American Helicopter Society*, Vol. 49, No. 4, October 2004, pp. 371–390.

[62] Gupta, B. P., and Lowey, R. G., "Theoretical Analysis of the Aerodynamic Stability of Multiple Interdigitated Helical Vortices," *AIAA Journal*, Vol. 12, No. 10, 1974, pp. 1382–1387.

[63] Leishman, J. G., *Principles of Helicopter Aerodynamics 2nd Edition* Cambridge University Press, New York, NY, 2006.

[64] McAlister, K. W., "Measurements in the Near Wake of a Hovering Rotor," Proceedings of the 27th AIAA Fluid Dynamic Conference, New Orleans LA, June 18–20, 1996.

[65] Ramasamy, M., Gold, N. P., and Bhagwat, M. J., "Rotor Hover Performance and Flowfield Measurements with Untwisted and Highly-Twisted Blades," European Rotorcraft Forum 36th Annual Forum Proceedings, Paris, France, September 7–9, 2010.

[66] Brown, R. E., and Whitehouse, G. R., "Modelling Rotor Wakes in Ground Effect," *Journal of the American Helicopter Society*, Vol. 49, No. 3, 2004, pp. 238–249.

[67] Ryerson, C. C., Haehnel, R. B., Koenig, G. G., and Moulton, M. A., "Visibility Enhancement in Rotorwash Clouds," Paper AIAA-2005-263, 43rd AIAA Aerospace Sciences Meeting and Exhibit, Reno, NV, January 10–13, 2005.

[68] Wenren, Y, Walter, J., Fan, M., and Steinhoff, J., "Vorticity Confinement and Advanced Rendering to Compute and Visualize Complex Flows," Paper AIAA-2006-945, 44th AIAA Aerospace Sciences Meeting and Exhibit, Reno, NV, January 9–12, 2006.

[69] Haehnel, R. B., Moulton, M. A., Wenren, W., and Steinhoff, J., "A Model to Simulate Rotorcraft-Induced Brownout," American Helicopter Society 64th Annual Forum Proceedings, Montréal, Canada, April 29–May 1, 2008.

[70] D'Andrea, A., "Numerical Analysis of Unsteady Vortical Flows Generated by a Rotorcraft Operating on Ground: A First Assessment of Helicopter Brownout," American Helicopter Society 65th Annual Forum Proceedings, Grapevine, TX, May 27–29, 2009.

[71] Wachspress, D., A., Whitehouse, G., R., Keller, J., D., and Yu, H., "A High Fidelity Brownout Model for Real-Time Flight Simulations and Trainers," 65th Annual Forum Proceedings of the American Helicopter Society, Grapevine, TX, May 27–29, 2009.

[72] Syal, M., Govindarajan, B., and Leishman, J. G., "Mesoscale Sediment Tracking Methodology to Analyze Brownout Cloud Developments," 66th Annual Forum of the American Helicopter Society, Phoenix, AZ, May 10–13, 2010.

[73] Syal, M., and Leishman, J. G., "Predictions of Brownout Dust Clouds Compared to Photogrammetric Measurements," *Journal of the American Helicopter Society*, Vol. 58, No. 1, 2013, pp. 1–18.

[74] Kalra, T., Lakshminarayan, V., and Baeder, J., "CFD Validation of Micro Hovering Rotor in Ground Effect," 66th Annual Forum Proceedings of the American Helicopter Society, Phoenix, AZ, May 11–13, 2010.

[75] Thomas, S., Lakshminarayan, V. K., Kalra, T. S., and Baeder, J. D., "Eulerian-Lagrangian Analysis of Cloud Evolution using CFD Coupled with a Sediment Tracking Algorithm," 67th Annual Forum Proceedings of the American Helicopter Society, Virginia Beach, VA, May 3–5, 2011.

[76] Wachspress, D. A., Quackenbush, T. R., and Boschitsch, A. H., "First-Principles Free-Vortex Wake Analysis for Helicopters and Tiltrotors," American Helicopter Society 59th Annual Forum Proceedings, Phoenix, AZ, May 6–8, 2003.

[77] Bagai, A., and Leishman, J. G., "Rotor Free-Wake Modeling using a Pseudoimplicit Relaxation Algorithm," *Journal of Aircraft*, Vol. 32, No. 6, November–December, 1995, pp. 1276–1285.

[78] Crouse, G.L., Leishman, J.G., Bi Nai-pei "Theoretical and Experimental Study of Unsteady Rotor/Body Aerodynamic Interactions," *Journal of the American Helicopter Society*, Vol. 37, No. 1, January 1992, pp. 55–65.

[79] Syal, M., Rauleder, J., Tritschler, J. K., and Leishman, J. G., "On the Possibilities of Brownout Mitigation Using a Slotted-Tip Rotor Blade," 29th AIAA Applied Aerodynamics Conference, Honolulu, Hawaii, June 27–30, 2011.

[80] Syal, M., "Development of a Lagrangian-Lagrangian Methodology to Predict Brownout Dust Clouds," Ph.d. dissertation, Department of Aerospace Engineering, University of Maryland, College Park, MD, 2012.

[81] Syal, M., and Leishman, J. G., "Modeling of Bombardment Ejection in the Rotorcraft Brownout Problem," *AIAA Journal*, Vol. 51, No. 4, April 2013, pp. 549–566.

[82] Tanner, P. E., "Photogrammetric Characterization of a Brownout Cloud," 67th Annual Forum Proceedings of the American Helicopter Society, Virginia Beach, VA, May 3–5, 2011.

[83] Wong, O. D., and Tanner, P. E., "Photogrammetric Measurements of an EH-60L Brownout Cloud," 67th Annual Forum Proceedings of the American Helicopter Society, Phoenix, AZ, May 10–13, 2010.

[84] Shao, Y., and Lu, H., "A Simple Expression for Wind Erosion Threshold Friction Velocity," *Journal of Geophysical Research*, Vol. 105, No. D17, 2000, pp. 22,437–22,443.

[85] Raffel, M., Willert, C., and Kompenhans, J., *Particle Image Velocimetry: A Practical Guide,* Springer Book Company, Berlin, Germany, 1998.

[86] Willert, C. E., and Gharib, M., "Digital Particle Image Velocimetry," *Experiments in Fluids*, Vol. 10, No. 4, January 1991, pp. 181–193.

[87] Huang, H., Dabiri, D., and Gharib, M., "On Errors of Digital Particle Image Velocimetry," *Measurement Science and Technology*, Vol. 8, No. 12, 1997, pp. 1427–1440.

[88] Scarano, F., "Iterative Image Deformation Methods in PIV," *Measurement Science and Technology*, Vol. 13, No. 1, 2002, pp. R1–R19.

[89] Leishman, J. G., "Aeroacoustics of 2-D and 3-D Blade Vortex Interaction Using the Indicial Method," American Helicopter Society 52th Annual Forum Proceedings, Washington D.C., June 4–6, 1996.

[90] Ramasamy, M., and Leishman, J. G., "Benchmarking PIV with LDV for Rotor Wake Vortex Flows," *AIAA Journal*, Vol. 45, No. 11, November 2007, pp. 2622–2633.

[91] Theunissen R., Scarano F., and Riethmuller, M. L., "On Improvement of PIV Image Interrogation Near Stationary Interfaces," *Experiments in Fluids*, Vol. 45, No. BLANK, 2008, pp. 557–572.

[92] Lazar, E., DeBlauw, B., Glumac, N., Dutton, C., and Elliott, G., "A Practical Approach to PIV Uncertainty Analysis," Proceedings of the 27th AIAA Aerodynamic Measurement Conference, Chicago, IL, June 28–July 1, 2010.

[93] Anderson, J. D., *Fundamentals of Aerodynamics* Mcgraw-Hill Companies Inc., New York, NY, 2005.

[94] Leishman, J. G., Bhagwat, M. J., and Bagai, A., "Free-Vortex Filament Methods for the Analysis of Helicopter Rotor Wakes," *Journal of Aircraft*, Vol. 39, No. 5, September–October, 2002, pp. 759–775.

[95] Hall, P., "Taylor–Görtler Vortices in Fully Developed Boundary Layer Flows," *Journal of Fluid Mechanics*, Vol. 124, No. 3, 1982, pp. 475–494.

[96] Leishman, J. G., "Measurements of the Aperiodic Wake of a Hovering Rotor," *Experiments in Fluids*, Vol. 25, No. 4, September 1998, pp. 352–361.

[97] Ramasamy, M., Paetzel, R., Bhagwat, M. J., "Aperiodicity Correction for Rotor Tip Vortex Measurements," American Helicopter Society 67th Annual Forum Proceedings, Virginia Beach, VA, May 3–5, 2011.

[98] Duraisamy, K. Ramasamy, M., Baeder, J. D., and Leishman, J. G., "High-Resolution Computational and Experimental Study of Rotary-Wing Tip Vortex Formation," *AIAA Journal*, Vol. 45, No. 11, November 2007, pp. 2593–2602.

[99] Hance, B. T., "Effects of Body Shapes on Rotor In-Ground-Effect Aerodynamics," M.s. thesis, Department of Aerospace Engineering, University of Maryland, College Park, MD, 2012.

[100] Glaurel, M. B., "The Wall Jet," *Journal of Fluid Mechanics*, Vol. 1, No. 6, 1956, pp. 625–643.